Engineering Nanoscale Materials for Solar Cells

Yahuitl Osorio Mayon

A thesis submitted for the degree of

Doctor of Philosophy

of

The Australian National University

Australian National University

To my parents

Declaration

The work in this thesis is my own, except where otherwise stated. I certify that this thesis does not incorporate, without acknowledgement, any material previously submitted for a degree or a diploma in any university, and that, to the best of my knowledge it does not contain any material previously published or written by another person except where due reference is made in the text. The work in this thesis is my own, except for the contributions made by others as described in the Acknowledgements.

Yahuitl Osorio Mayon

Acknowledgements

I am forever grateful for the advice, guidance, and support of my supervisor Dr. Kylie R. Catchpole, for always making herself available for much valuable discussions. I am also grateful to Dr. Thomas P. White for always providing much useful advice.

I am also grateful to Dr. Antonio Tricoli for his support and guidance with the flame aerosol system. I also want to thank Professor Barry Luther-Davis and Dr. Zhiyong Yang for generously facilitating and providing the antimony trisulphide pellets used for the research in Chapter 4. I also want to thank Dr. Zhiyong Yang for our discussions of chalcogenide glasses which were of great benefit.

I am also grateful to Sukanta Debbarma for assisting with the thermal evaporation of the antimony trisulphide material that was used in Chapter 4.

I am grateful to Guanyu Liu, Noushin Nasiri and Renheng Bo for their assistance and instruction to fabricate the flame-made porous layers used in Chapters 5, 6 and 7 respectively.

I am grateful to The Duong for assisting with the fabrication of the methyl ammonium lead iodide and spiro-OMeTAD that was used in Chapters 6 and 7.

I also want to thank all the of following academics, post-docs, PhD students, and research and technical officers whom also have enriched and made my research experience much more extraordinary than I could have ever imagined: Professor Andrew Blakers, Professor Andres Cuevas, Professor Hoe Tan, Professor Wojciech Lipinski, Dr. Mark Ridgway, Dr. Daniel Macdonald, Dr. Klaus Weber, Dr. Evan Franklin, Dr. Andreas Fell, Dr. Sachin Surve, Dr. Andrew Thomson, Dr. Marco Ernst, Dr. Niraj Lal, Dr. Er-Chien Wang, Dr. Fiona Beck, Dr. Angelika Basch, Dr. Arnold McKinley, Dr. Nicholas Grant, Dr. Elizabeth Thomsen, Dr. Daniel Walter, Dr. Jose Zapata, Dr. Teck Kong, Dr. Tom Ratcliff, Dr. Pheng Phang, Dr. Hang Sio, Dr. Chog Barugkin, Dr. Jelena Muric-Nusic, Dr. Beatriz Velasco, Dr. Xinyu Zhang, Dr. Wensheng Liang, Dr. Siew Lim, Dr. Anyao Liu, Dr. Kean Cheng, Dr. Jie Cui,

Dr. Fiacre Rougieux, Dr. Heping Chen, Dr. Mykalo Lysevych, Dr. Sudha Mokkapati, Dr. Naheem Shahid, Dr. Kaushal Vora, Dr. Li Li, Dr. Melanie Rug, Dr. Frank Brink, Dr. Hua Chen, Ingrid Haedrich, Hieu Nguyen, James Bullock, William Wong, Jin Jin Cong, Di Yan, Shakir Rahman, Erin Crisp, Kate Brooker, Jeremy Smith, Tom Allen, Mohsen Goodarzi, Young Han, Xiao Fu, Ryan Sun, Yiliang Wu, Dale Grant, Christoper Jones, Teng Kho, Rasin Ahmed Tasnim, Bruce Condon, James Cotsell, Nina De Caritat, Christian Samundsett, Maureen Brauers, Mark Saunders, Josephine McKeon, Judy Harvey and Greg Burgess. All of you have contributed one way or another to the development of my research work and experience, for which I am very fortunate and grateful.

ABSTRACT

The purpose of this work is to contribute towards developing high-efficiency low-cost solar cells that have the potential to decrease the cost of solar energy. The focus is on novel device structures that aim to minimise losses and/or allow high-throughput fabrication for antimony sulphide (Sb_2S_3) and the perovskite methyl ammonium lead iodide ($MAPbI_3$).

The first part of the research is on planar Sb_2S_3 solar cells, and led to a twofold efficiency increase through the use of a planar Sb_2S_3 layer with a high proportion of c-axis aligned crystal planes perpendicular to the substrate. The transport of photo-generated carriers along the c-axis aligned Sb_2S_3 crystal planes has a lower recombination rate and longer effective diffusion lengths than for other crystal planes. A completely planar top Sb_2S_3 surface on a textured (non-planar) substrate was fabricated from a non-planar sulphur-rich Sb_2S_3 layer. The planar top surface of the Sb_2S_3 layer facilitates the subsequent deposition of compact, thin and uniform layers of other materials which contributes to improve the photovoltaic performance.

The second part of the research focused on fabrication of porous TiO_2 layers via a flame aerosol system, applied to both Sb_2S_3 and $MAPbI_3$ solar cells. The flame aerosol system is a high-throughput deposition method that could rapidly coat a large area substrate as part of a continuous industrial production line. The mechanical stability of flame-made porous TiO_2 layers is crucial to withstanding the subsequent material depositions processes via solution methods. Different annealing methods were used to increase the mechanical stability of flame-made porous layers for solar cells. The porosity of the flame-made porous TiO_2 layers was easily adjusted over a wide range: from 97% to 35%. A porous TiO_2 layer with a high porosity could improve the solar cell efficiency by increasing the collection efficiency through better infiltration of the other solar cell materials in the porous layer. The optimised $MAPbI_3$ solar cell with flame-made porous TiO_2 layer had a comparable efficiency to the control $MAPbI_3$ solar cell with the standard spin-coated porous TiO_2 layer, demonstrating its potential with scope for further improvement.

The efficiency and stability of perovskite solar cells could be also improved by using SnO_2 instead of TiO_2 as the former has better electronic and photo-catalytic properties than the latter. For this reason, $MAPbI_3$ perovskite solar cells with a flame-made porous SnO_2 layer were also investigated. The $MAPbI_3$ solar cell with a flame-made porous SnO_2 had promising efficiencies even though the main limitation for a higher efficiency was the use of a compact TiO_2 layer with the porous SnO_2 layer.

The work contained in this thesis provides pathways to reduce recombination losses and fabricate a high-throughput low-cost porous structure for Sb_2S_3 and $MAPbI_3$ solar cells. The findings from this work could also be implemented with other materials; particularly with mixed-perovskites and sulphur-based materials.

Table of Contents

1. Introduction

Climate Change

Solar energy is a vast and free form of energy that can substitute the burning of fossil fuels such as coal and oil to generate electricity. It is imperative that the burning of fossil fuels is decreased to prevent a devastating warming of the planet because of the continuous build-up of CO_2 in the atmosphere at the highest concentrations in history [1]. The constant release of high levels of CO_2 and its accumulation in the atmosphere because of the human use of fossil fuels is the cause of climate change [2]. The consequences of this human induced climate change include, but are not limited to: rising sea levels, heating and acidification of the oceans, disruption of ecosystems caused by the extinction of plant and animal species, thriving pests and diseases, normalisation of extreme weather events, permanent flooding of sea level cities and food scarcity [3]. The likelihood and severity of these consequences can be decreased if humanity can minimise its dependence on fossil fuels by increasing the use of solar and other renewable energies [4].

Solar Energy

Solar energy can be considered infinite because the sun will last approximately 5000 million years [5]. The Sun is composed of mainly two gases: hydrogen (75% of mass) and helium (25% of mass) [5]. The electromagnetic energy emitted from the Sun is produced by the constant fusion and fission reaction of these two gases [5]. The energy from the Sun that reaches the Earth's outer atmosphere boundary has a power density (energy rate) of 1366 watts per square metre (W/m^2) (±1%) [6]. This power density value is also known as Air Mass 0 (AM0) because it does not go through the Earth's atmosphere [6, 7]. Figure 1.1 shows this AM0 solar power density, or irradiance, as a function of wavelength and a schematic of AM0 in space.

When the AM0 irradiance passes through the Earth's atmosphere some of its energy is absorbed by the water molecules, oxygen, nitrogen and particles present in the Earth's atmosphere [8]. Once it reaches the surface of the Earth, the solar spectral irradiance has a value which is dependent on the azimuthal angles, latitude, altitude and solar zenith as well as the amount of water and other particles in the atmosphere. For

example, AM1 or when the solar energy goes through exactly one atmosphere the irradiance has a value of 1042 W/m^2. This value is the irradiance at sea level on the equatorial line on a horizontal surface with the sun overhead (at solar noon) [8]. The irradiance value varies throughout both the course of the day and the day of the year (seasons). A standard solar spectral irradiance has been established to enable the testing and comparison of different solar cell technologies [6]. Figure 1.1 shows the international standard AM1.5G (solar zenith 48° and tilted surface at 37° facing the sun) that is used by researchers and manufacturers to test and compare solar cells and modules and that has a value of 1000 W/m^2 [6].

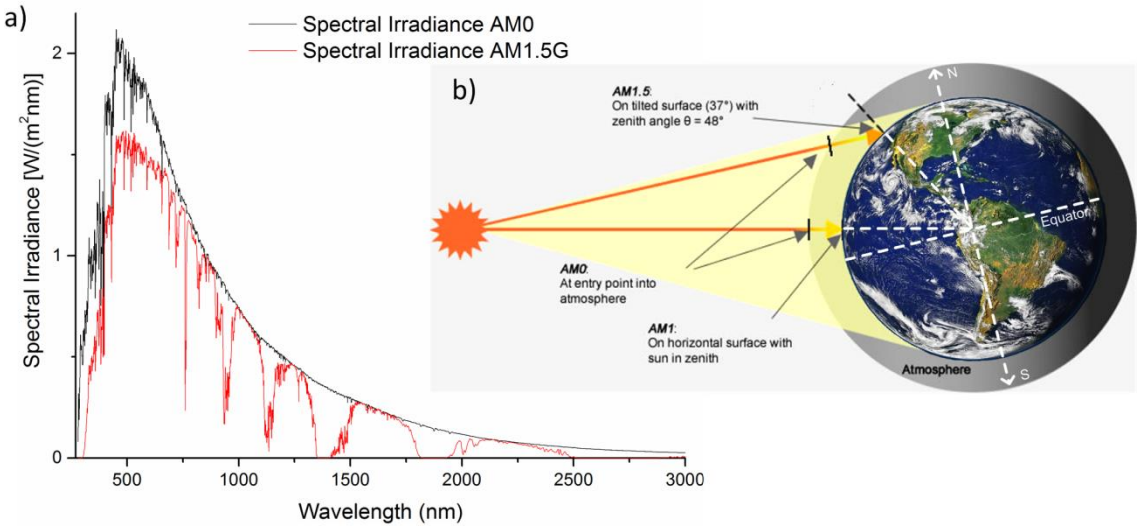

Figure 1.1 a) AM0 (black) and AM1.5G (red) irradiances as a function of wavelength [6]. b) Schematic representation of sunrays hitting the Earth for AM0, AM1 and AM1.5G (adapted from [7]).

Solar energy could provide all of the world's energy needs. The amount of solar energy that reaches the entire Earth's land surface in one year is about 1,186x10^3 terawatt hour (TWh). This amount is about 10 times larger than the world's total energy consumption in 2013 which was 108x10^3 TWh including all forms of energy [9]. The world's total electricity generation in 2013 was 23x10^3 TWh which is 1/5 of the total world's energy consumption in that same year and only 1/50 of the total solar energy reaching the Earth's land surface in one year [9]. Solar cells can conveniently harness the potential of solar energy because they directly convert the solar energy into electricity and can potentially be installed on every surface that is exposed to sunlight. Solar cells can provide all the electrical energy that is required during the day and even

during the night when combined with batteries or hydro-storage systems [10, 11]. Furthermore, solar cells can also provide the electricity for electric vehicles and for the generation of hydrogen to use in hydrogen powered vehicles.

Whilst there is much to be gained by harnessing solar energy, there are also challenges to overcome. Solar cells must become economically competitive to be the first choice over burning fossil fuels by having a high efficiency and low-cost. High efficiency and low-cost solar cells could potentially produce electricity at a much lower cost per kilowatt hour (kWh) than when it is generated from burning fossil fuels. This will also facilitate the installation of solar systems in low economic areas of the world and provide energy independence to individuals and countries.

Solar Cells

Current Status

Major factors influencing solar cells and modules are cost, capacity and demand. The cumulative installed capacity of solar modules has been exponentially growing for the last 30 years (Fig. 1.2). This has been driven by countries such as Germany that since the 1990s has been implementing government policies that facilitated large investments and deployment of solar module systems [12]. Other countries are applying similar policies to combat climate change and to compete for a share of the growing $96 billion dollar solar module market [13, 14]. To illustrate this growth, in four years between 2010 and 2014 the world added 3.5 times more solar capacity than in the previous 30 years [15-17]. The main reason for this is that since 2008, Asia (particularly China and Japan) has become a major driver of installed capacity along with the USA (Fig. 1.2b). If the current growth rate continues, China will soon become the country with the highest cumulative installed solar capacity. In 2014 Germany was the country with the highest cumulative installed capacity (38.2 gigawatt (GW)) followed by China (28.1 GW), Japan (23.3 GW), Italy (18.5 GW) and USA (18.3 GW) [18].

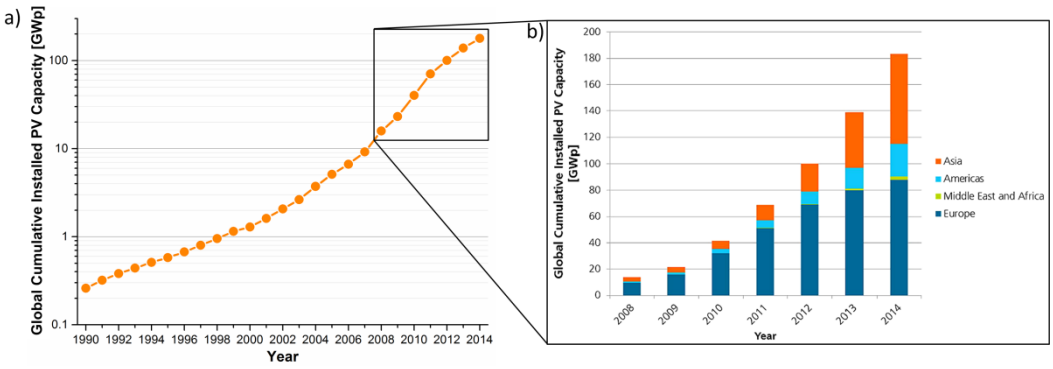

Figure 1.2 a) Global cumulative installed photovoltaic (PV) capacity in Giga watt-peak (GWp) from 1992 to 2014 and b) divided by region from 2008 to 2014 (adapted from [15-17]).

The cost of solar modules has been decreasing for the last 30 years because of technological innovations and economies of scale in large new production facilities (Fig. 1.3a-b) [15-17]. In 2014 the price of a solar module was 50 cents per watt-peak (Wp) (Fig. 1.3b) [15-17]. The main driver for the cost reduction has been the growing low-cost solar module production in China since 2005 (Fig. 1.3a). From 2005 to 2014 the solar module production in China grew from 0.1 GW (1% of the total global production in 2005) to 27 GW (69% of the total global production in 2014) [15]. This large reduction in cost has enabled the growth of installed solar modules in private households and large solar plants around the world [18]. In a relatively short time, the reduction in cost has also made the cost of electricity from solar cells equal to the cost of electricity from fossil fuels in many countries [14].

The global production of solar modules can be divided by technology types that are defined by the fabrication process of the solar cells put inside the solar modules. There are three main technological types of solar cells: mono-crystalline silicon, multi-crystalline silicon and thin film technologies. The 47.5 GW total global production of solar modules in 2014 was composed of 16.9 GW (36%) mono-crystalline silicon, 26.2 GW (55%) multi-crystalline silicon and 4.4 GW (9%) thin film technologies (Fig. 1.3c) [15]. The 4.4 GW (9%) of the thin film technology can be further divided by the material used to make the solar cells: 1.9 GW (4%) cadmium telluride (CdTe), 1.7 GW (3.6%) cadmium-indium-(gallium)-selenide/sulphur (CI(G)S) and 0.8 GW (1.4%) amorphous silicon (Fig. 1.3d) [15].

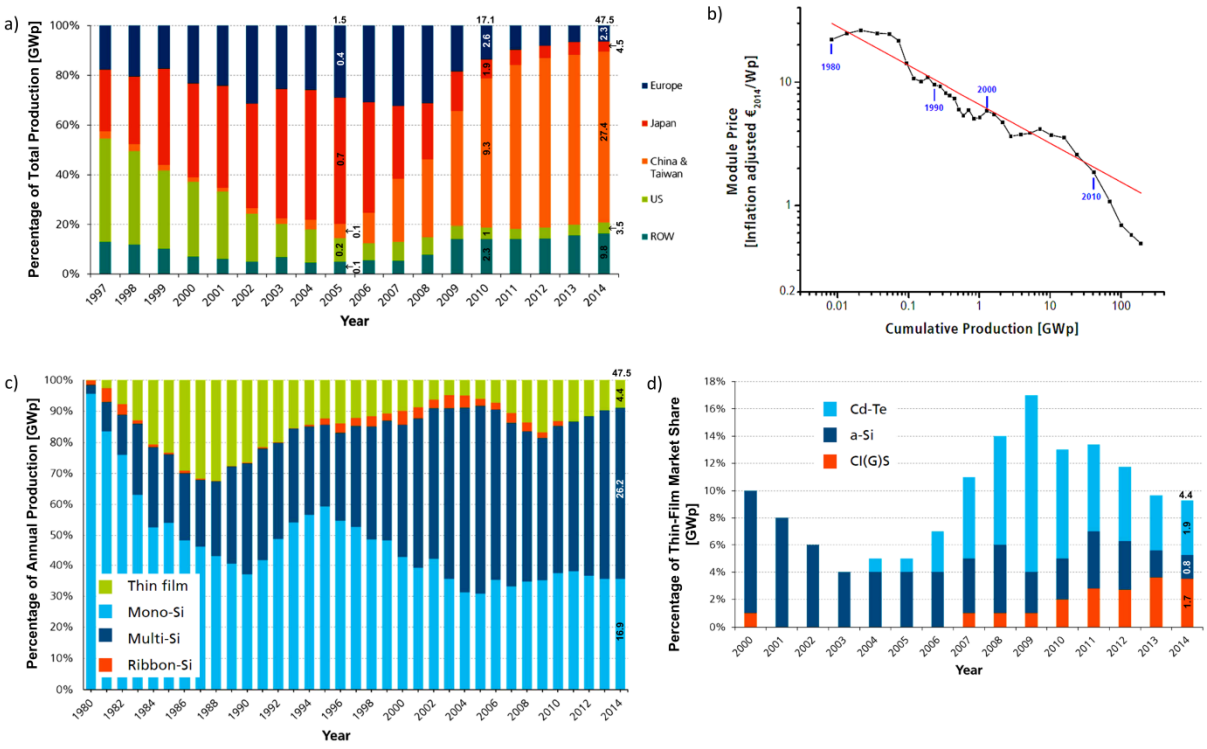

Figure 1.3. a) PV module production by region as a percentage of the total for each year from 1997 to 2014. b) Module price per Watt-peak as a function of cumulative production from 1980 to 2014. c) PV production by technology as a percentage of the global annual production. d) Market share of thin-film technologies as a percentage of the total global annual production divided by type of thin film technology (adapted from [15]).

Limitations

The majority of the production is dominated by a form of crystalline silicon solar cells (91%) because it is an established and reliable technology with module efficiencies of 14 to 21% [14]. However, crystalline silicon based solar cells have various limitations. The maximum possible intrinsic efficiency for a single junction silicon solar cell is 29% [19]. To further reduce the cost of solar cells, the efficiency has to increase whilst keeping the production cost low. The silicon wafer substrate required to make crystalline silicon solar cells is an energy intensive material to produce and therefore an expensive material. The silicon wafer can limit decreasing the costs of silicon based solar cells. Efficiencies of more than 29% at a low-cost for only crystalline silicon solar cells are not possible. The application of crystalline silicon solar cells are also limited by the thick and brittle silicon wafer substrate. Crystalline silicon solar cells are not

bendable and not transparent to visible light. Therefore, they can only be used in flat surfaces that do not bend and in opaque surfaces that do not need light to go through (i.e. they are not suitable for windows). More applications for high efficiency and low-cost solar cells can further increase the use of solar energy in portable and bendable applications such as solar powered portable energy supply for personal electronics. A variety of possible applications can further reduce the use of fossil fuels and give individuals energy autonomy at a low-cost and high efficiency.

Potential Solutions

Thin film solar cell technologies need much less energy intensive materials to make than silicon solar cells and can be just as efficient. The realisation of a high efficiency and low-cost solar cell can be possible with thin film technologies. Thin film solar cells are usually deposited on a glass substrate and the volume of material needed for its production can be about 100 to 200 times less per square metre (m^2) than crystalline silicon solar cells thus decreasing the cost. In addition the efficiency of thin film solar cells can be as high as crystalline silicon based solar cells. Further cost reduction can be achieved with the combination of high efficiency, low material cost, large scale production, efficient supply chains and low capital cost.

The best different thin film solar cells technologies are listed in Table 1.1. Amorphous silicon solar cells have relative low efficiencies of around 10%; plus are expensive to fabricate because of the long deposition times required for the amorphous silicon layer [20, 21]. Organic and dye-sensitised solar cells also have relative low efficiencies of about 10% to 11% with long term stability issues [20, 22, 23]. The best chalcogenide solar cells have efficiencies of about 22.6% however the scarcity and high price of its exotic elements make them unable to be produced at a low-cost and massive scale. Perovskite solar cells have high efficiencies of about 20% and its elements are abundant and of low-cost. The low-cost, abundant and high efficiency of perovskite solar cells makes them the most promising candidate from the available thin film solar cells at this point in time albeit resolving its stability issues (Table 1.1).

The attainable combination of high efficiency, low material cost, large scale production, efficient supply chain and low capital cost for a solar cell can eventually lower the cost of electricity from solar modules by a factor of 2 to 3 from where it is

now [24]. As an example, in Australia the levelised cost of electricity (LCOE) from solar modules in 2013 varied from 20 to 30 cents per KWh depending on the geographical location which could be eventually reduced to between 7 to 15 cents per kWh [14]. Grid parity in Australia was reached in 2013 and a further reduction in the LCOE will clearly make solar the most cost effective option [14].

Tandem solar modules of perovskites and crystalline silicon solar cells can have efficiencies of more than 30% with a theoretical limit of 44% with two junctions [24-27]. This significant increase in the efficiency could be achieved at a low overall cost as previously discussed. A high efficiency and low-cost perovskite solar cell can be made to overlay the existing crystalline silicon based solar cells to boost the electricity generation using the already existing infrastructure. This synergetic combination will lower the cost of electricity. Over a relatively short period of time perovskites are closer to achieving this than all the other thin film technologies. However, all thin film technologies based on Earth abundant materials can potentially achieve this outcome. At this moment in time, further research into perovskite and other thin film technologies is needed to keep building on the existing thin film efficiencies shown in Table 1 to make high efficiency and low-cost solar cells.

Research into how to reliably increase the efficiency and lower the cost of thin film technologies is highly valuable. Finding what can work and what does not work to improve the efficiency is important for the advancement of thin film technologies. Developing strategies or methods that can reduce the cost of thin film solar cells is also essential.

Table 1.1 Emerging thin film technologies with the best solar cells certified efficiencies [20, 28].

Thin film technology	Area (cm^2)	Efficiency (%)	Author (year)
Amorphous silicon:			
	1.0	14.0	AIST (2016)
Organic:			
	1.0	11.0	Toshiba (2013)
	0.04	11.5	Hong Kong UST (2015)
Dye-sensitised:			
	1.0	11.9	Sharp (2011)
Chalcogenides:			
Sb_2S_3	0.12	7.5	KRICT (2015)
Cu_2ZnSnS_4 (CZTS)	0.24	9.1	Toyota Central (2014)
$Cu_2ZnSnS_{4-y}Se_y$ (CZTSS)	0.42	12.6	IBM solution (2013)
CdTe	0.35	22.1	First Solar (2016)
	1.0	21.0	First Solar (2014)
CuInGaS (CIGS)	0.25	22.3	Solar Frontier (2015)
	1.0	21.0	Solibro (2014)
$CuInGaSe_2$	0.5	22.6	ZSW (2016)
Perovskites:			
$MAPbI_3$	1.0	15.0	NIMS (2015)
$(FAPbI_3)_{0.95}(MAPbBr_3)_{0.05}$	0.1	22.1	KRICT/UNIST (2016)

Thesis Research

Thesis Contributions

This thesis contains research on fully inorganic antimony trisulphide (Sb_2S_3) solar cells and methyl ammonium lead iodide ($CH_3NH_3PbI_3$ or $MAPbI_3$) perovskite solar cells. The findings from this research can also be applied to other chalcogenide materials and other perovskite solar cells. The Sb_2S_3 research reported here indicates which crystal planes can give an improved photovoltaic performance because of lower recombination along these planes (longer effective diffusion lengths). A perfectly flat top Sb_2S_3 surface was obtained from annealing a non-planar sulphur-rich Sb_2S_3 layer. The extremely flat top Sb_2S_3 surface facilitates the subsequent deposition of thin and uniform layers of other materials. All these features improved the photovoltaic performance of the planar Sb_2S_3 solar cells reported here.

The potential of a flame-made porous titanium oxide (TiO_2) layer as the electron transport material with Sb_2S_3 as the absorber and copper thiocyanate (CuSCN) as the hole transport material to make a fully inorganic solar cell was also investigated. This particular combination of these materials is not particularly efficient because of their low quality interfaces and materials properties. However, replacing the Sb_2S_3 with $MAPbI_3$ as the active absorber in this configuration is much more promising. The $MAPbI_3$ perovskite research shows that with a flame deposited porous TiO_2 layer, the $MAPbI_3$ perovskite solar cells can be as efficient as with the standard spin-coated porous TiO_2 layer. This can facilitate the low-cost industrial production of perovskite solar cells by implementing a continuous production line from the manufacture of glass to the deposition of the flame-made porous TiO_2 layer. The flame-made TiO_2 layer has the advantage that it can be done continuously over large areas as part of an industrial production line.

The potential of a flame-made tin oxide (SnO_2) porous layer to substitute the porous TiO_2 layer in $MAPbI_3$ solar cells was also investigated. This could potentially increase the overall solar cell performance because SnO_2 has a higher mobility and conductivity than TiO_2 and also is less reactive to ultraviolet (UV) light than the latter.

Thesis Layout

The main goal of the research presented here is to increase the knowledge of inorganic Sb_2S_3 and $MAPbI_3$ perovskite based solar cells to further increase their efficiency and lower their cost. The main rationale for choosing Sb_2S_3 was to build-upon what at the time (late 2011) was one of the best alternative absorbers to make solid dye-sensitised solar cells. This was before perovskites became widely known. I kept working with Sb_2S_3 even when perovskites exploded with the idea to produce a couple of papers. However, only one paper was possible using Sb_2S_3 as the absorber material. Then, I switched to perovskites which are superior absorber materials. The flame-made system can deposit TiO_2 and SnO_2 amongst many other metal oxides. The reason for choosing SnO_2 was because of its superior electronic and optical properties compared to TiO_2. With this in mind, the thesis is divided as follows:

Introduction: The motivation for this solar cell research is outlined here. Also included here is a summary of the current state of solar cells with its limitations and potential for the future.

Chapter 2: The fundamentals of solar cells and a review of the state-of-the-art of fully inorganic Sb_2S_3 solar cells and perovskite solar cells with a porous TiO_2 layer are presented here.

Chapter 3: The materials and deposition methods used in this work are presented here; including experimentally measured data and data collected from the literature.

Four research Chapters:

Chapter 4: Planar inorganic Sb_2S_3 solar cells

Chapter 5: Flame-made porous TiO_2 layers for inorganic Sb_2S_3 solar cells

Chapter 6: Ultra-porous TiO_2 layers for $MAPbI_3$ solar cells

Chapter 7: Flame-made porous SnO_2 layers for $MAPbI_3$ solar cells

Conclusion: Final remarks and future work are presented here.

2. Background Knowledge

2.1 Fundamentals of Solar Cells

Solar cells convert solar energy into electrical energy thereby harnessing a vast and free renewable form of energy. The principle behind solar cells is relatively simple; however they present a number of challenges, such as ensuring efficient absorption and carrier transport in addition to reducing recombination losses in the materials, interfaces, surfaces and contacts. Key concepts are the physical limits of solar cell efficiencies, extraction of photo-generated carriers and the various loss mechanisms. The recent advances of metal organic lead halide perovskite based solar cells are outstanding and highly promising However, more research is needed to make perovskite solar cells commercially available. The research work in this thesis seeks to contribute to the advancement of solar cells by providing ways to improve both efficiency and large scale production of thin film solar cells based on Sb_2S_3 and $MAPbI_3$ as the absorbers. In order to progress further, the basic principles and equations of solar cells need to be understood.

Light Absorption

The full absorption of the solar spectrum in solar cells is a key element of achieving high efficiency and power output. Figure 2.1 shows the solar spectrum as the number of photons per square metre per second (m^2/s) as a function of wavelength and photon energy. The wavelength range from 300 nm to 1130 nm contains about 81% (810 W/m^2) of the AM1.5G solar spectrum energy because the photons included in this range have a much higher energy and count than the rest. The remaining peaks of the solar spectrum account for about 7.8%, 7% and 3.2% each of the AM1.5G solar spectrum energy as depicted in Fig. 2.1. A solar cell that can absorb most of the solar spectrum will generate more electrical current because ideally every absorbed photon generates one electron that contributes to the electrical current output of the solar cell. This one-for-one photon to electron generation means the solar cell has an ideal 100% internal quantum efficiency (IQE).

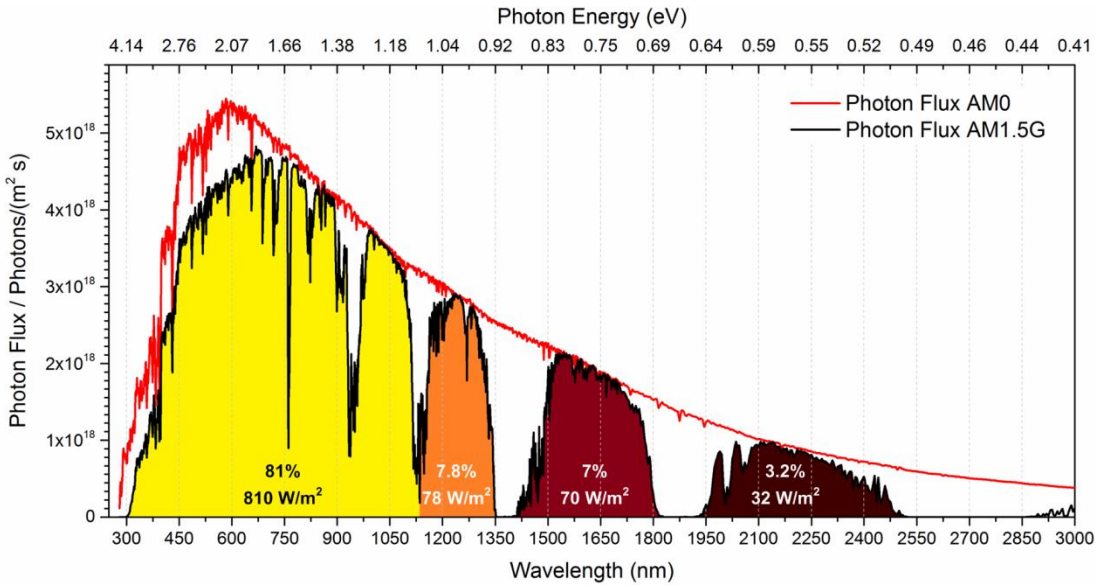

Figure 2.1 Solar spectrum AM0 and AM1.5G in photons per square metre per second as a function of wavelength and photon energy in units of electron Volts (eV). The solar spectrum AM1.5G has been divided into 4 sections marked by a different colour with its corresponding percentage of the total energy.

The photo-generated current in a solar cell depends on the reflection, transmission and absorption of light within the materials that make the solar cell. All of the absorbable light must ideally enter the absorber material in the solar cell and remain in this layer until it is completely absorbed. This can be done by optimising the thickness of the material layers that make the solar cell and with light trapping structures. The optical characteristics of the solar cells depend on the refractive index (n) and absorption coefficient (α) of the solar cell materials. The absorption length (1/α) indicates the thickness that is required to absorb 63% of the light energy in a single pass at a particular wavelength. The absorption coefficient and absorption length for several materials as a function of wavelength are shown in Fig. 2.2. Thin film solar cells require less material to make than crystalline silicon solar cells because they are made with an absorber material that has a higher absorption coefficient than silicon and thus a thinner layer is required to absorb all of the light. For example, to absorb most of the light up to its absorption-edge wavelength silicon has to be tens or hundreds of micrometres thick whereas Sb_2S_3 and $MAPbI_3$ can be ≤ 500 nanometres thick.

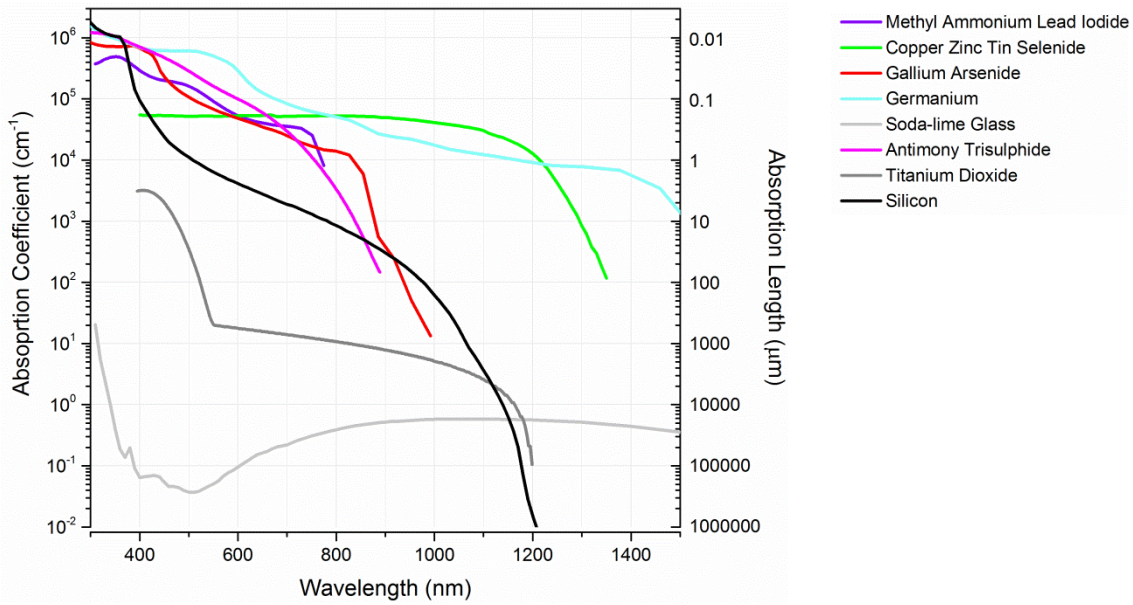

Figure 2.2 Absorption coefficient and absorption length as a function of wavelength of various materials. The absorption coefficients of methyl ammonium lead iodide, antimony trisulphide, titanium dioxide were calculated from experimentally measured data by ellipsometry. For the other materials the data was taken from the following references [29-31].

Photovoltaic Effect

Solar cells convert solar energy into electrical energy by means of the photovoltaic effect that consists of the creation of a voltage within a material when it absorbs photons of energy equal or greater than the band gap. The absorbed photons provide enough energy to the electrons so they can move from the valence band into the conduction band leaving holes behind. The valence and conduction energy bands are formed by the addition of single atomic orbitals when many atoms come together to form molecules and then a macroscopic solid as represented in Fig. 2.3a. For each element or compound, the position of their valence and conduction energy bands depends on its atomic and chemical configuration. The conduction and valence bands can become overlapped or half filled (as in a metal) or separated by a small (< 3 eV) or a large (> 3 eV) amount of energy for semiconductor and insulators as represented in Fig. 2.3b. The photo-generated voltage in a solar cell is set by the energy difference between the quasi-Fermi energy levels of the photo-generated carriers in the valence band and the conduction band of the absorber material. The photo-generated carriers

in the conduction and valence band are then extracted through the contacts of the solar cell to provide electricity.

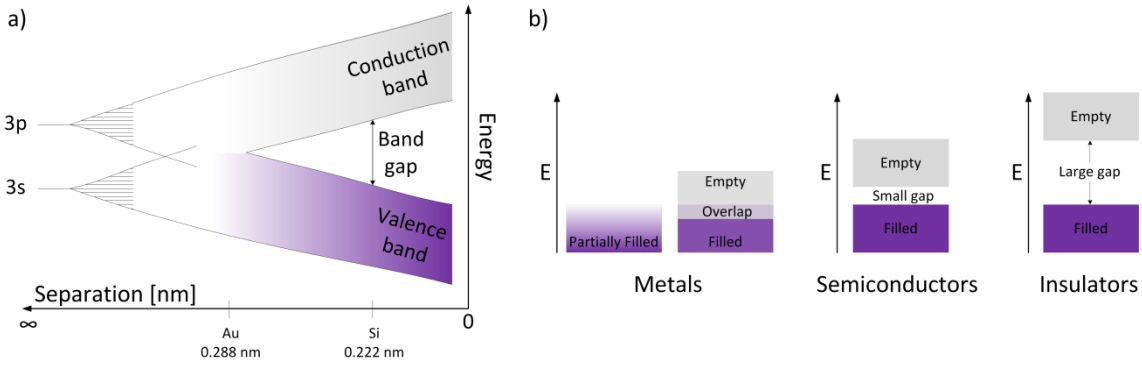

Figure 2.3 a) Schematic of the formation of the energy bands from single atoms. b) Representation of the conduction and valence bands in metals, dielectrics and semiconductors.

Utopic Efficiency Limits

Without taking into account neither thermodynamic laws nor losses of any kind, the ultimate voltage of a single junction solar cell can be defined solely by the energy value of the band gap. Therefore, the voltage of a solar cell depends linearly on the energy band gap of the absorber material as shown in Fig. 2.4. Absorber materials with a large band gap should ideally generate a higher voltage than materials with a small band gap. The ultimate current in a solar cell is defined by the maximum number of photons that can be absorbed which depends on the energy band gap of the absorber as shown in Fig. 2.4. Absorber materials with a small band gap can ideally absorb a larger number of photons and thus should generate a larger current than materials with a large band gap. The efficiency of a solar cell is defined as the ratio of the output power by the input power. The output power of the solar cell is the maximum product of its photo-generated current and voltage. The input power is the solar irradiance on the solar cell. An extremely simple and idealised estimation of the efficiency as a function of the absorber band gap is shown in Fig. 2.4. The highest efficiencies of about 43% are for absorbers with a band gap of 1.1 eV. However, these values are impossible to obtain because of thermodynamic laws that have not been taken into account. In reality, the maximum possible voltage and current values are lower than these idealised values as discussed in the next paragraph.

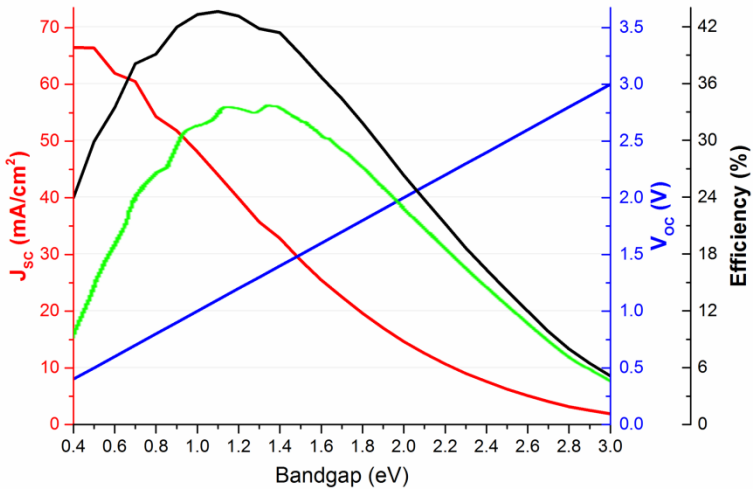

Figure 2.4 Ultimate solar cell efficiency (black line), voltage (blue line), current density (red line) and the Shockley-Queisser detailed balance limit of solar cell efficiency (green line) as a function of the absorber material band gap [32, 33].

Detailed Balance Efficiency Limit

The upper limit for the voltage is lower than the band gap energy because of the thermodynamic balance that requires the cell to be in thermal equilibrium with its environment. To be in equilibrium, the solar cell undergoes spontaneous light emission or radiative recombination that decreases the voltage. Radiative recombination occurs when an electron that was energised to the conduction band moves back to a hole in the valence band emitting a photon. In addition, absorbed photons with energies larger than the band gap generate only one electron-hole pair and the excess energy is lost as heat. The efficiency limit derived by Shockley and Queisser (SQ) takes these factors into account [32]. The SQ detailed balance limit of the solar cell efficiency as a function of the absorber bandgap is shown as a green line in Fig. 2.4. The SQ upper limit for the efficiency of a single junction solar cell is about 33%. Further improvements in the efficiency of solar cells use this limit as a benchmark for single junction solar cells.

Solar Cell Structure

The photo-generated carriers (electrons and holes) in the absorber material that move to the conduction band and valence band have to be extracted separately to produce an electric current. This is done by contacting the absorber with carrier selective

contacts of specific materials. The contact with an electron transport material (ETM) accepts electrons and blocks holes while the contact with a hole transport material (HTM) accepts holes and blocks electrons. These electron and hole selective contacts can be formed respectively with n-type and p-type semiconductors that are transparent to the incoming solar light and with good conductivities. These selective contacts do not usually have a high conductivity and other materials with a higher conductivity are needed to efficiently transport the photo-generated carriers out of the solar cell. These conductor materials are usually metals or transparent conductive oxides. Figure 2.5 shows schematically the ETM, absorber and HTM separating the photo-generated carriers.

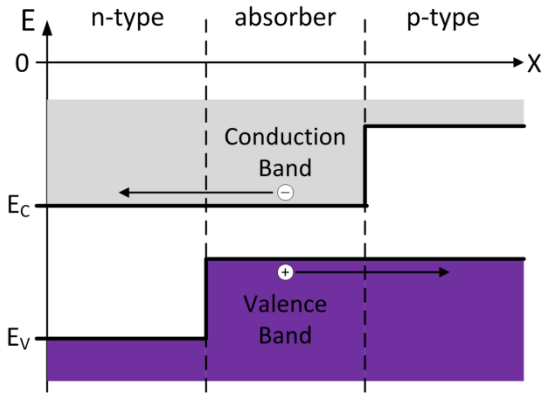

Figure 2.5. Simplified energy band diagram of an idealised heterojunction solar cell showing the absorber material and the selective contacts for electrons (n-type semiconductor) and holes (p-type semiconductor).

Solar Cell Performance Parameters

A conventional current density-voltage (J-V) characteristic curve of a solar cell under illumination is shown in Fig. 2.6. The open circuit voltage (V_{OC}) is the largest voltage that can be delivered by the solar cell with no current extraction. The short-circuit current density (J_{SC}) is the largest current per area that can be delivered by the solar cell with no voltage output. However, to produce power the solar cell has to deliver both voltage and current values that are somewhat lower than V_{OC} and J_{SC}. Therefore, solar cells have to operate at maximum power point (P_{mpp}) defined by the product of specific voltage and current density known as V_{mpp} and J_{mpp}.

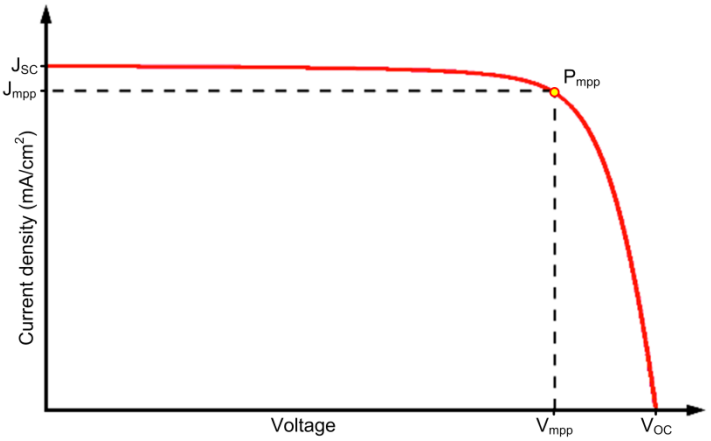

Figure 2.6 Characteristic J-V curve of a solar cell with labels for V_{OC}, J_{SC}, V_{mpp} and J_{mpp}.

The fill factor (FF) is a measure of series and parallel resistances within the solar cell and is defined as the ratio of P_{mpp} by the product of V_{OC} and J_{SC}, as in the following equations:

$$FF = \frac{P_{mpp}}{V_{OC} J_{SC}} = \frac{V_{mpp}\, J_{mpp}}{V_{OC}\, J_{SC}}$$

Solar cells with low resistance and contact losses have a FF of about ≥ 80%. The efficiency of a solar cell is the ratio of the power generated divided by the incident power (P_{in}), as in the following equations:

$$Efficiency = \frac{P_{mpp}}{P_{in}} = \frac{V_{mpp}\, J_{mpp}}{P_{in}} = \frac{V_{OC}\, J_{SC}\, FF}{P_{in}}$$

The equation that generally describes the J-V curve of a solar cell is:

$$J_{total} = -\left(J_{light} - J_0 e^{\left(\frac{qV}{nkT-1}\right)}\right)$$

The extracted photo-current (J_{total}) depends on the amount of the generated photo-current density (J_{light}) minus the value of the recombination current density (J_0). The value of J_0 depends on all of the recombination processes within the solar cell. The V_{OC} can be found from the general solar cell equation when the extracted photo-current is equal to zero (J_{total} = 0):

$$V_{OC} = \frac{kT}{q} ln\left(\frac{J_{light}}{J_0}\right)$$

Thus, the V_{OC} can be significantly reduced by a large value of J_0 which is a representation of all the recombination mechanisms happening within the solar cell. A reduction of the recombination processes in the solar cell will make the value of J_0 smaller and therefore increase the V_{OC} and J_{SC} and thus the efficiency of the solar cell.

Efficiency Losses

The voltage in a solar cell is decreased from its theoretical SQ limit by non-radiative recombination processes. These non-radiative processes can be Auger recombination, band tail recombination, bulk recombination, interface recombination and surface recombination. Auger recombination occurs when an electron-hole pair recombines giving its energy to another electron or hole whose gained energy is dissipated as heat. Band tail and bulk recombination occurs via energy levels within the band gap which originate from several types of defects in the crystal lattice. The energy levels within the band gap facilitate the recombination of electrons with holes releasing energy as heat. The surface and interfaces of semiconductors are a discontinuity in the crystal lattice and therefore have many defects such as dangling bonds and crystal lattice mismatch that are recombination centres for electrons and holes. These recombination mechanisms can significantly affect the lifetime and diffusion length of electrons and holes and consequently lower the voltage and efficiency of the solar cell. The non-radiative recombination processes can be alleviated by improving the crystal growth, surface passivation and interfaces of the materials of the solar cell. In addition, another voltage loss is the non-utilisation of the excess energy of the photons with energies larger than the band gap which instead is dissipated as heat.

The current in a solar cell is decreased from its theoretical SQ limit by the incomplete absorption of light and incomplete collection of photo-generated carriers. The probability of photon absorption depends on the thickness and properties of the absorber material. In addition, every absorbed photon generates only one electron-hole pair.

In addition to the voltage and current losses, the solar cell can also suffer from resistive and contact losses. The FF is a measure of resistive and contact losses. A FF value close to one means there are negligible resistive and contact losses.

While a FF value closer to zero means there are more resistive and contact losses within the solar cell. The resistive losses can originate from a large series resistance and/or small shunt resistance that the photo-generated carriers experience as they are extracted from the solar cell.

Remarks

Many materials and structures for solar cells are being investigated and optimised by researchers all over the world to aim for the highest possible efficiency and low-cost solar cell. Optimisation strategies include increasing the light absorption and minimising the recombination mechanisms of the solar cell materials. This is a difficult and complex research problem to solve that has been under research for about 60 years now, since the reports of the first silicon solar cell in the 1950s [34-36]. The research contained here on planar Sb_2S_3 solar cells seeks to reduce the recombination within Sb_2S_3 to improve its efficiency. In addition, the research on $MAPbI_3$ perovskite solar cells provides an alternative method for the development of high throughput and large area production of perovskite solar cells. The potential of using another electron transport material to improve the performance of $MAPbI_3$ solar cells is demonstrated. The concepts and equations outlined in this section are used throughout the thesis to assess the improvements and differences between different solar cells. The next section of this thesis focuses on reviewing the development and current state-of-the-art of fully inorganic Sb_2S_3 solar cells and $MAPbI_3$ solar cells.

2.2 Literature Review

The research in this thesis builds upon the entire body of work discussed in this literature review. The thesis research shows how to fabricate Sb_2S_3 layers with a completely planar top surface and a non-planar bottom surface to improve the efficiency of planar Sb_2S_3 solar cells. Further insights are given to decrease the recombination losses within the Sb_2S_3 layer. The potential and limitations of ultra-porous TiO_2 layers for fully inorganic Sb_2S_3 solar cells were also investigated. In addition, specifically regarding perovskite solar cells, ultra-porous TiO_2 and SnO_2 layers for perovskite solar cells were investigated with the goal to improve the efficiency and develop low-cost fabrication processes for perovskite solar cells. The thesis research will be explained in complete detail in the Chapters 4, 5, 6 and 7.

Note: To see the figures in this Chapter look for the journal paper cited in each figure.

Solar cells have to be developed with three key elements in mind: to maximise the absorption of light and the collection and transport of photo-generated carriers, and minimise the recombination mechanisms. Key to the success of high efficiency solar cells are a large current-density, high voltage and high fill factor at a low-cost. The development of high efficiency dye-sensitised solar cells was pioneered by O'Regan and Grätzel in 1991 [37]. Substantial research to optimise the performance of this type of solar cell led to the subsequent development of solid dye-sensitised solar cells, then solid semiconductor solar cells with many different types of absorber materials and then perovskite solar cells. Table 2.1 shows a summary of the highest efficiencies of all these types of solar cells. The solar cells in Table 2.1 along with other solar cells of the same type but with lower efficiencies will be discussed in more detail in the rest of this Chapter.

The research community has exerted its greatest efforts in finding and developing the combination of absorber, ETM and HTM that give the highest light absorption, transport and collection of the photo-generated carriers with minimum recombination at low-cost. This thesis further contributes to these efforts by providing evidence on how to improve the photovoltaic performance of Sb_2S_3 and on potential alternative ETM structures for high throughput and low-cost production of efficient perovskite solar cells.

Table 2.1 Summary of the highest efficiency solar cells of dye-sensitised solar cells with a liquid electrolyte, semiconductor-sensitised solid solar cells and perovskite solar cells. This table includes only solar cells that have been reported in peer-reviewed journals.

Solar Cell Type Author (year) Material detail	V_{OC} (volts)	J_{SC} (mA/cm^2)	FF	Efficiency (%)	Remarks
Dye-sensitised solar cells with liquid electrolyte					
Mathew et al. (2014)	0.910	18.1	0.78	13.0	70% porosity TiO_2 layer
Dye-sensitised solid solar cell (no liquid electrolyte)					
Ding et al. (2009)	0.860	6.9	0.68	4	Spiro-OMeTAD as HTM
Semiconductor-sensitised solid solar cells (no dye, no liquid electrolyte)					
Choi et al. (2014)	0.711	16.1	0.65	7.5	Sb_2S_3
Fully inorganic Sb_2S_3-sensitised solid solar cells					
Ito et al. (2013) Sb_2S_3 by CBD	0.607	16.3	0.57	5.6	Titanium doped Sb_2S_3 60% porosity TiO_2 layer
Fully Inorganic Planar or Flat Sb_2S_3 solar cell (without porous TiO_2)					
Muto et al. (2013)	0.550	4.3	0.35	0.8	Compact TiO_2/Sb_2S_3/CuSCN
Perovskite-sensitised solar cells with liquid electrolyte					
Im et al. (2011) $MAPbI_3$	0.706	15.8	0.57	6.5	Liquid electrolyte and a 3.6 µm porous TiO_2 layer with a $Pb(NO_3)_2$ treatment
Perovskite-sensitised solid solar cells					
Saliba et al. (2016) $Cs_{0.05}(MA_{0.17}FA_{0.83})_{(0.95)}Pb(I_{0.83}Br_{0.17})_3$	1.147	23.5	0.785	21.17	Lithium doped 150-200 nm porous TiO_2 layer and spiro-OMeTAD as HTM

2.2.1 Dye-Sensitised Solar Cells

Dye-sensitised cells are characterised by the use of a dye as the absorber material. The dye is deposited on a porous TiO_2 layer to increase its light absorption by increasing the effective area of the solar cell. In addition, the porous TiO_2 layer serves as the ETM and a liquid electrolyte is the HTM. This solar cell demonstrated a new way to make solar cells that enabled low-cost facilities and materials to be used. However, the requirement to encapsulate the liquid electrolyte and the low efficiency of these solar cells compared to commercially available silicon solar cells halted their commercial success. Nevertheless, the simple and easy construction of dye-sensitised solar cells facilitated wide spread solar cell research throughout the world. This allowed a large amount of research to be conducted on different absorber materials that eventually led to the discovery of metal-organic lead halide perovskites for high efficiency solar cells. The significant report of the first dye-sensitised solar cell is discussed next.

Grätzel Solar Cell

In 1991 O'Regan and Grätzel [37] reported the first high efficiency dye-sensitised solar cell. The reported efficiency was 7.12%, with a V_{OC} of 0.680 V, J_{SC} of 11.5 mA/cm^2, and FF was 0.68 at a light intensity of 750W/m^2. The dye served as the absorber, the porous TiO_2 was the ETM and the electrolyte was the HTM. The effective area of the solar cell was increased 780 times by using a 10 µm thick porous layer of TiO_2 nanoparticles which was then coated with dye molecules. It was reported as a majority carrier solar cell with no minority carriers involved in the photo-conversion process thereby minimising the recombination losses. The photo-generated voltage was set by the difference of the quasi-fermi energy levels in the TiO_2 and the electrolyte as shown in Fig. 2.7. In this report the current efficiency yield as a function of wavelength was defined as the product of the absorptance (generation of carriers) times the charge injection efficiency (transfer of carriers) times the collection efficiency (transport of carriers). The light absorption and subsequent collection of the photo-generated carriers was enhanced by using the porous TiO_2 layer and the liquid electrolyte.

See Figure 1 from O'Regan, B. and M. Grätzel, Low cost and highly efficient solar cells based on dye-sensitized colloidal TiO_2 films. Nature, 1991. 335(24): p. 737-740.

Figure 2.7 Schematic representation of the principle of the dye-sensitised solar cell. The thick black horizontal lines indicate the electron (e^-) energy level in the different materials. The voltage of the solar cell upon illumination corresponds to the difference, ΔV, between the quasi-Fermi energy level of the TiO_2 and the electrochemical potential of the electrolyte. (adapted from O'Regan and Grätzel (1991)).

Dye-Sensitised Solar Cells After 20 Years

Since the report in 1991 by O'Regan and Grätzel, there has been a substantial amount of work by different researchers to further improve the performance of this type of solar cell. The main strategies to improve the performance of dye-sensitised solar cells have been engineering of the dyes and electrolytes to increase the light absorption and the injection and transport efficiencies, in addition to reducing the recombination at their interfaces. Introducing a extremely thin layer of another material at the interface between the dye and the TiO_2 layer can also reduce the recombination at the

interfaces. In 20 years, these strategies have led to significant improvements as discussed in the following paragraphs.

Significant recombination rates can originate from the interface area between the porous TiO_2 layer, the dye and the electrolyte. The porous TiO_2 layer has a large surface area which amplifies the interface recombination losses. In a bid to reduce the interface recombination rates, an extremely thin layer of gallium oxide (Ga_2O_3) was deposited on the porous TiO_2 before the dye deposition [38, 39]. The extent of the reduction of the recombination losses by the Ga_2O_3 coating layer depended largely on the dye and electrolyte used. With certain dyes and electrolytes a slight improvement in V_{OC}, J_{SC} and FF was observed by the use of a Ga_2O_3 layer [39]. In contrast, with a different dye and electrolyte the V_{OC} increased slightly but J_{SC} decrease significantly [38]. The authors of these studies concluded that the gains depend on the Ga_2O_3 conduction band position and oxidation state as well as its surface isoelectric property with regards to the charge of the electrolyte redox species [38]. Therefore, in addition to controlling all the chemical, physical and electronic properties of the materials that make a solar cell, their interactions and interfaces must also be investigated and optimised.

Mathew et al. (2014) reported that the engineering of the dye and electrolyte have produced the highest dye-sensitised solar cell efficiency of 13% with a V_{OC} of 0.91 V, J_{SC} of 18.1 mA/cm^2, and FF of 0.78 [40]. This solar cell had a 7 µm thick porous TiO_2 layer with a porosity of 70% made of 32 nm (transparent) and 400 nm (scattering) nanoparticles. A summary of the performance parameters of the dye-sensitised solar cells discussed above is given below in Table 2.2.

Table 2.2 Summary of the performance parameters of the dye-sensitised liquid electrolyte solar cells mentioned above.

Dye-sensitised liquid electrolyte solar cells					
Author (year)	**V_{OC} (volts)**	**J_{SC} (mA/cm^2)**	**FF**	**Efficiency (%)**	**Remarks**
O'Regan & Gratzel (1991)	0.680	11.5	0.68	7.1	At 0.75 suns
Mathew et al. (2014)	0.910	18.1	0.78	13.0	70% porosity TiO_2 layer

Another strategy to improve the performance of dye-sensitised solar cells was to substitute the absorbing dyes for quantum dots of different materials such as lead sulphide (PbS), cadmium sulphide (CdS), silver sulphide (Ag_2S), bismuth sulphide (Bi_2S_3) and Sb_2S_3 which are known as metal chalcogenides. Liquid electrolyte solar cells with metal chalcogenide quantum dots were first reported in 1994 by Vogel et al. with an efficiency of 0.3% [41]. The metal chalcogenides were deposited on the porous TiO_2 layer by repetition of sequential dips in two different chemical solutions. The highest efficiency achieved so far for a liquid electrolyte quantum dot solar cell is 9.3% with a V_{OC} of 0.7 V, J_{SC} of 20.8 mA/cm^2 and FF of 0.64 measured at one sun intensity [42]. This solar cell was made with cadmium selenium telluride (CdSeTe) quantum dots on a 9 µm thick porous TiO_2 layer with a liquid polysulphide electrolyte as the HTM. The porous TiO_2/CdSeTe quantum dot matrix had a triple coating layer consisting of TiO_2, zinc sulphide (ZnS) and silicon oxide (SiO_2) to reduce recombination and improve collection efficiency.

However, the dye-sensitised solar cells described above with optimised efficiencies have not solved the issues of degradation and long term operation. Over time, the liquid electrolyte can cause some dyes and metal chalcogenide absorbers to decompose. Furthermore, the liquid electrolyte has to be enclosed and sealed in a reliable, durable and resistant structure. This is not an easy feat for a solar cell module with an encapsulated liquid electrolyte because it has to be able to last for 20 plus years exposed to the outside weather. The weather can heat the solar cell module to 80 °C or cool it to freezing temperatures depending on where it is on Earth and the season. Weather also leads to exposure to humidity and large quantities of UV rays. All these factors put the solar cell module structure and materials under severe stress. One possible solution to this problem is to substitute the liquid electrolyte with a solid material which will be discussed next.

Dye-Sensitised Solid Solar Cells (without Liquid Electrolyte)

Dye-sensitised solid solar cells were the next evolutionary step in a bid to overcome the disadvantages of dye-sensitised liquid electrolyte solar cells. The liquid electrolyte presents a number of disadvantages as discussed in the previous section which can be overcome by substituting it with a solid material. The substitution of the liquid

electrolyte with a solid material means fewer fabrication steps and potentially increased long term reliability, making dye-sensitised solid solar cells easier to fabricate and at a lower cost than dye-sensitised liquid electrolyte solar cells.

Over the course of the years, several solid materials have been used to substitute the liquid electrolyte. These can be divided into inorganic and organic HTMs; each with its own advantages and disadvantages. In general terms, a suitable solid p-type semiconductor to substitute the liquid electrolyte has to be able to efficiently transport holes and block electrons from the absorber material. It also has to be able to fill in all the pores within the porous TiO_2 layer. The performance of each solar cell depends on the combination of all the materials involved, their properties and interfaces, as discussed in the rest of this Chapter.

The first reported dye-sensitised solar cell with a solid HTM was in 1995 by Tennakone et al. (1995), using copper iodide (CuI) as the solid inorganic HTM [43]. The performance parameters of this solar cell were a V_{OC} of 0.375 V and J_{SC} of 2.5 mA/cm^2 measured at 800 W/m^2. The following year, O'Regan and Schwartz (1996) reported a planar or flat dye-sensitised solid solar cell with electrodeposited copper thiocyanate (CuSCN) as the inorganic HTM [44]. A planar or flat solar cell does not have the porous TiO_2 layer that is characteristic of dye-sensitised solar cells to increase the dye absorption and its effective area. In this planar dye-sensitised solid solar cell a single monolayer of dye was deposited on top of a planar compact TiO_2 layer. This solar cell had a V_{OC} of 550 mV and J_{SC} of 0.04 mA/cm^2 measured at 30 W/m^2 of white light with a wavelength (λ) > 470 nm.

An easier method to deposit the inorganic CuSCN HTM layer for dye-sensitised solid solar cells was first reported in 2001 by Kumara et al. (2001). Kumara et al. (2001) reported the deposition of CuSCN from a solution of CuSCN in n-propyl sulphide [45]. The deposition method consisted of covering the porous TiO_2 layer with drops of CuSCN solution and then evaporating the solvent to create a solid CuSCN layer. This process is repeated until the desired CuSCN thickness is achieved. This solar cell had an efficiency of 1.25% with a V_{OC} of 0.616 V, J_{SC} of 3.5 mA/cm^2 and FF of 0.58 measured at one sun intensity. The main contribution of this work, later employed by other

researchers, was the development of a solution based method to effectively deposit CuSCN into the porous TiO_2 layer.

The next significant development was the introduction of an organic HTM instead of the inorganic HTM. In 1998, the use of the organic solid HTM 2,2',7,7'-tetrakis(N,N-di-p-methoxyphenylamine)9,9'-spirobifluorene (spiro-OMeTAD) was first reported by Bach et al. (1998) in a solar cell with a 4.2 µm thick porous TiO_2 layer [46]. This solar cell had an efficiency of 0.74% with a V_{OC} of 0.342 V, J_{SC} of 0.32 mA/cm^2, and FF of 0.62 measured at one sun intensity. The main disadvantage of a solid HTM in dye-sensitised solid solar cells is the incomplete pore filling within the porous TiO_2 layer which means increased resistance and recombination of the photo-generated carriers. Optimisation of the pore filling of spiro-OMeTAD into the porous TiO_2 layer led to a dye-sensitised solid solar cell with an efficiency of 4%, a V_{OC} of 0.86 V, J_{SC} of 6.9 mA/cm^2 and FF of 0.68 measured at one sun intensity [47]. Other disadvantages of solid p-type semiconductors for dye-sensitised solid solar cells are their low conductivities and high recombination rates at the interface with the dyes and porous TiO_2 nanostructure [48]. Table 2.3 summarises the photovoltaic performance parameters of the dye-sensitised solid solar cells discussed in the previous paragraphs in chronological order.

Table 2.3 Summary of the dye-sensitised solid solar cells mentioned above in chronological order.

Dye-sensitised solid solar cells					
Author (year)	**V_{OC} (volts)**	**J_{SC} (mA/cm^2)**	**FF**	**Efficiency (%)**	**Remarks**
Tennakone et al. (1995)	0.375	2.5	NA	< 0.75	At 0.8 suns, with CuI as the inorganic HTM
O'Regan & Schwartz (1996)	0.550	0.04	NA	< 0.006	At 0.3 suns, planar solar cell, electrodeposited inorganic CuSCN as the HTM
Bach et al. (1998)	0.342	0.32	0.62	0.74	4.2 µm thick porous TiO_2 layer with spiro-OMeTAD as HTM,
Kumara et al. (2001)	0.616	3.5	0.58	1.25	Doctor-bladed CuSCN as the HTM
Ding et al. (2009)	0.860	6.9	0.68	4	Spiro-OMeTAD as HTM

As mentioned previously, another improvement strategy has been to substitute the absorbing dyes for quantum dots of different semiconductor materials, as well as the liquid electrolyte for a solid p-type semiconductor. Following this strategy along with optimising light absorption and minimising recombination has led to outstanding

results for different solar cell materials and structures. As an example, the highest efficiency for an all solid metal chalcogenide quantum dot solar cell was reported in 2015 by Carey et al. (2015). This solar cell has an efficiency of 9.2% with a V_{OC} of 0.54 V, J_{SC} of 29.5 mA/cm^2 and FF of 0.58 measured at one sun intensity [49]. It was made using a 600 nm thick layer of fused and passivated PbS quantum dots on top of a planar compact TiO_2 layer. The passivated PbS quantum dots resulted in a 3-fold increase in diffusion length compared to the un-passivated quantum dots. The HTM consisted of an evaporated molybdenum oxide (MoO_3)–metal contact on top of the PbS quantum dots.

The work with dye-sensitised solar cells and quantum dots solar cells has led to the use of extremely thin films of various semiconductors as absorbers instead of dyes or quantum dots. Even absorber materials with short diffusion lengths can be used in these types of solar cells because of the extremely thin absorber layers that are required. This strategy opened the door to the use of many absorber semiconductor materials as discussed in the following section.

2.2.2 Semiconductor-Sensitised Solid Solar Cells

Semiconductor-sensitised solid cells are a development of dye-sensitised solid solar cells where the dye is replaced by a semiconductor absorber material. Tennakone et al. reported the first semiconductor-sensitised solid solar cells in 1998. They used a 6 μm thick mesoporous TiO_2 layer coated with a 23 nm thick selenium layer (electrodeposited) and then coated with CuSCN [50]. The efficiency of this solar cell was 0.6% as calculated from the measured J-V curve under 800W/m^2 of simulated sunlight which generated a V_{OC} of 0.6 V, J_{SC} 3 mA/cm^2 and FF of 0.27. This solar cell did not have a compact TiO_2 layer between the transparent conducting oxide and the porous TiO_2 layer coated with selenium which decreased its shunt resistance and thus its FF and efficiency. In addition, the increase of the effective cell area by the porous TiO_2 layer increased the interface recombination processes which also decreased the solar cell efficiency.

Since 1998 many different absorber materials have been used to substitute the dye in this type of solar cell. The main absorber materials used are metal chalcogenides such

as cadmium selenide (CdSe), antimony triselenide (Sb_2Se_3), indium trisulphide (In_2S_3), copper indium disulphide ($CuInS_2$), lead selenide (PbSe), PbS, CdS, Sb_2S_3 and similar compounds. A chalcogen is defined as any element from the group VI-A of the periodic table: oxygen (O), sulphur (S), selenium (Se), tellurium (Te) and polonium (Po). A chalcogenide is a chemical compound that has at least one element from this group as a negative ion. Oxygen has different chemical behaviour compared to other chalcogens, and is often treated separately. Metal chalcogenides have a high absorption coefficient and useful bandgaps for solar energy absorption. Thin films of chalcogenide materials can be deposited on a variety of substrates by vapour or liquid techniques such as evaporation, sputtering and chemical solution baths. Many metal chalcogenides have been used to make semiconductor-sensitised solid solar cells. The metal chalcogenide absorbers that have produced the higher semiconductor-sensitised solar cell efficiencies are cadmium chalcogenides (CdS, CdSe and CdTe), lead chalcogenides (PbS and PbSe) and antimony chalcogenides (Sb_2S_3 and Sb_2Se_3). Table 2.4 presents a summary of semiconductor-sensitised solid solar cells with the aforementioned chalcogenide absorber materials.

Table 2.4 Summary of semiconductor-sensitised solid solar cells with different metal chalcogenide absorber materials.

Semiconductor sensitised solid solar cells					
Author (year)	**V_{OC} (volts)**	**J_{SC} (mA/cm^2)**	**FF**	**Efficiency (%)**	**Absorber material**
Arici et al. (2003)	0.790	0.26	0.44	0.1	CuInS
Ernst et al. (2003)	0.670	8.9	0.22	1.3	CdTe
Larramona et al. (2006)	0.850	2.3	0.66	1.3	CdS
Hernandez-Borja et al. (2011)	0.290	14	0.36	1.6	PbS
Huynh et al. (2002)	0.700	6	0.40	1.7	CdSe
Lee et al. (2008)	0.502	11.6	0.49	2.9	CdSe-ZnS
Dittrich et al. (2008)	0.546	11.1	0.53	3.2	In_2S_3
Nanu et al. (2004)	0.490	18	0.45	4	$CuInS_2$
Zhou et al. (2015)	0.400	25.1	0.56	5.6	Sb_2Se_3
Choi et al. (2014)	0.711	16.1	0.65	7.5	Sb_2S_3

There are some chalcogenide materials such as copper indium gallium selenide (CIGS) and CdTe that have produced high efficiency thin film solar cells. The highest certified efficiency for a CIGS and CdTe thin film solar cell are 22.6% and 21.5% respectively [20, 51]. In contrast to the solid semiconductor sensitised solid solar cells discussed above,

CIGS and CdTe thin film solar cells do not have a porous TiO_2 layer and the compact absorber layer thickness is ≥ 1 µm. However, the cost and rarity of indium and gallium precludes CIGS thin film solar cells from being commercialised in a vast industrial scale. Nonetheless, the company Solar Frontier is commercialising CIS solar cells [52]. The toxicity and rarity of tellurium excludes CdTe thin film solar cells from taking over the solar cell market. Nevertheless, the company FirstSolar is installing CdTe solar cells in commercial scale photovoltaic plants around the world [53]. There is also ongoing research to reduce the cost of CIGS and CdTe thin film solar cells. These thin films solar cells demonstrate that chalcogenide materials can make high efficiency solar cells. The continuous research progress with chalcogenide absorbers could result in a new low-cost and high efficiency chalcogenide solar cell.

Sb_2S_3-sensitised solid solar cells reported by Choi et al. (2014) have attained efficiencies of 7.5% whereas the other metal chalcogenide materials have resulted in sensitised solid solar cell with lower efficiencies [54]. The development of fully inorganic Sb_2S_3-sensitised solid solar cells will be discussed next.

2.2.3 Sb_2S_3-Sensitised Solid Solar Cells

Inorganic materials usually last longer and are more stable than organic materials. Silicon and gallium arsenide (GaAs) solar cells are completely made of inorganic materials and can last more than 20 years. The durability and stability of inorganic materials motivated the development of fully inorganic Sb_2S_3-sensitised solid solar cells. Fully inorganic semiconductor-sensitised solid solar cells based on other absorber materials are also subjects of a great deal of research. However, Sb_2S_3 has the advantage of being relatively cheap and abundant; with the added benefit of producing reasonable solar cell efficiencies. The following paragraphs outline the development of fully inorganic Sb_2S_3-sensitised solid solar cells which have a porous TiO_2 layer. The porous TiO_2 layer is an inheritance from its predecessor, the dye-sensitised solar cells, and its function is to increase the collection of carriers and the effective area of the solar cell.

Sb_2S_3 Solid Solar Cells with a Porous TiO_2 Layer

Fully Inorganic Sb_2S_3 Solid Solar Cells with a Porous TiO_2 Layer

The first Sb_2S_3-sensitised solid solar cell was reported in 2009 by Itzhaik et al. (2009). Figure 2.8a-b shows a schematic of the structure and energy band levels of this solar cell. The surface of the 2 µm thick porous TiO_2 scaffold was treated with an indium, hydroxyl and sulphur compound ($In_X(OH)_YS_Z$) before the Sb_2S_3 deposition to improve the stability of the Sb_2S_3 layer by stopping the Sb_2S_3 discolouration with no reported effect in the performance of the solar cell [55]. The Sb_2S_3 layer of 5 nm to 10 nm thickness was deposited on the porous TiO_2 layer via the chemical bath deposition (CBD) method previously reported by Nair et al. (1998) [56]. Before the CuSCN deposition, the Sb_2S_3 layer was coated with potassium thiocyanate (KSCN) at 65 °C to reduce interface resistance and increase the J_{SC}. Itzhaik et al. stated that the efficiency of this solar cell was increased by 30% because of passivation of the Sb_2S_3 layer via oxidation in air. This solar cell was composed of the following layers TiO_2/In-OH-S/Sb_2S_3/(KSCN)CuSCN and had an efficiency of 3.37% with a V_{OC} of 0.490 V, J_{SC} of 14.1 mA/cm^2 and FF of 0.49 measured at one sun intensity. Itzhaik et al. established that the finished solar cells required storage to reach their maximum efficiency through an increase in J_{SC} and FF. The efficiency improvement after storage was suggested to be a result of the CuSCN becoming more conductive as its solvent (di-*n*-propyl sulphide) completely evaporates.

For a) see Figure 1 of Nezu, S.L., G.; Chone, C.; Jacob, A.; Delatouche, B.; Pere, D.; Moisan C., Light Soaking and Gas Effect on Nanocrystalline TiO_2/Sb_2S_3/CuSCN Photovoltaic Cells following Extremely Thin Absorber Concept. J. Phys. Chem. C, 2010. 114: p. 6854–6859.

For b) see Figure 6 of Boix, P.P.L., G.; Jacob, A.; Delatouche, B.; Mora-Sero, I.; Bisquert, J., Hole Transport and Recombination in All-Solid Sb_2S_3-Sensitized TiO_2 Solar Cells Using CuSCN As Hole Transporter. J. Phys. Chem. C, 2012. 116: p. 1579–1587.

Figure 2.8 a) Diagram of the fully inorganic Sb_2S_3-sensitised solid solar cell including the transparent conductive oxide (TCO) glass substrate (adapted from Nezu et al.

(2010)). b) Energy Band diagram at equilibrium of the same cell (adapted from Boix et al. (2012)).

The following year Nezu et al. (2010) reported a fully inorganic Sb_2S_3 solar cell with an efficiency of 3.7%, a V_{OC} of 0.560 V, J_{SC} of 11.6 mA/cm^2 and FF of 0.58 measured at one sun intensity [57]. This solar cell consisted of a 3 µm thick porous TiO_2 layer treated with aluminium oxide (Al_2O_3), then a Sb_2S_3 layer, followed by a lithium thiocyanate (LiSCN) treatment and then a CuSCN coating which resulted in a 500nm CuSCN capping layer. The Sb_2S_3 deposition was also done using the CBD method reported by Nair et al. (1998). The particles of the porous TiO_2 layer (average size 40-50 nm) were treated with Al_2O_3 to act as a buffer layer to reduce back recombination. The porous TiO_2 layer had a 50% porosity [58].They reported a 4.6 times increase in efficiency from its initial value after 100 minutes of light soaking (exposure to 1 sun light intensity at open circuit conditions in air atmosphere) with an increase in V_{OC}, J_{SC}, and FF of 20%, 50% and 130% respectively. The FF had the largest increase from about 0.25 to 0.58 after light soaking. Figure 2.9 shows this improvement in V_{OC}, J_{SC}, FF and efficiency with the measured J-V curves at different times of light soaking. The rate of increase in the efficiency per time was higher with the solar cell temperature in the 40 to 60 °C range than with the cell temperature in the 25 to 30 °C range. They also indicated that the UV light component had no relationship with the increase in efficiency with light soaking.

See Figure 2 of Nezu, S.L., G.; Chone, C.; Jacob, A.; Delatouche, B.; Pere, D.; Moisan C., Light Soaking and Gas Effect on Nanocrystalline TiO_2/Sb_2S_3/CuSCN Photovoltaic Cells following Extremely Thin Absorber Concept. J. Phys. Chem. C, 2010. 114: p. 6854–6859.

Figure 2.9 Measured efficiencies (η) and J-V curves of a TiO_2/Sb_2S_3/(LiSCN)CuSCN cell at one sun intensity at different times after starting light soaking under ambient air at open circuit (cell active area of 0.54 cm^2) (adapted from Nezu et al. (2010)).

Nezu et al. (2010) investigated the use of sodium thiocyanate (NaSCN) and KSCN for the surface treatment of Sb_2S_3/TiO_2 porous structure before the CuSCN deposition with similar results to the previously reported LiSCN treatment by Nezu et al. (2010). The performance enhancement after light soaking was determined to be related to the oxygen in the air. The suggested mechanism was that the CuSCN layer filled with

thiocyanate molecules $(SCN)_2$ formed via active oxygen species such as OH radicals and/or formed by photocatalytic oxidation of the negative ion, SCN^-, or its solvent (di-*n*-propyl sulphide). Nevertheless, humidity in the air was found to degrade the solar cell performance over a long period of time. These significant changes with light and humidity were mostly attributed to the CuSCN material although other possibilities were not ruled out.

Studies of Limiting Factors of Sb_2S_3 Solid Solar Cells

From 2010 to 2012 the best efficiencies for the fully inorganic Sb_2S_3-sensitised solar cells remained at around 3.5% with V_{OCs} at around 0.5 V. This prompted research to find the intrinsic causes for these V_{OCs} and low efficiencies despite the 1.6 eV bandgap and high attenuation coefficient of Sb_2S_3. In 2012 Boix et al. (2012) characterised a 3 µm porous $TiO_2/Al_2O_3/ Sb_2S_3$/(KSCN)CuSCN solar cell using impedance spectroscopy [59]. Based on these measurements, they proposed an analytical model to determine the essential features of this type of solar cell. The porous TiO_2 layer had a porosity of 50% [58]. The solar cell used in this study had an efficiency of 3.2% with a V_{OC} of 0.6 V, J_{SC} of 10 mA/cm^2 and FF of 0.53 measured at one sun intensity. Two main factors were identified to limit the efficiency of this solar cell: one is the inefficient transport of holes within the CuSCN that reduces the FF and the other is the large recombination that limits the V_{OC}. The inefficient hole transport was attributed to a high resistance in the CuSCN. The large recombination was attributed to the Sb_2S_3 itself. The Sb_2S_3 for this work was deposited using the now widely used CBD method [56].

The following year, Christians and Kamat (2013) used transient absorption spectroscopy to determine the hole transfer rate of photo-generated holes from traps or defects within the Sb_2S_3 [60]. They found that the hole transfer rate into the traps/defects in the Sb_2S_3 is 3 orders of magnitude faster than the transfer rate of the holes from these Sb_2S_3 traps/defects to the CuSCN. This significant difference makes the overall transfer of holes from the Sb_2S_3 to the CuSCN slower than the transfer of electrons from the Sb_2S_3 to the TiO_2. Consequently, the build-up of holes in the Sb_2S_3 might increase recombination with electrons at the TiO_2-Sb_2S_3 interface. The traps for holes within the bulk crystalline Sb_2S_3 were assigned to the breakage of the weaker long range antimony-sulphur (Sb-S) bonds where a hole is trapped by the sulphur

radical. The estimated hole transfer rate to the traps (sulphur radicals) was $4.5x10^{11}s^{-1}$ whereas the hole transfer rate from these traps to the CuSCN was $5.9x10^{8}s^{-1}$. The Sb_2S_3 was deposited using the CBD method reported by Nair et al. (1998) in a 2µm TiO_2/Sb_2S_3/(KSCN)CuSCN configuration which generated an efficiency of 3.3% with a V_{OC} of 0.455 V, J_{SC} of 12.4 mA/cm^2 and FF of 0.59 measured after 2 hours of light soaking. The porous TiO_2 layer had a porosity of about 50% [61]. The strategy suggested to improve the transfer of holes was to modify the Sb_2S_3-CuSCN interface. Similarly, the suggested approach to reduce the recombination of photo-generated electrons in the TiO_2 with the traps/defects within the Sb_2S_3 was to modify the TiO_2-Sb_2S_3 interface. Other improvement strategies are to reduce the number of traps/defects in the Sb_2S_3 or use a different HTM.

Darga et al. (2013) used a wide range of techniques to characterise the Sb_2S_3 layer to explain why the V_{OC} and efficiency remained low in Sb_2S_3-sensitised solar cells [62]. It was found that the dependency of J_{SC} on light intensity is not linear thus the dominating recombination is also not linear. The diffusion length decreases with light intensity; at one sun intensity the estimated ambipolar diffusion length was about 75 nm. The non-linear relationship of J_{SC} and diffusion length with increasing light intensity (carrier density) was associated with a continuous availability of recombination centres that stems from a continuum exponential distribution of states within the Sb_2S_3 bandgap. Darga et al. suggested that in this type of solar cell the recombination may be assisted by a strong tunnelling effect because of the extremely thin Sb_2S_3 layer and the availability of recombination centres within the bandgap. It was also suggested that vacancies or substitutional defects may create these recombination centres within the bandgap. The Sb_2S_3 layer used in this study was also deposited with the CBD method [56].

Fully Inorganic ALD Sb_2S_3 Solid Solar Cell with a Porous TiO_2 layer

Most of the Sb_2S_3 used for semiconductor-sensitised solid solar cells has been deposited using the CBD method from Nair et al. (1998) [56]. This method is relatively easy to implement but because of the nature of the method the resulting Sb_2S_3 is neither pure nor stoichiometric. This motivated the development of other deposition methods that could produce a pure and stoichiometric Sb_2S_3 layer in order to minimise

the recombination mechanisms discussed in the previous paragraphs. Wedemeyer et al. (2013) deposited Sb_2S_3 via atomic layer deposition (ALD) in a 2µm porous TiO_2/Sb_2S_3/(LiSCN)CuSCN solar cell configuration which produced an efficiency of 2.4% with a V_{OC} of 0.470 V, J_{SC} of 3.2 mA/cm^2 and FF 0.48 at one sun intensity [63]. The ALD Sb_2S_3 was found to be free of antimony oxides with an Sb to S ratio of 2:3 for the as-deposited Sb_2S_3 layer. Consequently, the Sb_2S_3 layer deposited by ALD is stoichiometric and free of oxide compounds. The optimised ALD Sb_2S_3 coating thickness for maximum solar cell efficiency was 10nm with an ALD growth rate of 0.66 nm per cycle. The as-deposited Sb_2S_3 had a homogeneous thickness across the depth of the porous TiO_2 layer that became non-continuous after the 300°C annealing step. Regardless of the Sb_2S_3 being oxide free and with an ideal Sb:S ratio of 2:3, the photo-generated V_{OC} and efficiency remained low. This could have been in part because of the Sb_2S_3 itself and also because of the other materials used and their interfaces.

Improvement of Fully Inorganic Sb_2S_3 Solar Cells

Tsujimoto et al. (2012) reported that thin coatings of barium titanate ($BaTiO_3$) and magnesium oxide (MgO) on the surface of the 2.5 µm thick porous TiO_2 (30 nm TiO_2 particle size) improved the cell performance [64]. The improved efficiency was 4.1% with a V_{OC} of 0.584 V, J_{SC} of 13.4 mA/cm^2 and FF of 0.53 measured at one sun intensity. This was a 20% increase in efficiency with respect to previously reported efficiency values. It was reported that the TiO_2 surface treatment with MgO improved the J_{SC} and with $BaTiO_3$ improved the V_{OC} and FF. The thickness of the $BaTiO_3$ and MgO layers were assumed to be ≤ 1 nm because they could not be observed by transmission electron microscopy (TEM). Electron probe micro analysis (EPMA) was used to confirm the existence of barium and magnesium. It was suggested that these surface treatments reduce the back recombination from TiO_2 to CuSCN. They also suggested the possible existence of a new phase between $BaTiO_3$, MgO and Sb_2S_3 or doping of Sb_2S_3. The thickness of the Sb_2S_3 deposited by CBD on the porous TiO_2 was estimated to be in the 0.5 to 2 nm range. In the following year, the same research group via Ito et al. (2013) reported that doping the Sb_2S_3 with titanium together with the previously reported $BaTiO_3$ and MgO coatings of the 2.5 µm thick porous TiO_2 layer further improved the cell efficiency to 5.6% with a V_{OC} of 0.607 V, J_{SC} of 16.3 mA/cm^2 and FF of

0.57 at one sun intensity [65]. This was a 37% increase in efficiency from the previously reported efficiency of 4.1% where the V_{OC}, J_{SC} and FF increased by 4%, 22% and 8% respectively. The porous TiO_2 layer had a porosity of about 60% [61]. X-ray photoelectron spectroscopy (XPS) measurements of Sb_2S_3 doped with titanium revealed the formation of the titanium-antimony (Ti-Sb) bond whereas bismuth doped Sb_2S_3 formed the compound Bi_2S_3 by making Bi-S bonds. This research shows that titanium doped Sb_2S_3 could have fewer traps for the holes thus increasing the transfer rate of holes and consequently improved efficiency.

A summary of all the fully inorganic Sb_2S_3-sensitised solid solar cells discussed so far is presented in Table 2.5.

Table 2.5 Photovoltaic performance parameters of the fully inorganic Sb_2S_3-sensitised solid solar cells previously discussed in chronological order.

Fully inorganic Sb_2S_3-sensitised solid solar cells					
Author (year) Sb_2S_3 deposition method TiO_2 porosity value	**V_{OC} (volts)**	**J_{SC} (mA/cm^2)**	**FF**	**Efficiency (%)**	**Remarks**
Itzhaik et al. (2009) Sb_2S_3 by CBD TiO_2 porosity 40-50%	0.490	14.1	0.49	3.37	2 µm TiO_2/In-OH-S/Sb_2S_3/(KSCN)CuSCN
Nezu et al. (2010) Sb_2S_3 by CBD TiO_2 porosity 40-50%	0.560	11.6	0.58	3.7	3 µm TiO_2/Al_2O_3/ Sb_2S_3/(LiSCN)CuSCN
Boix et al. (2012) Sb_2S_3 by CBD TiO_2 porosity 40-50%	0.600	10	0.53	3.2	3 µm TiO_2/Al_2O_3/ Sb_2S_3/(KSCN)CuSCN
Tsujimoto et al. (2012) Sb_2S_3 by CBD TiO_2 porosity 50-60%	0.584	13.4	0.53	4.1	2.5 µm thick porous TiO_2 with $BaTiO_3$ and MgO coatings
Wedemeyer et al. (2013) Sb_2S_3 by ALD TiO_2 porosity 40-50%	0.470	3.2	0.48	2.4	2µm porous TiO_2/Sb_2S_3/(LiSCN)CuSCN
Christians and Kamat (2013) Sb_2S_3 by CBD TiO_2 porosity 40-50%	0.455	12.4	0.59	3.3	2µm TiO_2/Sb_2S_3/(KSCN)CuSCN
Ito et al. (2013) Sb_2S_3 by CBD TiO_2 porosity 50-60%	0.607	16.3	0.57	5.6	2.5 µm thick porous TiO_2 Titanium doped Sb_2S_3

Organic-Inorganic Sb_2S_3 Solid Solar Cells with a Porous TiO_2 Layer

It should be noted that many reports have been published of Sb_2S_3-sensitised porous TiO_2 solar cells with organic HTMs such as poly(3-hexylthiophene) (P3HT), poly(2,6-(4,4-bis(2-ethylhexyl)-4H-cyclopenta[2,1-*b*;3,4,*b'*]di-thiophene)-*alt*-4,7)2,1,3-benzothiadiazole (PCPDTBT) and poly(3,4-ethylenedioxythiophene) doped with poly(4-styrenesulphonate) (PEDOT:PSS) [54, 66-70]. When these organic HTMs are used, the efficiency improves to a value between 3.6% and 6%. This efficiency improvement is because of the higher conductivity of organic HTMs and the reduction in resistance/recombination at the interface between Sb_2S_3 and the organic HTM. The highest efficiency for a Sb_2S_3-sensitised solid solar cell with an organic HTM was obtained by sulphurisation of the CBD Sb_2S_3 deposited on a 1.3 µm thick porous TiO_2 layer in conjunction with a PCPDTBT/PEDOT:PSS layer [54]. This optimised Sb_2S_3-sensitised solar cell had an efficiency of 7.5% with a V_{OC} of 0.711 V, J_{SC} of 16.1 mA/cm^2 and FF of 0.65 measured at one sun intensity [54]. Nevertheless, a high efficiency fully inorganic Sb_2S_3 solar cell remains a challenge and a desirable outcome as inorganic materials tend to be more stable, durable and cheaper than organic materials.

Planar Sb_2S_3 Solar Cells (without a Porous TiO_2 Layer)

The Sb_2S_3-sensitised solar cells discussed so far were made using a porous TiO_2 layer with a thickness of 1 to 3 µm. The elimination of the porous TiO_2 layer simplifies the solar cell by reducing the surface recombination or interface effects between the large surface area of the porous TiO_2 and the Sb_2S_3 layers. This planar solar cell configuration can provide additional insights into the properties of solar cell materials and their interface properties. However, to make high-efficiency extremely thin planar solar cells a light trapping scheme is usually necessary to enhance its light absorption. The absorber thickness has to be comparable to its ambipolar diffusion length to efficiently collect all the photo-generated carriers. The publications that have reported the solar cell performance of fully inorganic planar Sb_2S_3 solar cells will be discussed next.

Fully Inorganic Planar Sb_2S_3 Solar Cell

In 2013 Muto et al. (2013) reported a planar or flat solar cell with a $TiO_2/Sb_2S_3/CuSCN$ structure as represented in Fig. 2.10. This planar solar cell had an efficiency of 0.8% with a V_{OC} of 0.550 V, J_{SC} of 4.3 mA/cm^2 and FF of 0.35 measured at one sun intensity [70]. The thickness of the planar Sb_2S_3 layer was between 45 to 65 nm and it was deposited via the CBD method. The V_{OC} was larger and the FF lower than in their control porous $TiO_2/Sb_2S_3/CuSCN$ solar cell. The increase of the V_{OC} was attributed to a reduced surface area recombination in the planar solar cell compared to the cells with a porous TiO_2 layer. The decrease of the FF was attributed to an inefficient charge screening that increases the carrier resistance. Muto et el. (2013) estimated a less than 80 nm ambipolar diffusion length in Sb_2S_3 at one sun intensity. This is the only paper so far that has reported the solar cell performance of a fully inorganic Sb_2S_3 planar solar cell.

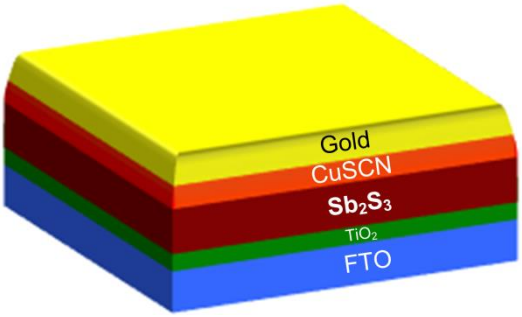

Figure 2.10 Schematic of the fully inorganic Sb_2S_3 solar cell structure which consists of planar layers of fluorine-doped tin oxide (FTO), TiO_2, Sb_2S_3, CuSCN and gold.

The thickness of the Sb_2S_3 layer in a planar solar cell configuration has to be ≤ 100 nm as mentioned previously because of the short diffusion length of Sb_2S_3. This extremely thin planar Sb_2S_3 solar cell configuration is particularly equivalent to that of commercial thin film solar cells except that the thickness of the absorber is in 10s of nanometres and not in micrometres. Improvement strategies from the development of commercial thin film solar cells could be investigated for use in this extremely thin film solar cell.

Organic-Inorganic Planar Sb_2S_3 Solar Cell

It should also be noted that there have been several reports of planar Sb_2S_3 solar cells with organic HTM such as P3HT, PCPDTBT and PEDOT:PSS [66, 70-72]. The injection of carriers from Sb_2S_3 to an organic HTM is more efficient than to CuSCN and as a result the efficiency increases from 0.8% to between 1.4% and 3.6%. The highest efficiency for a planar Sb_2S_3 solar cell with organic HTMs was 5.7% with a V_{OC} of 0.667 V, J_{SC} of 14.9 mA/cm^2 and FF of 0.58. [71]. This solar cell used P3HT/PEDOT:PSS as the organic HTM and a 90 nm Sb_2S_3 layer deposited by ALD. Nevertheless, this efficiency is still low and a high efficiency extremely thin planar Sb_2S_3 solar cell remains a challenge. In order to develop a high efficiency Sb_2S_3 solar cell it is necessary to further increase our understanding of how to reduce the recombination within the Sb_2S_3 layer and at the interfaces of this solar cell.

2.2.4 Perovskite-Sensitised Solid Solar Cells

The development of sensitised solar cells since 1991 has allowed the use and testing of many absorber materials. Since 2009, organic-metal halide perovskites have emerged as suitable absorber materials to make high efficiency sensitised solar cells. A halide is a chemical compound between a halogen anion and a cation of another element. A halogen is any element from the group VII-A of the periodic table: fluorine (F), chlorine (Cl), bromine (Br), iodine (I) and astatine (At). A perovskite is any material that has a chemical structure similar to calcium titanate ($CaTiO_3$) which is an ABX_3 structure where A and B are two cations (A larger than B) and X is an anion that bonds to both. Organic-metal halide perovskites with different cations and anions have been used as absorber materials in solar cells with different results. The development of organic-metal halide perovskite-sensitised porous TiO_2 solar cells will be discussed next.

Perovskite-Sensitised Solar Cells with Liquid Electrolyte

The first report of a perovskite-sensitised solar cell was by Kojima et al. (2006). In this first report, the perovskite material replaced the dye in a dye-sensitised liquid

electrolyte solar cell. A methyl ammonium lead-bromide perovskite compound ($CH_3NH_3PbBr_3$ or $MAPbBr_3$) was spin-coated on a porous TiO_2 electrode and then a liquid electrolyte was used as the HTM. The energy levels of the valence band and the conduction band of the perovskite estimated by photoelectron spectroscopy and optical measurements were 5.27 eV and 3.25 eV, respectively. Therefore the bandgap of $MAPbBr_3$ was estimated to be 2.02 eV. The efficiency of this solar cell was 2.2% with a V_{OC} of 0.64 V, J_{SC} of 6.44 mA/cm^2 and FF of 0.53 measured at one sun intensity [73].

Following on from the report above, Kojima et al. (2009) reported 8-12 µm thick porous TiO_2 layers sensitised with either spin-coated $MAPbBr_3$ or methyl ammonium lead iodide ($CH_3NH_3PbI_3$ or $MAPbI_3$) perovskite with a liquid electrolyte as the HTM [74]. The perovskites were reported to form nanoparticles of 2 nm to 3 nm in size on the surface of the porous TiO_2 layer. The estimated $MAPbBr_3$ and $MAPbI_3$ bandgaps using photoelectron spectroscopy and optical measurements were reported to be 2.02 eV and 1.44 eV respectively. The estimated bandgap values could have been affected by the nano-sized perovskite particles (quantum confinement effect). The estimated bandgap values indicate that $MAPbI_3$ should absorb more light and have a larger J_{SC} than $MAPbBr_3$. The $MAPbBr_3$ solar cell had an efficiency of 3.1% with a V_{OC} of 0.96 V, J_{SC} of 5.6 mA/cm^2 and FF of 0.59 whereas the $MAPbI_3$ solar cell had an efficiency of 3.8% with a V_{OC} of 0.61 V, J_{SC} of 11 mA/cm^2 and FF of 0.57 measured at one sun intensity [74]. Kojima et al. (2009) mentioned that the photo-generated current decreased upon continuous irradiation. These first results showed that good photovoltaic performance using perovskites was possible.

The third report of a perovskite-sensitised solar cell was by Im et al. (2011) which consisted of spin-coated $MAPbI_3$ perovskite on a 3.6 um thick porous TiO_2 layer that had been treated with lead nitrate $Pb(NO_3)_2$ [75]. A liquid electrolyte served as the HTM. The efficiency of this solar cell was 6.5% with a V_{OC} of 0.706 V, J_{SC} of 15.8 mA/cm^2 and FF of 0.57 at one sun intensity [75]. Im et al. (2011) investigated different $MAPbI_3$ solution concentrations along with several annealing temperatures. The optimum annealing temperature was found to be 100°C and the optimum $MAPbI_3$ solution concentration was 40 weight percent (wt%). The lead to iodide ratio of the deposited $MAPbI_3$ was 1:3 as measured by scanning electron microscope-energy dispersive spectroscopy (SEM-EDS). The porous TiO_2 was found to be covered with perovskite

dots of about 2.5 nm in diameter as observed by TEM. The research reported that the perovskite solar cell is not stable when exposed to continuous sunlight as it degrades by 80% after 10 minutes of continuous exposure. This significant increase in efficiency from the previous reports of Kojima et al. (2006, 2009) was achieved by optimising only the perovskite layer.

Perovskite Solid Solar Cell (without liquid electrolyte)

The first published paper of a perovskite-sensitised solid solar cell (with a solid HTM instead of the liquid electrolyte) was by Kim et al. (2012) in August 2012. This solar cell had a thin porous TiO_2 layer sensitised with $MAPbI_3$ perovskite. Its efficiency was 9.7% with a V_{OC} of 0.888 V, J_{SC} of 17.6 mA/cm^2 and FF of 0.62 measured at one sun intensity [76]. This was an important and impressive milestone for perovskite-sensitised solid solar cells because the efficiency value was much higher than that of any other semiconductor-sensitised solar cell and was attained in the first report on a solar cell of this kind. The thickness of the porous TiO_2 layer was varied from 600 nm to 1.5 µm and the optimum value was found to be 600 nm because thicker porous TiO_2 layers increased the surface area recombination therefore reducing the V_{OC} and FF. The perovskite layer was deposited by spin-coating a $MAPbI_3$ solution in γ-butyrolactone (GBL) and then drying at 100°C for 15 min. On top of the perovskite-sensitised porous TiO_2 layer, a 550 nm spiro-OMeTAD layer was used as the organic HTM. Figure 2.11a shows the complete structure of such solar cell. The 1.5 eV optical band gap and 5.43 eV valence band maximum of $MAPbI_3$ were determined from reflectance and ultraviolet photoelectron spectroscopy (UPS) measurements. The conduction band energy level was estimated at 3.93 eV from optical measurements. These values were reported to be at suitable energy levels for transfer of electrons into the TiO_2 conduction energy band and holes to the spiro-OMeTAD valence energy band. Figure 2.11b shows a diagram of the estimated energy levels of the conduction and valence bands of such solar cell materials. Efficient and complete hole injection from the absorber to the HTM was confirmed by transient absorption spectra measurements. The porous TiO_2-$MAPbI_3$–spiro-OMeTAD junction was recognised as a non-space-charge limited structure because of the linear proportionality between J_{SC} and light intensity which is associated with no significant difference between electron and hole mobility. The stability of these solar cells was assessed in a time period of 500

hours by storing them in air atmosphere without encapsulation. The cell efficiency was reported to increase by 14% after 500 hours of storage because of an increase in FF.

For a) see Figure 2 of Park, N.G., Organometal Perovskite Light Absorbers Toward a 20% Efficiency Low-Cost Solid-State Mesoscopic Solar Cell. Journal of Physical Chemistry Letters, 2013. 4(15): p. 2423-2429.

For b) see Figure 2d of Kim, H.S., et al., Lead iodide perovskite sensitized all-solid-state submicron thin film mesoscopic solar cell with efficiency exceeding 9%. Sci Rep, 2012. 2: p. 591.

Figure 2.11 a) Photograph of the solar cell with a diagram of the cross-sectional structure of the device and a high magnification cross section image of the solar cell by SEM. b) Schematic energy level diagram of the solar cell materials: TiO_2, $MAPbI_3$, and spiro-OMeTAD (adapted from Park et al. (2013) and Kim et al. (2012)).

Two months later that year Lee et al. (2012) reported a methyl ammonium lead iodide chloride ($CH_3NH_3PbI_2Cl$ or $MAPbI_2Cl$) perovskite-sensitised solid solar cell with an efficiency of 10.9% with a V_{OC} of 0.98 V, J_{SC} of 17.8 mA/cm^2 and FF of 0.63 measured at one sun intensity [77]. This solar cell had a 500 nm thick insulating porous aluminium oxide (Al_2O_3) layer instead of the usual electron conducting porous TiO_2 layer as schematically shown in Fig. 2.12a. This work demonstrated that a conducting porous TiO_2 layer was not necessary to obtain high efficiency perovskite solar cells because the perovskite can function as an absorber and electron conductor material as schematically shown in Fig. 2.12b. The energy bands of these perovskite solar cells with a porous TiO_2 and Al_2O_3 layer are shown in Fig. 2.12c.This work planted the idea that a high efficiency planar perovskite solar cell could be possible. The electron diffusion was shown to be faster through the $MAPbI_2Cl$ layer than through the porous n-type TiO_2 layer as estimated from transient photocurrent decay measurements. The $MAPbI_2Cl$ solar cells with a porous Al_2O_3 layer had a higher V_{OC} than those with a porous TiO_2 layer. This was attributed to the TiO_2 density of states that extend into its bandgap and increase recombination at the TiO_2–perovskite interface. The hole transfer from the $MAPbI_2Cl$ to the HTM (200 nm thick spiro-OMeTAD layer) was corroborated to be highly effective by transient absorption spectra measurements.

For a) see Figure 1c of Lee, M.M., et al., Efficient hybrid solar cells based on meso-superstructured organometal halide perovskites. Science, 2012. 338(6107): p. 643-7.

For b) and c) see Figure 3a of Lee, M.M., et al., Efficient hybrid solar cells based on meso-superstructured organometal halide perovskites. Science, 2012. 338(6107): p. 643-7.

Figure 2.12 a) Schematic of the complete solar cell structure, where the porous oxide layer is either Al_2O_3 or TiO_2. b) Illustration of the charge transfer and charge transport in a perovskite-sensitised porous TiO_2 solar cell and a non-injecting porous Al_2O_3 solar cell. c) Diagram of the solar cell energy bands levels where the electrons are shown as solid circles and the holes as open circles. (adapted from Lee et al. (2012)).

At that same time Etgar et al. (2012) published a report of a $MAPbI_3$ perovskite-sensitised porous TiO_2 solar cell without a HTM layer. The $MAPbI_3$ was spin-coated on a 500 nm thick porous TiO_2 layer and then a metal contact was evaporated. The efficiency of this solar cell was 5.5% with a V_{OC} of 0.631 V, J_{SC} of 16.1 mA/cm^2 and FF of 0.57 measured at one sun intensity [78]. The perovskite was found to act as an absorber and HTM. This is significant because it makes the case that $MAPbI_3$ is a material with outstanding photovoltaic properties only found previously in high purity crystalline materials such as silicon. It also pushed the case for the possibility of developing a high efficiency planar perovskite solar cell.

These first three papers of perovskite-sensitised solid solar cells with efficiencies as high as 10% were most impressive and caught the attention of the solar cell research community. Previously, the solar research community had been working for decades on many other absorber materials for sensitised solar cells and had only achieved a maximum efficiency of about 6% with Sb_2S_3 and a solid HTM and 12% with a dye and a liquid HTM [68, 79]. In these reports, the perovskite layer was made via a simple solution deposition method consisting of spin-coating a perovskite solution in GBL or N,N-dimethylformamide (DMF) followed by a drying step. The ease of fabrication of perovskite-sensitised solid solar cells and relatively high efficiencies achieved in a relatively short time surprised and captivated the solar research community. This then led to a surge in research and publications of perovskite solid solar cells with different structures by many research groups around the world. The main perovskite solid solar

cell structures under current investigation are porous, planar, inverted and tandem. The striking evolution of the efficiency of perovskite solar cells from about 10% to 20% in just about 4 years can be divided into research that has been done to: optimise the coverage and morphology of the perovskite layer via various deposition methods, increase the absorptance and stability of perovskites via varying its composition (mixed perovskites), and optimise the HTM and ETM layers for perovskite solar cells. The rest of this Chapter is divided into the following sections:

i. Evaporated Perovskite Layer
ii. Inclusion of a Perovskite Capping Layer
iii. Optimising the HTM Layer
iv. Improving the One-Step Deposition Method
v. Improving the Two-Step Deposition Method
vi. Mixed Perovskites: Varying the Perovskite Composition
vii. Alternative Compact ETM Layer for Perovskite Solar Cells

Each section summarises the most significant publications that have contributed to push the efficiency of laboratory perovskite solid solar cells to similar values to that of commercial silicon solar cells.

Evaporated Perovskite Layer

Liu et al. (2013) published a comparison between planar perovskite solar cells with either an evaporated perovskite layer or a solution deposited perovskite layer [80]. A dual-source vapour deposition system was used to evaporate and deposit the mixed halide $CH_3NH_3PbI_{3-X}Cl_X$ perovskite. The ETM and HTM consisted of compact planar layers of TiO_2 and spiro-OMeTAD respectively. The solution deposited perovskite layer was made via the previously mentioned simple solution deposition method of Lee et al. (2012) [77, 81]. The planar evaporated perovskite film had a uniform thickness of 330 nm whereas the solution deposited perovskite films had a non-uniform thickness that varied from 50 nm to 410 nm. The high uniformity of the evaporated perovskite films resulted in substantially improved solar cell performance as shown below in Fig. 2.13. The solution deposited perovskite solar cells had lower

V_{OC} and FF because of pinholes which resulted in direct contact between the TiO_2 and spiro-OMeTAD layers thus creating a shunting path for the carriers. The structure of this solar cell consisted of a 60 nm thick compact TiO_2 layer (non-porous TiO_2 layer), a 350 nm thick perovskite layer and a 400 nm thick spiro-OMeTAD layer. This worked showed that proximity and contact between the TiO_2 and spiro-OMeTAD decreases the solar cell performance by decreasing the V_{OC}. Furthermore, this report planted the idea that a uniform and thick perovskite capping layer would be beneficial for perovskite solar cells with a porous TiO_2 layer, as discussed next.

See Figure 3 of Liu, M., M.B. Johnston, and H.J. Snaith, Efficient planar heterojunction perovskite solar cells by vapour deposition. Nature, 2013. 501(7467): p. 395-8.

Figure 2.13 J-V curves and values of the best performing solution deposited and evaporated perovskite solar cells measured at one sun intensity (adapted from Liu et al. (2013)).

Inclusion of a Perovskite Capping Layer

Ball et al. (2013) reported a $MAPbI_{3-X}Cl_X$ sensitised porous Al_2O_3 solid solar cell with a perovskite capping layer on top of the porous layer as shown below in Fig. 2.14a [81]. Ball et al. (2013) reported that this perovskite capping layer is only formed if the thickness of the porous layer is ≤ 400 nm because the volume of deposited perovskite exceeds the pore volume of the porous layer. In contrast, if the thickness of the porous oxide layer is > 400 nm there will be no capping layer because the perovskite volume is entirely infiltrated inside the porous oxide layer. Figure 2.14b shows a plot of the measured perovskite capping layer thickness as a function of the porous Al_2O_3 layer thickness. The solar cells with a capping layer exhibited higher calculated wavelength-averaged IQE (≥ 90%) than the cells without the capping layer. Having a perovskite capping layer minimises the possibility of physical contact between the HTM and the underlying porous TiO_2 layer which would increase the recombination losses.

Ball et al. (2013) also reported that the perovskite crystal size increased from 100 nm to 500 nm as the underlying porous layer thickness decreased from 600 nm to 80 nm,

which suggests a reduction of the grain boundary recombination; although no correlation with the solar cell performance was reported. The solar cell with the highest efficiency reported here had a 400 nm porous Al_2O_3 layer and was fabricated at temperatures of ≤ 150°C. This solar cell had an efficiency of 12.3% with a V_{OC} of 1.02 V, J_{SC} of 18 mA/cm^2 and FF of 0.67 measured at one sun intensity [81]. This work was the first report on the formation of a perovskite capping layer on top of the porous oxide layer which resulted in higher IQEs and efficiencies. This work encouraged many other researchers to use thin porous oxide layers with perovskite capping layers to improve the efficiency of perovskite-sensitised solid solar cells.

For a) see Figure 1d of Ball, J.M., et al., Low-temperature processed meso-superstructured to thin-film perovskite solar cells. Energy & Environmental Science, 2013. 6(6): p. 1739.

For b) see Figure S2 of Supporting Information of Ball, J.M., et al., Low-temperature processed meso-superstructured to thin-film perovskite solar cells. Energy & Environmental Science, 2013. 6(6): p. 1739.

Figure 2.14 a) Colour-enhanced and annotated SEM cross section image of a solar cell with a 80 nm thick Al_2O_3 porous layer and a 300 nm perovskite capping layer. b) Perovskite capping layer thickness as a function of the porous oxide thickness (adapted from Ball et al. (2013)).

Leijtens et al. (2014) clearly demonstrated that having a perovskite capping layer improves the photovoltaic performance of porous TiO_2 sensitised $MAPbI_{3-x}Cl_x$ perovskite solar cells [82]. The benefits of having a perovskite capping layer had been previously suggested by Ball et al. (2013) and Liu et al. (2013) but not methodically investigated in detail. Leijtens et al. (2014) varied the thickness of the porous TiO_2 layer between 260 nm and 750 nm along with the perovskite solution concentration to gradually form and increase the thickness of a perovskite capping layer. This gradual change meant going from having the perovskite acting as a sensitiser with non-uniform coverage of the porous TiO_2 layer, to having the perovskite completely covering the TiO_2 porous layer and forming a capping layer. A porosity of 50% was reported for the porous TiO_2 layer used in this work. The J_{SC} and V_{OC} increased as the porous TiO_2 layer thickness decreased even though the absorption of light in the films decreased, as

shown below in Fig. 2.15a-b. The improvement in J_{SC} and V_{OC} was attributed to the enhancement of the charge collection efficiency and to a positive shift of the quasi-electron fermi level due to a higher electron density in the porous TiO_2 layer. A perovskite capping layer on top of the porous TiO_2 layer minimises the recombination losses that stem from the physical contact between the porous TiO_2 and the spiro-OMeTAD. The perovskite layer was deposited using the simple solution deposition method of Lee et al. (2012). After these reports, the aim of having a perovskite capping layer became the norm for perovskite solar cells.

For a) and b) see Figure 2b and 2a of Leijtens, T., et al., The Importance of Perovskite Pore Filling in Organometal Mixed Halide Sensitized TiO_2-Based Solar Cells. J Phys Chem Lett, 2014. 5(7): p. 1096-102.

Figure 2.15 a) J-V curves of the relevant solar cells with a (i) 750 nm porous TiO_2 layer with 30 wt% perovskite precursor solution (grey diamonds), (ii) 750 nm porous TiO_2 layer with 40 wt% (black squares), (iii) 440 nm porous TiO_2 layer with 40 wt% (blue circles) and (iv) 260 nm porous TiO_2 layer with 40 wt% (red triangles). b) UV−vis spectra of the same solar cells before electrode deposition (adapted from Leijtens et al. (2014)).

Optimising the HTM Layer

Heo et al. (2013) compared the performance of $MAPbI_3$ sensitised solar cells with different organic HMTs such as poly-trialyl-amine (PTAA), poly(N-9''-heptadecanyl--2,7-carbazole-alt-5,5-(4',7'-di-2-thienyl-2',1',3'-benzothiadiazole)) (PCDTBT), P3HT, PCPDTBT, and spiro-OMeTAD [83]. The $MAPbI_3$ was spin-coated on a 600 nm thick TiO_2 porous layer and then dried at 100°C. Then, the different HTMs were spin-coated on top of the perovskite-sensitised porous TiO_2 substrates. A schematic diagram and SEM image of the solar cell are shown in Fig. 2.16a-b. Heo et al. (2013) proposed that $MAPbI_3$ can act as an efficient ambipolar charge transport material depending on the type of the neighbouring semiconductors that have the largest contact area with the perovskite. For instance, in a solar cell with a thick porous TiO_2 layer, such as the solar cell reported here, the photo-generated excitons in the $MAPbI_3$ were estimated to

mainly dissociate at the TiO_2–$MAPbI_3$ interface via electron injection into the conduction band of the TiO_2. Then, the $MAPbI_3$ itself acts as a HTM. Nevertheless, to make a high efficiency perovskite solar cell it was necessary to add a dedicated HTM layer.

In this report, the solar cell with the highest efficiency had a PTAA layer as the HTM. The enhanced efficiency was attributed to the higher hole mobility and possibly better injection/transfer of carriers between the PTAA and the perovskite compared to all the other HTM, as demonstrated by the J-V curves in Fig. 2.16c. The highest efficiency of 12% that was achieved with PTAA as the HTM had a V_{OC} of 0.997 V, J_{SC} of 16.5 mA/cm^2 and FF of 0.73 measured at one sun intensity [83]. This was the first reported perovskite solar cell with PTAA as the HTM. Heo et al. (2013) also demonstrated that PTAA as the HTM in $MAPbI_3$ solar cells improved the photovoltaic performance over the commonly used spiro-OMeTAD as shown in Fig. 2.16d. Since this research was published, many researchers started using PTAA as the HTM in perovskite solar cells.

For a), b), c) and d) see Figure 1a, 1c, 2a and 3a respectively of Heo, J.H., et al., Efficient inorganic–organic hybrid heterojunction solar cells containing perovskite compound and polymeric hole conductors. Nature Photonics, 2013. 7(6): p. 486-491.

Figure 2.16 a) SEM image of the $MAPbI_3$ sensitised solar cell showing its cross section and top surface. b) Schematic of the device architecture based on the SEM images with electron (e^-) and holes (h) trajectories. c) J–V curves of the $MAPbI_3$ solar cells with a 1 µm thick porous TiO_2 layer and different HTM layers. d) J-V curve of $MAPbI_3$ solar cells with a 600 nm thick porous TiO_2 layer and either a PTAA or spiro-OMeTAD layer (adapted from Heo et al. (2013)).

Ryu et al. (2014) compared $MAPbI_3$ and $MAPbBr_3$ perovskite solar cells made with various HTM of different highest occupied molecular orbital (HOMO) levels and distinct molecular structures [84]. The HTM used were poly[[(2,4-dimethylphenyl)imino]-1,4-phenylene(9,9-dioctyl-9H-fluorene-2,7-diyl)-1,4-phenylene] (PF8-TAA), poly[[(2,4-dimethylphenyl)imino]-1,4-phenylene(6,12-dihydro-6,6,12,12-tetraoctylindeno[1,2-b] fluorene-2,8-diyl)-1,4-phenylene] (PIF8-TAA), PTAA and spiro-OMeTAD [85, 86]. The corresponding J-V curves are shown in Fig. 2.17a-b. These solar cells had a 250 nm thick porous TiO_2 layer with a perovskite capping layer of about 250 nm. The porous

TiO_2/$MAPbBr_3$/PIF8-TAA solar cell had an efficiency of 6.7% with a V_{OC} of 1.4 V, J_{SC} of 6.1 mA/cm^2 and FF of 0.79 measured at one sun intensity [84]. The porous TiO_2/$MAPbI_3$/PTAA solar cell in contrast had an efficiency of 16.2% with a V_{OC} of 1.04 V, J_{SC} of 21.3 mA/cm^2 and FF of 0.73 measured at one sun intensity. The perovskite layers were deposited using the one-step solvent induced deposition method reported by Jeon et al. (2014) which is discussed later [87]. The HTM that produced the highest efficiency with $MAPbI_3$ perovskite was PTAA and with $MAPbBr_3$ perovskite was PIF8-TAA. These highest efficiencies were attributed to the HOMO energy levels of PTAA and PIF8-TAA having a higher value than the valence band energy level of the perovskite and to the PIF8-TAA's higher mobility value. This report also validated the advantage of having a perovskite capping layer to make high efficiency perovskite solar cells. Additionally, this work corroborated the previously mentioned report of Heo et al. (2013) that compared the performance of $MAPbI_3$ solar cells with different HTM such as P3HT, PCPDTBT, PCDTBT, PTAA and spiro-OMeTAD where PTAA was found to outperform the other HTM.

For a) and b) see Figure 2b and 2d respectively of Ryu, S., et al., Voltage output of efficient perovskite solar cells with high open-circuit voltage and fill factor. Energy & Environmental Science, 2014. 7(8): p. 2614.

Figure 2.17 a) J-V curves of $MAPbBr_3$ perovskite solar cells with different HTM measured at one sun intensity. b) J-V curves of $MAPbI_3$ perovskite solar cells with different HTM measured at one sun intensity (adapted from Ryu et al. (2014)).

Improving the One-Step Deposition Method

In July 2014, Jeon et al. (2014) published a one-step, solvent induced, deposition method for the mixed $MAPb(I_{0.9}Br_{0.1})_3$ perovskite [87]. This method consists of using a combination of different solvents to produce extremely uniform and dense perovskite layers. Jeon et al. (2014) used the mixed $MAPb(I_{0.9}Br_{0.1})_3$ perovskite because they found that the substitution of 10-15 mole percent (mol%) Br^- for I^- in $MAPbI_3$ greatly improves the stability in ambient atmosphere and reduces the hysteresis with no impact on the photovoltaic performance. This mixed perovskite was deposited on porous TiO_2 layers by spin-coating a solution composed of lead iodide (PbI_2), lead bromide ($PbBr_2$), methyl ammonium iodide (MAI), methyl ammonium bromide (MABr),

dimethyl sulphoxide (DMSO) and GBL. During the spin-coating process, toluene was dripped on the substrate, which produced a highly uniform 200 nm thick perovskite capping layer on top of the 200 nm thick porous TiO_2 layer as represented in Fig. 2.18a. The mixed perovskite surface exhibited a dense-grained uniform morphology with grain sizes in the range of 100-500 nm as shown in Fig. 2.18b. The absorption edge of this mixed perovskite is below 770 nm whereas for $MAPbI_3$ it is 776 nm. The HTM was PTAA which was spin-coated on top of the perovskite capping layer. This method produced solar cells with a highest efficiency of 16.5% with a V_{OC} of 1.1 V, J_{SC} of 19.6 mA/cm^2 and FF of 0.76 measured at one sun intensity [87].

This method can also be used to deposit $MAPbI_3$ and $MAPbBr_3$, as published a couple of months earlier by the same research group [84]. In this one-step, solvent induced, deposition method for perovskite layers the toluene droplets led to the immediate solidification of the constituents via the quick removal of the excess DMSO solvent. This quick removal forms a uniform and transparent MAI-PbI_2-DMSO layer as portrayed below in Fig. 2.18a. This flat film is then converted into a pure crystalline $MAPbI_3$ perovskite layer after annealing at 130 °C. The role of DMSO in the MAI-PbI_2-DMSO phase is to retard the rapid reaction between PbI_2 and MAI during the evaporation of the solvent in the spin-coating process. A uniform and thin MAI-PbI_2-DMSO layer can only be achieved with the toluene drip treatment during the spin-coating process; without it, the resulting material adopts a textile-like inhomogeneous layer that does not fully cover the substrate as shown below in Fig. 2.18c.

For a) see Figure 1c of Jeon, N.J., et al., Solvent engineering for high-performance inorganic-organic hybrid perovskite solar cells. Nat Mater, 2014. 13(9): p. 897-903.

For b) see Figure S1b of Supplementary Information of Jeon, N.J., et al., Solvent engineering for high-performance inorganic-organic hybrid perovskite solar cells. Nat Mater, 2014. 13(9): p. 897-903.

For c) see Figure 3c of Jeon, N.J., et al., Solvent engineering for high-performance inorganic-organic hybrid perovskite solar cells. Nat Mater, 2014. 13(9): p. 897-903.

Figure 2.18 a) Diagram of the one-step solvent induced deposition method to deposit a uniform and dense perovskite layer. b) Top view SEM image of the perovskite film without toluene dripping and c) with toluene dripping (adapted from Jeon et al. (2014)).

Also in July 2014, Xiao et al. (2014) reported their own one-step solvent-induced method to deposit flat and uniform $MAPbI_3$ perovskite layers via spin-coating [88]. This method consists of spin-coating a $MAPbI_3$ (45 wt%) solution in DMF on top of the desired substrate. Soon after the spin-coating starts, droplets of chlorobenzene are dropped on top of the spinning wetted substrate to induce fast crystallisation. Afterwards the transparent films are dried at 100°C to produce highly crystalline perovskite films. The role of the chlorobenzene droplets is to rapidly reduce the solubility of $MAPbI_3$ and thereby promote the fast nucleation and growth of perovskite crystals. The thickness of the perovskite layer was easily controlled by changing the concentration of the perovskite solution. For instance, 25, 35, 45, 55 wt% $MAPbI_3$ solutions in DMF produced $MAPbI_3$ films with a thickness of 150, 250, 350, 550 nm respectively. Flat polygonal grains with 5 or 6 sides were the predominant microstructural feature in these perovskite films where the grain sizes became larger as the thickness of the perovskite layer increased.

The single perovskite grains were believed to be single crystals and adjacent grains did not appear to have the same crystal orientation. Larger perovskite grains can have less recombination losses because of the reduced number of grain boundaries which are a source of defects and trap states. No horizontal grain boundaries with respect to the substrate surface were observed along the depth of the perovskite layer, suggesting that most perovskite grains span the entire thickness of the film. The best solar cell had an efficiency of 16.2% with a V_{OC} of 1.04 V, J_{SC} of 21.2 mA/cm^2 and FF of 0.74 measured at one sun intensity [88]. This solar cell had a planar configuration with only a 30 nm compact TiO_2 layer (non-porous TiO_2 layer) and a 180 nm thick spiro-OMeTAD layer as the HTM. The efficiency reported in this work by Xiao et al. (2014) is higher than that achieved by Liu et al. (2013) that used an evaporated mixed halide $CH_3NH_3PbI_{3-X}Cl_X$ perovskite layer in a similar planar solar cell configuration.

The one-step solvent induced methods for perovskite deposition reported by Xiao et al. (2014) and Jeon et al. (2014) were of great importance because they demonstrated that highly uniform and dense perovskite layers can be deposited via a solution method [87, 88]. Previously, the deposition of highly uniform and dense perovskite layers had only been possible by evaporation as all the previously reported simple solution deposition methods resulted in non-uniform perovskite layers [77, 80, 81]. The importance of continuous and uniform perovskite capping layers on porous oxide layers had been previously emphasised as indispensable for producing high efficiency perovskite solar cells [80-82]. These one-step solvent induced deposition methods served as a basis for the development of other one-step deposition methods that produced higher efficiency perovskite solar cells as discussed next.

Yang et al. (2015) reported an intramolecular exchange method to fabricate a mixed $(FAPbI_3)_{0.95}(MAPbBr_3)_{0.05}$ perovskite layer that produced solar cells with an efficiency of 20% [89]. This intramolecular exchange deposition method can produce a dense and uniform formamidinium lead iodide ($HN{=}CHNH_3PbI_3$ or $FAPbI_3$) layer with a (111) preferred crystallographic orientation with a large grain structure without any residual PbI_2. Pure $FAPbI_3$ perovskite solar cells can potentially have a higher efficiency because of their broad absorption spectrum (up to 840 nm) and reduced hysteresis. A uniform and pinhole free $FAPbI_3$ layer with the intramolecular exchange method was fabricated by first depositing a transparent PbI_2(DMSO) layer by spin-coating a PbI_2(DMSO) solution in DMF on the substrate. A formamidinium iodide (FAI) solution in 2-propanol was then spin-coated on top of the transparent PbI_2(DMSO) layer during which the resulting film turned dark. Afterwards, the film was dried at 150°C. However, pure $FAPbI_3$ perovskite is unstable at ambient temperature. The stabilisation of the $FAPbI_3$ perovskite phase independently of the temperature can be achieved by mixing it with other perovskite compounds. Mixed $(FAPbI_3)_{0.95}(MAPbBr_3)_{0.05}$ perovskite solar cells fabricated using this intramolecular exchange method achieved an efficiency of 20% with a V_{OC} of 1.06 V, J_{SC} of 24.7 mA/cm^2 and FF of 0.77 measured at one sun intensity as shown in Fig. 2.19b. This mixed perovskite with a high proportion of $FAPbI_3$ has a broader absorption wavelength range and a larger J_{SC} as can be seen in Fig. 2.19c. The mixed $(FAPbI_3)_{0.95}(MAPbBr_3)_{0.05}$ perovskite layer was deposited by firstly spin-coating a PbI_2(DMSO) layer and subsequently a FAI solution in 2-propanol containing 15 wt%

MABr which formed a 500 nm thick $(FAPbI_3)_{0.95}(MAPbBr_3)_{0.05}$ perovskite capping layer on top of the 150 nm porous TiO_2 layer as shown in Fig. 2.19a. The mixed $(FAPbI_3)_{0.95}(MAPbBr_3)_{0.05}$ perovskite layer was then annealed at 150°C and had an absorption edge of 830 nm. A 50 nm thick PTAA layer was spin-coated on top of the perovskite as the HTM.

For a) see Figure 2a of Yang, W.S., et al., High-performance photovoltaic perovskite layers fabricated through intramolecular exchange. Science, 2015. 348(6240): p. 1234-7.

For b) and c) see Figure 2c of Yang, W.S., et al., High-performance photovoltaic perovskite layers fabricated through intramolecular exchange. Science, 2015. 348(6240): p. 1234-7.

Figure 2.19 a) Cross-sectional SEM image of the mixed $(FAPbI_3)_{0.95}(MAPbBr_3)_{0.05}$ perovskite solar cell. b) J-V curves of the same solar cell (in reverse and forward sweep) measured at one sun intensity. c) EQE and integrated J_{SC} of the same solar cell (adapted from Yang et al. (2015)).

The intramolecular exchange method of Yang et al. (2015) can deposit dense, uniform and thick mixed perovskite layers with a high proportion of $FAPbI_3$ for high efficiency perovskite solar cells [89]. In contrast, the previously reported one-step solvent-induced method of Jeon et al. (2014) produced $FAPbI_3$ and $(FAPbI_3)_{0.95}(MAPbBr_3)_{0.05}$ perovskite layers full of pinholes and with a rough surface [87]. On the other hand, the two-step method reported by Burschka et al. (2013) in which a spin-coated compact PbI_2 layer is then immersed in a MAI or FAI solution to produce the corresponding perovskite phase has been ineffective in producing thick (≥ 500 nm) perovskite films [90, 91]. The two-step method of Bruschka et al. (2013) could not produce thick perovskite films because considerable volume expansion (≈ 44%) is required for the insertion of MAI or FAI into the compact PbI_2 layer. However, the two-step method eventually evolved to produce thick perovskite layers. The progress of the two-step deposition methods is discussed next.

Improving the Two-Step Deposition Method for Perovskites

Burschka et al. (2013) reported a two-step method for the deposition of $MAPbI_3$ into the porous TiO_2 layer [90]. This two-step method eliminated the large morphological variations of the perovskite layer from previously used single-step deposition methods. The large morphological variations of the perovskite layer produced by the previous single-step deposition method resulted in a wide range of the measured efficiencies of such perovskite solar cells. The first step of Burschka et al.'s (2013) two-step method is to deposit PbI_2 within the porous TiO_2 layer by immersion in a PbI_2 solution. The second step is to fully convert the PbI_2 within the porous TiO_2 layer into $MAPbI_3$ via 30 seconds to 60 seconds immersion in a MAI solution. However, when PbI_2 is deposited on a flat surface to form a compact planar PbI_2 layer, the conversion to perovskite on exposure to the MAI solution is incomplete as large amounts of PbI_2 remain unconverted even after a dipping time of 45 minutes. This is because the infiltration of MAI into the compact planar PbI_2 layers hardly proceeds beyond the PbI_2 layer surface. The crystal size of the PbI_2 is limited to 22 nm when it is deposited within a porous TiO_2 layer and to 50 nm to 200 nm when it is deposited on a flat surface. The nanometre scale confinement of the PbI_2 within the nanostructure of the porous TiO_2 layer enables efficient and complete perovskite formation via the two-step method. Solar cells were fabricated using this two-step method to deposit $MAPbI_3$ on a 350 nm thick porous TiO_2 layer with spiro-OMeTAD as the HTM. The best solar cell had an efficiency of 15% with a V_{OC} of 0.993 V, J_{SC} of 20 mA/cm^2 and FF of 0.73 measured at one sun intensity [90]. An encapsulated cell was held at a temperature of 45°C and exposed to white light equivalent to one sun intensity for 500 hours. After the period of 500 hours, the efficiency decreased by 20% because of a decrease in the V_{OC} and FF. There was no change in J_{SC} which indicated that there was no degradation of the perovskite. However, the white light used for this test had no UV component which has been reported to quickly degrade sensitised porous TiO_2 based solar cells [92]. This was the first report of a two-step method for the deposition of the perovskite layer. This work eventually led to the development of a two-step method for the formation of thick uniform perovskite layers as discussed next.

Yi et al. (2016) presented another two-step method to deposit uniform and compact high quality $FA_{0.85}MA_{0.15}Pb(I_{0.85}Br_{0.15})_3$ perovskite layers for solar cells with an efficiency

of 20.4% [93]. This method consists of first introducing a porous PbX_2 (85:15 molar ratio of PbI_2 to $PbBr_2$) capping layer that is a network of interconnected nano-pores which provide the space needed to accommodate the large volume expansion accompanying the subsequent insertion of the MAI/FAI cations into the PbX_2 lattice. The pores are filled during the conversion step, resulting in the formation of a uniform and compact perovskite film. The mixed perovskite $FA_{1-x}MA_xPb(I_{1-x}Br_x)_3$ has a greater thermal stability, broader absorption (higher photo-generated currents) and negligible hysteresis. The mixed $FA_{0.85}MA_{0.15}Pb(I_{0.85}Br_{0.15})_3$ perovskite layer is deposited by first spin-coating a PbI_2:$PbBr_2$ (85:15 molar ratio) solution in DMSO/DMF (mix 2/8 v/v) on a 150 nm thick porous TiO_2 layer and then evaporating the solvents at 70°C for 10 minutes. This forms a 300 nm thick porous PbX_2 capping layer, as shown in Fig. 2.20a. The density and size of the pores within the porous PbX_2 layer increase when the DMSO volume content is increased because the pores are created when the DMSO evaporates. Yi et al. (2016) found that the PbX_2 infiltrates well into the porous TiO_2 layer with the pores becoming smaller as they get closer to the uppermost porous PbX_2 surface where only a small percentage are visible. These interconnected pores offer a large volume and surface area for the rapid transport, promotion and formation of the perovskite during the subsequent immersion of the porous PbX_2 layer in a 0.1 M MAI and formamidinium bromide (FABr) (85:15 molar ratio) isopropanol solution for 90 seconds. This pore enhanced conversion of the porous PbX_2 layer into its corresponding compact perovskite layer occurs with a remarkably small change in thickness of the porous PbX_2 layer. The fabrication of solar cells with this new two-step method was accomplished by depositing a mixed $FA_{0.85}MA_{0.15}Pb(I_{0.85}Br_{0.15})_3$ perovskite capping layer with a thickness of 350 nm on top of a 150 nm thick TiO_2 porous layer. Then, a 250 nm thick spiro-OMeTAD layer was deposited as the HTM as shown in Fig. 2.20b. This solar cell had an efficiency of 20.4% with a V_{OC} of 1.1 V, J_{SC} of 23 mA/cm^2 and FF of 0.79 measured at one sun intensity as shown in Fig. 2.20c. The corresponding EQE of this solar cell is shown in Fig. 2.20d. This mixed perovskite has the same cations and anions as the mixed perovskite deposited by Jeon et al. (2015) and Yang et al. (2015) using a different deposition method. However, in this report the EQE peaks at a higher value than the EQE reported previously for similar mixed perovskites. These differences may originate from an enhanced light absorption and

reduced parasitic absorption. Also the high FF suggests reduced resistance losses and improved contacts.

For a), b), c) and d) see Figure 2c, 4b, 3c and 3d respectively of Yi, C., et al., Perovskite Photovoltaics with Outstanding Performance Produced by Chemical Conversion of Bilayer Mesostructured Lead Halide/TiO2 Films. Adv Mater, 2016. 28(15): p. 2964-70.

Figure 2.20 a) 3D tomography of the porous PbX_2 layer deposited on the porous TiO_2 layer. b) Cross-sectional image of the finished solar cell by SEM. c) J-V curves of the same solar cell in forward and backward scan measured at one sun intensity plus the average J-V curve. d) EQE spectrum (red line) with integrated J_{SC} curve (black line) of the same solar cell (adapted from Yi et al. (2016)).

Mixed Perovskites: Varying the Perovskite Composition

Noh et al. (2013) reported a method to vary the perovskite band gap from 1.5 eV to 2.3 eV [94]. This method consisted of varying the iodine and bromine concentration in the $MAPb(I_{1-X}Br_X)_3$ perovskite compound from x = 0 to x = 1 in 10 steps as shown below in Fig. 2.21a-c. The $MAPbI_3$ is a tetragonal crystal structure with a 1.5 eV bandgap whereas the $MAPbBr_3$ is a cubic crystal structure with a 2.2 eV bandgap. The good miscibility of $MAPbI_3$ with $MAPbBr_3$ was demonstrated by the fine-tuning of the bandgap by varying the concentrations of iodine and bromine. The perovskite-sensitised solid solar cells were made by spin-coating the different perovskite compositions on top of a 600 nm thick porous TiO_2 layer, followed by spin-coating a layer of PTAA as the organic HTM. The cells fabricated from x = 0 to 0.2 in $MAPb(I_{1-X}Br_X)_3$ had an average efficiency of more than 10%. The highest efficiency of 12.3% was obtained at x = 0.2 with a V_{OC} of 0.91 V, J_{SC} of 19.1 mA/cm^2 and FF of 0.7 measured at one sun intensity [94]. Perovskite-type hybrids such as $MAPbI_3$ and $MAPbBr_3$ easily decompose in the presence of moisture because of the hygroscopic amine salts. However, Noh et al. (2013) found that $MAPbI_3$ is more sensitive to moisture than $MAPbBr_3$. Solar cells made of $MAPb(I_{1-X}Br_X)_3$ ($x \geq 0.2$) did not degrade when exposed to 35% and 55% humidity levels and therefore have a low sensitivity to humidity. This work showed that the bandgap of perovskites could be easily changed

by mixing different perovskite compounds which eventually led to higher efficiencies by reducing the bandgap to absorb more photons and increase the photo-generated current.

For a), b) and c) see Figure 3a, 3b and 3c respectively of Noh, J.H., et al., Chemical management for colorful, efficient, and stable inorganic-organic hybrid nanostructured solar cells. Nano Lett, 2013. 13(4): p. 1764-9.

Figure 2.21 a) Absorptance of the solar cells as a function of wavelength. b) Photographs of the glass/FTO/porous TiO_2/$MAPb(I_{1-X}Br_X)_3$ samples. c) Bandgap of the $MAPb(I_{1-X}Br_X)_3$ as a function of x estimated from optical measurements (adapted from Noh et al. (2013)).

Pellet et al. (2014) reported the use of a mixture of methyl ammonium ($CH_3NH_3^+$ or MA) and formamidinium ($HN{=}CHNH_3^+$ or FA) lead iodide perovskite to extend the optical absorption further into longer wavelengths and thus increase the photo-generated current [91]. This concept is similar to varying the bandgap of perovskites by a mixture of $MAPb(I_{1-X}Br_X)_3$ presented by Noh et al. (2013).

In the work of Pellet et al. (2014) a 300 nm porous TiO_2 layer was first coated with PbI_2 and then immersed in a solution of FAI and MAI in 2-propanol to form the $(MA)_X(FA)_{1-X}PbI_3$ perovskite. The 300 nm thick porous TiO_2 layer follows on from previous reports of thinner porous TiO_2 layers producing higher efficiencies than thicker ones (Ball et al. (2013)). The photoluminescence (PL) emission peak wavelength of $MAPbI_3$ is λ_{max} = 776 nm and of $FAPbI_3$ is λ_{max} = 803 nm which is a 27 nm difference. A solution with a MAI:FAI ratio of 4:1 caused the absorption onset of the resulting perovskite to move towards longer wavelengths (red shift) by 27 nm from 776 nm to 803 nm as can be seen in Fig. 2.22b. The mixed $MA_{0.6}FA_{0.4}PbI_3$ perovskite improved the photovoltaic performance compared to the non-mixed perovskites as shown in Fig. 2.22a. This improved performance was attributed to the increase in J_{SC} caused by the red-shifted absorption onset and to a higher carrier collection efficiency probably caused by longer exciton lifetimes in the mixed perovskite as can be seen in Fig. 2.22b. The mixed $MA_{0.6}FA_{0.4}PbI_3$ perovskite solar cell had a highest efficiency of 14.9% with a V_{OC} of 1 V, J_{SC} of 21.2 mA/cm^2 and FF of 0.70 measured at one sun intensity [91]. This was the first report of a mixture of two different organic cations (MA and FA) to make

a mixed perovskite layer. It also corroborated that mixed perovskites can improve the solar cell efficiency over non-mixed perovskites by adjusting the bandgap [94].

For a) and b) see Figure 3a and 4c respectively of Pellet, N., et al., Mixed-organic-cation perovskite photovoltaics for enhanced solar-light harvesting. Angew Chem Int Ed Engl, 2014. 53(12): p. 3151-7.

Figure 2.22 a) J-V curves of the solar cells fabricated using either $FAPbI_3$, mixed $MA_{0.6}FA_{0.4}PbI_3$ or $MAPbI_3$ perovskite and b) corresponding IQE spectra of the same solar cells (adapted from Pellet et al. (2014)).

Jeon et al. (2015) reported the fabrication of mixed $(FAPbI_3)_{0.85}(MAPbBr_3)_{0.15}$ perovskite solar cells with an 18.4% efficiency [95]. Jeon et al. (2015) demonstrated that $FAPbI_3$ can exist as either two polymorphs (perovskite α-phase and non-perovskite δ-phase) depending on the temperature or only as one of the two depending on the atomic size of its cations and anions. The $FAPbI_3$ perovskite α-phase is stable at temperatures above 160°C and turns into the non-perovskite δ-phase at ambient temperature. However, it was found that co-substitution of 15 mol% of both MA^+ and Br^- into $FAPbI_3$ to obtain $(FAPbI_3)_{0.85}(MAPbBr_3)_{0.15}$ led to the stabilisation of the $FAPbI_3$ perovskite phase independently of the temperature. This mixed perovskite had a uniform and dense morphology with well-developed crystallites and an absorption edge at 800 nm. However, when increasing the ratio of $FAPbI_3$ to $MAPbBr_3$ to more than 85:15 the resulting layer is full of pinholes. The pure $FAPbI_3$ perovskite has an absorption band-edge wavelength of 840 nm whereas the mixed $MAPb(I_{0.9}Br_{0.1})_3$ perovskite has an absorption band-edge wavelength of 770 nm.

Jeon et al.'s (2015) mixed $(FAPbI_3)_{0.85}(MAPbBr_3)_{0.15}$ perovskite solar cell had an average efficiency of 18.4% with a V_{OC} of 1.11 V, J_{SC} of 22.5 mA/cm^2 and FF of 0.73 measured at one sun intensity [95]. The corresponding measured J-V curves and EQE spectrum of this solar cell are shown below in Fig. 2.23a-b. This solar cell was fabricated by depositing a 300 nm mixed $(FAPbI_3)_{0.85}(MAPbBr_3)_{0.15}$ perovskite capping layer on top of a 200 nm thick porous TiO_2 layer using the previously reported one-step, solvent induced, deposition method by Jeon et al. (2014). The HTM was a spin-coated 50 nm thick PTAA layer on top of the perovskite capping layer. In addition, this solar cell showed minor hysteresis as can be observed in Fig. 2.23a.

For a) and b) see Figure 3a and 3b of Jeon, N.J., et al., Compositional engineering of perovskite materials for high-performance solar cells. Nature, 2015. 517(7535): p. 476-80.

Figure 2.23 a) J-V curves of mixed $(FAPbI_3)_{0.85}(MAPbBr_3)_{0.15}$ perovskite solar cell in forward and reverse bias sweep measured at one sun intensity plus the averaged J-V curve. b) EQE spectrum and integrated J_{SC} of the same solar cell (adapted from Jeon et al. (2015)).

Saliba et al. (2016) reported $Cs_x(MA_{0.17}FA_{0.83})_{(100-x)}Pb(I_{0.83}Br_{0.17})_3$ perovskite solar cells with a highest efficiency of 21.1% [96]. The addition of cesium (Cs) reduced the variability of the mixed perovskite to temperature variations and other factors during the processing steps. Also upon addition of Cs the photo-inactive δ-phase $FAPbI_3$ and PbI_2 disappeared from the X-ray diffraction (XRD) spectra. These photo-inactive phases could have been present to a certain extent in the previous reports of high efficiency mixed perovskite solar cells by Jeon et al. (2015), Yang et al. (2015) and Yi et al. (2016). The use of Cs produces mixed perovskites of higher purity because it shifts the $FAPbI_3$ towards its photoactive cubic phase because of the large size difference between Cs and FA. However, only a small Cs percentage should be used because with large Cs concentrations the perovskite phases separate. The Cs-mixed perovskite layers were more stable to thermal degradation than the mixed perovskite layers without Cs. Additionally, Saliba et al. (2016) noted that the increase of Br content in the mixed perovskite also improved the thermal stability. The mixed $Cs_{0.05}(MA_{0.17}FA_{0.83})_{(0.95)}Pb(I_{0.83}Br_{0.17})_3$ perovskite solar cell was fabricated with a lithium doped 150-200 nm porous TiO_2 layer and spiro-OMeTAD as the ETM and HTM respectively. The solar cell reported by Saliba et al. (2016) had a highest efficiency of 21.17% with a V_{OC} of 1.147 V, J_{SC} of 23.5 mA/cm^2 and FF of 0.785 measured at one sun intensity as shown in Fig. 2.24a. The Cs-mixed perovskite solar cell efficiency remained stable at about 18% after 250 hours of continuous operation at one sun intensity in nitrogen atmosphere as shown in Fig. 2.24b. These aging test conditions resemble sealed solar cells under operating conditions. Furthermore, the performance parameter that degrades the most is the FF which can be related to the HTM. In contrast, the mixed perovskite solar cells without Cs under the same conditions degrade to half their initial efficiency value in about 75 hours. Triple or multiple cation

mixtures are an efficient compositional strategy to make stable high efficiency perovskite solar cells.

For a) and b) see Figure 5a and 5b of Saliba, M., et al., Cesium-containing triple cation perovskite solar cells: improved stability, reproducibility and high efficiency. Energy Environ. Sci., 2016. 9(6): p. 1989-1997.

Figure 2.24 a) J-V curves for the Cs mixed perovskite solar cell at forward and reverse scans measured at one sun intensity. The inset shows the power output for 60 seconds starting from forward bias and resulting in a stabilised power output of 21.1% at 0.960 volts. b) Aging for 250 hours of the mixed perovskite solar cell with and without Cs at the maximum power point in nitrogen atmosphere at room temperature under constant illumination (resembling sealed devices under operation conditions) (adapted from Saliba et al. (2016)).

Alternative Compact ETM Layer for Perovskite Solar Cells

Correa Baena et al. (2015) reported high efficiency planar perovskite solar cells with a compact SnO_2 layer as the ETM instead of the usual compact TiO_2 layer [97]. The SnO_2 layer was deposited on FTO substrates using an ALD system. A better electron extraction in pristine SnO_2 than in TiO_2-based devices was assumed based on the faster decay in carrier population (60% decay in 1.5 ns) of the SnO_2/perovskite sample compared to the TiO_2/perovskite sample (20% decay in 1.5 ns). The decay in carrier population was estimated from transient absorption measurements. Solar cells with a 15 nm thick compact SnO_2 layer on FTO were made by depositing either $MAPbI_3$ or $(FAPbI_3)_{0.85}(MAPbBr_3)_{0.15}$ using the one-step, solvent induced, deposition method reported by Jeon et al. (2014). This formed a 450 nm thick perovskite layer which was then coated with a 200 nm thick spiro-OMeTAD layer as the HTM. The planar mixed $(FAPbI_3)_{0.85}(MAPbBr_3)_{0.15}$ perovskite solar cell had an efficiency of 18% with a V_{OC} of 1.14 V, J_{SC} of 21.3 mA/cm^2 and FF of 0.74 measured at one sun intensity [97]. The $MAPbI_3$ planar solar cell had an efficiency of 11.8% with a V_{OC} of 1.03 V, J_{SC} of 19.7 mA/cm^2 and FF of 0.58 measured at one sun intensity. The planar solar cell with a compact SnO_2 layer had negligible hysteresis whereas the planar solar cells with TiO_2 had a much more pronounced hysteresis. The reduced hysteresis of the planar solar cells with a compact SnO_2 layer was attributed to a better alignment of the conduction

bands between the compact SnO_2 layer and the mixed perovskite. The non-encapsulated solar cells stored in dry air were measured for over 30 days with no significant drop in efficiency. This work demonstrated that SnO_2 can be a better material than TiO_2 to make high efficiency perovskite solar cells which is remarkable given the wide-spread use of TiO_2 as the usual ETM for high efficiency solar cells. However, there has been no study that methodically compares porous SnO_2 and porous TiO_2 perovskite solar cells.

Conclusion from the Literature Review

From the Sb_2S_3 solar cell reviewed literature is it evident that the main limitation for high efficiency Sb_2S_3 solar cells are the large recombination losses within the Sb_2S_3 itself. The recombination losses seem to originate from bulk or surface defects within the Sb_2S_3 layer. These recombination losses have been minimised to some extent by sulphurisation of the Sb_2S_3 layer, use of organic HTM and surface treatments of the interfaces between Sb_2S_3 and the other materials. However, the highest reported efficiency values for a Sb_2S_3 solar cell remain much lower than the theoretical efficiency limit of about 25% for a solar cell with an absorber such as Sb_2S_3 whose bandgap is 1.7 eV. At present, the thickness of Sb_2S_3 for planar solar cells must be ≤ 100 nm because of its short diffusion length. To increase the effective area of a Sb_2S_3 solar cell a micrometre thick porous TiO_2 layer can be coated with a thin layer of Sb_2S_3. Nevertheless, the recombination losses from the bulk and interfaces of the Sb_2S_3, HTM and ETM layers must be significantly reduced to make high efficiency Sb_2S_3 solar cells with a micrometre thick porous layer.

There are many important conclusions that can be drawn from the reviewed perovskite solar cell literature. The most important findings are that a uniform and dense perovskite capping layer is critical to avoiding the possibility of the detrimental contact between the TiO_2 layer and the HTM. A thin porous TiO_2 layer (≤ 200 nm) is best for high efficiency porous TiO_2 perovskite-sensitised solid solar cells. Regardless of the deposition method used, it seems that for higher photovoltaic performance, the amount of unreacted PbX_2 or other non-perovskite compounds in the final deposited perovskite layer should be minimised. However, the enhanced solar cell efficiency

from minimising the amount of unreacted PbX_2 or other non-perovskite compounds has not been unequivocally determined yet. The most recently reported solution deposition methods are able to form high quality films with large grains in uniform and dense layers. Therefore, there is no justification for a deposition method that requires expensive equipment like an evaporator or ALD system because solution methods are producing high efficiency perovskite solar cells. The one-step solution deposition methods require a spin-coating step which can limit the area and throughput for large scale production of perovskite solar cells. The two-step solution deposition method is the most likely to be scaled up for large-area high-throughput industrial production as it only requires the substrate to be immersed sequentially in two solutions.

The main strategy for efficiency enhancement of perovskite solar cells has been to increase the perovskite light absorption by using mixed perovskites of smaller bandgaps. However, optimising the ETM and HTM layers can also contribute to making stable and high efficiency perovskite solar cells. As reported and discussed above, a compact SnO_2 layer can make better planar mixed perovskite solar cells than a compact TiO_2 layer. Nevertheless, the stability and hysteresis observed in the photovoltaic performance of the porous and planar perovskite solar cells depends mainly on the structure of the solar cell and the combination of the particular perovskite, ETM and HTM used. The rapid improvement of the efficiency of perovskite solar cells to values similar to that of commercial silicon solar cells in just 4 years (from 2012 to 2016) has been unprecedented in the history of solar cell research. A summary of the discussed perovskite solar cells with their photovoltaic parameters is given in Table 2.6.

Table 2.6 Summary of the discussed perovskite solar cells in chronological order.

Perovskite solar cells					
Author (year) Perovskite Material	**V_{OC} (volts)**	**J_{SC} (mA/cm^2)**	**FF**	**Efficiency (%)**	**Remarks**
Kojima et al. (2006) $MAPbBr_3$	0.640	6.44	0.53	2.2	Liquid electrolyte as HTM
Kojima et al. (2009) $MAPbBr_3$	0.960	5.6	0.59	3.1	Liquid electrolyte and a 8-12 µm porous TiO_2 layer
$MAPbI_3$	0.610	11	0.57	3.8	Liquid electrolyte and a 8-12 µm porous TiO_2 layer
Im et al. (2011) $MAPbI_3$	0.629	16	0.62	6.2	Liquid electrolyte and a 3.6 µm porous TiO_2 layer
Kim et al. (2012) $MAPbI_3$	0.888	17.6	0.62	9.7	Spiro-OMeTAD as HTM and a 600 nm porous TiO_2 layer
Lee et al. (2012) $MAPbI_2Cl$	0.980	17.8	0.63	10.9	500 nm porous Al_2O_3 layer and spiro-OMeTAD as HTM
Etgar et al. (2012) $MAPbI_3$	0.631	16.1	0.57	5.5	Without a HTM layer
Noh et al. (2013) $MAPb(I_{0.8}Br_{0.2})_3$	0.910	19.3	0.70	12.3	PTAA as the HTM and a 600 nm porous TiO_2 layer
Ball et al. (2013) $MAPbI_2Cl$	1.02	18	0.67	12.3	400 nm porous Al_2O_3 layer and spiro-OMeTAD as HTM
Heo et al. (2013) $MAPbI_3$	0.997	16.5	0.73	12	PTAA as HTM and a 600 nm porous TiO_2 layer
Burschka et al. (2013) $MAPbI_3$	0.993	20	0.73	15	Two-step method, 350 nm porous TiO_2 layer and spiro-OMeTAD as HTM
Liu et al. (2013) $MAPbI_2Cl$	1.07	21.5	0.67	15.4	Evaporated perovskite, planar solar cell structure, spiro-OMeTAD as HTM
Pellet et al. (2014) $MA_{0.6}FA_{0.4}PbI_3$	1.0	21.2	0.70	14.9	Mixed cation perovskite, 300 nm porous TiO2 layer and spiro-OMeTAD as HTM
Ryu et al. (2014) $MAPbBr_3$	1.4	6.1	0.79	6.7	250 nm porous TiO_2 and PIF8-TAA as HTM
$MAPbI_3$	1.04	21.3	0.73	16.2	250 nm porous TiO_2 and PTAA as HTM
Jeon et al. (2014) $MAPb(I_{0.9}Br_{0.1})_3$	1.1	19.6	0.76	16.5	One-step solvent induced deposition method, 200 nm porous TiO_2 and PTAA as HTM
Xiao et al. (2014) $MAPbI_3$	1.04	21.2	0.74	16.2	One-step solvent assisted deposition method, planar solar cell with spiro-OMeTAD as HTM
Jeon et al. (2015) $(FAPbI_3)_{0.85}(MAPbBr_3)_{0.15}$	1.11	22.5	0.73	18.4	200 nm porous TiO_2 and PTAA as HTM
Yang et al. (2015) $(FAPbI_3)_{0.95}(MAPbBr_3)_{0.05}$	1.06	24.7	0.77	20	Intramolecular exchange deposition method, 150 nm porous TiO2 and PTAA as HTM
Correa Baena et al. (2015) $(FAPbI_3)_{0.85}(MAPbBr_3)_{0.15}$	1.14	21.3	0.74	18	Planar solar cell structure with SnO_2 as ETM and spiro-OMeTAD as HTM

Yi et al. (2016) $FA_{0.85}MA_{0.15}Pb(I_{0.85}Br_{0.15})_3$	1.1	23	0.79	20.4	Two-step capping layer deposition method, 150 nm porous TiO_2 and spiro-OMeTAD as HTM
Saliba et al. (2016) $Cs_{0.05}(MA_{0.17}FA_{0.83})_{(0.95)}Pb(I_{0.83}Br_{0.17})_3$	1.147	23.5	0.785	21.17	Lithium doped 150-200 nm porous TiO_2 layer and spiro-OMeTAD as HTM

Building upon the Literature

The research work in this thesis builds upon the entire body of work discussed in this literature review. The thesis research will be explained in complete detail in the corresponding research Chapters 4, 5, 6 and 7. However, a brief summary of the corresponding research topics is given below.

The defects and recombination mechanisms of Sb_2S_3 that have been reported by several researchers can be reduced to some extent by sulphurisation of the Sb_2S_3 layer or the use of buffer layers [54, 59, 60, 62, 64]. Chapter 4 shows that these recombination losses can also be reduced by having Sb_2S_3 with certain preferential crystal planes. The efficiency of Sb_2S_3 solar cells is higher with a sulphur-rich Sb_2S_3 film than with a Sb-rich Sb_2S_3 film. It also shows how to obtain a perfectly planar top Sb_2S_3 surface with an underlying textured (non-planar) substrate.

In Chapter 5, a highly porous TiO_2 layer was used in a bid to improve the efficiency of fully inorganic Sb_2S_3 solar cells. Standard Sb_2S_3 solar cells have a spin-coated porous TiO_2 layer with a porosity of about 50% to 60% [55, 57-61, 63-65]. A porous TiO_2 layer with a higher porosity could improve the solar cell efficiency by increasing the infiltration of the inorganic HTM and thus the collection efficiency. The enhanced infiltration of the HTM in the porous TiO_2 layer can increase the transfer of carriers between the absorber and the inorganic HTM.

The laboratory high efficiency perovskite solar cells could become commercially available at a low retail cost [89, 93, 96]. However there are some issues that have to be solved before this can happen at a large commercial scale. The stability of perovskite solar cells has to be significantly improved and the presence of lead eliminated. Furthermore, low-cost industrial production would require high-throughput with a high yield or minimum manufacturing losses of large area

perovskite solar cells. This could be achieved with low-cost, high-throughput and robust fabrication processes. The deposition of the porous TiO_2 layer with a flame aerosol system can have a higher throughput than with the usual spin-coating or screen-printing methods. The flame-made porous TiO_2 layer could be part of a continuous production line of large area perovskite solar cells. With this in mind, in Chapter 6 $MAPbI_3$ perovskite solar cells with a flame-made porous TiO_2 layers were fabricated. The effect of the morphology and porosity of the flame-made porous TiO_2 layers in $MAPbI_3$ solar cells was investigated. The morphology and porosity of the flame-made porous TiO_2 layers are significantly different than those of the standard spin-coated porous TiO_2 layers [61, 98]. These differences could enhance the performance of perovskite solar cells.

Planar perovskite solar cells with a compact SnO_2 layer instead of a compact TiO_2 layer have been reported as more stable and with similar efficiencies as with TiO_2 [97]. The inherent better properties of SnO_2 could further enhance the performance and stability of perovskite-sensitised solar cells [99-103]. In Chapter 7, the potential of substituting the flame-made porous TiO_2 layer with a flame-made porous SnO_2 porous layer in $MAPbI_3$ perovskite solar cells was investigated. The results from this substitution are promising with concrete scope for further improvement.

3. Materials and Methods

All the materials and deposition processes discussed in this Chapter were used to fabricate the different solar cells that are discussed in the following research Chapters. Most of the deposition processes described in this Chapter required extensive optimisation to improve each of the solar cell structures that were investigated. Also a wide range of characterisation equipment was used to characterise the materials and photovoltaic performance of the solar cells. The characterisation equipment that was used is mentioned throughout this Chapter as well as in the following research Chapters. All the material properties discussed in this Chapter were used to the guide the solar cell research that is discussed in detail in the following Chapters. The materials in this Chapter are divided into: absorbers, electron transport, hole transport and conductor materials. Each of the absorber and electron transport materials has the following sub-sections: chemical and physical properties, optical properties, electronic properties and deposition methods.

3.1 Absorber Materials

3.1.1 Antimony Trisulphide

Chemical and Physical Properties

Compounds of antimony with sulphur can exist in the form of antimony trisulphide (Sb_2S_3), antimony tetrasulphide (Sb_2S_4) or antimony pentasulphide (Sb_2S_5) [104]. However, Sb_2S_3 is the only antimony sulphide compound that can adopt a crystalline form called stibnite whereas all other antimony sulphide compounds exist only as amorphous materials. Amorphous Sb_2S_3 is a yellow-red powder and crystalline Sb_2S_3 is a dark lead-grey coloured solid with a melting temperature of 550°C under standard conditions. [105, 106].

Crystalline Sb_2S_3 has an orthorhombic crystal lattice with parallel ribbon-like $(Sb_4S_6)_n$ moieties or chains running parallel to the c-axis as depicted in Fig. 3.1a-b. In a $(Sb_4S_6)_n$ ribbon, the Sb and S atoms are linked together by short covalent bonds [107].

A perfect cleavage parallel to the c-axis having a [010] direction as shown in Fig. 3.1a results in no short covalent bonds being broken and no dangling bonds being formed; only Van der Waals forces being overcome [108]. The compounds Sb_2S_3, Bi_2S_3, Sb_2Se_3 and Bi_2Se_3 have the same crystal structure and therefore will share similarities in their properties [108].

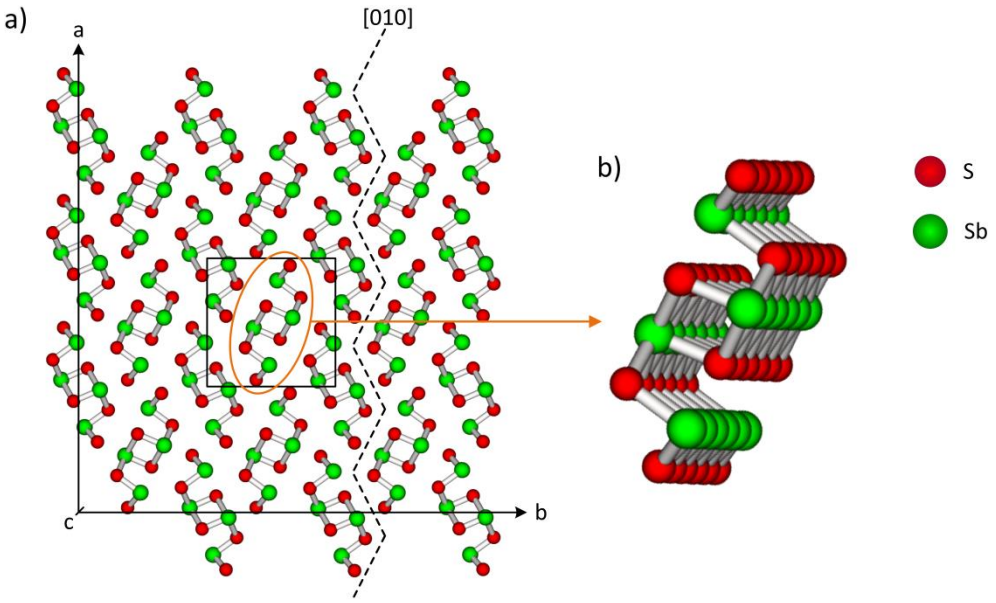

Figure 3.1 a) Sb_2S_3 crystalline structure looking down the c-axis (the dashed-broken line shows the cleavage trace along the [010] crystal direction and the solid line square shows the unit cell projection on the a-b plane). b) Single $(Sb_4S_6)_n$ ribbon aligned parallel to the c-axis (adapted from Zakaznova-Herzog et al. (2005) and Vadapoo et al. (2011)).

An X-ray diffraction (XRD) spectrum can be used to identify the crystalline Sb_2S_3 phase. Crystalline materials such as Sb_2S_3 have a unique XRD spectrum where each peak in the spectrum corresponds to a crystal plane. The relative height of the peaks indicates which crystal planes are preferential or more abundant with respect to other crystal planes. Additionally, the crystal size can be estimated from the measured XRD spectrum using Scherrer's equation [109]. The stoichiometry of Sb_2S_3 can be evaluated by measuring the antimony to sulphur (Sb:S) ratio with an EDS system [110, 111]. An antimony to sulphur ratio of 4:6 means the Sb_2S_3 is perfectly stoichiometric. For the experimental work in this thesis, the XRD spectrum of the Sb_2S_3 pellets used for the deposition of thin Sb_2S_3 films along with its atomic ratio were measured using a PANalytical X'Pert Pro XRD system and a Hitachi 4300 SE/N FE-SEM system. From the

corresponding results of the measurements, shown in Fig. 3.2, it can be determined that Sb_2S_3 is the only compound present (no other antimony or sulphur compounds are present) in the Sb_2S_3 pellets and that antimony and sulphur exist in a nearly perfect stoichiometric ratio. After acquiring Sb_2S_3 source material or fabricating Sb_2S_3 films it is important to do these measurements to determine the stoichiometry and purity of Sb_2S_3 because the material can contain a large amount of metallic antimony or antimony oxide [105, 112-114].

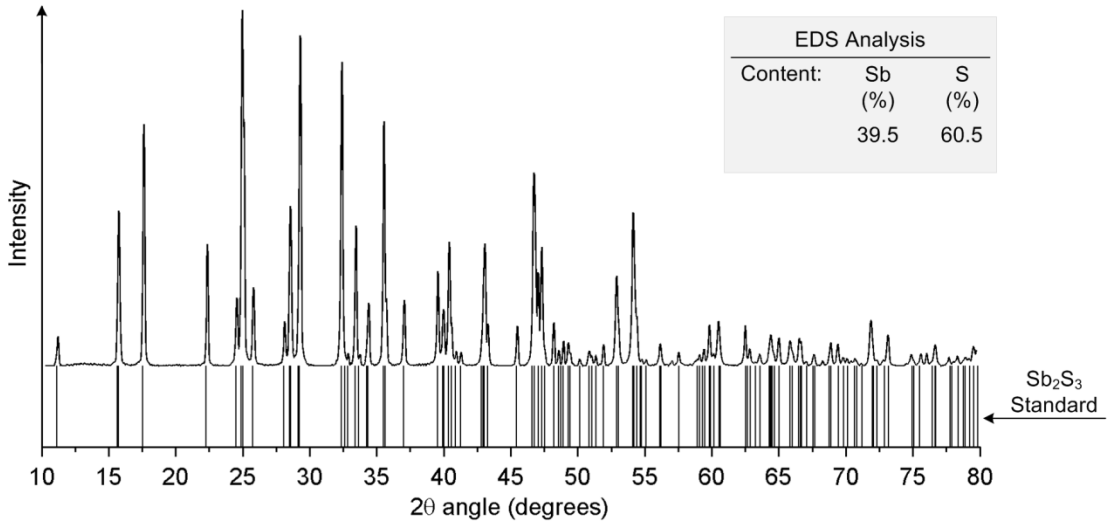

Figure 3.2 Measured XRD spectrum of the Sb_2S_3 pellets that were used for thermal evaporation and the Sb_2S_3. JCPDS standard #42-1393. Inset: measured antimony to sulphur (Sb:S) ratio by EDS of the same Sb_2S_3 pellets.

Optical Properties

The absorptance as a function of wavelength of crystalline Sb_2S_3 thin films was measured using a spectrophotometer with integrating sphere. These are shown in Fig. 3.3. The Sb_2S_3 refractive index as a function of wavelength calculated by fitting of ellipsometry measurements is shown in Fig. 3.3. The band gap of crystalline Sb_2S_3 was estimated to be 1.66-1.7 eV from the optical data.

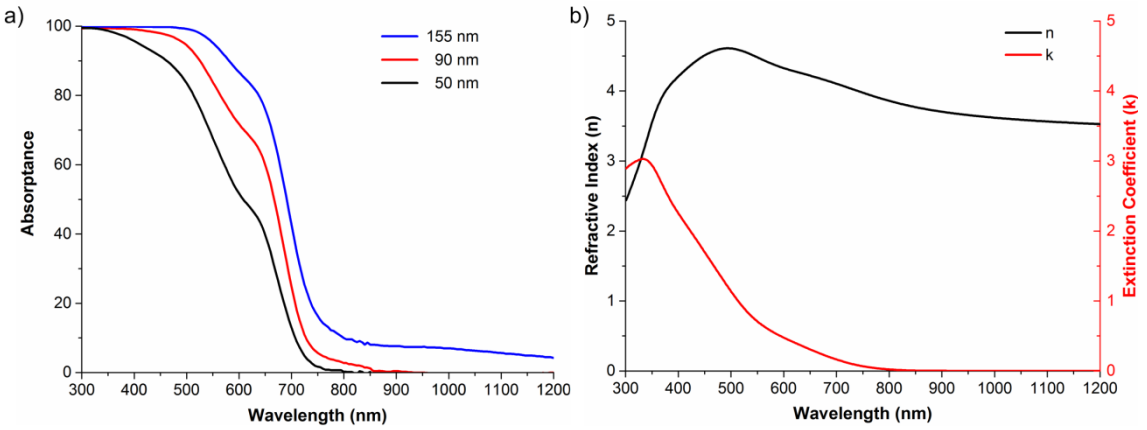

Figure 3.3 (a) Absorptance of crystalline Sb_2S_3 films as a function of wavelength for different Sb_2S_3 film thickness deposited by thermal evaporation (measured with a spectrophotometer with an integrating sphere). (b) Refractive index and extinction coefficient (k) of crystalline Sb_2S_3 as a function of wavelength calculated from ellipsometry measurements.

Electronic Properties

The conduction and valence band energy levels plus the Fermi energy level of crystalline Sb_2S_3 deposited by different methods are shown in Fig. 3.4 [72, 115]. The energy levels for the crystalline Sb_2S_3 deposited by different methods are slightly different because of variations in the composition, crystal structure and surface properties [71].

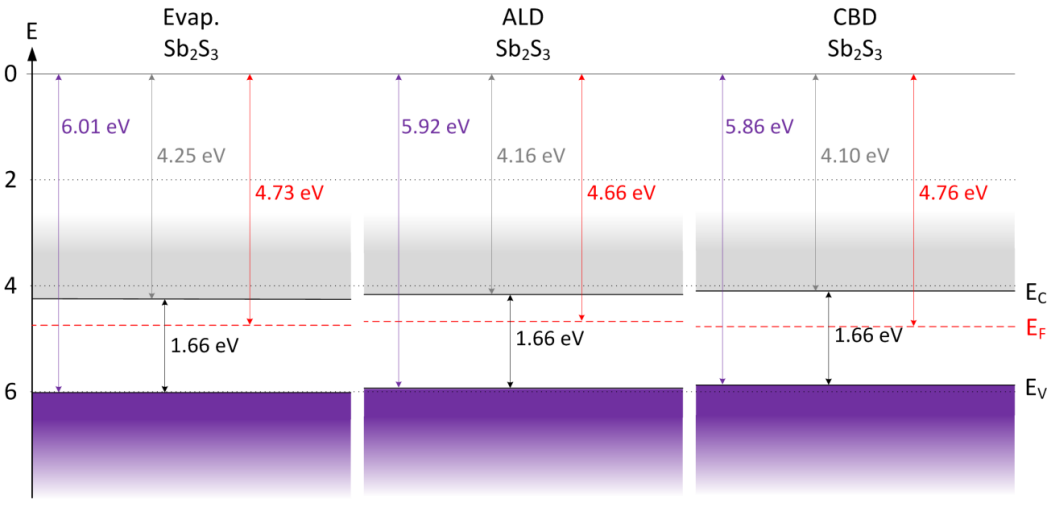

Figure 3.4 Energy band diagram of crystalline Sb_2S_3 deposited by thermal evaporation, ALD and CBD calculated from UPS and optical measurements (adapted from Lee et al. (2013), Liu et al. (2012) and Kim et al. (2014)).

Several groups have reported crystalline Sb_2S_3 to be an n-type semiconductor with a band gap of 1.66-1.76 eV [115-121]. A compilation of the electronic properties of crystalline Sb_2S_3 from the published literature is presented below in Table 3.1.

Table 3.1 Compilation of the electrical properties of crystalline Sb_2S_3 from the literature.

Electrical property	Sb_2S_3	Author (year)
Ambipolar diffusion length	80 nm at one sun	Darga et al. (2013)
Mobility	1 $cm^2/V{\cdot}s$	Curran et al. (1982), Bohac and Kaufmann (1975)
	10 $cm^2/V{\cdot}s$	Savadogo et al. (1992, 1994), Bohac (1975)
Drift mobility from J-V measurements	40 $cm^2/V{\cdot}s$ along the c-axis	Bohac and Kaufmann (1975)
	3 $cm^2/V{\cdot}s$ perpendicular to the c-axis	Bohac and Kaufmann (1975)
Resistivity	4-5x10^8 Ω·cm on glass	Savadogo et al. (1992), Calixto et al. (2010), Bohac and Kaufmann (1975)
	5x10^6 Ω·cm on FTO susbtrate	Savadogo et al. (1992, 1994)
Donor density	10^{14} cm^{-3}	Curran et al. (1982)
Carrier concentration	10^{12} cm^{-3}	Savadogo et al. (1992, 1994)
Density of states in the valence band largely from long range Sb p bonds	2.5x10^{19} cm^{-3} for amorphous Sb_2S_3	Mady et al. (1987), Ghosh and Varma (1979)

From Table 3.1 it can be observed that at least some of the electronic parameters depend on the crystal orientation. Bohac and Kaufmann (1975) found that the specific resistivity along the c-axis is smaller than perpendicular to the c-axis by a factor of 100. Also the estimated drift mobility from J-V measurements was 40 $cm^2/V{\cdot}s$ along the c-axis and 3 $cm^2/V{\cdot}s$ perpendicular to the c-axis. Furthermore, the Hall mobility measured along the c-axis ranges from 1 to 10 $cm^2/V{\cdot}s$ depending on the sample [105]. The asymmetric crystal structure of Sb_2S_3 makes it easier for the electrons to flow along the c-axis than perpendicular to it. The electrons flow more efficiently along the ribbons of covalently bonded atoms which are aligned along the c-axis. Conversely, when the electrons flow perpendicular to the c-axis, they have to cross between ribbons held together by Van der Walls forces.

There is a difference in the reported values for the electronic parameters in Table 3.1. These differences may be because of the deposition or fabrication method used to make Sb_2S_3 films or crystals. Different methods can produce Sb_2S_3 with significant

differences in preferential crystal planes, Sb:S ratio, grain size and proportion of impurities. For instance, two methods to make Sb_2S_3 films will be described in the following sections. The following methods were used to make the solar cells discussed in Chapters 4 and 5.

Deposition Methods

Chemical Bath Deposition of Sb_2S_3

The solution deposition method known as chemical bath deposition (CBD) is a simple method to deposit thin semiconductor films. This method consists of immersing the substrate into a solution for a period of time that is proportional to the desired film thickness. For the solar cells discussed in Chapters 4 and 5, crystalline Sb_2S_3 films were fabricated using the following CBD method [56, 122, 123] and annealing step:

The solution was prepared using antimony trichloride ($SbCl_3$) and sodium thiosulphate ($Na_2S_2O_3$) as follows:

1) 650 mg of $SbCl_3$ was dissolved in 2.5 ml of acetone in a glass beaker.
2) 25 ml of 1M sodium thiosulphate aqueous solution at a temperature of 10°C was added to the $SbCl_3$ acetone solution.
3) 72.5 ml of deionised water at a temperature of 10°C was also added and the solution was stirred well for 30 seconds whilst keeping it at 10°C.
4) The substrates were immersed vertically in the solution to coat them with a Sb_2S_3 film. The substrates had one side facing the wall of the glass beaker. The Sb_2S_3 film thickness was proportional to the immersion time. During the deposition process the solution was kept at 10°C. Under these conditions, the deposition rate of amorphous Sb_2S_3 was about 1.7 nm per minute.
5) Once the desired thickness was deposited, the coated substrates were removed from the solution.
6) The coated substrates were rinsed with deionised water and dried with a nitrogen (N_2) gun.
7) The Sb_2S_3 film deposited on the substrate surface facing the wall of the beaker was visibly uniform while the film on the other surface was not. The non-uniform Sb_2S_3 film was removed with diluted hydrochloric (HCl) acid.

8) The amorphous Sb_2S_3 films were then annealed at 300°C for 30 minutes in nitrogen atmosphere to obtain crystalline Sb_2S_3.

The CBD solution of Sb_2S_3 contains antimony cations (Sb^{3+}) and sulphur anions (S^{2-}) that are deposited on the surface of the substrate to form a Sb_2S_3 layer. The CBD solution of Sb_2S_3 also contains antimony thiosulphate complexes ($Sb_x(S_2O_3)_y$) and thiosulphate ions ($S_2O_3^{2-}$) as shown in Fig. 3.5. The solution tends to be slightly acidic (pH ≈ 3.5). A schematic of the CBD method to deposit Sb_2S_3 is shown in Fig. 3.5. Ideally only Sb^{3+} cations and S^{2-} ions should be deposited on the surface of the substrate to form the Sb_2S_3 film. However, the deposited Sb_2S_3 film can contain a measurable amount of antimony oxide. The antimony oxide comes from the deposition of the antimony thiosulphate complexes and thiosulphate ions depicted in Fig. 3.5. The main advantage of this method is its simplicity and low-cost as it does not require sophisticated equipment. However, the produced film can contain some amounts of antimony oxide which is inherent to this method.

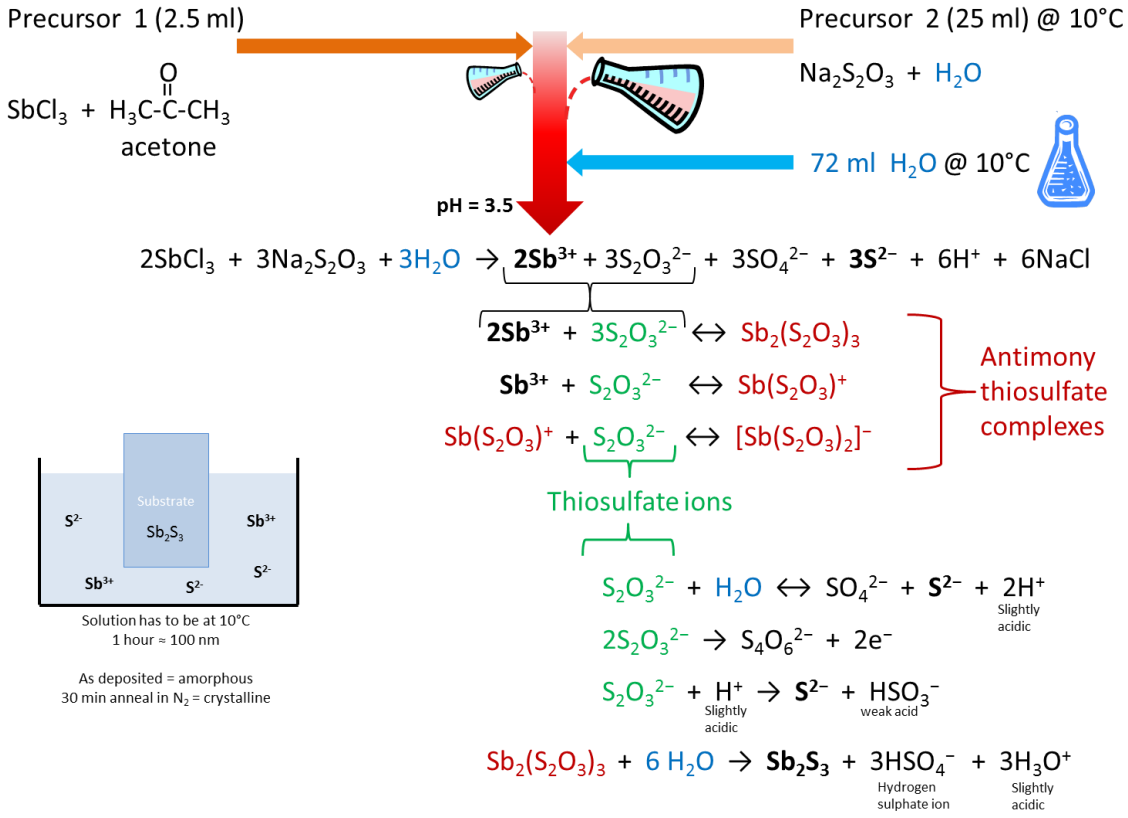

Figure 3.5 Schematic of the CBD method used to deposit Sb_2S_3 films (created after reports from Nair et al. (1998), Messina et al. (2007) and Grozdanov et al. (1994)).

Thermal Evaporation of Sb_2S_3

The thermal evaporation takes places in a high vacuum chamber to be able to vaporise the Sb_2S_3 pellets at a lower temperature than at atmospheric pressure. The mean free path of the evaporated Sb_2S_3 is increased at high vacuum. High vacuum is also required to prevent film oxidation and reduce the density of contaminants. All of these factors contribute to achieving a uniform and dense Sb_2S_3 film deposition. At atmospheric pressure, Sb_2S_3 melts at 550°C and it starts to evaporate at 650°C [105, 106]. However, evaporation of Sb_2S_3 at low pressures can be done at a much lower temperature because of the reduction in vapour pressure. For example, at a pressure of $1x10^{-4}$ Torr, Sb_2S_3 can start to evaporate at about 200°C [124].

An ANGSTROM coat thermal system was used to deposit the Sb_2S_3 thin films discussed in Chapter 4. The commercially acquired Sb_2S_3 pellets were thermally evaporated at a base pressure of $1x10^{-6}$ Torr at a deposition rate of 0.8 Å/s. The substrates were placed 40 cms above the Sb_2S_3 pellets that were placed in a SiO-baffled box heater made of Tantalum. The baffled box filled with Sb_2S_3 pellets heated up to melt and evaporate the Sb_2S_3 at a base pressure of $1x10^{-6}$ Torr, as schematically shown in Fig. 3.6. A thin-film thickness monitor kept track of the deposition rate and thickness.

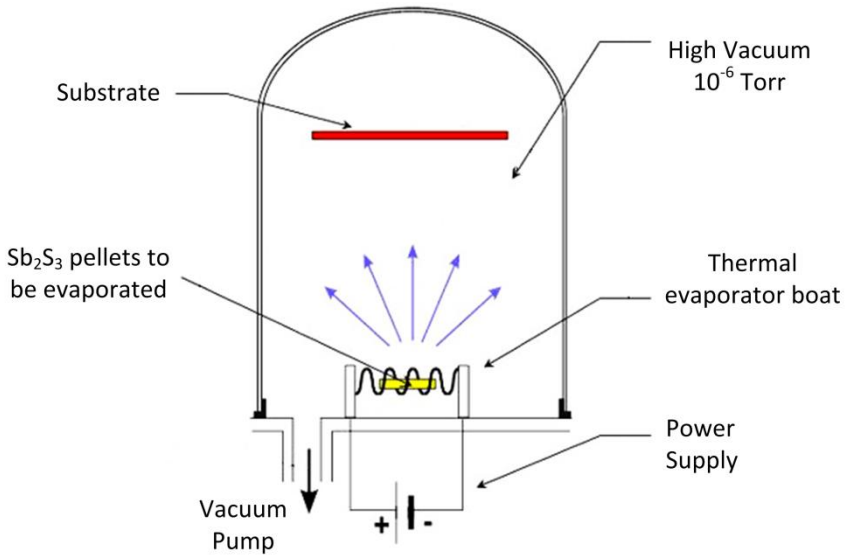

Figure 3.6 Schematic of the thermal evaporator system used for thin film depositions of various materials.

The importance of the homogeneity and stoichiometry of the Sb_2S_3 pellets which are the starting material should not be overlooked. Highly pure and stoichiometric crystalline Sb_2S_3 pellets can be synthesized from high purity (99.9999%) Sb and S elements melted at 800°C under high vacuum ($1x10^{-6}$ Torr). However, the facilities to carry out this process were not available. Instead, commercially-available 99.99% pure Sb_2S_3 pellets were bought and used in the thermal evaporation system for deposition of thin films of Sb_2S_3 to make solar cells. However, all of the solar cells made from this commercial Sb_2S_3 material did not generate any voltage or current upon illumination. This was unexpected and prompted the analysis of the commercial Sb_2S_3 pellets.

The homogeneity and stoichiometry of the commercial Sb_2S_3 pellets was assessed using the previously mentioned XRD and EDS systems. From the XRD and EDS analyses it was determined that the commercial Sb_2S_3 pellets consisted of a mix of metallic antimony and Sb_2S_3 in a ratio of about 50/50. Therefore, a search was done for reliable suppliers and manufacturers of high purity Sb_2S_3 pellets. In the end, the truly stoichiometric and homogenous Sb_2S_3 pellets were provided by Dr. Zhiyong Yang from Jiangsu Key Laboratory of Advanced Laser Materials and Devices in Jiangsu, China. The homogeneity and stoichiometry of Dr. Zhiyong Yang's Sb_2S_3 pellets was assessed by XRD and EDS analyses. The results from these analyses show that the Sb_2S_3 pellets provided by Dr. Zhiyong Yang are of high purity and stoichiometry. These XRD and EDS analyses results were shown in Fig. 3.2.

3.1.2 Methyl Ammonium Lead Iodide

Chemical and Physical Properties

The organic-metal halide perovskite absorber materials for solar cells are composed of organic cations, metal cations and halogen anions in a cubic crystal structure. The general formula for the organic-metal halide perovskite is ABX_3 where A is the organic/inorganic cation, B the metal cation and X the halogen anion. The organic/inorganic, metal and halogen ions can be made of many different materials. The most commonly used materials are methyl ammonium (MA, $CH_3NH_3^+$), formamidinium (FA, $HN{=}CHNH_3^+$) or cesium (Cs) for the organic/inorganic cation, lead (Pb^+) or tin (Sn^+) for the metal cation, and chlorine, (Cl^-), iodine (I^-) or bromine (Br^-) for

the halogen ion. Nevertheless, other materials are yet to be investigated [125, 126]. The perovskite cubic crystal structure has the halogen (Cl, I, Br) situated at the face centres of the cube, the metal (Pb, Sn) at its centre and the organic/inorganic compounds (MA, FA, Cs) at the corners of the cube as can be seen in Fig. 3.7a. The crystal structure can also be seen as organic/inorganic cations being surrounded by octahedra made of halogen ions (in the octahedron corners) and metal ions (in the octahedron centre) as shown in Fig. 3.7b.

The $MAPbI_3$ perovskite was one of the first perovskites used as absorber layers for solar cells and therefore it has been one of the most used and studied [73-76, 78]. The measured XRD spectrum of $MPbI_3$ is shown in Fig. 3.7c which can be used to identify and distinguish the $MAPbI_3$ perovskite phase from other non-perovskite phases that could be present, such as PbI_2. The XRD spectra can also reveal whether there are any preferential perovskite crystal planes in the $MAPbI_3$ layer.

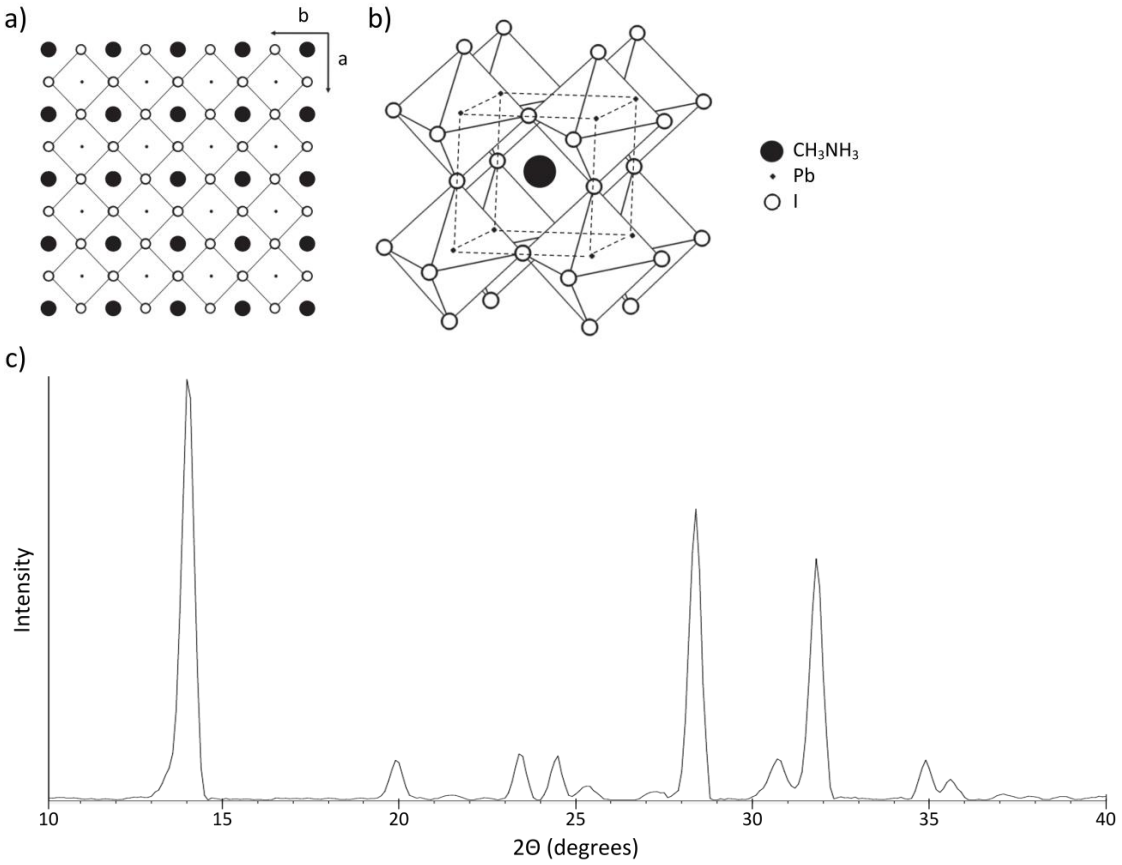

Figure 3.7 a) Crystal lattice of $MAPbI_3$ viewed from the c axis. b) Diagram of the crystal unit cell structure of $MAPbI_3$ (adapted from Lee et al. (2012)). c) Measured XRD spectrum of a thin film of $MAPbI_3$ deposited using the one-step solvent assisted method.

It should be noted that $MAPbI_3$ presents some problems such as degradation to PbI_2 when exposed to air atmosphere or temperatures ≥ 55°C [127-130]. This is partly because $MAPbI_3$ degrades on contact with moisture [127]. Also, $MAPbI_3$ is not thermally stable and there are concerns with respect to the structural phase transition at 55 °C [129-131]. Encapsulation of $MAPbI_3$ solar cells can temporarily alleviate some of these problems. A more promising solution is to use mixed perovskites that do not have the aforementioned problems [91, 94-96]. However, at this time the well-established preparation and deposition of $MAPbI_3$ is an advantage over mixed perovskites. In addition, $MAPbI_3$ has been a useful platform to test structures and concepts that subsequently can be enhanced by the use of a mixed perovskite.

Optical Properties

The measured optical absorbance as a function of wavelength of the $MAPbI_3$ using a spectrophotometer with an integrating sphere is shown in Fig. 3.8a. The refractive index as a function of wavelength calculated by fitting of the ellipsometry measurements is shown in Fig. 3.8b. From this optical data, the band gap of $MAPbI_3$ was estimated to be 1.55 eV, which is consistent with values reported by others [25, 76, 77, 84, 94, 97, 132, 133].

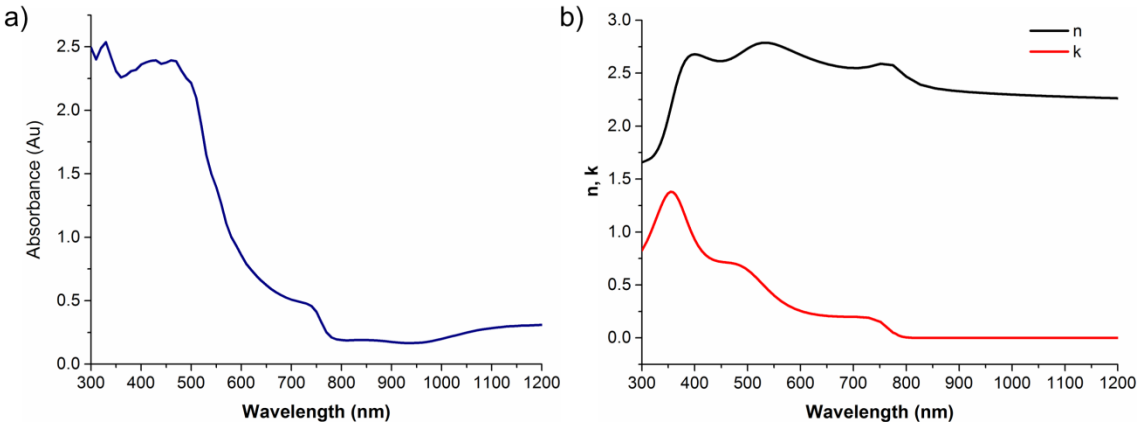

Figure 3.8 a) Measured absorbance of $MAPbI_3$ as a function of wavelength. b) Refractive index and extinction coefficient of $MAPbI_3$ as a function of wavelength calculated from ellipsometry measurements.

Electronic Properties

The energy levels of the conduction and valence band of $MAPbI_3$ are shown in Fig. 3.9 [76, 134]. UPS can be used to measure the Fermi energy level and the valence band energy level, while inverse photoemission spectroscopy (IPES) can be used to measure the conduction band energy level [134]. The difference between the electronic band gap in Fig. 3.9 and the optical band gap is because of the exciton binding energies in the perovskite [134].

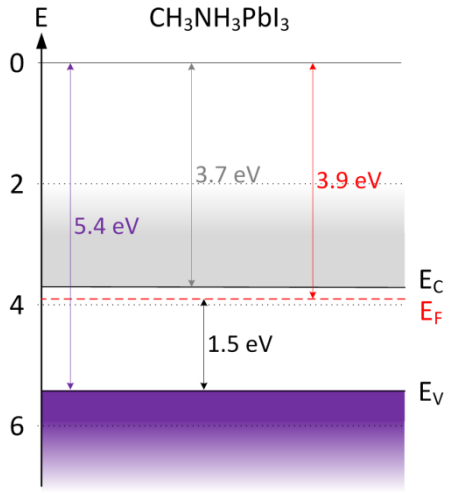

Figure 3.9 Energy levels of the Fermi, conduction and valence band of $MAPbI_3$ as estimated by UPS, IPES and optical measurements (adapted from Schulz et al. (2014) and Kim et al. (2012)).

Several groups have reported crystalline $MAPbI_3$ to be a direct n-type semiconductor with a band gap of 1.5–1.56 eV [76, 97, 131]. However, there have been reports that $MAPbI_3$ can be a p-type semiconductor [135]. The p-type or n-type character of $MAPbI_3$ seems to depend on its type and number of defects and impurities which mainly come from the preparation method and conditions [136, 137]. A compilation of the electronic properties of $MAPbI_3$ from the literature is presented below in Table 3.2.

Table 3.2 Compilation of the electrical properties of $MAPbI_3$ collected from the referenced literature.

Electrical property	$MAPbI_3$	Author (year)
Electron diffusion length	129 ± 41 nm	Stranks et al. (2013)
Hole diffusion length	105 ± 32 nm	Stranks et al. (2013), Xing et al. (2013)
Electron mobility	2 $cm^2/V{\cdot}s$	Stranks et al. (2013)
Hole mobility	2 $cm^2/V{\cdot}s$	Stranks et al. (2013)
Electron diffusion coefficient	0.03 cm^2/s	Xing et al. (2013)
Resistivity	$1x10^7$ Ω·cm for single crystal $4x10^7$ Ω·cm for polycrystalline	Pisoni et al. (2014), Stoumpos et al. (2013), Shi et al. (2015)
Doping density	$2x10^{17}$ cm^{-3}	Laban and Etgar (2013)
Charge carrier concentration	10^{18} cm^{-3}	Wehrenfenning et al. (2014)

Deposition Method

One-Step Solvent Assisted Method of $MAPbI_3$

The deposition method used to make $MAPbI_3$ layers for solar cells was based on the one-step solvent assisted method reported by Xiao et al. (2014). The $MAPbI_3$ layer was spin-coated from a solution composed of 0.9 M equimolar of methyl ammonium iodide (MAI) and lead iodide (PbI_2) in 7/3 (v/v) of N,N-dimethylformamide (DMF) and dimethyl sulphoxide (DMSO). This solution was poured on top of the desired substrates and then spun for 60 seconds at 5000 rpm/s using a Laurell WS-650SZ-6NPP/Lite spin-coater. After 10 seconds into the spin-coating process, 100 µl of chlorobenzene was dropped onto the spinning substrate for fast crystallisation. The perovskite coated substrate was then annealed on a hotplate at 105 °C for 10 minutes. This entire process was done inside a nitrogen filled glove box.

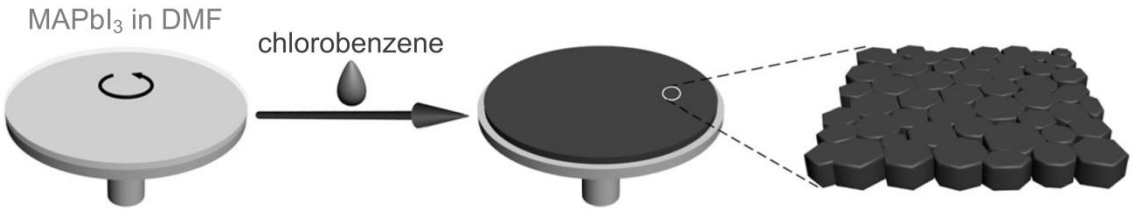

Figure 3.10 Schematic illustration of the one-step solvent assisted method used to deposit $MAPbI_3$ layers via spin-coating process (adapted from Xiao et al. (2014)).

3.2 Electron Transport Materials (ETM)

3.2.1 Titanium Oxide

Chemical and Physical Properties

Titanium oxide (TiO_2) can exist as an amorphous or crystalline material. Crystalline TiO_2 can adopt three different crystal structures: tetragonal (anatase), rhombohedral (brookite) and tetragonal (rutile); all of which can be made under the right conditions. Anatase and brookite are metastable phases which can be transformed to the stable phase rutile (irreversible process) upon heating to temperatures > 700°C [138, 139]. The anatase phase is the most widely used TiO_2 phase because it has better electronic properties than rutile and brookite [139-141]. The TiO_2 XRD spectra and anatase crystal structure are shown in Fig. 3.11a-b.

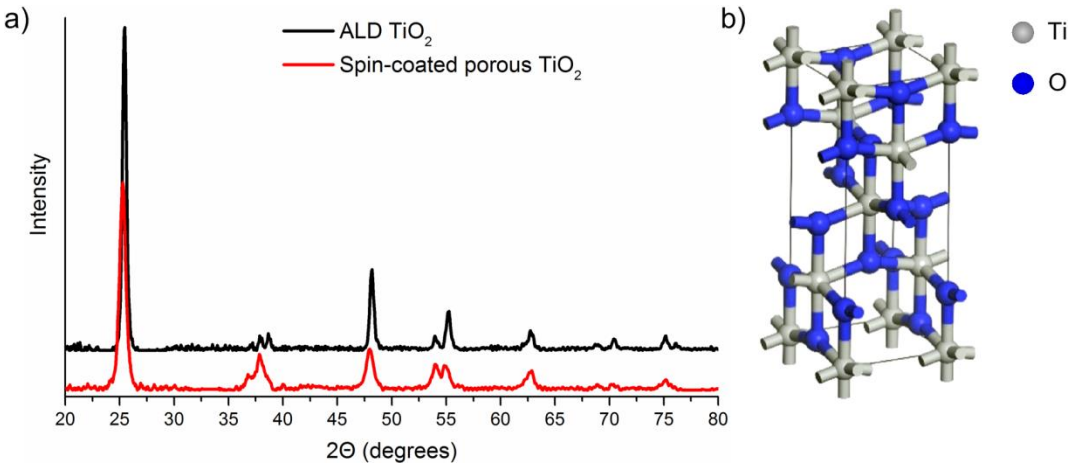

Figure 3.11 a) Measured XRD spectra of an experimentally made compact anatase TiO_2 layer deposited via ALD and of a spin-coated porous TiO_2 layer b) Schematic representation of the TiO_2 anatase crystal structure (adapted from Asahi et al. (2014) and Yang et al. (2015)).

Optical Properties

The absorption onset of TiO_2 is at about 385 nm which is at the ultraviolet light portion of the spectrum with a photon energy of 3.2 eV as shown in Fig. 3.12a. The solar spectrum starts at about 300 nm so in principle only a small fraction can be lost by absorption within the TiO_2 and the rest can be transmitted to the absorber material of

the solar cell. The TiO_2 refractive index as a function of wavelength calculated by fitting of ellipsometry measurements is shown in Fig. 3.12b.

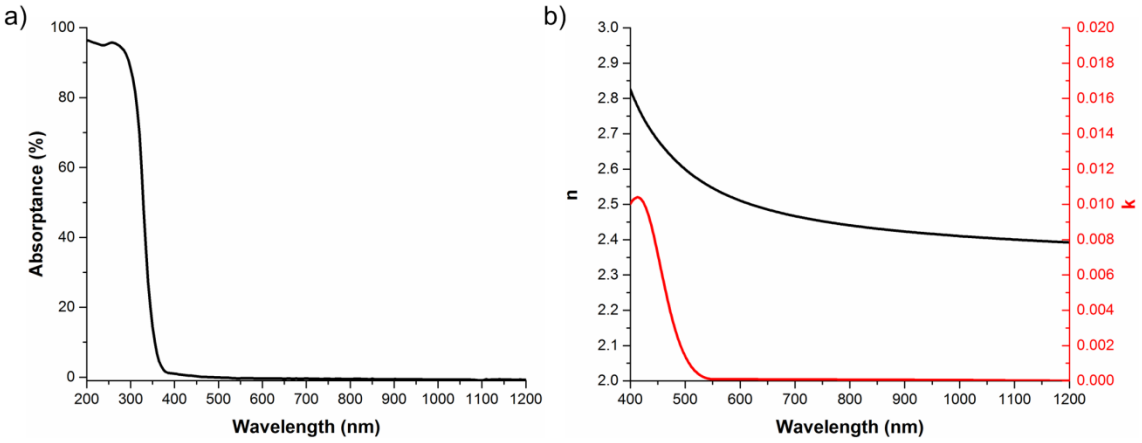

Figure 3.12 a) Absorptance of TiO_2 as a function of wavelength from optical measurements made with a spectrophotometer with an integrating sphere. b) Refractive index and extinction coefficient of anatase TiO_2 as a function of wavelength calculated from ellipsometry measurements.

Electronic Properties

The anatase TiO_2 valence band energy level and work function are at 6.9 eV and 3.7 eV respectively as schematically shown in Fig. 3.13. TiO_2 is an n-type semiconductor with a band gap value of 3.2 eV [142, 143].

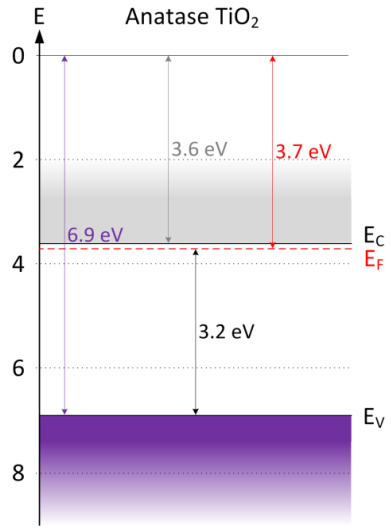

Figure 3.13 Energy band levels of the conduction and valence bands of anatase TiO_2 that were calculated and measured by UPS, IPES and optical measurements (adapted from Scanlon et al. (2013), Asahi et al. (2014), Schulz et al. (2014)).

A compilation of the relevant electronic properties of TiO_2 collected from the literature is presented below in Table 3.3.

Table 3.3 Compilation of the electrical properties of TiO_2 from the referenced literature.

Electrical property	TiO_2	Author (year)
Mobility	1 to 4 $cm^2/V{\cdot}s$	Tang et al. (1994), Yagi et al. (1996)
Resistivity	0.1 to 10 Ω·cm increases with time as exposed to air	Forro et al. (1994), Tang et al. (1994)
Carrier concentration	$> 10^{18}$ cm^{-3} degenerate $< 10^{18}$ cm^{-3} non-degenerate	Forro et al. (1994), Tang et al. (1994)

It should be noted that TiO_2 based solar cells have been found to have an inherent instability under UV illumination which has been linked to the oxygen desorption within the TiO_2 upon UV illumination [92]. This is a problem for the long-term stability of TiO_2 based solar cells. It can be alleviated by doping the TiO_2 to reduce its UV reactivity or by substituting the TiO_2 layer with another ETM [97].

Deposition Methods

Atomic Layer Deposition of TiO_2

The atomic layer deposition (ALD) method is a self-limiting and conformal fabrication process for making compact films. The ALD process for the material of interest is separated into two sequential chemical reactions referred to as the first and second half reaction. Each one of these half reactions involves a chemical compound referred accordingly as the first and second reactant. Both reactants must be volatile, thermally stable and must chemically bind onto the surface or react rapidly with the surface groups and also react aggressively with each other [144]. The first reactant is the metal chemical compound. The second reactant is the oxidiser which can be either water (H_2O), hydrogen peroxide (H_2O_2), ozone (O_3) or oxygen (O_2) plasma.

The first half reaction occurs when the first reactant is pulsed into the reactor chamber where it bonds with the surface functional groups to form a single layer on the entire surface of the substrate (Fig. 3.14a). This is followed by a purge step of an inert gas (nitrogen or argon) to remove the excess reactant and the by-product compound from

the reactor chamber (Fig. 3.14b). Then the second half reaction occurs when the second reactant is pulsed into the reactor chamber where it bonds to the previous reactant layer and creates a by-product compound (Fig. 3.14c). This is followed by another purge step of an inert gas to remove the by-product compound and excess reactant from the reactor chamber (Fig. 3.14d). The aforementioned ALD cycle is repeated until the desired film coating thickness is obtained.

The separation of the reactions (first and second half reactions) makes the film coating process self-limiting. In other words, the amount of material deposited in each cycle (growth rate) is constant and the film thickness varies linearly with the number of deposition cycles [144, 145]. The film growth rate can be as low as 1 Å per cycle. This makes ALD a highly uniform and conformal coating method suited for either small or large area substrates with precise control of the deposited film thickness.

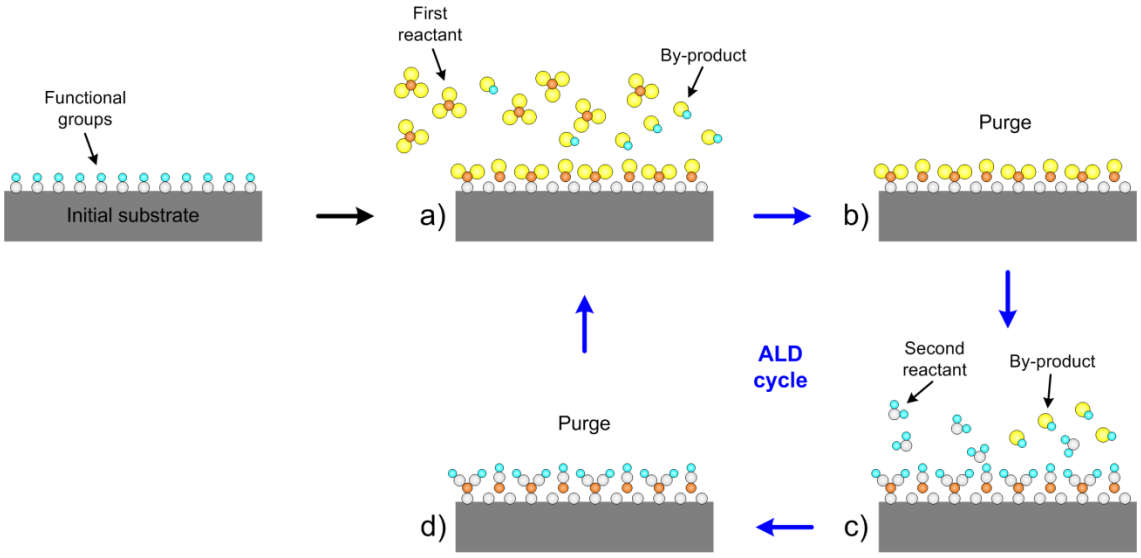

Figure 3.14 ALD cycle from the initial substrate with hydroxyl (OH) surface functional groups: a) The first reactant bonds with the substrate's surface functional groups forming a monolayer. b) The excess reactant and the created by-product are purged. c) The second reactant bonds with the previously deposited reactant monolayer. d) The excess reactant and the created by-product are purged (made based on www.merc.zju.edu.cn/htw/research accessed 19 March 2016).

Two titanium reactants were used for the ALD of TiO_2 films: titanium tetra-isopropoxide (TTIP, $Ti(O^iPr)_4$) or titanium tetrachloride ($TiCl_4$). These chemical compounds react and bond with the hydroxyl groups of the substrate surface [144].

The oxidiser was H_2O. The ALD system used to deposit TiO_2 was a BENEQ TFS 200 system [146]. Depending on which titanium precursor was used the corresponding ALD process was:

- Pulse $TiCl_4$ for 50 ms, purge with N_2 for 750 ms, pulse H_2O for 50 ms, purge with N_2 for 750 ms with a reactor chamber temperature of 210°C which had a growth rate of 0.45 Å per cycle.
- Pulse TTIP for 1 s, purge with N_2 for 2 s, pulse H_2O for 500 ms, purge with N_2 for 2 s with a reactor chamber temperature of 230°C which had a growth rate of 0.30 Å per cycle.

Both processes produce similar TiO_2 films, which were then annealed at 500°C for 30 minutes in air atmosphere to ensure the film has a crystalline anatase phase. Figure 3.15 shows a cross section image of the ALD TiO2 deposited on top of an uneven substrate. The use of $TiCl_4$ or TTIP as the first reactant depended solely on the availability of the precursor at the time of the depositions.

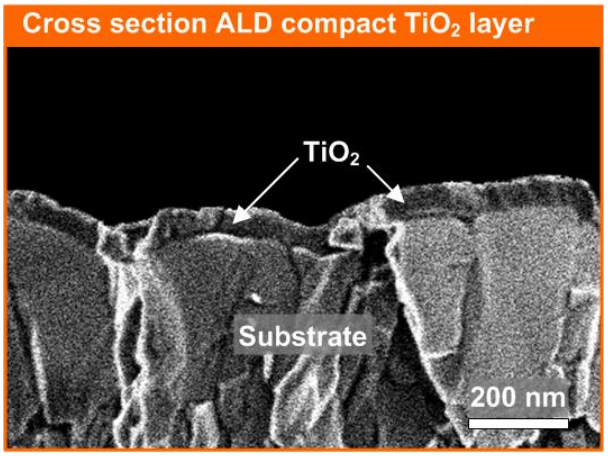

Figure 3.15 Cross section SEM image of a 50 nm ALD TiO2 layer on top of an uneven substrate.

Spin-coating of porous TiO_2

A porous TiO_2 layer can be deposited on the substrate surface by spin-coating a solution of commercial TiO_2 paste (Dyesol 18NR-T) and ethanol (Sigma-Aldrich) at a weight ratio of 1:6. This solution was spin-coated on the substrate surface at 5500 rpm for 60 seconds using a Polos 200 spin-coater. After spin-coating the substrates were heated to 100°C for 10 minutes in air atmosphere and then annealed at 500°C for

1 hour in air atmosphere to ensure the evaporation of all the organics, the anatase crystal phase and the connection of the TiO_2 nanoparticles. Dyesol's 18NR-T transparent TiO_2 paste has highly dispersed and stable anatase TiO_2 nanoparticles with an average size of 20 nm. Figure 3.16 shows a top view image of a spin-coated TiO_2 layer.

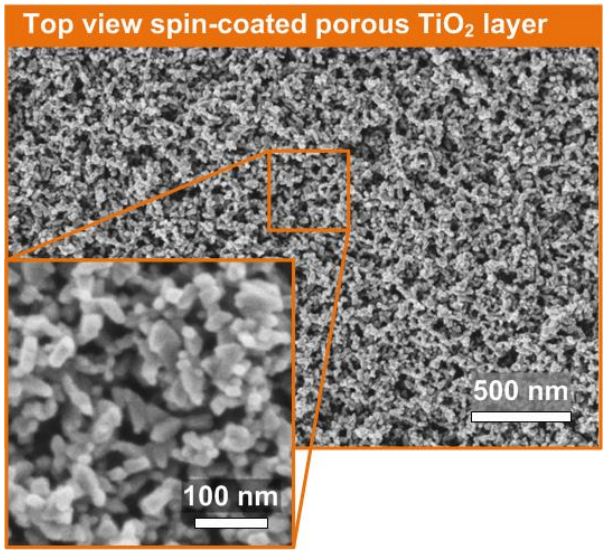

Figure 3.16 Top view SEM image of a spin-coated TiO_2 layer.

Flame Aerosol Deposition of Porous TiO_2

Flame aerosol pyrolysis is a deposition method used to deposit ultra-porous nanostructured metal oxide layers. The flame aerosol deposited metal oxide porous layers have a porosity ≥ 95%. Metal oxide nanostructured porous layers by flame aerosol pyrolysis systems have been previously used in gas sensors, biosensors, photo-detectors, batteries, dye-sensitised solar cells and fuel cells [98, 147-153]. However, the integration of nanostructures into devices is not easy as the nanostructures require stabilisation and optimisation of their electrical and optical properties [98, 151, 154]. The main advantage of the flame aerosol pyrolysis system is that it can be done continuously on an extremely large area substrate. This can enable its integration in a high-throughput low-cost continuous industrial production line.

The custom made flame aerosol deposition system that was used to deposit ultra-porous metal oxide layers is schematically represented in Fig. 3.17. The flame aerosol system consists of a nozzle that has a ring of methane/oxygen flames which

ignite the atomised liquid precursor that is sent through the centre of the nozzle as shown in Fig. 3.17. The liquid precursor is made of a metal chemical compound dissolved in a solvent. This solution is combusted by the flame and then the metal oxide particles nucleate and agglomerate to deposit a porous metal oxide nanostructured film on the substrate. The flame aerosol deposition process is done in open atmospheric conditions.

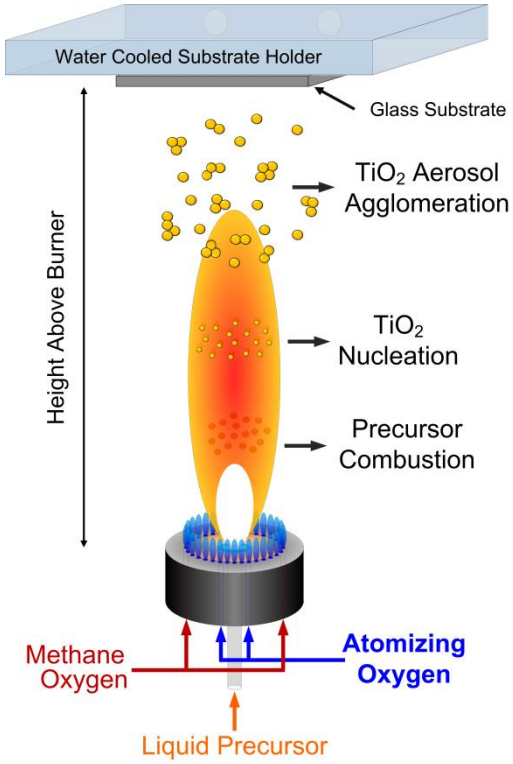

Figure 3.17 Schematic of the custom made flame aerosol deposition system and process.

The flame-made porous TiO_2 layers were deposited using the custom made flame aerosol system shown in Fig. 3.17 with the following settings. The liquid precursor consisted of a 0.1 M TTIP (Sigma-Aldrich, purity > 97%) solution in xylene (Fluka, purity > 98%). This solution was fed into the custom built atomiser at a rate of 5 ml/min and dispersed into a fine spray with an oxygen flow of 7 l/min at a pressure drop of 2 bar. The aerosol was ignited by a surrounding ring-shaped methane/oxygen flame (CH_4 = 1.2 l/min and O_2 = 2 l/min). The distance between the nozzle that expels the solution to make the flame and the substrates (height above burner) was 13 cm. The substrates with the compact TiO_2 film as the uppermost structure were held perpendicular to the ignited aerosol by means of a water-cooled sample holder.

A deposition time of 3 seconds was required to deposit a 300 nm thick flame-made porous TiO_2 layer. After the flame aerosol deposition, the substrates were annealed at 500°C for 30 minutes in air atmosphere to ensure the evaporation of all the organics, the anatase crystal phase and the linking of the TiO_2 nanoparticles.

As an example of as deposited flame-made porous layers, the top view and lateral view of an as deposited 7.5 µm thick flame aerosol deposited ultra-porous TiO_2 layer are shown in Fig. 3.18a-b. The size of the TiO_2 nanoparticles and the thickness of the porous layer depend on the deposition conditions including precursor solution concentration, flow rate of the liquid precursor and distance from the flame to the substrate. The flame-made porous metal oxide layers that were made and used for solar cells are discussed in more detail in Chapters 5, 6 and 7.

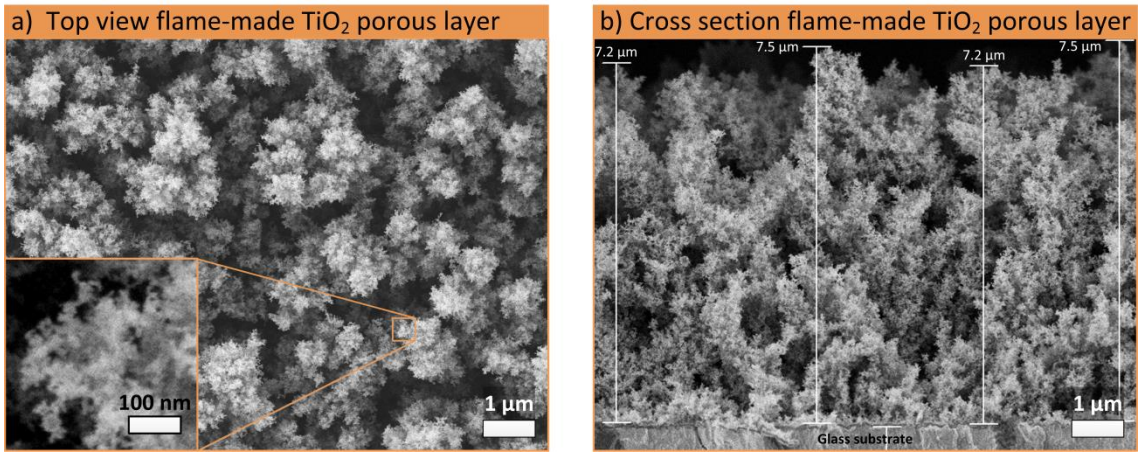

Figure 3.18 a) Top view and b) cross section image of an experimentally as deposited 7.5 µm thick flame aerosol deposited TiO_2 porous layer.

3.2.2 Tin Oxide

Chemical and Physical Properties

Tin oxide (SnO_2) can exist as an amorphous or crystalline material depending on the deposition method and temperature. Crystalline SnO_2 has a rutile (TiO_2) tetragonal structure [102, 155]. Polycrystalline rutile SnO_2 can be made from amorphous SnO_2 by annealing at 600°C [156]. Crystalline SnO_2 can also be formed at lower temperatures by different deposition methods such as chemical vapour deposition (CVD), ALD or sputtering. [99, 101, 103, 157-159].

The SnO_2 tetragonal unit cell has three perpendicular axes with two axes of equal length and a shorter third c axis as shown schematically in Fig. 3.19a. The Sn atoms sit at the corners and centre of this cell where each Sn atom is inside an octahedron of oxygen atoms as shown in Fig. 3.19a. The (110) SnO_2 crystal surface is schematically shown in Fig. 3.19b where the Sn atoms are represented by small black circles and the O atoms by large circles. All the visible Sn atoms are in the second atomic layer. Increased shading of the O atoms represents increased depth away from the surface. Several uppermost O atoms have been removed to represent O vacancies and to give a clearer view of the (normally) sixfold-coordinated Sn cations in the second layer [155]. Surface defects and oxygen vacancies can alter the conductivity and work function of SnO_2 [155, 160, 161]. The measured XRD spectrum of crystalline SnO_2 and the international standard are also shown in Fig. 3.19c.

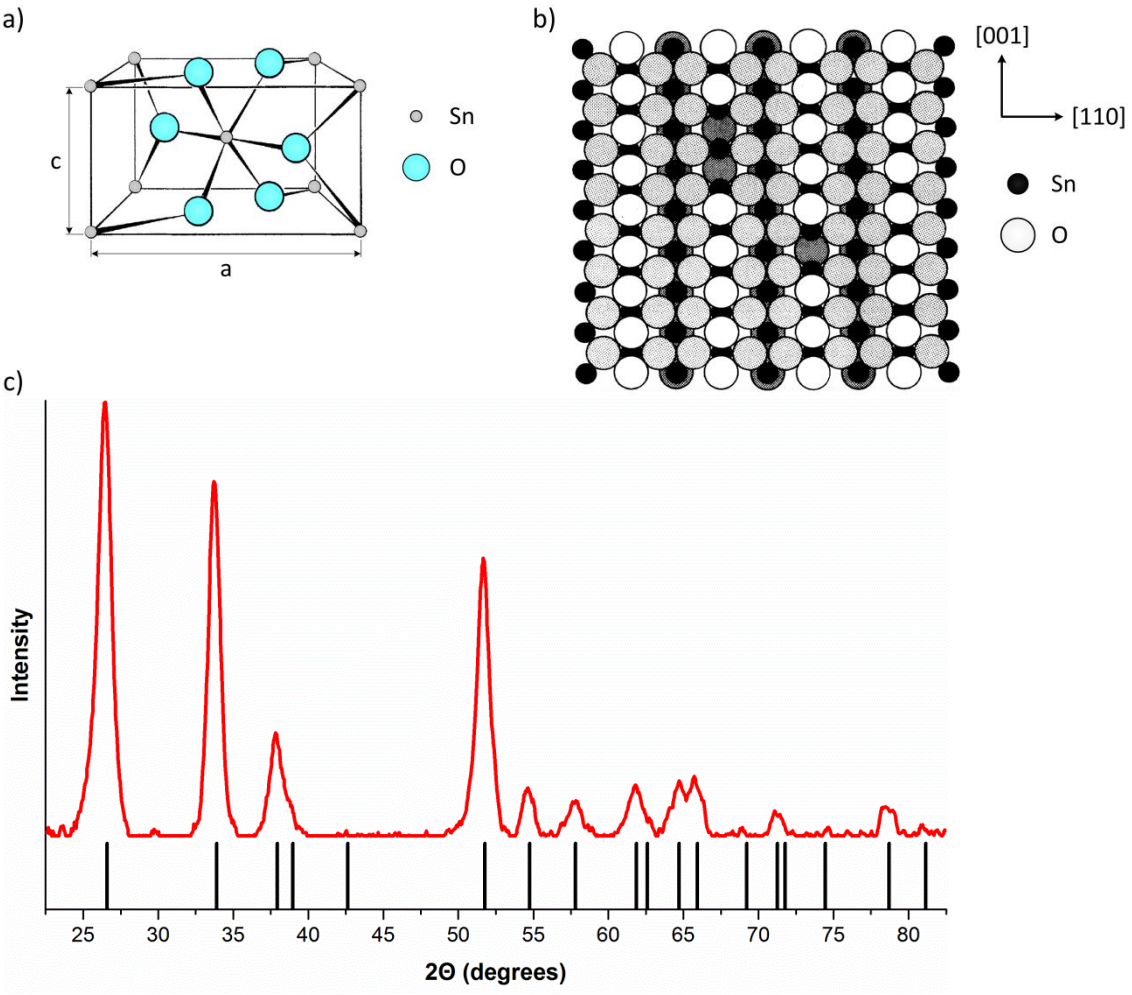

Figure 3.19 a) Unit cell of the crystal structure of SnO_2 where the cyan large circles represent O atoms and the grey small circles Sn atoms (adapted from Jarzebski and Marton (1976)). b) (110) SnO_2 crystalline surface ball model representation where the

Sn atoms are represented by small black circles and the O atoms by the white and shaded large circles (adapted from Cox et al. (1998)) c) Measured XRD spectrum of crystalline SnO_2 (red line) and SnO_2 standard JCPDS-41-1445 (black vertical lines).

Optical Properties

The measured absorptance of a SnO_2 layer is shown in Fig. 3.20a along with the absorptance of a TiO_2 layer for comparison. The absorption onset of SnO_2 is at about 345 nm which corresponds to UV light with a photon energy of 3.6 eV as shown in Fig. 3.20a. The absorption onset of SnO_2 is blue-shifted by 40nm compared to the TiO_2 absorption onset. This implies that SnO_2 is more transparent than TiO_2 and should let more solar energy through to the absorber material of the solar cell. The calculated refractive index of SnO_2 by fitting of measured ellipsometry data is shown in Fig. 3.20b.

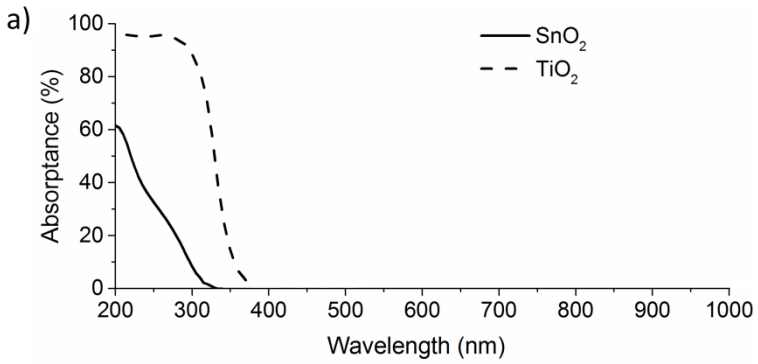

For b) see Figure 9a of Mullings, M.N., C. Hägglund, and S.F. Bent, Tin oxide atomic layer deposition from tetrakis(dimethylamino)tin and water. Journal of Vacuum Science & Technology A: Vacuum, Surfaces, and Films, 2013. 31(6): p. 061503.

Figure 3.20 a) Absorptance of a 100 nm SnO_2 and a 100 nm TiO_2 layers as a function of wavelength measured with a spectrophotometer with an integrating sphere. b) Refractive index of ALD SnO_2 as a function of wavelength for different deposition temperatures (adapted from Mullings et al. (2013)).

Electronic Properties

SnO_2 is an n-type semiconductor with a band-gap of 3.6 eV [99, 100, 102, 155, 157, 162]. A work function of 4.75 to 4.79 eV for thin SnO_2 films (400 nm ± 80nm) on glass has been determined from UPS measurements [162, 163]. A constant work function of 4.2 eV regardless of illumination for glass/ITO/SnO_2 substrates has been determined by Kelvin probe measurements [164, 165]. A constant work function regardless of illumination indicates that SnO_2 is not a photo-reactive material. The energy band levels for SnO_2 are schematically shown below in Fig. 3.21. A summary of the electronic properties of SnO_2 collected from the literature is shown below in Table 3.4.

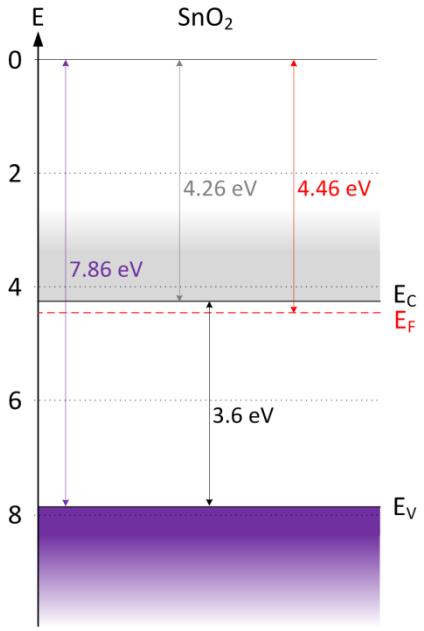

Figure 3.21 Fermi energy level and conduction and valence band energy level for ALD SnO_2 on FTO with post O_3/UV treatment and pre plasma treatment (adapted from Correa et al. (2015), Trost et al. (2015) and Liu et al. (2013)).

Table 3.4 Summary of the electronic properties of SnO_2 collected from the referenced literature.

Property	SnO_2	Reference
Mobility	12 $cm^2/V{\cdot}s$ made by ALD/O_3 at 125°C 32 $cm^2/V{\cdot}s$ made by ALD/O_3 at 200°C 41 $cm^2/V{\cdot}s$ made by sputtering at 500°C 260 $cm^2/V{\cdot}s$ made by CVD at 1250°C 7 to 20 $cm^2/V{\cdot}s$ made by sputtering at ambient temperature	Choi and Park (2014), Cavicchi et al. (1992), Fonstad and Rediker (1971), Goodchild et al. (1985), Stjerna et al. (1994)
Resistivity	$5.6x10^{-4}$ Ω·cm made by ALD/O_3 at 200°C $4.4x10^{-3}$ Ω·cm made by e-beam at 300C $1x10^{-2}$ Ω·cm made by sputtering at 500°C $3x10^{-1}$ Ω·cm made by CVD $2.8x10^{-1}$ Ω·cm made by ALD/H_2O_2 at 150°C $1.9x10^{-3}$ Ω·cm made by ALD/H_2O_2 at 150°C $3x10^{-3}$ Ω·cm made by sputtering at ambient temperature From 1 to 10^{-2} Ω·cm made by spray from 300°C to 450°C	Choi and Park (2014), Khan et al. (2009), Cavicchi et al. (1992), Fonstad and Rediker (1971), Elam et al. (2008), Goodchild et al. (1985), Stjerna et al. (1994), Manifacier et al. (1977)
Carrier concentration	$3.2x10^{20}$ cm^{-3} made by ALD/O_3 at 200°C $2x10^{15}$ cm^{-3} made by ALD/O_3 at 125°C $8.5x10^{15}$ cm^{-3} made by CVD $2x10^{20}$ cm^{-3} made by sputtering at ambient temperature $2x10^{17}$ cm^{-3} made by sputtering at ambient temperature	Choi and Park (2014), Fonstad and Rediker (1971), Goodchild et al. (1985), Stjerna et al. (1994), Minami et al. (1998)

The electronic properties of SnO_2 vary by large amounts depending on the growth conditions as noted in Table 3.4. Nevertheless, even with the large variation in the value of the electronic properties of SnO_2 the mobility of SnO_2 is higher than that of TiO_2; and the resistivity of SnO_2 is lower than that of TiO_2.

Deposition Methods

Atomic Layer Deposition of SnO_2

The ALD method described previously in more detail in section 3.2.1 was used to deposit the compact SnO_2 layer. The ALD of SnO_2 was done with tetrakis dimethylamino tin ($Sn(DMA)_4$ or TDMA-Sn) as the tin-reactant and either H_2O or O_3 as the oxidiser. The ALD system used to deposit SnO_2 was a BENEQ TFS 200 system [146]. The chemical structure of TDMA-Sn is schematically shown in Fig. 3.22a. The ALD reactions of TDMA-Sn with H_2O to grow SnO_2 are shown in Fig. 3.22b.

a)

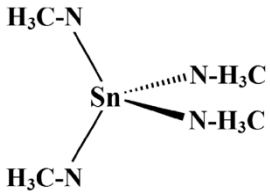

b)

$$(OH)_x^* + Sn(DMA)_4 \longrightarrow (O)_xSn(DMA)_{4-x}^* + HDMA_x$$

$$(O)_xSn(DMA)_{4-x}^* + 2H_2O \longrightarrow (OH)_x^* + HDMA_{(4-x)} + SnO_2$$

Figure 3.22 a) Chemical structure of TDMA-Sn (adapted from Nazarov et al. (2015)). b) First and second half reactions for ALD growth of a SnO_2 compact layer; DMA is the dimethylamino ligand, HDMA is the dimethylamino released to gas phase, the * refers to surface-bound species, and x is the number of DMA ligands released during the TDMA-Sn pulse [156].

Depending on which oxidiser was used (H_2O or O_3) the corresponding ALD process was:

- Pulse TDMA-Sn for 650 ms, purge with N_2 for 15 s, pulse H_2O for 500 ms, purge with N_2 for 15 s (5 s) with a reactor chamber temperature of 100°C which deposits 0.9 Å per cycle. Base pressure: 1.5 mbar; or
- Pulse TDMA-Sn for 650 ms, purge with N_2 for 15 s, pulse O_3 for 500 ms, purge with N_2 for 5 s with a reactor chamber temperature of 120°C which deposits 0.65 to 0.9 Å per cycle.

Both ALD processes produce amorphous SnO_2 that can be converted into crystalline SnO_2 by annealing it in air at 500°C for 30 minutes.

Flame Aerosol Deposition of Porous SnO_2

The flame-made SnO_2 porous nanostructure was deposited with the custom made flame aerosol system shown previously in Fig. 3.17 with the following settings. The liquid precursor consisted of a 0.5 M tin(II)2-ethylhexanoate (Sigma-Aldrich, purity > 97%) solution in xylene (Fluka, purity > 98%). This solution was fed into the custom built atomiser at a rate of 5 ml/min and dispersed into a fine spray with an oxygen flow of 7 l/min at a pressure drop of 2.5 bar. The aerosol was ignited by a surrounding ring-shaped methane/oxygen flame (CH_4 = 1.2 l/min and O_2 = 2 l/min). The distance between the nozzle that expels the solution to make the flame and the substrates was 20 cm. The substrates were held perpendicular to the ignited aerosol by means of a water-cooled sample holder. A deposition time of 3 seconds was required to deposit

300 nm of flame-made SnO_2 porous nanostructure. Figure 3.23 shows a top view image of a flame-made porous SnO_2 layer.

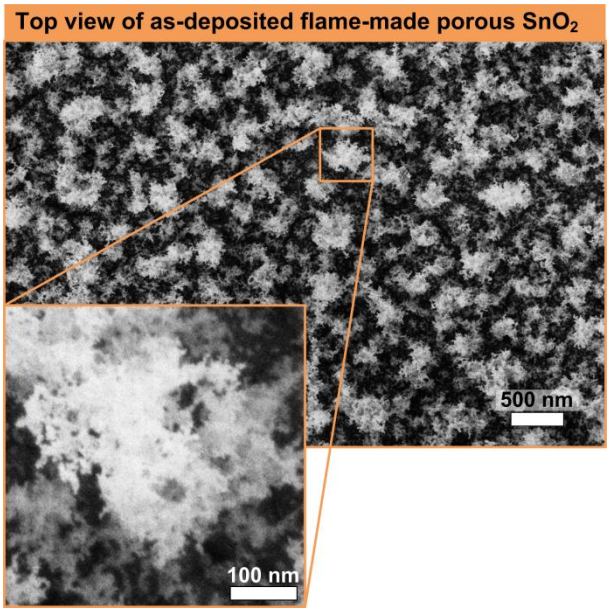

Figure 3.23 Top view SEM image of an as deposited flame-made SnO_2 layer.

3.3 Hole Transport Materials (HTMs)

3.3.1 Copper Thiocyanate

Copper thiocyanate (CuSCN) can be an n-type or p-type inorganic semiconductor depending upon whether copper (Cu) or SCN is in excess [166]. Cu deficient CuSCN is a p-type inorganic semiconductor with a band gap of 3.6 to 3.7 eV and a work function of 4.85 eV [167, 168]. The resistivity of stoichiometric CuSCN has been reported to be 10 kΩ·cm while for SCN-rich CuSCN it is decreased to 100 Ω·cm [45, 169].

Two solution based methods to deposit CuSCN were used. The first deposition method is best suited to coat flat or planar surfaces. A 10 nm CuSCN layer can be made by spin-coating a saturated solution of CuSCN in di-propyl-sulphide at 2500 rpm followed by a drying step at 80°C in air atmosphere for 5 minutes. A thicker layer can be obtained by repeating this process as many times as required. This process produces a uniform and continuous CuSCN layer only if the underlying layer is flat or planar. The

spin-coating was done using a Laurell WS-650SZ-6NPP/Lite spin-coater in air atmosphere.

The second method is best used to coat and fill thick porous substrates with CuSCN. The CuSCN deposition method for efficient coverage of thick porous substrates is known as doctor blading. It consists of spreading the saturated CuSCN di-n-propyl sulphide solution over the porous substrate with a glass rod as schematically shown in Fig. 3.24. Drops of the CuSCN solution are placed at the glass rod/substrate interface and the glass rod is moved forward and backward several times until the solvent evaporates and solid CuSCN is left on the porous substrate. This process is repeated until the desired CuSCN thickness or coverage is obtained. During this process, the substrate is kept at 80°C.

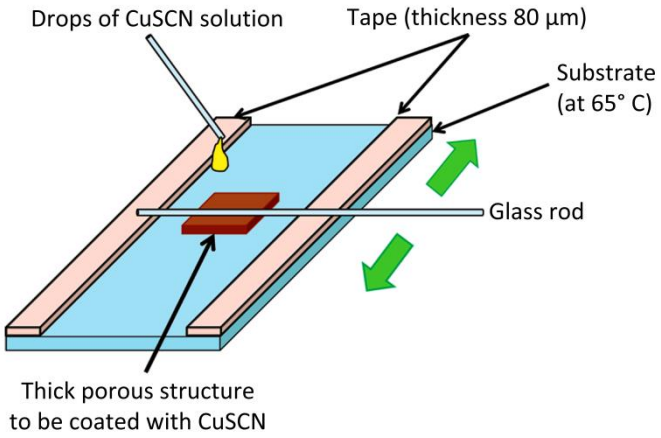

Figure 3.24 Deposition method of CuSCN for thick porous substrates. (adapted from Tsujimoto et al. (2012)).

3.3.2 Spiro-OMeTAD

Spiro-OMeTAD (2,2',7,7'-tetrakis(N,N-di-p-methoxyphenylamine)9,9'-spirobifluorene) is an organic p-type semiconductor with a work function of 4.9 eV, electron affinity of 2.45 eV, band gap of 3 eV and a hole mobility of $2x10^{-4}$ $cm^2/V{\cdot}s$ [170, 171]. Spiro-OMeTAD has to be doped with lithium to decrease its resistivity from 4 MΩ·cm to 50 kΩ·cm [46, 172]. In addition, lithium-doping of spiro-OMeTAD increases its mobility by a factor of 10, from $1.6x10^{-4}$ to $16x10^{-4}$ $cm^2/V{\cdot}s$ [172].

The spiro-OMeTAD layers to make solar cells were deposited by spin-coating the following solution: 0.170 M spiro-OMeTAD (manufactured by Merck), 0.064 M

bis(trifluoromethane) sulphonimide lithium salt (LiTFSI, 99.95%, Aldrich) and 0.198 M 4-tert-butylpyridine (TBP, 96%, Aldrich) in the mixed solvent of chlorobenzene (99.8%, Aldrich) and acetonitrile (99.8%, Aldrich) (chlorobenzene : acetonitrile = 1 : 0.1 v/v) [76]. A few drops of this solution were laid on top of the substrates and then spun for 30 seconds at 3000 rpm. This process was performed with a Laurell WS-650SZ-6NPP/Lite spin-coater inside a nitrogen filled glove box.

3.4 Conductors

3.4.1 Fluorine doped Tin Oxide

Fluorine doped tin oxide (FTO) was used as the front contact material for the solar cells. FTO is a highly conductive material with a low resistivity of $6x10^{-4}$ Ω·cm [173]. A 2.2 mm thick soda lime glass coated with a 600 nm thick FTO layer, commercially known as TEC7, was acquired from Dyesol. The sheet resistance of this commercial FTO coated glass is 7 Ω/square. The absorptance of TEC7 is ≤ 15% in the wavelength range from 400 nm to 1000 nm as shown in Fig. 3.22. The work function of FTO post UV ozone treatment is 4.8 to 5 eV [174]. The minimum band gap of FTO is 3.2 eV but the strong optical absorption is at 3.9 eV because of forbidden optical transitions between 3.2 and 3.9 eV [173, 174].

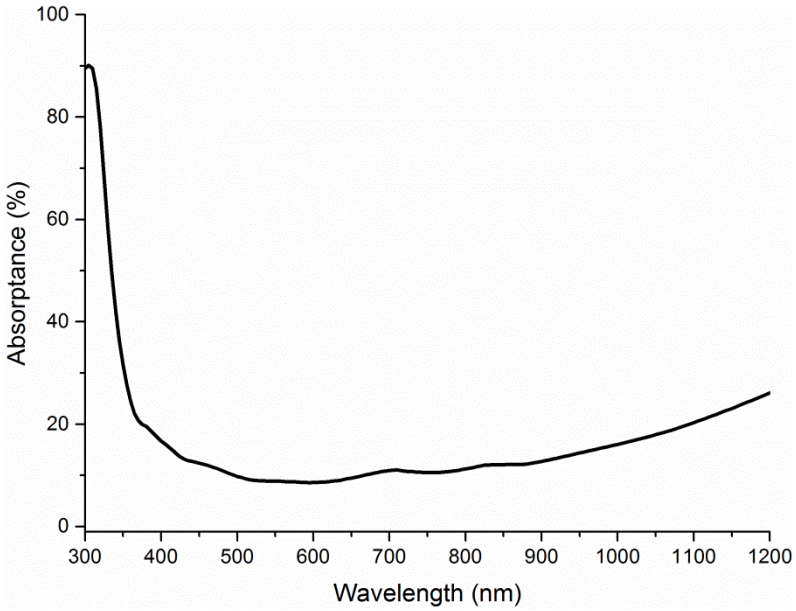

Figure 3.22 Absorptance of TEC7 as a function of wavelength measured with a spectrophotometer with an integrating sphere.

3.4.2 Gold

Gold was used to form the back contact of the solar cells. Gold is a noble, non-reactive, and highly conductive metal. The work function of gold is 5.5 eV [175]. The deposition of a 100 nm thick gold layer was done using a TEMESCAL BJD-2000 electron beam thermal evaporator system at a base pressure of 6 mTorr and a deposition rate of 2 Å/s.

4. Evaporated and Solution Deposited Planar Sb_2S_3 Solar Cells: A Comparison and its Significance§

Sb_2S_3 is an alternative emerging material for chalcogenide solar cells. In this Chapter, fully inorganic planar solar cells in which the Sb_2S_3 absorber was deposited by either the thermal evaporation or the chemical bath deposition method were compared. The planar inorganic solar cell with evaporated Sb_2S_3 had an efficiency of 1.7%. This is much higher than the efficiency of 0.8% for the solution deposited Sb_2S_3, and to the best of my knowledge the highest known reported efficiency for a fully inorganic planar Sb_2S_3 solar cell. The evaporated Sb_2S_3 film is sulphur-rich, which results in flattening of the film surface after annealing at 300°C, thereby reducing the likelihood of contact between the Sb_2S_3 and metallic back contact. In addition, the crystal size of the evaporated Sb_2S_3 film is about 30% larger than that of the solution deposited Sb_2S_3 and has different preferential crystal planes. These features significantly improve the photovoltaic performance of the fully inorganic planar Sb_2S_3 solar cells. Flat solar cells made from sulphur-based semiconducting materials can benefit from these features via a thermal evaporation deposition method.

§ The contents of this Chapter have been published in the following journal paper: Y. Osorio Mayon, T. P. White, R. Wang, Z. Yang and K. R. Catchpole, Evaporated and solution deposited planar Sb_2S_3 solar cells: A comparison and its significance, Phys. Status Solidi A 213, No. 1, 108-113 (2016) / DOI 10.1002/pssa.201532438

Introduction

There is ongoing research to develop stable, low-cost photovoltaic materials for thin film solar cells. One promising group are the chalcogenides, which include PbS, In_2S_3 and Sb_2S_3. In its crystalline form Sb_2S_3 has a band gap of 1.7-1.8 eV with a high absorption coefficient of approximately 7.5 x 10^4 cm^{-1} at 550 nm [121, 176]. It can be easily deposited by different methods such as thermal evaporation, sputtering, ALD and CBD [56, 63, 121, 177, 178]. The most widely used method is CBD. The main disadvantage of this method is that it is difficult to prevent the formation of antimony

oxide during the Sb_2S_3 deposition [55, 113, 114]. Currently, thin films of Sb_2S_3 for solar cells have a continuum of electronic states within the band gap which translates into a relatively high recombination rate and limited diffusion lengths [62]. However, Sb_2S_3 remains an interesting photovoltaic material because it is stable, inorganic and it can be deposited in continuous and uniform thin layers.

Inorganic solid solar cells can be made using Sb_2S_3 as the absorber layer with TiO_2 as the ETM and CuSCN as the HTM [55]. These solar cells can be made using a porous TiO_2 layer of a few microns thick or with only a flat dense TiO_2 layer of tenths of nanometres thick [57, 70]. The porous TiO_2 layer increases the efficiency of the solar cell by increasing the volume of the absorber and the scattering of light within the cell. However, solar cells with a porous TiO_2 layer have an augmented effective junction area compared to planar cells, leading to more junction recombination losses and potentially lower voltages [59].

Several groups have reported efficiencies between 3.2% and 4.1% for fully inorganic Sb_2S_3 solar cells with a porous TiO_2 layer [55, 57, 59, 60, 64, 65, 70]. Efficiencies up to 7.5% have been achieved by replacing the inorganic CuSCN with an organic HTM along with post-sulphurisation of the Sb_2S_3 layer [54, 67, 179]. On the other hand, fully inorganic planar Sb_2S_3 solar cells with CuSCN as the HTM have reported efficiencies of 0.8% [70], and of 1.4%-5.7% with an organic HTM [66, 70-72, 180].

The majority of Sb_2S_3 solar cells reported to date have been deposited using the CBD method for the Sb_2S_3 layer [55, 57, 59, 60, 64-67, 70, 179]. While there have been a few reports of cells produced using thermal evaporation and ALD [63, 72, 180], no studies have directly compared Sb_2S_3 solar cells with the Sb_2S_3 layer deposited by different methods. In this Chapter, fully inorganic planar Sb_2S_3 solar cells in which the only difference is the method used to deposit the Sb_2S_3 layer are compared. This research shows that the evaporated film differs in composition and crystallinity from the solution deposited film resulting in notably different photovoltaic characteristics with a significant improvement in the efficiency.

Experimental

Solar Cell Fabrication

Fully inorganic planar Sb_2S_3 solar cells were fabricated on FTO coated glass with a sheet resistance of 7 Ω/square. A 50 nm dense compact layer of TiO_2 was deposited on top of the FTO using a BENEQ® ALD system. The ALD TiO_2 deposition was performed with a reactor chamber temperature of 235°C using TTIP and H_2O as reactants. The ALD TiO_2 growth rate was 0.3 Å/s. The compact TiO_2 layer was annealed in air at 500°C for 30 minutes to ensure it has a crystalline anatase phase.

The Sb_2S_3 absorber layer was deposited using either CBD or thermal evaporation. The Sb_2S_3 CBD method used is described in detail in Chapter 3. Succinctly, the Sb_2S_3 CBD method was as follows: 0.65 grams of $SbCl_3$ was dissolved in 2.5 ml of acetone and then mixed with 25 ml of 1M aqueous solution of $Na_2S_2O_3$ and 72 ml of water. Some samples were fabricated using dry acetone to dissolve the $SbCl_3$ and other samples using regular (not dry) acetone. The regular acetone had a water content of 0.3% as specified by the supplier (Chem-Supply). The regular acetone was dried using a 0.3 nm molecular sieve to an estimated water content of 0.001%. The use of dry acetone was to prevent the formation of antimony oxides. The samples made using dry acetone are labelled as “dry solution” throughout this Chapter. The substrates were immersed in the final CBD mixed solution for 1 hour at a temperature of 10°C to deposit approximately 100 nm of Sb_2S_3. The deposited amorphous Sb_2S_3 was rinsed with deionised water and dried using a nitrogen gun.

For the Sb_2S_3 evaporated solar cells, 60 nm,100 nm and 178 nm films of Sb_2S_3 were thermally evaporated in an ANGSTROM evaporator system under a pressure of $1x10^{-6}$ Torr with a deposition rate of 0.8 Å/s. The Sb_2S_3 pellets used for evaporation were stoichiometric Sb_2S_3 as corroborated by SEM-EDS and XRD analysis (discussed in detail in Chapter 3). These thickness values were selected to be distributed around the previously reported diffusion length values of Sb_2S_3 [62, 181]. The solar cells with a 178 nm Sb_2S_3 layer had an 85% lower efficiency than the solar cells with a 60 nm and 100 nm Sb_2S_3 layer. Therefore, only the latter cells are analysed in this Chapter.

The cells with the as-deposited Sb_2S_3 (either by CBD or by thermal evaporation), were annealed for 30 minutes at a temperature of 300°C with a nitrogen atmosphere to form crystalline Sb_2S_3. The CuSCN layer was deposited on top of the Sb_2S_3 by spin-coating a saturated solution of CuSCN in di-propyl sulphide. Six layers of CuSCN were spin-coated at 2500 rpm to obtain a final thickness of 50 nm. Each CuSCN layer was dried for 5 minutes at a temperature of 80°C in air atmosphere. A 100 nm thick gold back contact was then thermally evaporated on top of the CuSCN layer. The area of the solar cell was defined by the area of the gold back contact that was 0.0625 cm^2. In this way, it was possible to have two solar cells where the only difference is the deposition method used for the Sb_2S_3 layer.

Solar Cell Characterisation

The J-V measurements were performed under a simulated AM1.5G spectrum using a solar simulator from Photo Emission Tech., Inc. The focused ion beam (FIB)-SEM images were obtained using a FEI Helios NanoLab 600 System. The EDX analysis used a Hitachi 4300 SE/N FE-SEM system. The XRD spectra of the thin films of Sb_2S_3 were acquired using a PANalytical X'Pert Pro system with the grazing incidence angle configuration. The XRD spectrum of the Sb_2S_3 pellets was obtained using a D2 PHASER X-ray powder Bruker system. The absorptance measurements were performed using a Perkin Elmer Spectrophotometer Lambda 1050 with an integrating sphere. The quantum efficiency measurements used a ProtoFlex Quantum Efficiency QE-1400-03 measurement system.

Results and Analysis

The J-V curves of the fully inorganic planar Sb_2S_3 solar cells measured at one sun intensity are shown in Fig. 4.1. Table 4.1 shows the photovoltaic parameters of the same solar cells. The efficiency of the solar cells with solution deposited Sb_2S_3 improves after light soaking as observed by other groups [45, 57]. The highest efficiency for the non-dry solution deposited Sb_2S_3 solar cell was measured after 2.5 hours of light soaking under a simulated AM1.5G spectrum during which the J_{SC}, FF and the efficiency improved by 12%, 45% and 53% respectively; while the V_{OC} decreased by 4%. For the dry solution Sb_2S_3 solar cell the highest efficiency was measured after 1.5

hours of light soaking during which the J_{SC}, FF and efficiency improved by 5%, 24% and 27% respectively whereas the V_{OC} decreased by 2%.

On the other hand, the efficiency of the evaporated Sb_2S_3 solar cells does not improve after light soaking and the data shown here for these cells is without light soaking. Other groups have attributed the light soaking improvement to the change in the properties of the CuSCN layer [45, 57]. However, the different light soaking effects observed in this work indicate that the properties of the Sb_2S_3 layer also play an important role in light soaking.

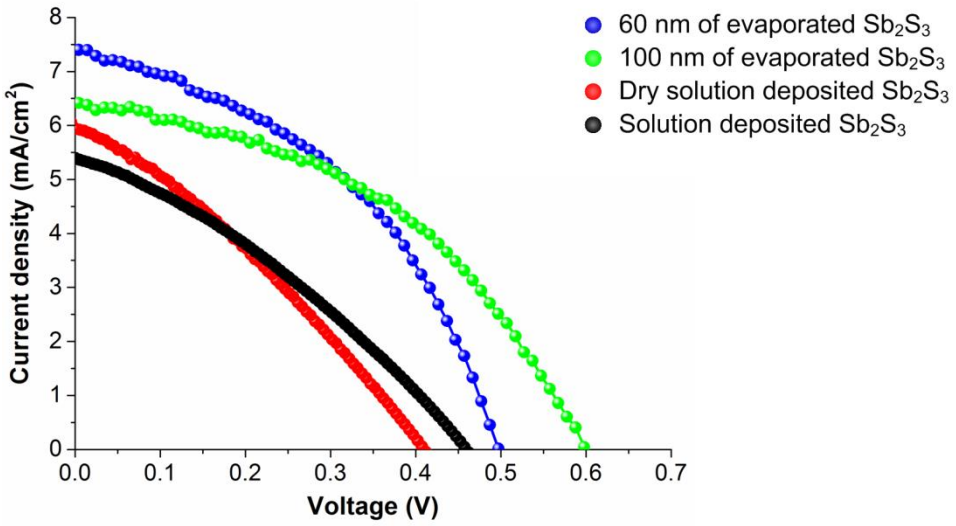

Figure 4.1 J-V curves of the best fully inorganic planar Sb_2S_3 solar cells with a different Sb_2S_3 layer measured under a simulated AM1.5G spectrum using a solar simulator.

Table 4.1 Photovoltaic parameters of the fully inorganic planar Sb_2S_3 solar cells of the J-V curves shown in Fig. 4.1.

Sb_2S_3 solar cell layer	**V_{OC} (V)**	**J_{SC} (mA/cm^2)**	**FF**	**Efficiency (%)**
60 nm of evaporated Sb_2S_3	0.497	7.42	0.43	1.59
100 nm of evaporated Sb_2S_3	0.599	6.43	0.44	1.69
Dry solution deposited Sb_2S_3	0.410	6.02	0.30	0.75
Solution deposited Sb_2S_3	0.460	5.44	0.32	0.80

The decrease in J_{SC} from 60 nm to 100 nm of evaporated Sb_2S_3 solar cells is in part likely to originate from the short diffusion length of Sb_2S_3 that limits the current when the thickness is larger than the diffusion length [62, 181]. Plus, the decrease of J_{SC} can

also originates from the difference in the preferential crystal planes of the Sb_2S_3 layers, as discussed later in this Chapter. The decrease in V_{OC} from the 100 nm to the 60 nm evaporated Sb_2S_3 solar cell is most likely to come from the possible contact between the compact TiO_2 layer and the CuSCN layer. A thin Sb_2S_3 evaporated layer on a FTO substrate will most likely leave uncovered FTO peaks after it flattens out because of the annealing step, as discussed later in this Chapter.

The cross section views of the fully inorganic planar Sb_2S_3 solar cells by FIB-SEM are shown in Fig. 4.2. The Sb_2S_3 deposited using the solution based method is relatively conformal to the TiO_2 and CuSCN interfaces (Fig. 4.2a and 4.2b). In contrast, after the 300°C annealing step, the top surface of the thermally evaporated Sb_2S_3 layer becomes flat (Fig. 4.2c). This dramatic change in the film morphology is illustrated more clearly in Fig. 4.3, which shows evaporated Sb_2S_3 films on the same FTO/TiO_2 substrate before and after annealing at 300°C. To determine the reason for this behaviour, the relative content of antimony and sulphur was measured by EDS in the evaporated Sb_2S_3 layers and in the evaporation source Sb_2S_3 pellets. The EDS analysis results are shown in Table 4.2.

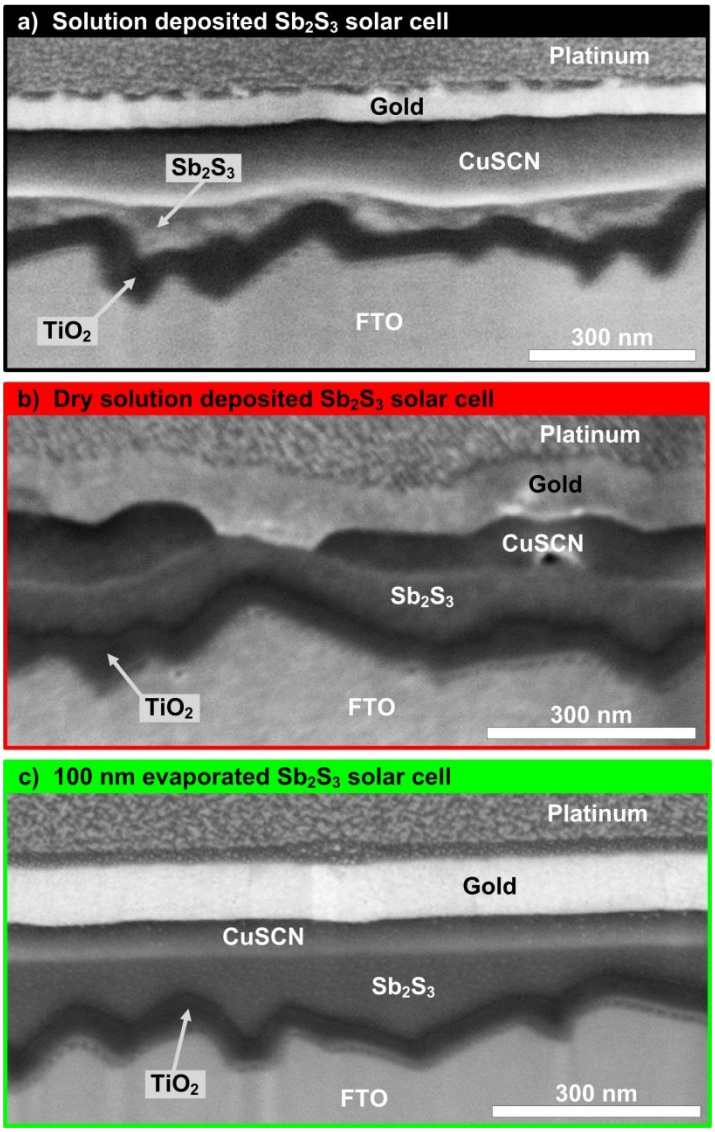

Figure 4.2 Cross section images of the fully inorganic planar Sb_2S_3 solar cells with a) solution deposited Sb_2S_3 layer, b) dry solution deposited Sb_2S_3 layer and c) 100 nm evaporated Sb_2S_3 layer. The platinum layer was deposited on top of the gold contact to prevent damage to the solar cell from the FIB milling process. All images were obtained by FIB-SEM.

Even though the Sb_2S_3 pellets are stoichiometric (Table 4.2), the resulting evaporated Sb_2S_3 film is sulphur-rich. This is because sulphur is easier to evaporate than antimony. As a result, the evaporated film has a lower mean coordination number (MCN) than the stoichiometric Sb_2S_3, which for chalcogenide glasses such as Sb_2S_3 means that it is malleable, thus becoming flat at the annealing temperature of 300°C (Fig. 4.3b) [182]. On the other hand, the solution deposited Sb_2S_3 is antimony rich which results in a higher MCN than the stoichiometric Sb_2S_3, meaning that it is rigid and does not flatten

out after the annealing step [182]. Having a flat top surface for the Sb_2S_3 layer makes it easier to deposit a thin and uniform CuSCN layer by spin-coating (Fig. 4.2c). In contrast, a rough Sb_2S_3 surface makes it harder to deposit a thin and uniform CuSCN layer as can be observed in Fig. 4.2b. A uniform and thin CuSCN layer provides a better recombination barrier, leading to an increase in the V_{OC}. Non-stoichiometric ratios in the Sb_2S_3 layer may also create traps and surface defect states, which are likely to have a detrimental effect on the photovoltaic performance, especially for sulphur deficient Sb_2S_3 [54].

Table 4.2 EDS analysis of the material used for thermal evaporation and of the deposited Sb_2S_3 films by CBD (solution deposited Sb_2S_3) and by thermal evaporation.

Sample	**Antimony Content (%)**	**Sulphur Content (%)**
Ideal stoichiometric Sb_2S_3	40	60
Sb_2S_3 pellets for evaporation	**39.5**	**60.5**
Evaporated Sb_2S_3 film	**35**	**65**
Dry solution deposited Sb_2S_3	**44**	**56**
Solution deposited Sb_2S_3	**49**	**51**

It is worth noting that when the evaporation source Sb_2S_3 pellets are not of the highest purity and stoichiometry, the resulting film can contain significant amounts of metallic antimony. Thus, to ensure the best evaporated Sb_2S_3 layer for solar cells, the Sb_2S_3 pellets for evaporation must have high purity and close-to-ideal stoichiometry (discussed in detail in Chapter 3).

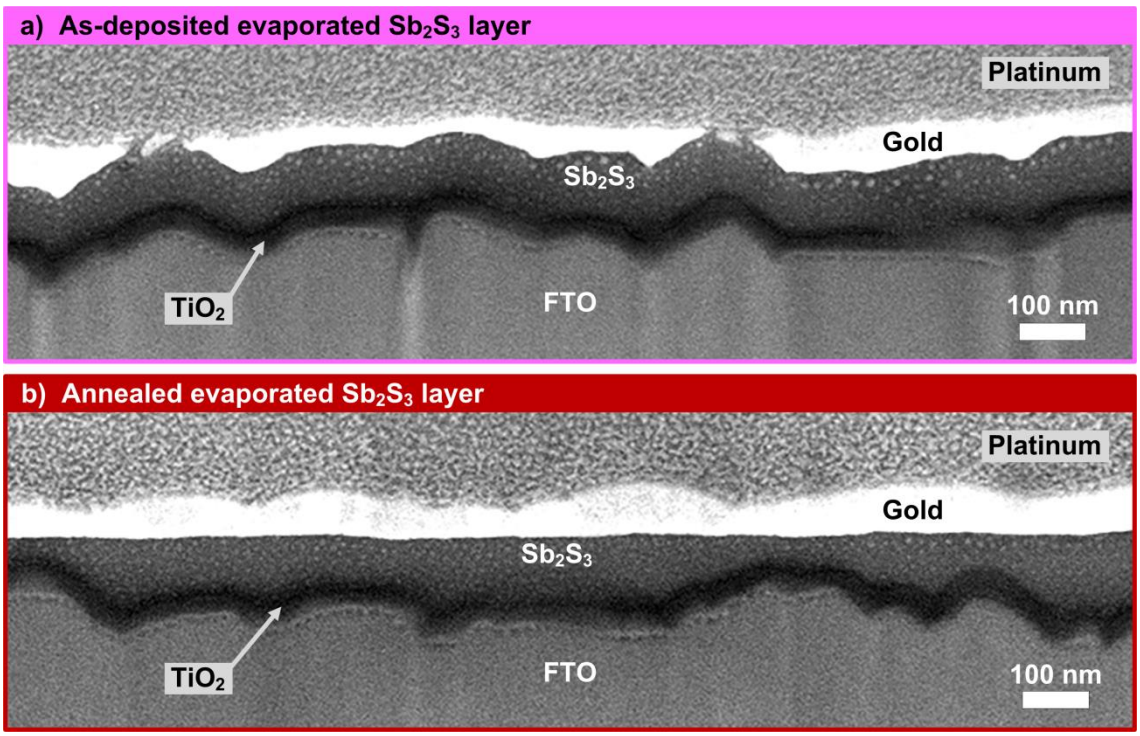

Figure 4.3 Cross section images of the thermally evaporated Sb_2S_3 layer a) as-deposited and b) after annealing at 300°C. The gold and platinum layers were deposited on top of the Sb_2S_3 layer to prevent any possible damage from the FIB milling process. All images were obtained by FIB-SEM.

To further investigate the differences between the deposition methods, XRD analysis on the Sb_2S_3 films was performed. The XRD spectra of the different Sb_2S_3 layers are shown in Fig. 4.4. The Sb_2S_3 deposited from the regular (non-dry) acetone solution has at least 15% of its antimony content as oxide compounds as estimated from the EDS data, but nevertheless has a comparable V_{OC} and J_{SC} to the dry solution deposited Sb_2S_3, which has at least 7% of its antimony content as other compounds. Apart from the oxide peaks, both solution deposited films have similar crystal planes. However, compared to the solution deposited Sb_2S_3, the thermally evaporated Sb_2S_3 has different preferred crystal planes, namely the planes (020), (211), (221), (041) and (141) as highlighted in Fig. 4.4. The crystal planes (211), (221), (041) and (141) represent between 32% and 47% of the total crystal planes in the thermally evaporated Sb_2S_3, but only between 12% and 19% of the total crystal planes in the solution deposited films. In contrast, the crystal plane (020) represents between 2% and 10% for the evaporated Sb_2S_3 and between 17% and 25% of the total crystal planes for the solution deposited Sb_2S_3. The crystal plane percentages were calculated

relative to the highest peak of each spectrum. This suggests that having a crystalline Sb_2S_3 film with a high proportion of (211), (221), (041) and (141) crystal planes, and low proportion of the (020) crystal plane, might produce a material with better electronic properties.

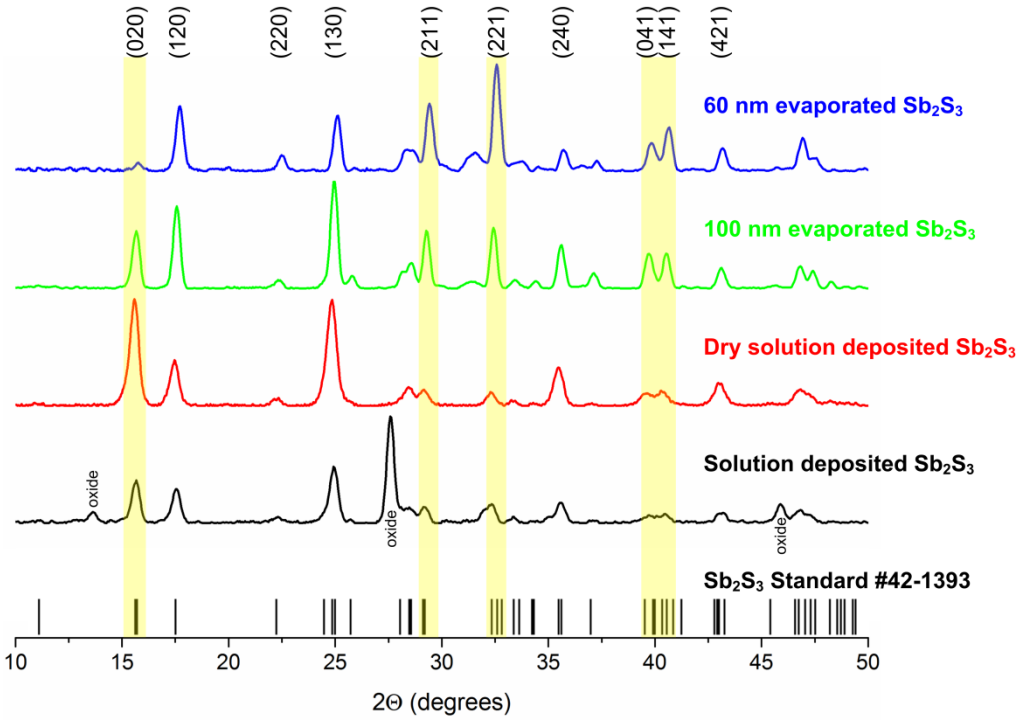

Figure 4.4 XRD spectra of the Sb_2S_3 layers deposited by solution and by thermal evaporation. The highlighted peaks are the major differences in the preferential crystal planes between the evaporated and solution deposited Sb_2S_3.

This observation is consistent with recent studies of Sb_2Se_3 solar cells that showed a correlation between crystal plane in the Sb_2Se_3 thin films and photovoltaic performance [183]. Solar cells made with Sb_2Se_3 films with a high proportion of (211) and (221) crystal planes displayed higher J_{SC} and FF than films with other preferential crystal planes [183]. This was attributed to more efficient carrier transport along the covalently bonded ribbons of the (211) and (221) orientations, whereas transport in other crystal orientations is through hops between ribbons held together by Van der Waals forces and thus less efficient. Also the grain boundaries of the (211) and (221) planes have a lower recombination rate than the grain boundaries of other planes because of their inherently benign grain boundaries that have no dangling bonds [183]. Given that Sb_2S_3 and Sb_2Se_3 have the same crystal structure [108, 184], it is most likely that the results for Sb_2S_3 cells can be explained by the same mechanism.

The observation of enhanced electronic properties in Sb_2S_3 with crystal planes oriented along the c-axis is also consistent with past studies that showed a higher carrier mobility and smaller resistivity along the c-axis of Sb_2S_3 than perpendicular to the c-axis [105]. However, a strict confirmation of this would require a detailed theoretical analysis of atomic bonding in Sb_2S_3, which is beyond the scope of this Chapter.

The crystal sizes of the Sb_2S_3 layers estimated from the XRD data using the Scherrer equation are in Table 4.3 [109]. The crystal sizes of the evaporated Sb_2S_3 layers are about 30% larger than those of the solution deposited Sb_2S_3 layers. This may also contribute to the better photovoltaic performance of the solar cells with the evaporated Sb_2S_3 layers. The crystal size and orientation of the solution deposited Sb_2S_3 layers could possibly be controlled by the deposition conditions, thickness of the film, annealing temperature and annealing time, but this would require further experimental study.

Table 4.3 Crystal sizes of Sb_2S_3 layers deposited by solution and by thermal evaporation calculated from the XRD spectra.

Sample description	**Crystal size (nm)**
60 nm of evaporated Sb_2S_3	23.0
100 nm of evaporated Sb_2S_3	24.0
Dry solution deposited Sb_2S_3	17.4
Solution deposited Sb_2S_3	18.2

The absorptance of the fully inorganic planar Sb_2S_3 solar cells and the glass/FTO/TiO_2 substrate without the back gold contact, measured using a spectrophotometer with an integrating sphere are shown in Fig. 4.5. The absorptance is slightly higher for the 100 nm evaporated Sb_2S_3 layer; other than that the absorptance of the different Sb_2S_3 layers is similar. The absorptance of the 100 nm evaporated Sb_2S_3 layer is slightly higher because the film is on average slightly thicker than the other Sb_2S_3 layers. The absorptance of the 60 nm evaporated Sb_2S_3 layer is close to that of the solution deposited Sb_2S_3 layers. The absorptance at the long wavelengths beyond the band gap of the Sb_2S_3 can be attributed to absorptance in the FTO and light trapping in the glass superstrate. Overall, the small differences in absorption cannot explain the large differences in photovoltaic performance between the evaporated and solution deposited Sb_2S_3 solar cells.

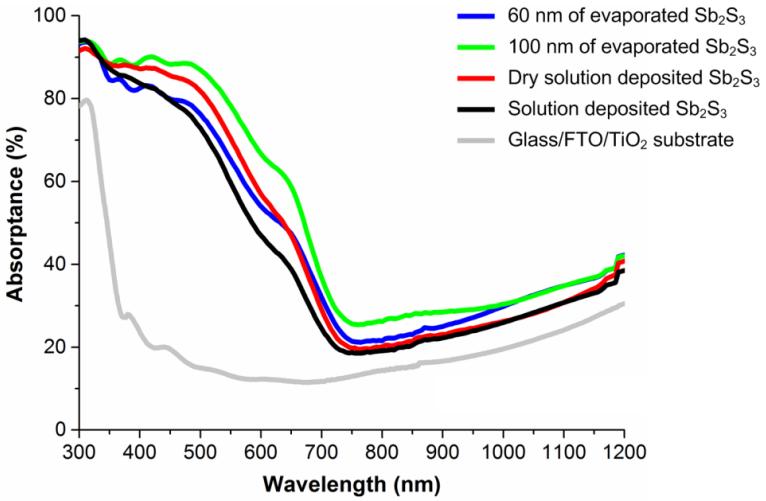

Figure 4.5 Absorptance of the finished solar cells and the glass/FTO/TiO_2 substrate without the gold back contact measured with a spectrophotometer with an integrating sphere.

The IQE of the fully inorganic planar Sb_2S_3 solar cells is shown in Fig. 4.6. The two solar cells with solution deposited Sb_2S_3 have similar IQE profiles. The IQE of the evaporated Sb_2S_3 solar cells is significantly higher than the solution deposited Sb_2S_3 solar cells. Higher IQE implies higher collection efficiency which indicates a larger effective diffusion length in the evaporated Sb_2S_3. Considering that the IQE is larger for the 60 nm evaporated Sb_2S_3 than for the 100 nm evaporated Sb_2S_3 suggests the diffusion length is less than 100 nm; a value consistent with previous estimates [62, 181]. Given that the preferred crystal planes are different for evaporated and solution deposited Sb_2S_3 layers, the results suggest a lower recombination for the (211), (221), (141) and (041) crystal planes and also larger grain sizes of the evaporated Sb_2S_3 layers.

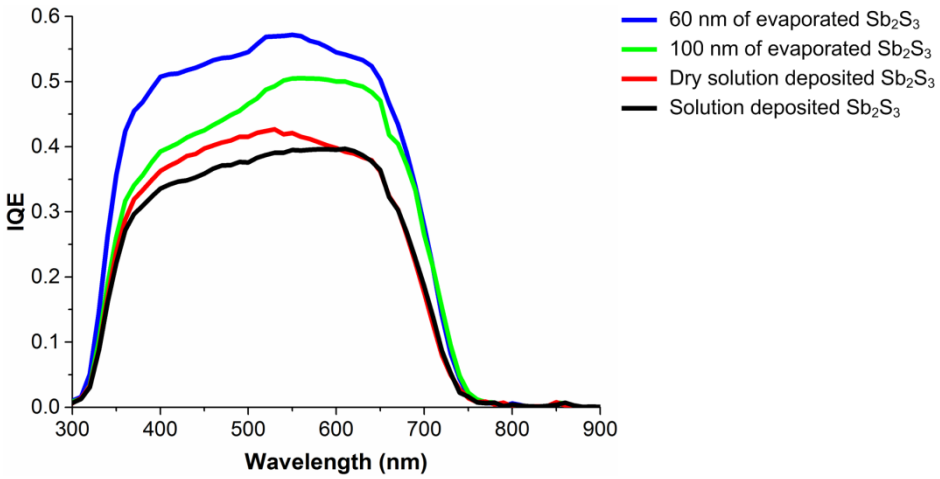

Figure 4.6 IQE of the solution and evaporated Sb_2S_3 solar cells.

Conclusion

A direct comparison of the performance of fully inorganic planar Sb_2S_3 solar cells using two different deposition methods for the active layer, while keeping all other cell parameters identical was made. The evaporated Sb_2S_3 layer is sulphur rich, which results in the films flattening during the post-deposition annealing step. Having a top flat Sb_2S_3 surface allows deposition of a thin and uniform CuSCN layer. The solution deposited Sb_2S_3 layer is sulphur deficient and does not become planar during the annealing. Thermally evaporated Sb_2S_3 solar cells are found to perform better than solution deposited Sb_2S_3 solar cells. The IQE is higher for the evaporated Sb_2S_3 solar cells, suggesting longer diffusion lengths in the Sb_2S_3 layer. The preferred crystal plane orientation is different for the evaporated and solution deposited Sb_2S_3 layers, and the grain sizes are about 30% larger in the evaporated Sb_2S_3 layers. Both of these factors result in an increased effective carrier diffusion length in the evaporated Sb_2S_3 layers. These findings provide a novel pathway to further improve the efficiency of Sb_2S_3 solar cells. These insights can also be relevant to other solar cell materials where different deposition methods are available and particularly for sulphur-based materials where evaporation is likely to lead to a sulphur-rich film.

5. Flame-Made TiO_2 Layers for Fully Inorganic Sb_2S_3 Solar Cells

This research Chapter discusses investigation of the potential for a flame-made porous TiO_2 layer to improve the efficiency of fully inorganic Sb_2S_3 solar cells. In order to make solar cells, the flame-made porous TiO_2 layer has to be stabilised by coating it with a 10 nm to 20 nm thick compact ALD TiO_2 layer. Stabilised flame-made porous TiO_2 layers can undergo subsequent solution processes without breaking down. In contrast to spin-coated porous TiO_2 layers, the large pore size of the hierarchical morphology of the flame-made porous TiO_2 layer enables greater infiltration of the solid HTM into the porous layer. The improved infiltration of the solid HTM into the porous layer has the potential to increase the J_{SC} of the solar cells. However, the actual J_{SC} value is significantly reduced by a low collection efficiency and low shunt resistance as discussed here.

Introduction

Many groups have previously reported fully inorganic Sb_2S_3 solar cells with a spin-coated porous TiO_2 layer with efficiencies between 2.4% and 3.3% [60, 63]. The widely used spin-coated porous TiO_2 layers have a porosity of about 50% to 60% [58, 61]. The spin-coated porous TiO_2 layers usually have a thickness of about 2 µm to 3 µm [55, 57, 59, 60, 63-65]. The morphology and porosity of such spin-coated porous TiO_2 layers can lead to incomplete infiltration of the solid HTM material [47]. An improvement in the infiltration of the solid HTM into the porous TiO_2 layer can improve the transfer of carriers between the absorber and the HTM [46, 185]. A better transfer of carriers between the absorber and the HTM can increase the J_{SC} and the efficiency of the solar cell.

Flame-made porous TiO_2 layers have a hierarchical morphology which is completely different to the uniform morphology of the spin-coated porous TiO_2 layers. This hierarchical morphology of the flame-made porous TiO_2 layers can facilitate the infiltration of the solid CuSCN into the porous TiO_2 layer. However, the as-deposited

flame-made porous TiO_2 layer has a poor mechanical stability that has to be improved to make solar cells via solution processes. Also, the unique morphology of the solar cell with a flame-made porous TiO_2 layer has to be optimised taking into consideration the properties of all the different material layers involved.

In this research Chapter, fully inorganic Sb_2S_3 solar cells with a flame-made porous TiO_2 layer are discussed. The flame-made porous TiO_2 layer was stabilised for subsequent solution processes. The advantages and limitations of the fully inorganic Sb_2S_3 solar cells with a flame-made porous TiO_2 layer are also discussed.

Experimental

Solar Cell Fabrication

The solar cells were fabricated on commercial glass substrates coated with FTO (7 Ω/square) that were coated with a compact 50 nm ALD TiO_2 layer. Afterwards, flame-made porous TiO_2 layers of thickness between 1.5 µm and 6 µm were deposited on top of the 50 nm thick compact TiO_2 layer using a flame aerosol system. Then, the flame-made porous TiO_2 layers were coated with a 10 nm or 20 nm thick compact ALD TiO_2 layer. For comparison, spin-coated porous TiO_2 layers were also deposited on compact TiO_2/FTO substrates. The flame-made and spin-coated porous TiO_2 layers were coated with Sb_2S_3 via the CBD method. Afterwards, the Sb_2S_3 coated substrates were annealed at 300°C for 30 minutes in nitrogen atmosphere. Then, a CuSCN layer was deposited on top of the Sb_2S_3 coated porous TiO_2 layers using the doctor blading method. To finish the solar cells, a 100 nm gold layer was deposited by thermal evaporation on top of the CuSCN. The area of the gold back contact was 0.0625 cm^2. It is worth noting that evaporated Sb_2S_3 was not used because it may not completely infiltrate the porous TiO_2 layer; plus after the annealing step it may flatten out or agglomerate within the porous TiO_2 layer.

Solar Cell Characterisation

J-V measurements were done under simulated AM1.5G spectrum using a Solar Simulator from Photo Emission Tech., Inc. The absorptance measurements were calculated from transmittance and reflectance measurements using a Perkin Elmer

Spectrophotometer Lambda 1050 with an integrating sphere. The quantum efficiency measurements were done using a ProtoFlex Quantum Efficiency QE-1400-03 measurement system. The SEM images were obtained with a Zeiss Ultra-plus FE-SEM system. The SEM-FIB images were taken using a FEI Helios NanoLab 600 System.

Results and Analysis

The key findings of this research were the successful stabilisation of the flame-made porous TiO_2 layers and the factors limiting the efficiency of the fully inorganic Sb_2S_3 solar cells with a flame-made porous TiO_2 layer. The as-deposited flame-made porous TiO_2 layers disintegrate and wash away upon contact with solutions. The flame-made TiO_2 nanostructure is made of thin filaments of agglomerated TiO_2 nanoparticles (Fig. 5.1a) that pile up in a hierarchical manner with a low mechanical stability. The as-deposited flame-made porous TiO_2 layers have to be modified to withstand solution processes in order to fabricate Sb_2S_3-sensitised solar cells via solution methods. Two different methods to stabilise the flame-made porous TiO_2 layers were tested: in-situ flame annealing and coating with a thin compact ALD TiO_2 layer.

The in-situ flame annealing was done by placing the flame-made porous TiO_2 layer in contact with a xylene CH_4/Oxygen flame for 10 seconds. The temperature of the exposed substrate with the flame-made porous TiO_2 layer can reach as high as 900°C after several seconds. However, the substrates were held by a holder that was actively cooled to ensure the temperature of the substrate is ≤ 600°C. Five substrates with as-deposited flame-made porous TiO_2 layers were in-situ flame annealed and then tested for stability with a water droplet. All the in-situ flame annealed flame-made porous TiO_2 layers were disintegrated and washed away with a water droplet.

The other option to stabilise the flame-made porous TiO_2 layers was to coat them with a 20 nm thick TiO_2 compact layer deposited by ALD. After the ALD coating step, the samples were annealed in a furnace at 500°C for 8 hours in air atmosphere to fuse together all the TiO_2 layers. The flame-made porous TiO_2 layers coated with a 20 nm compact ALD TiO_2 layer (Fig. 5.1b) were found to be mechanically robust via the water droplet test. The flame-made porous TiO_2 layers coated with a 20 nm compact ALD TiO_2 layer remained intact after immersion in water. It should be noted that a flame-made porous TiO_2 layer without ALD TiO_2 coating annealed for 8 hours

disintegrates and washes away with a water droplet. Therefore, the flame-made porous TiO_2 layer coated with a 20 nm compact ALD TiO_2 layer were used to make Sb_2S_3 solar cells via the CBD method. Figure 5.1 shows a flame-made porous TiO_2 layer before and after coating it with a 20 nm thick compact ALD TiO_2 layer.

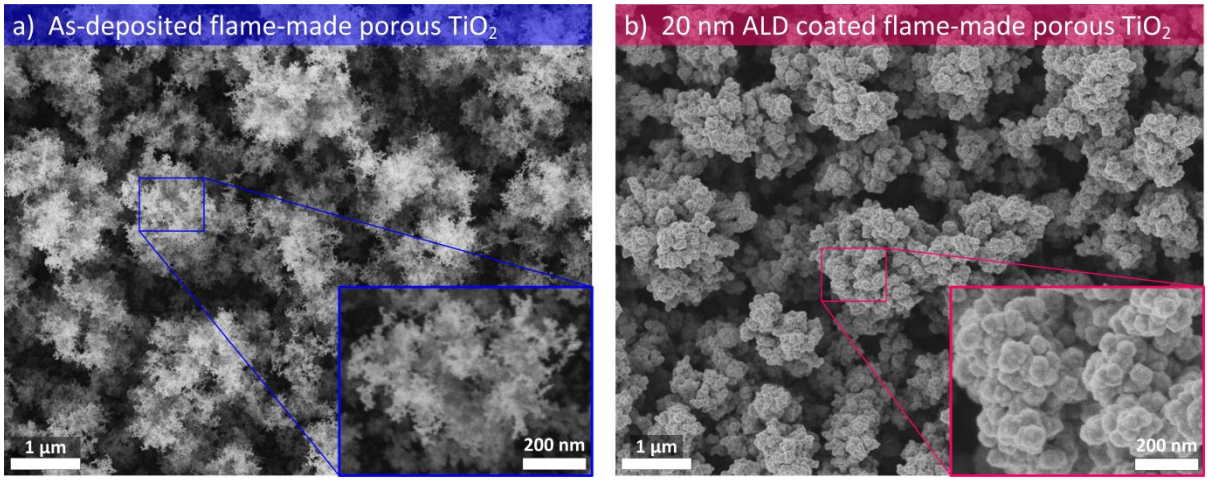

Figure 5.1 a) Top view image of the as-deposited flame-made porous TiO_2 layer. b) Top view image of the flame-made porous TiO_2 layer coated with a 20 nm compact ALD TiO_2 layer.

Fully inorganic Sb_2S_3 solar cells were fabricated using mechanically stable (coated with a 20 nm compact ALD TiO_2 layer) flame-made porous TiO_2 layers of the following thicknesses: 2.5 µm, 4.5 µm, 6 µm and 7.5 µm. A thin Sb_2S_3 layer with a non-uniform thickness of a few nm to 20 nm was deposited on top of the porous TiO_2 layers via 3 hours of the Sb_2S_3 CBD method [55, 64, 65, 69]. The subsequent CuSCN deposition resulted in a 3 µm thick capping layer on top of the flame-made porous TiO_2 layer. The photovoltaic performance parameters of the fully inorganic Sb_2S_3 solar cells with the aforementioned CuSCN and stabilised flame-made porous TiO_2 layer after 3 hours of light soaking are given in Table 5.1. The corresponding measured J-V curves are shown in Fig. 5.2a. The measured absorptance as a function of wavelength of the relevant Sb_2S_3 solar cells with a flame-made porous TiO_2 layer and of a planar Sb_2S_3 solar from Chapter 4 are shown in Fig. 5.2b. A lateral view image of the fully inorganic Sb_2S_3-sensitised solar cell with a 4.5 µm thick stabilised flame-made porous TiO_2 layer is shown in Fig. 5.2c.

Table 5.1 Photovoltaic performance parameters of fully inorganic Sb_2S_3 solar cells with a flame-made porous TiO_2 layer coated with a 20 nm compact ALD TiO_2 layer after 3 hours of light soaking.

Flame-made porous TiO_2 layer thickness (µm)	V_{OC} (V)	J_{SC} (mA/cm^2)	FF	Efficiency (%)
2.5	0.527	0.8	0.60	0.3
4.5	0.490	3.5	0.57	1.0
6.0	0.492	4.3	0.48	1.0
7.5	0.476	5.0	0.39	0.9

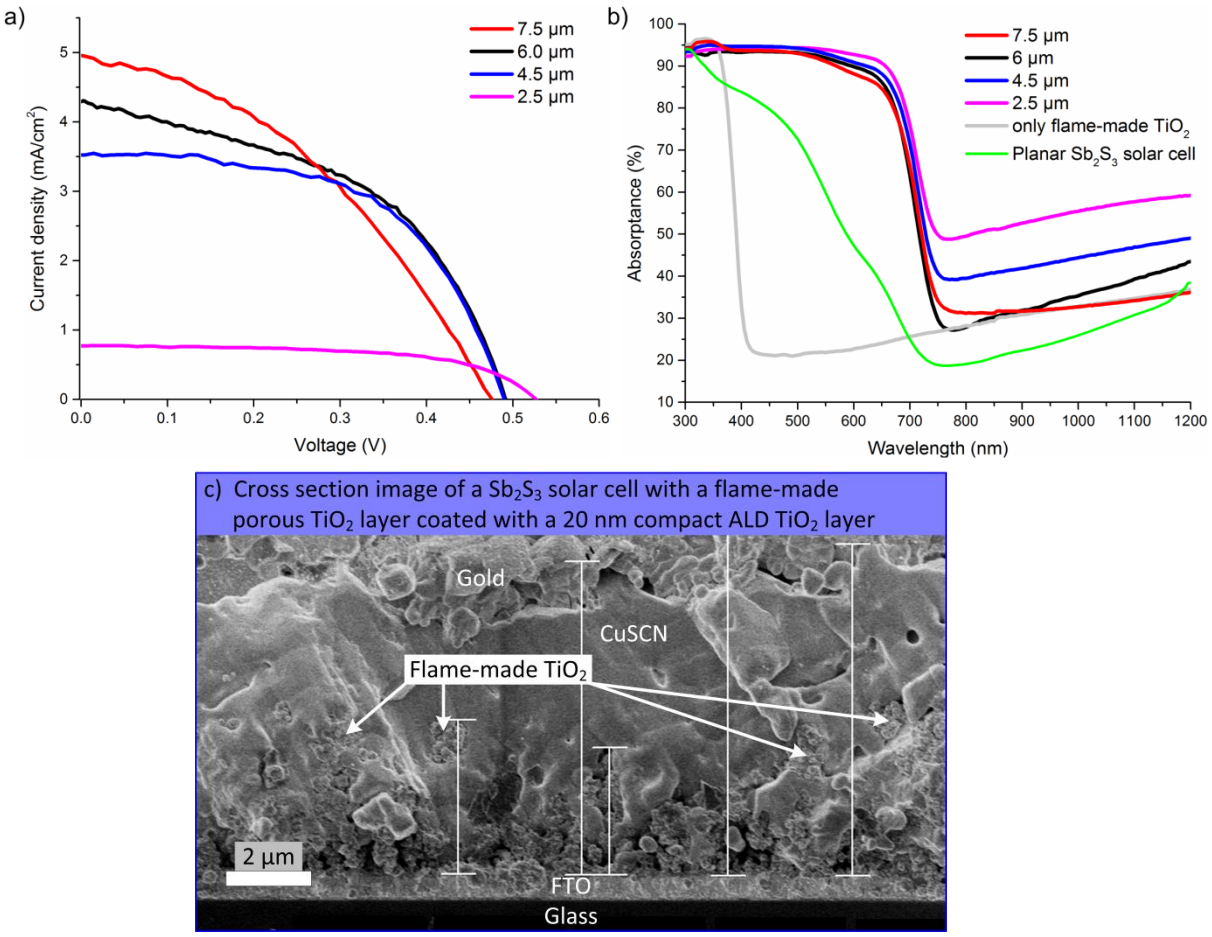

Figure 5.2 a) J-V curves of the fully inorganic Sb_2S_3 solar cells with 2.5 µm, 4.5 µm, 6 µm and 7.5 µm of a flame-made porous TiO_2 layer coated with a 20 nm compact ALD TiO_2 layer measured under one sun intensity. b) Corresponding absorptance of the same Sb_2S_3 solar cells in (a) with a stabilised flame-made porous TiO_2 layer and a planar Sb_2S_3 solar cell from Chapter 4. c) Cross section SEM image of the finished Sb_2S_3 solar cell with a 4.5 µm thick flame-made porous TiO_2 layer coated with a 20 nm compact ALD TiO_2 layer.

The rise of J_{SC} with the increasing thickness of the porous TiO_2 layer originates from the corresponding enlargement of the effective surface area of the solar cell. However, the values of J_{SC} of the porous Sb_2S_3 solar cells are lower than the J_{SC} values of the planar Sb_2S_3 solar cells of Chapter 4; even though the measured optical absorptance of the porous Sb_2S_3 solar cells is higher than that of the planar Sb_2S_3 solar cells of Chapter 4 (Fig. 5.2b). These results suggest that the majority of the photo-generated carriers are not being efficiently collected and recombine before reaching the contacts. The low collection efficiency of the porous Sb_2S_3 solar cells could be attributed to recombination of photo-generated carriers at the interfaces or in the bulk of the TiO_2 and CuSCN layers [59, 60, 186].

The slight decrease of V_{OC} as the thickness of the porous TiO_2 layer is increased could be attributed to the corresponding enlargement of the effective solar cell area. A larger effective solar cell area increases J_0 which is area dependent and thus decreases V_{OC}. Nevertheless, the values of V_{OC} of the porous Sb_2S_3 solar cells are similar to the V_{OC} values of the planar Sb_2S_3 solar cells. The similarity in V_{OC} indicates that recombination losses at open circuit are equivalent in both porous and planar Sb_2S_3 solar cells. This is in line with previous reports that the V_{OC} is mainly limited by the Sb_2S_3 itself [62, 115].

The decrease of the FF as the thickness of the porous TiO_2 layer increases could be attributed to the corresponding increase of the series resistance. As the thickness of the porous TiO_2 layer is enlarged, the volume of TiO_2 and CuSCN in the solar cell also increases thus increasing the series resistance. Nevertheless, the FF values of the porous Sb_2S_3 solar cells are higher than the FF values of the planar Sb_2S_3 solar cells. This difference in FF can be attributed to a higher shunt resistance in the porous Sb_2S_3 solar cells because of its larger overall thickness. As a result of the aforementioned effects on the values of V_{OC} and FF, and particularly the low collection efficiency implied by the low J_{SC}, the solar cell efficiency remained low and almost constant for thicknesses of 4.5 µm and above.

To improve the collection efficiency of the photo-generated carrier in the Sb_2S_3 solar cells with the flame-made porous Sb_2S_3 layer, the infiltration of the CuSCN within the porous TiO_2 layer was improved. To enhance the infiltration of CuSCN the thickness of

the compact ALD TiO_2 layer that coated the flame-made porous TiO_2 layer was decreased from 20 nm to 10 nm as shown in Fig. 5.3a-b. The decrease of the thickness of the compact ALD TiO_2 layer enlarged the pore size of the flame-made porous TiO_2 layer (Fig. 5.3a-b) and reduced the TiO_2 volume thereby enabling the better infiltration of CuSCN within the porous TiO_2 structure. In addition, the thickness of the CuSCN capping layer was reduced to ≤ 0.5 µm in order to minimise the series resistance and bulk recombination in the CuSCN layer [59].

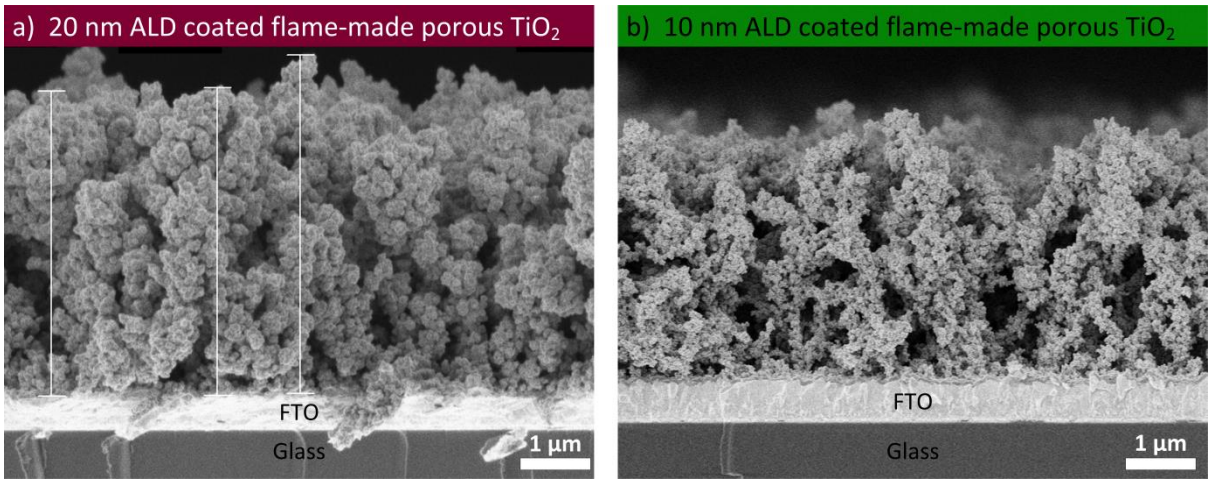

Figure 5.3 Cross section SEM image of a flame-made porous TiO_2 layer coated with a) 20 nm compact ALD TiO_2 layer and b) 10 nm compact ALD TiO_2 layer.

The next step was to compare fully inorganic Sb_2S_3 solar cells with flame-made porous TiO_2 layers coated with a 10 nm compact TiO_2 layer and reference cells with the usual spin-coated porous TiO_2 layer. The J-V curves and corresponding photovoltaic parameters of the fully inorganic Sb_2S_3 solar cells with flame-made porous TiO_2 layers with a 10 nm compact ALD TiO_2 layer are shown below in Table 5.2 and Fig. 5.4a. The efficiency of 2.3% reported here (Table 5.2) for a fully inorganic Sb_2S_3 solar cell with a spin-coated porous TiO_2 layer is similar to what other groups have reported [60, 63].

The J_{SC} values are higher for the Sb_2S_3 solar cells with a 10 nm coated flame-made porous TiO_2 layer (Table 5.2) than with a 20 nm coated flame-made TiO_2 layer (Table 5.1). The improvement in J_{SC} can be attributed to a better infiltration of CuSCN into the flame-made porous TiO_2 nanostructure, as discussed in detail below. The better infiltration of CuSCN enlarges the contact area between CuSCN and Sb_2S_3, and between Sb_2S_3 and the flame-made porous TiO_2 layer, which facilitates the collection of more

photo-generated carriers to produce a larger J_{SC}. However, the J_{SC} decreases when the thickness of the porous TiO_2 layer increases because of the large volume within the solar cell of CuSCN and TiO2. A large volume of these materials is detrimental to the solar cell because they are source of parasitic absorption and recombination losses, as discussed in this Chapter and in the following Chapter.

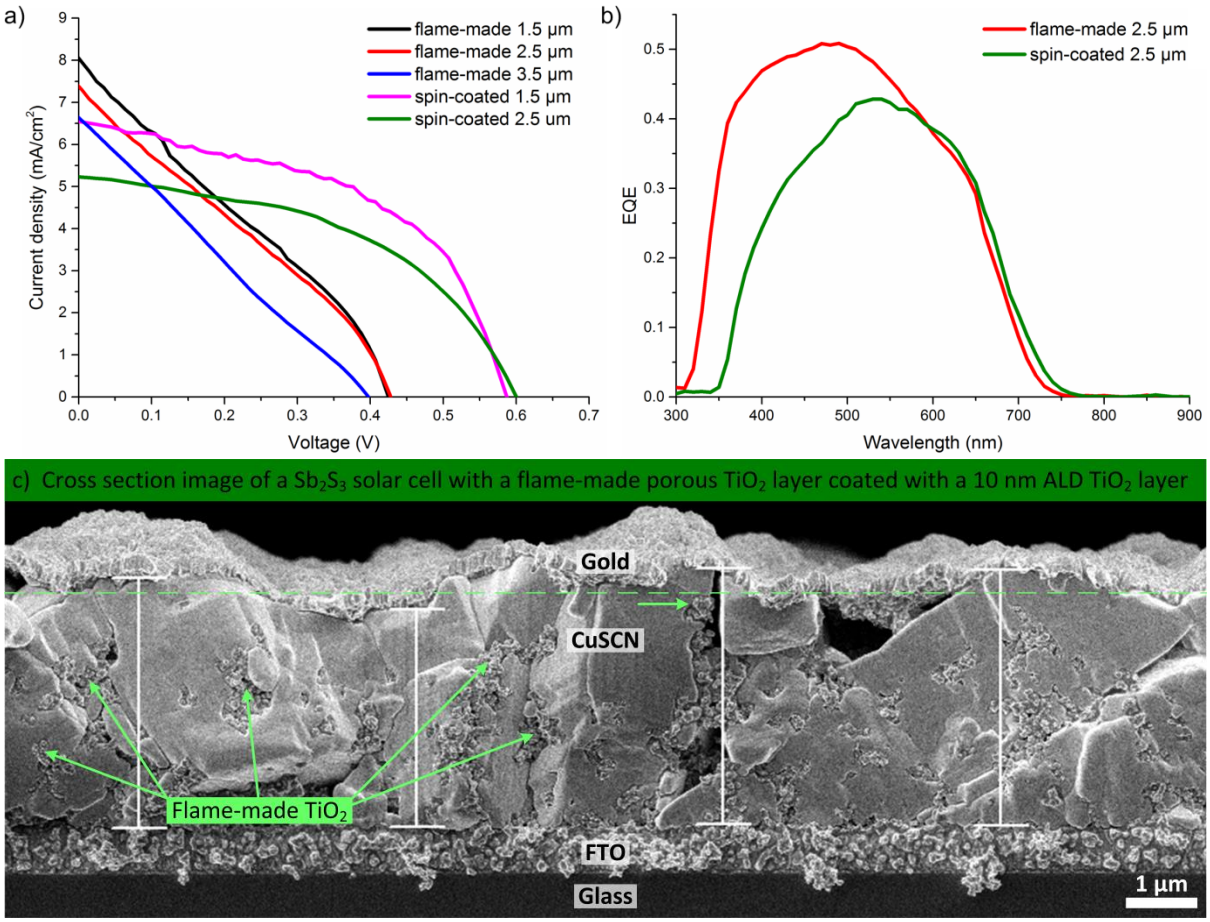

Figure 5.4 a) J-V curves of the fully inorganic Sb_2S_3 solar cells with flame-made porous TiO_2 layers coated with a 10 nm compact ALD TiO_2 layer measured at one sun intensity. b) Corresponding EQE of two of the solar cells from the J-V curves in (a). c) Cross section image of the Sb_2S_3 solar cell with a 3.5 µm thick flame-made porous TiO_2 layer coated with a 10 nm compact ALD TiO_2 layer. The dashed line marks the height level of the porous layer.

Table 5.2 Performance parameters of fully inorganic Sb_2S_3 solar cells with a flame-made porous TiO_2 layer coated with a 10 nm compact ALD TiO_2 layer and with a spin-coated porous TiO_2 layer.

Flame-made porous TiO_2 layer thickness	**V_{OC} (V)**	**J_{SC} (mA/cm^2)**	**FF**	**Efficiency (%)**
1.5 µm	0.425	8.0	0.29	1.0
2.5 µm	0.428	7.4	0.29	0.9
3.5 µm	0.404	6.6	0.25	0.7
Spin-coated porous TiO_2 layer thickness				
1.5 µm	0.587	6.9	0.59	2.3
2.5 µm	0.603	5.3	0.49	1.6

However, the V_{OC} and FF are lower for the Sb_2S_3 solar cells with a 10 nm coated flame-made porous TiO_2 layer (Table 5.2) than with a 20 nm coated flame-made TiO_2 layer (Table 5.1). The reduction in V_{OC} and FF can be attributed to a low shunt resistance that originates from a direct contact between the gold layer and the flame-made porous TiO_2 layer. The separation between the porous TiO_2 layer and the gold layer is determined by the thickness of the capping CuSCN layer. This batch of Sb_2S_3 solar cells were fabricated with a CuSCN capping layer of ≤ 500 nm with the aim of reducing the resistance and recombination in the CuSCN layer. However, the inherent non-uniformity of the top surface of the flame-made porous TiO_2 layer resulted in a partial coverage of the flame-made porous TiO_2 layer by the relatively thin CuSCN capping layer (≤ 500 nm). The spacing and difference in height between the branches or stems of the flame-made porous TiO_2 makes it difficult to deposit a uniform and thin CuSCN capping layer as shown in Fig. 5.4c. The uppermost surface of the CuSCN layer in Fig. 5.4c does not have a uniform height. The dashed horizontal green line in Fig 5.4c sits at the level of the tallest visible branch of the flame-made porous TiO_2 layer. The gold layer goes under the horizontal green line which indicates that shunts by direct contact between the gold layer and the flame-made porous TiO_2 layer are possible.

The Sb_2S_3 solar cells with a spin-coated porous TiO_2 layer have a higher V_{OC} and FF than with a flame-made porous TiO_2 layer. The Sb_2S_3 solar cells with a spin-coated porous TiO_2 layer have a much higher shunt resistance because there is no direct contact

between the gold layer and the porous TiO_2 layer as shown in Fig. 5.5a. The spin-coated porous TiO_2 layer has a uniform height and top surface thus facilitating the formation of a thin and uniform CuSCN capping layer.

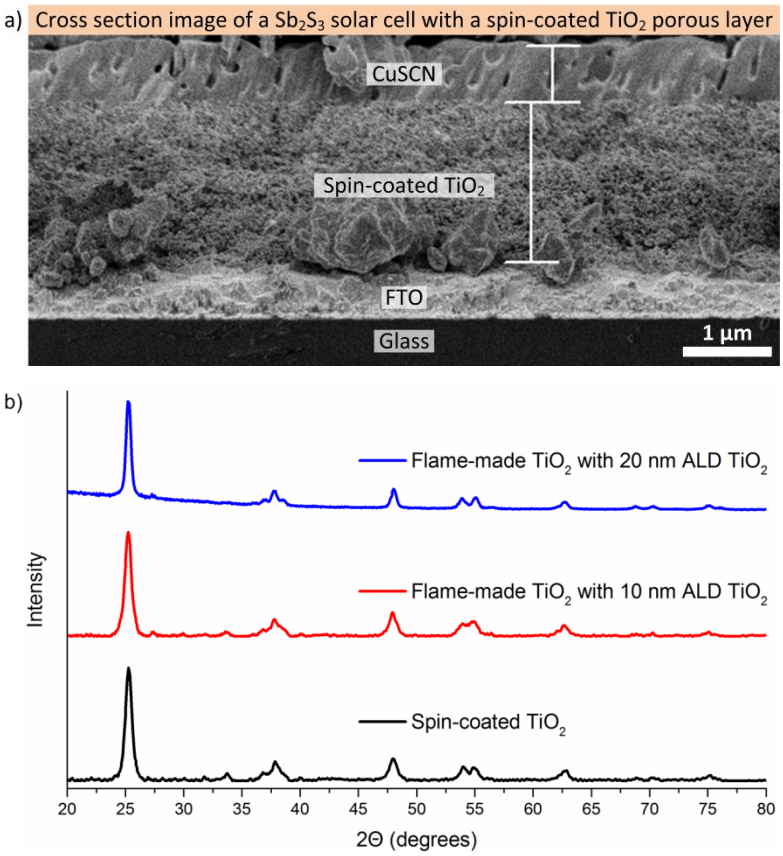

Figure 5.5 a) Cross section image of a Sb_2S_3 solar cell with a spin-coated porous TiO_2 layer by SEM. b) XRD spectra of the flame-made porous TiO_2 layers coated with 10 nm and 20 nm of compact ALD TiO_2 and of the spin-coated porous TiO_2 layer.

As a result of the low shunt resistance, the efficiencies of the fully inorganic Sb_2S_3 solar cells with a 10 nm coated flame-made porous TiO_2 layer were lower than those of the solar cells with spin-coated porous TiO_2 layer.

The TiO_2 crystalline structure is equivalent in all the porous TiO_2 layers as shown in Fig. 5.5b. The porosity of the 10 nm coated flame-made porous TiO_2 layer is about 35% as discussed in Chapter 6. The porosity of the spin-coated TiO_2 porous layer is about 50% [58]. This could result in different Sb_2S_3 loading due to the inherently higher surface area of the porous layer with the highest porosity.

Nonetheless, the measured EQE in Fig. 5.4b shows that there is a higher collection of photo-generated carriers for a Sb_2S_3 solar cell with a flame-made porous TiO_2 layer coated with a 10 nm compact ALD TiO_2 layer than with a spin-coated porous TiO_2 layer. The EQE difference was attributed to a better CuSCN infiltration into the flame-made porous TiO_2 layer than into the spin-coated porous TiO_2 layer as shown in Fig. 5.6a-b. The hierarchical morphology of the flame-made porous TiO_2 layer facilitates the infiltration of CuSCN (Fig. 5.6a). In contrast to the high infiltration of CuSCN into the flame-made TiO_2 layer, the CuSCN does not fully infiltrate into the spin-coated porous TiO_2 layer (Fig. 5.6b).

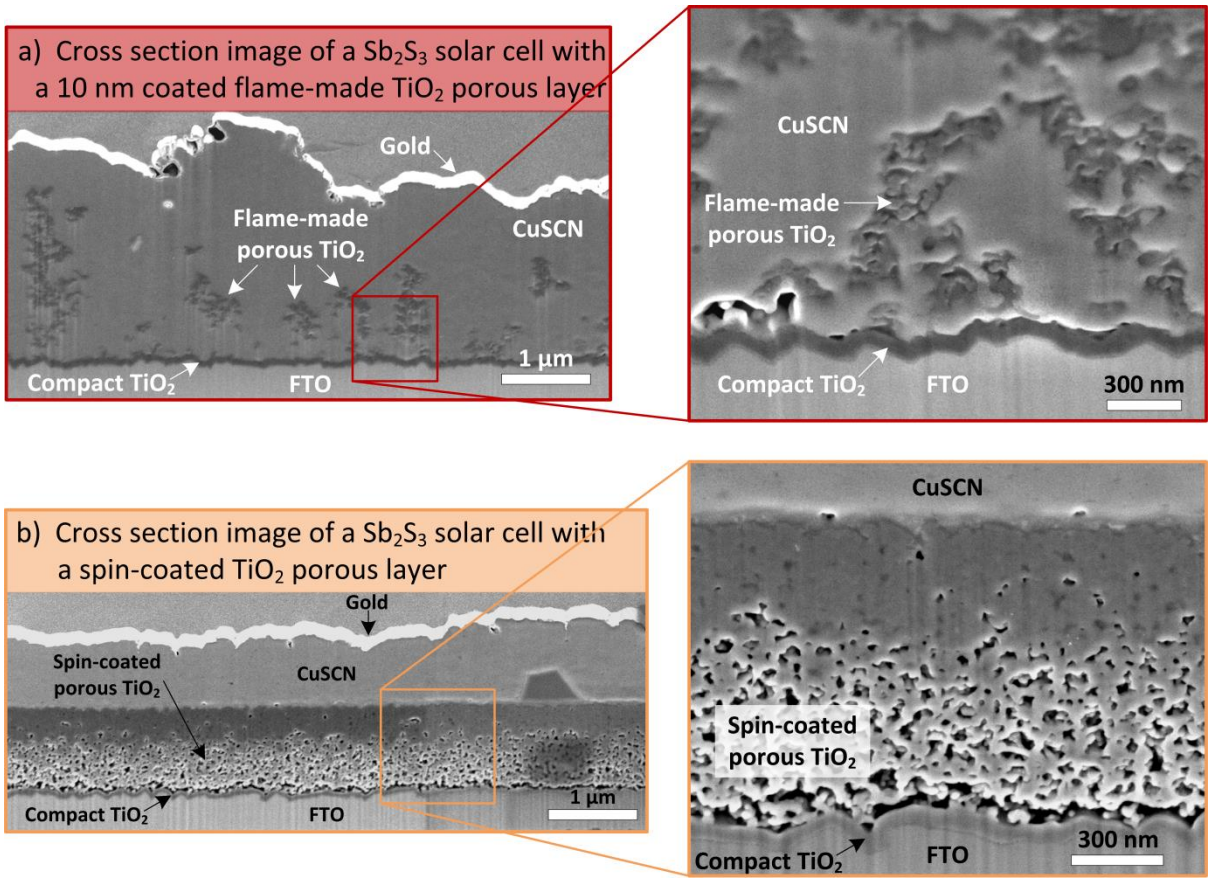

Figure 5.6 a) Cross section image of the Sb_2S_3 solar cell with a flame-made porous TiO_2 layer coated with a 10 nm compact ALD TiO_2 layer. b) Cross section image of the Sb_2S_3 solar cell with a spin-coated porous TiO_2 layer (both images by FIB-SEM).

The extent of the effect of the shunt resistance on the J_{SC} of the fully inorganic Sb_2S_3 porous solar cells with a flame-made porous TiO_2 layer can be observed in the negative bias measurements of the J-V curves in Fig. 5.7. The J_{SC} does not reach its maximum value at zero voltage, but continues to increase rapidly with larger negative voltages,

until it stabilises and reaches its maximum attainable value at about -1 volt (Fig. 5.7) [187]. Therefore, the Sb_2S_3 solar cells with the flame-made porous TiO_2 layer can attain a significantly higher J_{SC} than the Sb_2S_3 solar cells with the spin-coated porous TiO_2 layer if the low shunt resistance of the former solar cells can be improved.

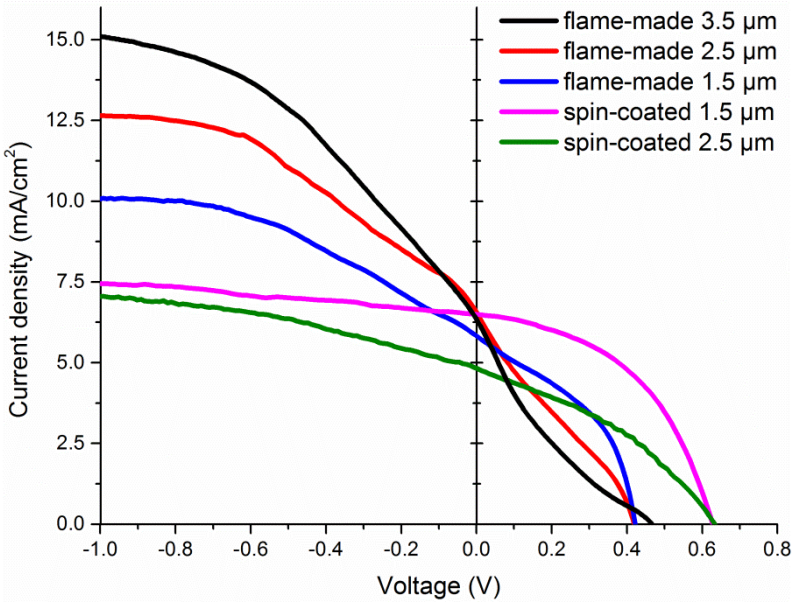

Figure 5.7 J-V curves with large negative bias of the fully inorganic Sb_2S_3 solar cells with a flame-made porous TiO_2 layer and with a spin-coated porous TiO_2 layer measured at one sun intensity. The flame-made TiO_2 layers were stabilised with a 10 nm compact ALD TiO_2 layer.

The shunt resistance could be improved by depositing a much thicker CuSCN capping layer, albeit at the cost of increasing the series resistance [59]. The flame-made porous TiO_2 layer could also work better with another HTM or absorber material. One possible solution is to use another HTM material such as P3HT that has a better conductivity than CuSCN [45, 179, 188]. Alternatively, the thickness of the flame-made porous TiO_2 layer could be reduced to minimise the volume of CuSCN, but this would also be expected to significantly decrease the active area coated with Sb_2S_3 and in turn decrease the photo-generated current. These suggestions could be for future work. Overall however, the theoretical high efficiencies of the Sb_2S_3 solar cells are still mainly limited by the Sb_2S_3 itself because at this point in time the deposited Sb_2S_3 material has a very short diffusion length and intrinsic high recombination losses [62, 115].

Conclusion

The improvement of the mechanical stability of the flame-made porous TiO_2 layer is necessary to prevent its disintegration upon subsequent solar cell fabrication processes. As discussed above, this can be achieved by coating the flame-made porous TiO_2 layer with a 10 nm to 20 nm thick compact ALD TiO_2 layer. The compact ALD TiO_2 layer provides enough mechanical stability to the flame-made porous TiO_2 layer to remain intact after the subsequent solution processes to fabricate solar cells. The flame-made porous TiO_2 layer coated with a 10 nm compact ALD TiO_2 layer has a larger pore size than when coated with a 20 nm compact ALD TiO_2 layer. A larger pore size facilitates the infiltration of CuSCN into the flame-made porous TiO_2 layer which enlarges the effective contact area of the solar cell. A better infiltration of the CuSCN into the porous TiO_2 layer results in a larger J_{SC} because of a higher collection efficiency. However, the Sb_2S_3 solar cells with the higher collection efficiency suffered from shunts formed by the direct contact of the gold layer with the porous TiO_2 layer. The low shunt resistance significantly decreased the V_{OC} and FF of such solar cells. The Sb_2S_3 solar cells with a flame-made porous TiO_2 layer need a particularly thick CuSCN capping layer to avoid the likelihood of shunts because of the hierarchical morphology of the flame-made porous layer. The higher attainable J_{SC} and efficiency of the Sb_2S_3 solar cell with a flame-made porous TiO_2 layer was significantly diminished by the effects of the low shunt resistance. As discussed in the next Chapter, these problems were lessened by using a different solar cell layout with a different absorber material and HTM.

6. Ultra-Porous TiO_2 Layers for $MAPbI_3$ Solar Cells§

This Chapter discusses the $MAPbI_3$ solar cells that were made with an ultra-porous TiO_2 electron transport layer fabricated using sequential flame aerosol and atomic layer depositions of TiO_2. Flame aerosol pyrolysis allows rapid deposition of nanostructured and ultra-porous TiO_2 layers that could be scaled-up for high throughput industrial solar cell production. An efficiency of 13.7% was obtained with a flame-made porous TiO_2 layer stabilised with a compact 2 nm thick ALD TiO_2 coating layer. This efficiency is comparable to the control $MAPbI_3$ solar cell made with the well-established spin-coated porous TiO_2 layer. The combination of the flame aerosol and atomic layer deposition methods provides precise control of the porosity of the TiO_2 layer. Notably, the porosity of the as-deposited flame-made TiO_2 layers was 97% which was then fine-tuned down to 87%, 56% and 35% by varying the thickness of the subsequent compact ALD TiO_2 coating layer. The effect of the porosity of the flame-made TiO_2 layers on the photovoltaic performance was investigated. It is shown that the $MAPbI_3$ infiltrates more deeply into the nanostructured flame-made TiO_2 porous layers than into the spin-coated TiO_2 porous layers.

§ The contents of this Chapter have been published in the following journal paper: Y. Osorio Mayon, T. Dong, N. Nasiri, T. P. White, A. Tricoli and K. R. Catchpole, Flame-made ultra-porous TiO_2 layers for perovskite solar cells, Nanotechnology Volume 27,Number 50 (2016) /dx.doi.org/10.1088/0957-4484/27/50/505403

Motivation for this Work

Over the years, several materials have been used in porous scaffold type solar cells in a bid to increase the efficiency and reduce the cost of solar cells. Recently, the combination of organic-inorganic halide perovskites with TiO_2 has shown great promise for high efficiency solar cells [76, 189-191]. Organic-inorganic halide perovskites can have a band gap value from 1.5 eV to 2.2 eV depending on their composition [94]. The efficiency of perovskite solar cells has improved from 2.2% to more than 20% in just over 9 years [73, 74, 89, 93, 96, 192]. This is a remarkable increase in efficiency over a relatively short period of time compared with silicon based

solar cells which took over 30 years to develop [34, 35, 193]. The typical perovskite solar cell structure consists of a perovskite absorbing layer placed between an electron transport (hole blocking) TiO_2 layer, and a hole transport (electron blocking) spiro-OMeTAD layer. This layer structure facilitates the separation, transport and collection of the photo-generated carriers.

The most widely used ETM in perovskite solar cells is TiO_2 [76, 83, 87, 89, 90, 93-96, 189, 190, 192]. A porous TiO_2 layer is commonly added on top of the compact TiO_2 layer to increase the carrier collection efficiency and reduce shunting and thus increase the overall photovoltaic performance [189, 190]. The porous TiO_2 layer is commonly deposited via screen printing, doctor-blading or spin-coating from an organic paste that typically contains TiO_2 nanoparticles in the range of 20 nm to 100 nm [47, 61, 194-196]. The TiO_2 porous layer is usually a few hundreds of nanometres (150 nm to 500 nm) thick with a reported porosity range from 50 to 60% [47, 61, 76, 83, 90, 194-196]. The preferred TiO_2 crystalline phase is anatase because it has a higher mobility and conductivity than the other TiO_2 crystalline phases as well as a lower formation temperature [141, 196]. The porous TiO_2 layer is especially important for high device yield and low hysteresis in high efficiency perovskite solar cells [87, 89, 189]. The reported 21.2% efficiency for a perovskite solar cell by Saliba et al. (2016) has a 150 nm to 200 nm thick spin-coated porous TiO_2 layer [96]. However, the aforementioned porous TiO_2 deposition techniques are unsuitable for rapid manufacturing of a porous TiO_2 layer on large area substrates for low-cost industrial production [197].

Other deposition methods for the porous TiO_2 layers include pulsed laser deposition [198, 199], flame deposition [98, 200, 201] and electrospinning [202-204]. Flame aerosol methods for direct deposition of the porous TiO_2 layer have been previously reported for dye-sensitised solar cells, leading to an increase in the efficiency, mainly because of an increase in the J_{SC} [98, 201]. The time needed for the deposition and the resulting film morphology depend on the flame system conditions and the desired thickness of the porous TiO_2 nanostructure. Flame aerosol deposition times are typically of the order of seconds or a few minutes [98, 200, 201]. In contrast to the flame aerosol deposition, which can be done in open atmospheric conditions, pulsed laser deposition requires a medium vacuum chamber with a controlled atmosphere [153, 198, 199, 205]. This limits the substrate size and time required for depositing a

porous TiO_2 layer by pulsed laser deposition [153, 198, 199, 205]. Electrospinning produces TiO_2 fibres of about 200 nm to 600 nm thick and tens of microns long which is a completely different morphology to the widely used porous TiO_2 layers for perovskite solar cells [202-204].

The flame aerosol deposition method of porous TiO_2 layers is a remarkably fast, simple and relatively cost-effective deposition method [206-209]. A similar deposition method has been used for several decades in the glass industry for in-line pyrolytic coating of glass with transparent conductive oxides [207, 210, 211]. The flame aerosol deposition method can be integrated into a continuous production line of metre wide area substrates by increasing the number of flame aerosol nozzles similarly to the spray pyrolysis system shown in Fig. 6.1 [208]. However, the flame aerosol deposited porous TiO_2 layers are usually highly fragile [153] and undergo morphological reorganisation upon contact with liquid solutions [98]. Therefore it is valuable to investigate the prospects of flame aerosol deposition to make the porous layer of perovskite solar cells.

Figure 6.1 Sono-teck's array system of spray pyrolysis nozzles designed to deposit uniform transparent conductive oxide (TCO) layers for mass production of TCO coated glass substrates for thin film solar cell manufacturing (photograph from Sono-Teck Corporation).

This Chapter demonstrates the nanofabrication of stable high porosity TiO_2 layers by combining flame aerosol and atomic layer depositions of TiO_2. The thickness of the compact ALD TiO_2 coating layer on the flame-made ultra-porous TiO_2 layers was varied and the impact of the resultant porous TiO_2 layer morphology on the solar cell efficiency was investigated. Promising efficiency results for $MAPbI_3$ solar cells using a flame-made TiO_2 porous layer are reported.

Experimental

Solar Cell Fabrication

The $MAPbI_3$ solar cells in this Chapter were fabricated on 1 cm^2 commercial FTO coated soda-lime float glass substrates. A 50 nm thick compact TiO_2 layer was deposited on top of the FTO by ALD. A 300 nm thick porous TiO_2 layer was deposited on top of the compact ALD TiO_2 layer by the flame aerosol deposition method described in detail in Chapter 3. Then, the $MAPbI_3$ and spiro-OMeTAD layers were deposited following the solution methods described in Chapter 3. The 0.64 x 0.64 cm back metal contact area was made of a 100 nm thick gold layer using the e-beam evaporation system discussed in Chapter 3. The active size of the $MAPbI_3$ solar cells in this Chapter was 0.4 cm^2. Also $MAPbI_3$ solar cells with a spin-coated porous TiO_2 layer of equal size were fabricated to be used as a reference for comparison purposes.

Solar Cell Characterisation

J-V measurements were performed under simulated AM1.5G illumination using a solar simulator from Photo Emission Tech., Inc. All the J-V measurements were done in the reverse scan mode (from V_{OC} to J_{SC}) with a 50 mV/s scan rate. The cross section images of the finished solar cells by FIB-SEM were done using a FEI Helios NanoLab 600 system. The top views of the porous TiO_2 scaffold by SEM were obtained with a Zeiss Ultraplus FE-SEM system. The high magnification nanoparticle images by TEM were obtained using a Hitachi H7100 TEM system. The XRD measurements of thin films were done using a PANalytical X'Pert Pro system. The transmittance and reflectance measurements were done using a Perkin Elmer Spectrophotometer Lambda 1050 with an integrating sphere.

Results and Analysis

The optimum thickness of the flame-made porous TiO_2 layer for $MAPbI_3$ solar cells was found to be 300 nm. To find this optimum thickness, several $MAPbI_3$ solar cells with flame-made porous TiO_2 layers of different thickness were fabricated. The thicknesses of the flame-made porous TiO_2 layers were 200, 300, 500, 700 and 1000 nm. All of the flame-made porous TiO_2 layers were stabilised by coating them with a 10 nm thick compact ALD TiO_2 layer. The photovoltaic parameters of the $MAPbI_3$ solar cells with different thickness of the flame-made porous TiO_2 layer are shown in Fig. 6.2a-d.

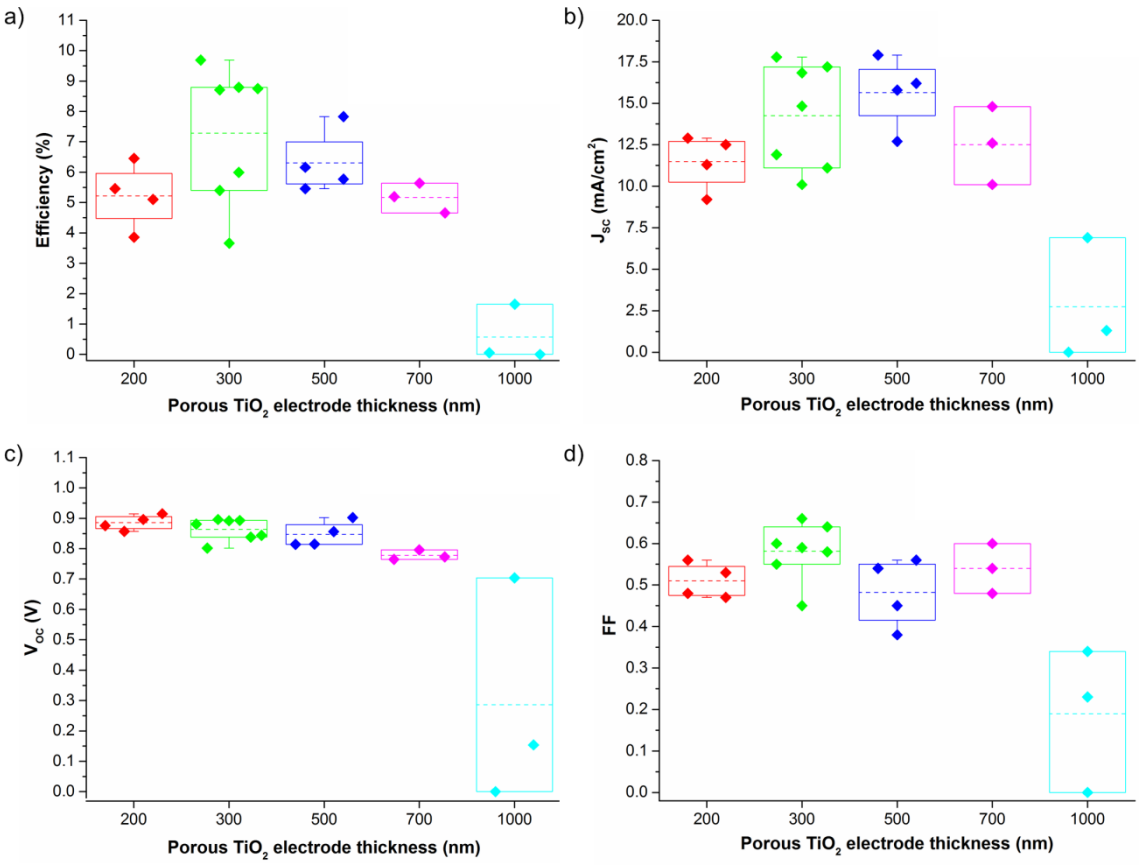

Figure 6.2 a) Efficiency, b) J_{SC}, c) V_{OC} and d) FF of the $MAPbI_3$ solar cells as a function of the thickness of the flame-made porous TiO_2 layer coated with a 10 nm thick ALD TiO_2 layer. All data was measured at one sun intensity.

The optimum thickness of the flame-made porous TiO_2 layer for $MPbI_3$ solar cells was 300 nm (Fig. 6.2a), which was deposited in 3 seconds using a flame aerosol pyrolysis system as described in the experimental section. The coverage of the flame-made porous TiO_2 layer by the $MAPbI_3$ perovskite layer was better for a 300 nm thick flame-made porous TiO_2 layer than for the 500, 700 and 1000 nm thick flame-made

porous TiO_2 layers. The better coverage of the flame-made porous TiO_2 layer by the $MAPbI_3$ improved the performance of the solar cell. However, a flame-made porous TiO_2 layer thinner than 300 nm was found to be detrimental to the performance of the solar cell. This was probably because of a reduction in the collection carrier efficiency thus resulting in a lower J_{SC}.

The top-view image of the 300 nm thick as-deposited flame-made TiO_2 layer is shown in Fig. 6.3a. The porosity (Φ) of the flame-made porous TiO_2 layers was estimated as follows:

$$\phi = \frac{1 - t_{optical}}{t_{physical}}$$

Here the physical thickness ($t_{physical}$) was measured from SEM images and the optical thickness ($t_{optical}$) was calculated using the measured transmittance (T_{TiO2}) and reflectance (R_{TiO2}) of the film plus the TiO_2 absorption coefficient (α_{TiO2}) at 400 nm (TiO_2 band edge), as given by the following equation:

$$t_{optical} = \frac{\ln\left(\frac{T_{TiO_2}}{1 - R_{TiO_2}}\right)}{\alpha_{TiO_2}}$$

This calculation assumes that there is no scattering by the nanostructure and thus underestimates the film porosity.

The as-deposited flame-made TiO_2 layer has a porosity of about 97% which is in line with previous reports [98]. The as-deposited porosity can be fine-tuned by a subsequent ALD TiO_2 coating step. Figure 6.3b shows the same flame-made TiO_2 layer after coating with 2 nm of TiO_2 via ALD. The estimated porosity is reduced from 97% as-deposited to 87% when coated with a 2 nm thick compact ALD TiO_2 layer. The optical thickness and estimated porosity values of the flame-made TiO_2 layer as a function of the ALD TiO_2 coating thickness are shown in Fig. 6.3c. The optical thickness increases from 9 nm to 195 nm as the compact TiO_2 coating increases from 0 to 10 nm confirming ALD TiO_2 deposition within the ultra-porous flame-made morphology. This results in an ALD TiO_2 mass deposition of 0.23 mg/cm^2 per cycle that is 22 times higher than that expected on a flat substrate as the ultra-porous TiO_2 layer has a larger surface area. For comparison, the porosity of a spin-coated TiO_2 porous film following

the previously mentioned method was calculated. The calculated porosity of 65% for a spin-coated TiO_2 porous film is within the range of previously reported values [47, 61, 194-196].

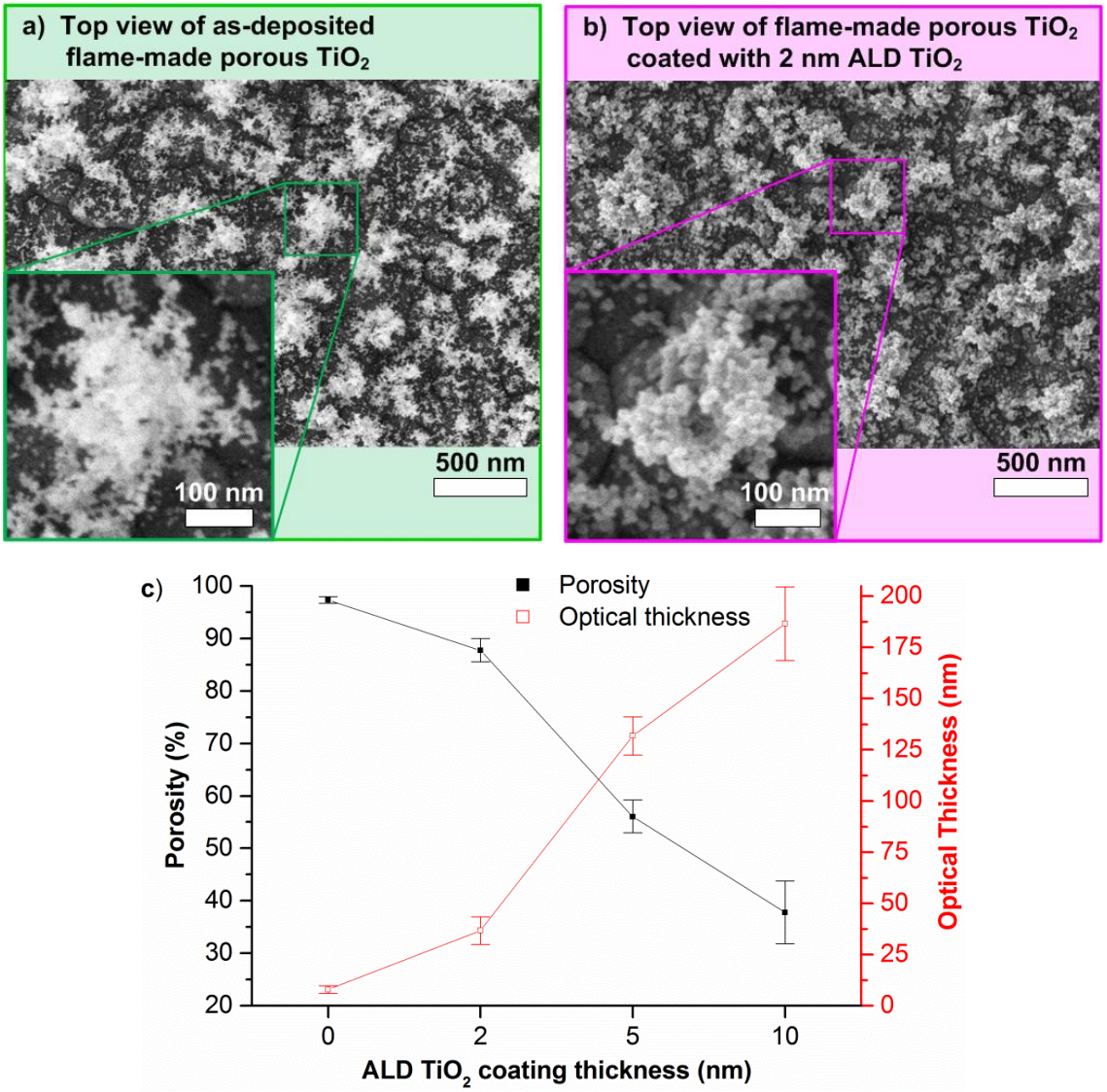

Figure 6.3 a) Top view image of a 300 nm thick film of as-deposited flame-made TiO_2 porous nanostructure by SEM. b) Top view image of the same flame-made TiO_2 porous nanostructure as in (a), but coated with 2 nm of ALD TiO_2. c) Porosity and optical thickness of the flame-made TiO_2 layers with ALD TiO_2 coatings of different thickness.

The TiO_2 single particle size was estimated from the TEM images in Fig. 6.4a-d. The single particle size for the flame-made TiO_2 porous layers ranges from 8 nm to 40 nm as a function of the ALD TiO_2 coating thickness as shown in Fig. 6.4e. For comparison, the single particle size for the spin-coated TiO_2 porous layer is 30 nm. Each TiO_2 single

particle is composed of TiO_2 crystals. The TiO_2 crystal sizes for each TiO_2 single particle are detailed in the next paragraph.

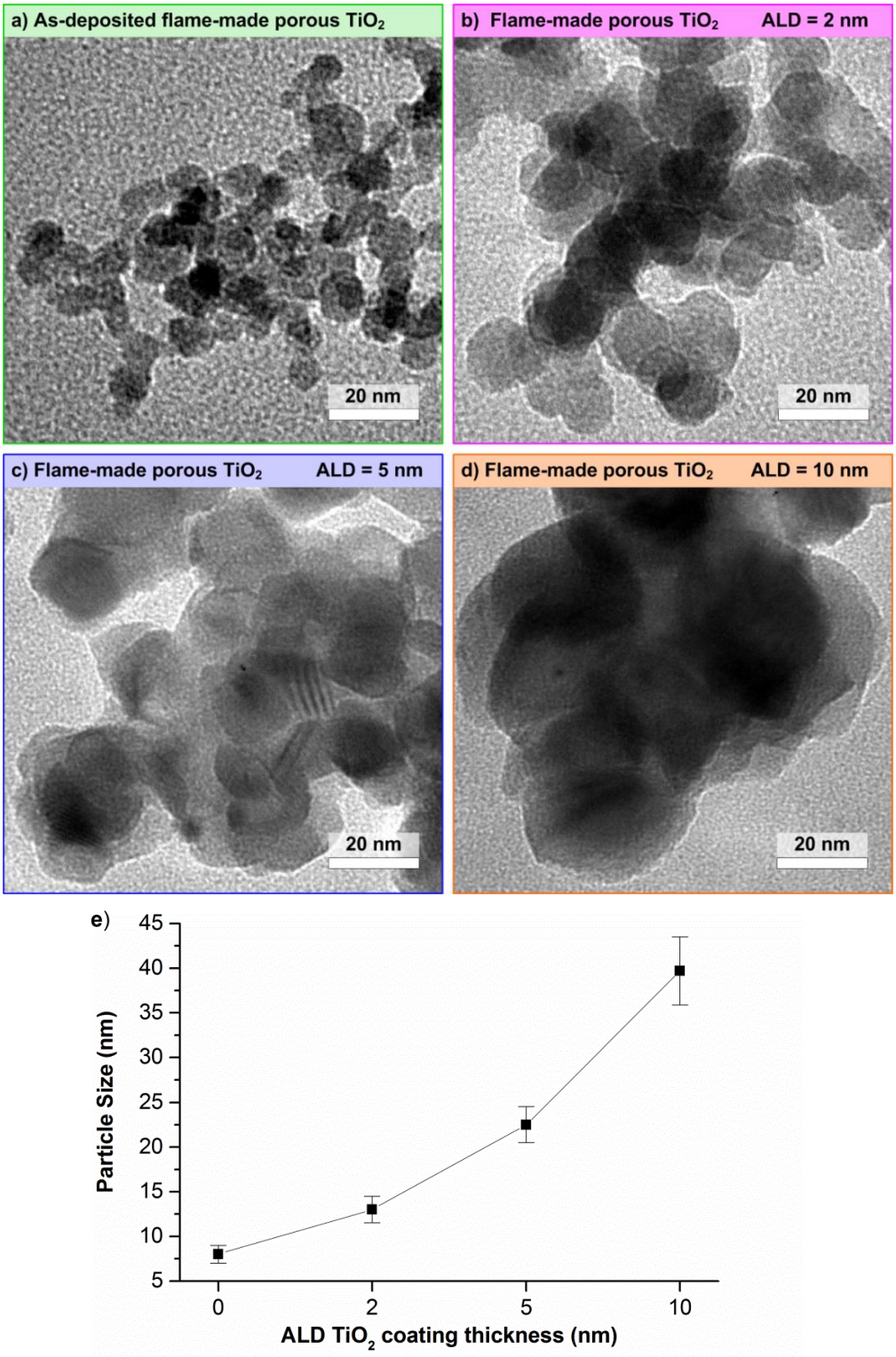

Figure 6.4 TEM images of the nanoparticles of the flame-made TiO_2 porous layer: a) as-deposited and same as (a) but coated with a (b) 2 nm, (c) 5 nm and (d) 10 nm thick compact ALD TiO_2 layer. e) Particle size of the flame-made TiO_2 nanoparticles as a function of the ALD TiO_2 coatings of thickness.

The as-deposited and ALD TiO_2 coated flame-made TiO_2 layers have an anatase crystal phase as confirmed by the measured XRD spectra shown in Fig. 6.5a. There are no significant differences in the measured XRD spectra as a function of the ALD TiO_2 thickness other than the relative intensity of the peaks between the different spectra which arises from the amount of TiO_2 present in the samples. The crystal size for the different samples was estimated from the XRD spectra using Scherrer's method [109]. The crystal size of the flame-made TiO_2 nanostructures as estimated from the XRD spectra increases from about 8 nm to 10 nm when increasing the TiO_2 ALD coating thickness from 0 nm to 10 nm as shown in Fig. 6.5b. For comparison, the spin-coated TiO_2 crystal size from the XRD spectra is 12 nm which is 20-30% larger than the flame-made samples depending on the coating thickness.

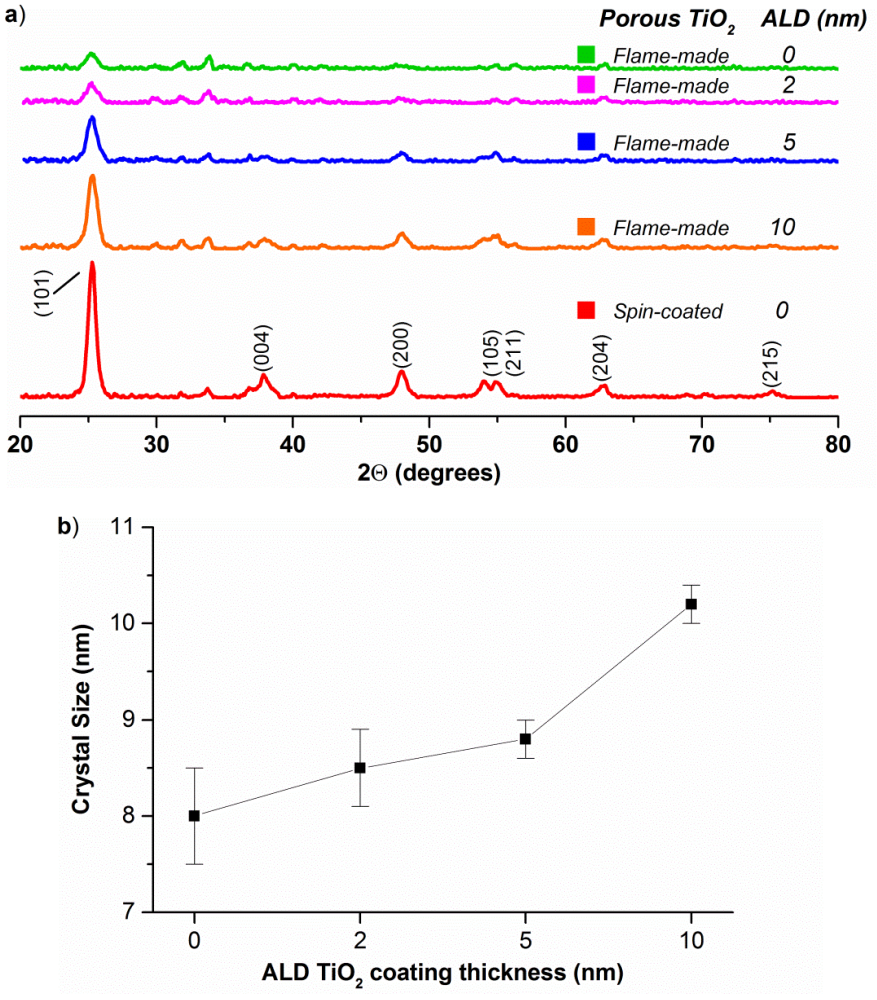

Figure 6.5 a) XRD spectra of the as-deposited flame-made TiO_2 porous layer and with a compact ALD TiO_2 coatings thickness of 2, 5 and 10 nm. Also shown is the XRD spectrum of the spin-coated TiO_2 porous layer. b) Crystal size of the flame-made TiO_2 nanoparticles as a function of the ALD TiO_2 coatings thickness.

The as-deposited flame-made TiO_2 nanoparticles are likely to be almost single crystals as the estimated crystal size is similar to the single particle size. The increase in the single particle size is consistent with the expected increase from a uniform and isotropic ALD coating. The single nanoparticle size scales linearly with the ALD TiO_2 coating thickness, but the particle volume scales as the cube of the coating thickness, producing the large drop in porosity observed with a thin ALD TiO_2 coating. The flame-made TiO_2 porous layer is formed of agglomerates of single particles that are 100 nm to 200 nm wide and spaced 100 nm to 250 nm apart as can be observed in Fig. 6.3a-b. In contrast, the spin-coated TiO_2 porous nanostructure is a continuous film with a more homogeneous particle distribution as shown in Fig. 6.6a-b [82, 83, 90, 212]. The reason for this difference is the nature of the deposition methods because the flame aerosol deposition system operates in a diffusion or randomly-oriented ballistic regime, which results in flame-made layers with the aforementioned hierarchical morphology [213].

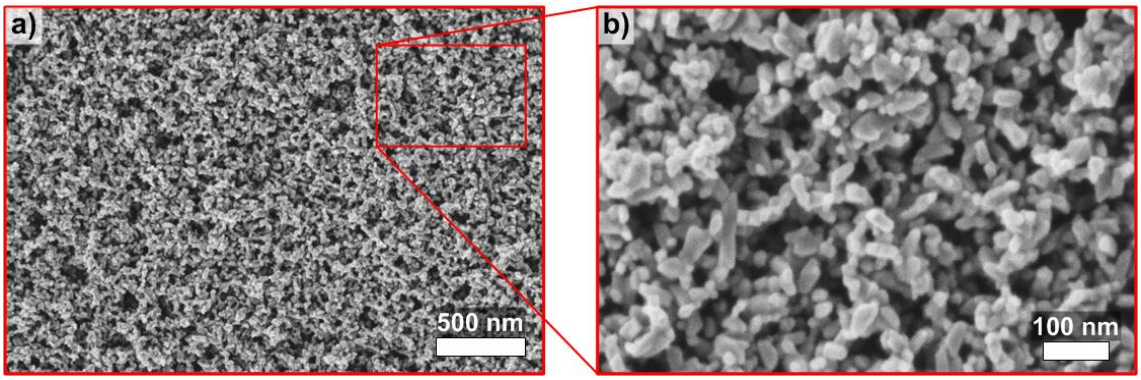

Figure 6.6 Top view image of a 300 nm thick spin-coated porous TiO_2 layer by SEM at a) low and b) high magnification.

To make the solar cells, the 300 nm thick flame-made TiO_2 porous layers discussed above were fabricated on glass/FTO/compact TiO_2 substrates. Then, the flame-made TiO_2 porous layers were coated with $MAPbI_3$ perovskite followed by spiro-OMeTAD and gold as described in detail in Chapter 3. The cross section views of the finished solar cells using the flame-made TiO_2 porous nanostructures with different ALD TiO_2 coating thicknesses are shown in Fig. 6.7a-d.

In Fig. 6.7a the uncoated flame-made TiO_2 porous nanostructure can barely be seen as it has a porosity of 97%. In contrast, the coated flame-made porous TiO_2 layer can

clearly be seen as intricate branches or agglomerates with a coral-like structure enclosed with $MAPbI_3$ in Fig. 6.7b-d. The single nanoparticles within the flame-made porous TiO_2 nanostructured agglomerates fuse together into larger nanoparticles as the ALD TiO_2 coating thickness increases from 0 nm to 10 nm (Fig. 6.7b-d). The $MAPbI_3$ infiltrates more into the flame-made porous TiO_2 layer than into the spin-coated TiO_2 porous layer shown in Fig 6.7e. Moreover, the $MAPbI_3$ does not completely cover the tallest branches of the flame-made TiO_2 porous layers (no $MAPbI_3$ capping layer). In contrast, the spin-coated TiO_2 layer has an observable $MAPbI_3$ capping layer of about 150 nm (Fig. 6.7e).

The measured J-V curves of the best solar cells are shown in Fig. 6.8a and the corresponding photovoltaic parameters are given in Table 6.1. The V_{OC}, FF and J_{SC} of the entire batch of flame-made porous TiO_2 nanostructured solar cells as a function of the ALD TiO_2 coating thickness are shown in Fig. 6.8b and similarly the efficiency is shown Fig. 6.8c. In Figure 6.8b-c the symbol represents the average value and the horizontal bars represent the variation of the corresponding measured values of a batch of 12 solar cells.

Table 6.1 Photovoltaic parameters of the $MAPbI_3$ perovskite solar cells with different flame-made TiO_2 porous layers and with a spin-coated TiO_2 layer for comparison.

Porous TiO_2 layer	**ALD TiO_2 (nm)**	**V_{OC} (V)**	**J_{SC} (mA/cm^2)**	**FF**	**Efficiency (%)**
Flame-made	0	0.983	22.2	0.58	12.7
Flame-made	2	0.964	21.2	0.67	13.7
Flame-made	5	0.947	21.1	0.63	12.6
Flame-made	10	0.953	18.6	0.59	10.4
Spin-coated	0	1.026	21.6	0.69	15.3

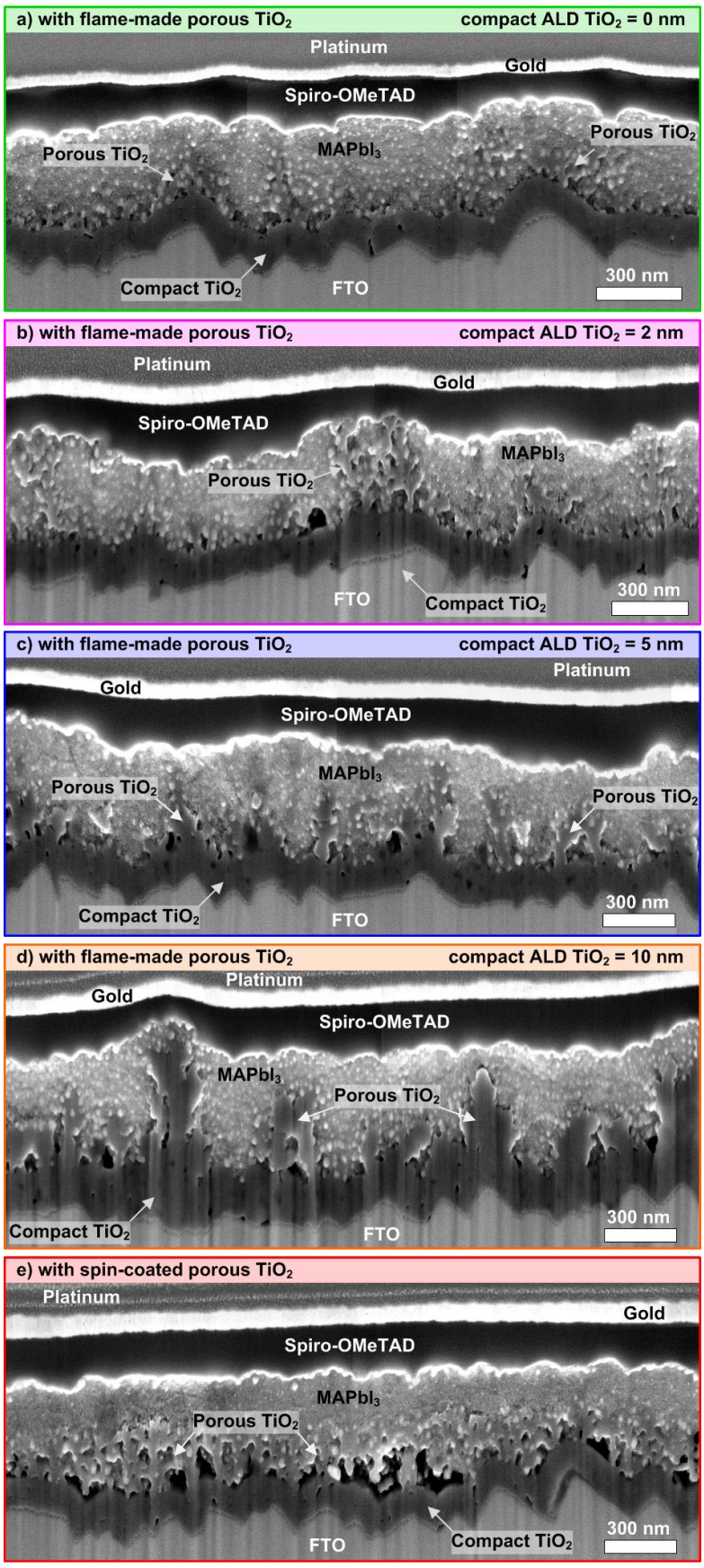

Figure 6.7 Cross section images of the $MAPbI_3$ perovskite solar cells with flame-made TiO_2 porous layers with ALD TiO_2 coatings of different thickness (a, b, c, d) and with a spin-coated TiO_2 porous layer (e).

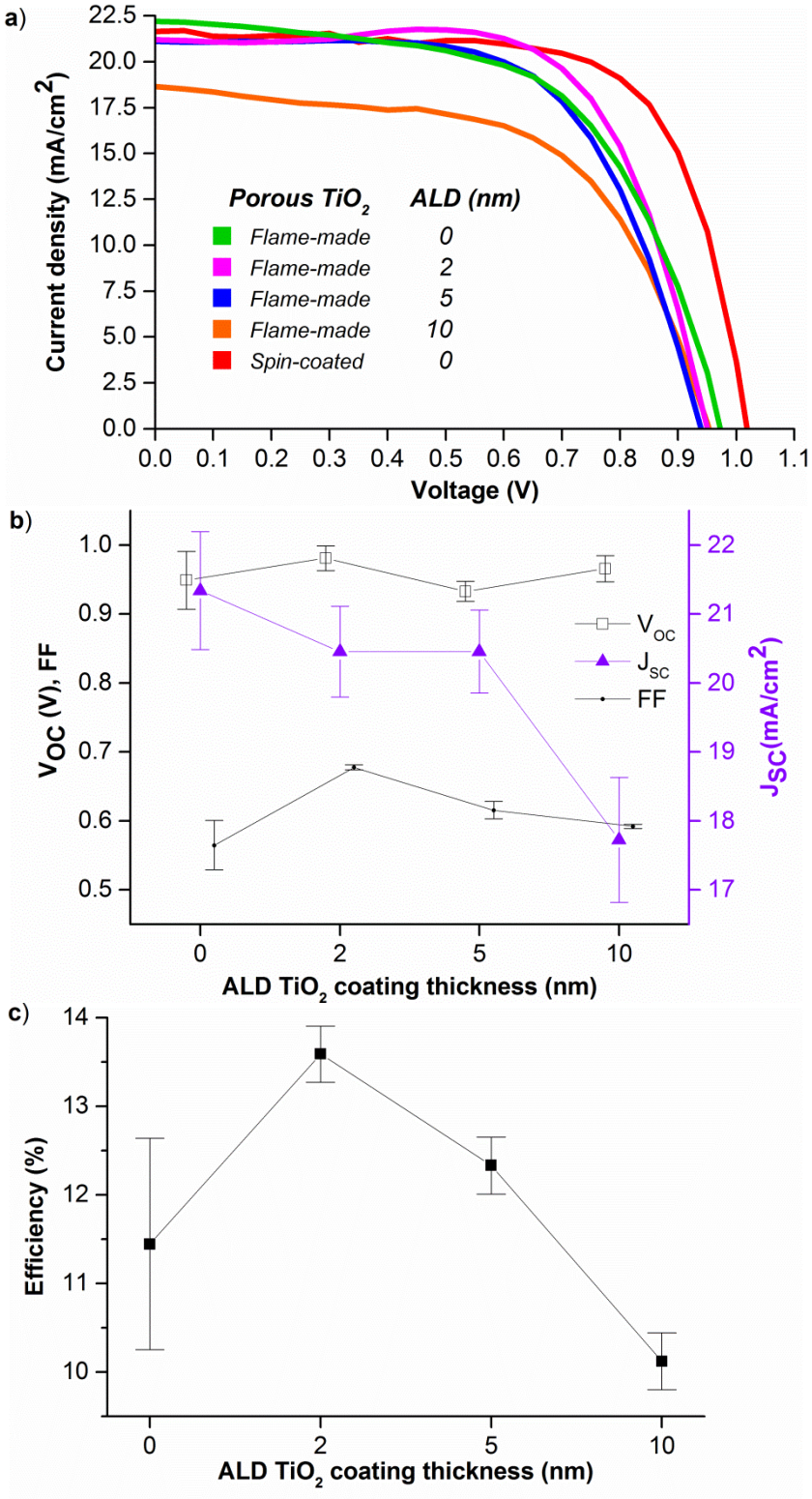

Figure 6.8 a) J-V curves of the best $MAPbI_3$ solar cells with a flame-made TiO_2 porous layer as a function of the ALD TiO_2 coating thickness and with a spin-coated TiO_2 porous layer for comparison. b) Values of V_{OC}, FF, J_{SC} and c) efficiency of the $MAPbI_3$ perovskite solar cells with a flame-made TiO_2 porous layer as a function of the ALD TiO_2 coating thickness. The symbol represents the average value and the horizontal bars represent the data variation of the corresponding batch of solar cells.

A decreasing J_{SC} trend from 22.2 mA/cm^2 to 18.6 mA/cm^2 as the ALD TiO_2 coating thickness is increased from 0 nm to 10 nm can be seen in Fig. 6.8b and Table 6.1. In contrast, the highest FF of 0.67 for the flame-made porous TiO_2 nanostructured solar cell was achieved with an ALD TiO_2 coating thickness of 2 nm which is 16% higher than the FF of the solar cell with the as-deposited flame-made TiO_2. The change in the TiO_2 coating thickness does not significantly affect V_{OC} which varies only by ±2%. As a result, the flame-made TiO_2 porous nanostructured solar cell with the highest efficiency of 13.7% was achieved with a 2nm thick compact ALD TiO_2 coating layer.

To explain these trends, the measured absorptance of the solar cells as a function of the ALD TiO_2 coating thickness is shown in Fig. 6.9a. The absorptance curves of the solar cells clearly show the $MAPbI_3$ band-edge wavelength of 780 nm. The absorptance spectra show most dissimilarities at short (300 nm to 500 nm) and long wavelengths (780 nm to 1200 nm). An ideal current density value ($J_{SC\ Ideal}$) can be calculated by integration of the product of each absorptance curve times the solar photon flux up to the $MAPbI_3$ band-edge wavelength. The ideal J_{SC} values calculated in this manner (inset Fig. 6.9a) assume a perfect IQE of 100% and vary at most by only 0.56 mA/cm^2. From the similar calculated ideal J_{SC} values it can be concluded that all of the solar cells absorb a similar number of photons and the differences in the measured J_{SC} are because of a reduction in the IQE. This reduction in IQE was attributed to parasitic absorption in the porous TiO_2 layer. The parasitic absorption of the porous TiO_2 layer can be clearly observed in Fig. 6.9b which shows the measured absorptance of only the porous TiO_2 layer as a function of the compact ALD TiO_2 coating thickness. A parasitic current density value ($J_{Parasitic}$) can be calculated following the same procedure as for the aforementioned ideal J_{SC}. The calculated $J_{Parasitic}$ values (inset Fig. 6.9b) fit the trend of the measured J_{SC} as a function of the ALD TiO_2 coating thickness and vary by a comparable amount. This parasitic absorption is due to free carriers within the TiO_2 that compete with the $MAPbI_3$ for photon absorption. It has already been reported that TiO_2 can absorb light above its 385 nm band-edge [186]. Therefore, the measured J_{SC} decreases when the ALD TiO_2 coating thickness increases, because the amount of TiO_2 and its associated parasitic absorption are augmented. This means that the total volume of TiO_2 in the device should not be too high for optimum device performance.

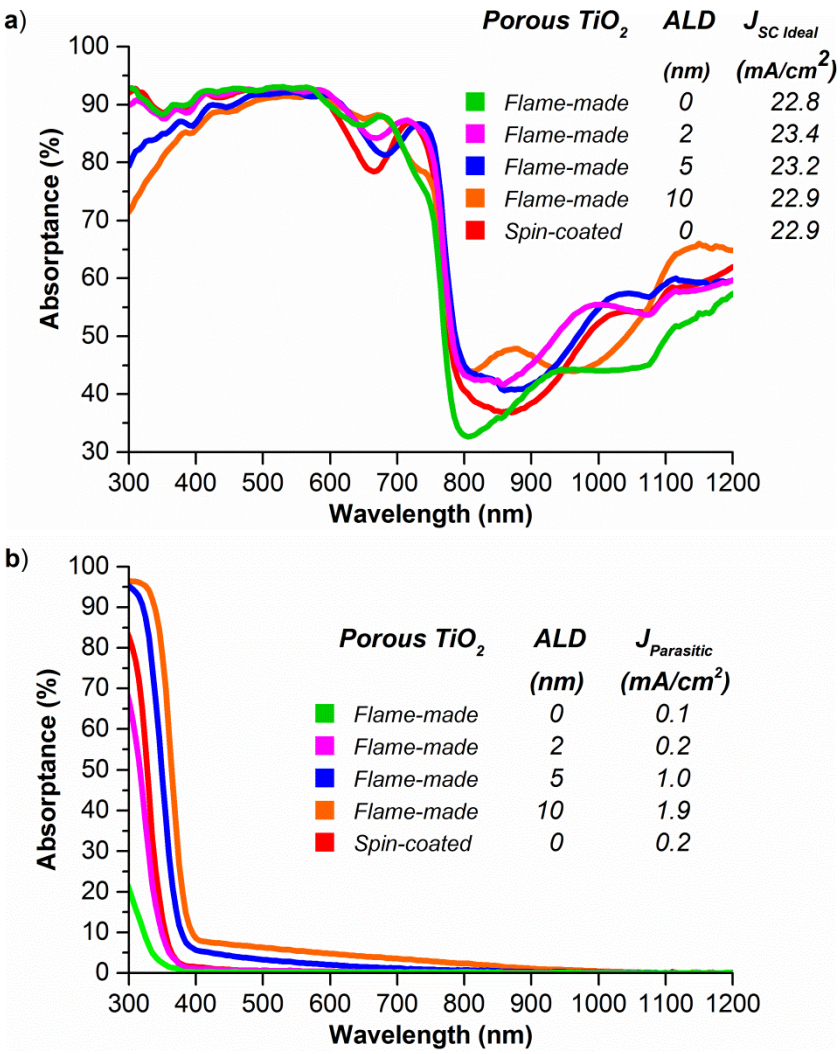

Figure 6.9 a) Absorptance of the $MAPbI_3$ perovskite solar cells with a flame-made TiO_2 porous layer as a function of the ALD TiO_2 coating thickness and with a spin-coated TiO_2 porous layer for comparison. (b) Absorptance of the flame-made TiO_2 porous layers as a function of ALD TiO_2 coating thickness and of the spin-coated TiO_2 porous layer.

The difference in V_{OC} between the $MAPbI_3$ solar cell with a spin-coated porous TiO_2 layer and the solar cells with an uncoated, 2 nm, 5 nm and 10 nm ALD TiO_2 coated flame-made porous TiO_2 layers is 43 mV, 62 mV, 79 mV and 73 mV or 4.2%, 6%, 7.7% and 7.1% respectively. The lower V_{OC} of the solar cells with a flame-made TiO_2 porous layer is likely to originate from: i) the increase in the contact area between the $MAPbI_3$ and the TiO_2 because the $MAPbI_3$ deeply infiltrates into the flame-made porous nanostructure because of its high porosity and morphology; and ii) the lack of a $MAPbI_3$ capping layer for the solar cells with a flame-made TiO_2 porous layer which enables the spiro-OMeTAD to come in contact with the porous TiO_2 layer as can be

seen in Fig. 6.7b and Fig. 6.7d. The detrimental effect from the contact between spiro-OMeTAD and the porous TiO_2 layer in $MAPbI_3$ solar cells has already been reported [81, 82].

The differences in FF between the $MAPbI_3$ solar cell with a spin-coated TiO_2 porous layer, which has the highest FF, and the solar cells with the flame-made TiO_2 porous layers are likely to originate from two causes. Firstly, the contact area between the uppermost nanoparticles of the flame-made TiO_2 porous layer and spiro-OMeTAD increases as the ALD TiO_2 coating thickness increases the size of such nanoparticles, thus reducing the shunt resistance. Secondly, the TiO_2 volume that the carriers have to go through increases as the ALD TiO_2 coating thickness is varied from 2 nm to 10 nm, thus increasing the series resistance. However, the as-deposited flame-made TiO_2 solar cell has the lowest FF of all the solar cells reported here because of the uncontrollable disintegration of the flame-made TiO_2 nanostructure during the deposition process of the $MAPbI_3$ layer. The as-deposited flame-made TiO_2 nanostructure has narrower branches and smaller particles, and thus a lower mechanical stability than when coated with a compact ALD TiO_2 layer. Nevertheless, the $MAPbI_3$ solar cell with the as-deposited flame-made TiO_2 porous layer had a maximum efficiency of 12.7% but also the largest variation in the measured photovoltaic parameters.

The highest efficiency of 13.7% for a $MAPbI_3$ solar cell with a flame-made TiO_2 porous layer with a 2 nm thick ALD TiO_2 layer (Fig. 6.8c) is encouraging because it is comparable to the 15.3% efficiency of the spin-coated TiO_2 solar cell. The efficiency of the $MAPbI_3$ solar cell with a flame-made TiO_2 porous layer could be improved by adding a perovskite capping layer and by reducing the parasitic absorption of the TiO_2 porous layer. The parasitic absorption of the TiO_2 porous layer could be avoided if another material is used instead of TiO_2, which is investigated in the following Chapter.

Conclusion

The combined flame aerosol and ALD approach reported here is a notably efficient alternative method to deposit porous TiO_2 layers for high efficiency perovskite solar cells. The porosity of the flame-made TiO_2 porous layers can be easily adjusted over a

wide range by coating them with a thin compact ALD TiO_2 layer. The flame aerosol deposition of porous TiO_2 layers could be integrated into an industrial production line of large area glass substrates for solar cells. The highest efficiency for a $MAPbI_3$ solar cell with a flame-made porous TiO_2 layer was 13.7% which was achieved by coating the as-deposited flame-made TiO_2 ultra-porous layer with a 2 nm thick ALD TiO_2 layer. The 2 nm thick ALD TiO_2 layer provided mechanical stability and reduced the porosity of the flame-made TiO_2 layer to 87%. The larger pore size of the flame-made TiO_2 porous layer facilitates the deeper infiltration of the $MAPbI_3$ layer compared to spin-coated TiO_2 porous layers. The highest efficiency of 13.7% for the $MAPbI_3$ solar cell with a flame-made TiO_2 porous layer is already comparable to the $MAPbI_3$ solar cell with a spin-coated TiO_2 perovskite solar cell. There is scope for further optimisation of the efficiency by adding a $MAPbI_3$ capping layer or by reducing the parasitic absorption of the porous TiO_2 layer. This is highly positive because the flame aerosol system can contribute to minimising the cost of solar cells via its high throughput and potential large area coverage for industrial solar cell production.

7. Flame-Made SnO_2 Layers for $MAPbI_3$ Solar Cells

The mechanical stability of flame-made porous metal oxide layers is crucial to withstand the subsequent perovskite deposition and make high efficiency solar cells. In this Chapter, perovskite solar cells with a flame-made porous SnO_2 layer were investigated. SnO_2 has a higher mobility, UV stability and lower resistivity than TiO_2 and thus may have the potential to produce high efficiency and stable perovskite solar cells. Furthermore, two different methodologies to increase the mechanical stability of flame-made porous SnO_2 layers were investigated as they result in two different porosities and morphologies.

The mechanical stability of the as-deposited flame-made porous SnO_2 layer was increased using two different anneal step methods: furnace anneal and in-situ flame anneal (henceforth referred to as in-situ anneal). The in-situ annealed flame-made porous SnO_2 layer has a porosity of 60% whilst the furnace annealed flame-made porous SnO_2 layer has a porosity of 98%. The best $MAPbI_3$ solar cells made with the in-situ annealed flame-made porous SnO_2 layer had an 8% efficiency that was mainly limited by a low FF and J_{SC} because of resistive and recombination losses at the SnO_2-TiO_2 interface. In contrast, the best $MAPbI_3$ solar cells made with the furnace annealed flame-made porous SnO_2 layer had an efficiency of 12%. The higher efficiency of the $MAPbI_3$ solar cells with the furnace annealed flame-made porous SnO_2 layer is attributed to the higher porosity of the former. There is scope to further improve the efficiencies of these solar cells, as discussed later in this Chapter.

Motivation for this Work

Perovskite solar cells with efficiencies ≥ 20% have always been fabricated with two TiO_2 layers: a compact and a porous TiO_2 layer [89, 93, 96]. The TiO_2 matrix acts as the ETM by blocking holes and conducting electrons from the perovskite layer to the highly conductive FTO layer. TiO_2 is the most widely used ETM because of its fast injection dynamics, chemical stability and low-cost [37, 214]. The compact layer prevents contact between the FTO and the perovskite layer which would shunt the solar cell.

The porous layer also contributes to reduce the hysteresis and to efficiently extract electrons from the perovskite layer [76, 87, 215].

However, TiO_2 based solar cells have been found to have an inherent instability under solar irradiation which has been linked to the oxygen desorption in the TiO_2 layer upon UV illumination [92]. This is a problem for the long-term stability of TiO_2 based solar cells. It can be alleviated by substituting the TiO_2 with another ETM [92, 97]. Alternative inorganic ETMs to TiO_2 are zinc oxide, (ZnO), tungsten oxide (WO_x), niobium pentoxide (Nb_2O_5) and SnO_2 [97, 165, 216-226].

One of the most promising alternative ETM is SnO_2 because it has better electronic, mechanical and photo-catalytic properties than TiO_2 [92, 97, 165, 214, 220, 221, 224, 226]. The electron mobility of bulk single-crystal SnO_2 is about 2 orders of magnitude higher than that of TiO_2. [99, 100, 103, 158, 159, 214]. Also, SnO_2 has a lower resistivity than TiO_2 [99-103, 158, 159, 214, 227]. In addition, SnO_2 has shown excellent thermal and UV stability which increases the durability of $MAPbI_3$ solar cells in ambient environmental conditions [92, 97, 165, 220, 221, 223].

Stable and high efficiency perovskite solar cells with a compact SnO_2 layer have already been reported [216-218, 220, 221, 224, 226]. Efficiencies ranging from 8% to 16% have been reported for $MAPbI_3$ solar cells with a compact SnO_2 layer as the ETM [216-218, 220, 221, 224, 226]. The compact SnO_2 layer of these perovskite solar cells was deposited by using the spin-coating or dip-coating methods [216-218, 220, 221, 224, 226]. The highest efficiency for a planar mixed perovskite solar cell with a compact ALD SnO_2 layer as the ETM was 18% [97]. These efficiencies have been improving over the last few years, although they are still lower than the best efficiencies of perovskite solar cells with a TiO_2 layer.

Most of the above-mentioned perovskite solar cells only have a compact SnO_2 layer and not a porous SnO_2 layer. Inclusion of a porous SnO_2 layer can further increase the solar cell efficiency through an improvement in long-term stability and photo-generated carrier collection [220]. For instance, 16% efficiency has already been reported for a $MAPbI_3$ solar cell with a hydrothermally grown hierarchically porous SnO_2 layer on top of a compact SnO_2 layer [220]. Nonetheless, it took several hours to grow the hierarchically porous SnO_2 layer [220]. A faster deposition of porous SnO_2

layers over large areas can be done using a flame aerosol system [153]. However, the as-deposited flame-made porous SnO_2 layer has a low mechanical stability that has to be increased for its use with solution-made perovskite solar cells.

In this Chapter, two different methods to increase the mechanical stability of the as-deposited flame-made porous SnO_2 layers were used. The photovoltaic performances of $MAPbI_3$ solar cells with the two different stabilised flame-made porous SnO_2 layers are discussed. In addition, the efficiency limitations of such solar cells are discussed and insights into how to improve the efficiency of the solar cells are provided. To the best of the author's knowledge, up to now there has been no report about a perovskite solar cell with a flame-made porous SnO_2 layer.

It should be noted that the $MAPbI_3$ solar cells reported here have a flame-made porous SnO_2 layer on top of a compact TiO_2 layer. The substitution of the compact TiO_2 layer with a compact SnO_2 layer was not possible because the equipment used for this purpose (an ALD system) had a critical malfunction that rendered the tin ALD reactant unusable. Furthermore, due to time constraints the acquisition of a new tin reactant canister for the ALD system was not possible.

Experimental

Solar Cell Fabrication

The $MAPbI_3$ solar cells in this Chapter were fabricated on 1 cm^2 commercial FTO coated soda lime float glass substrates. A 50 nm thick compact TiO_2 layer was deposited on top of the FTO by ALD as discussed in Chapter 3. A flame-made porous SnO_2 layer was deposited on top of the compact ALD TiO_2 layer with a flame aerosol deposition method described in detail in Chapter 3. The as-deposited flame-made porous SnO_2 layers were annealed by either the in-situ anneal step or the furnace anneal step. The furnace anneal step of the flame-made porous SnO_2 layer was done at 500°C for 5 hours in air atmosphere. The in-situ anneal step was carried out with the flame aerosol system as discussed later in this Chapter. The $MAPbI_3$ and HTM (spiro-OMeTAD) layers were deposited following the solution methods described in

Chapter 3. The 0.55 cm x 0.55 cm back metal contact area was made of a 100 nm thick gold layer using the e-beam evaporation system discussed in Chapter 3. The active size of the $MAPbI_3$ solar cells in this Chapter was 0.35 cm^2.

Solar Cell Characterisation

J-V measurements were conducted under simulated AM1.5G spectrum using a Solar Simulator from Photo Emission Tech., Inc. All the J-V measurements were done in the reverse scan mode (from V_{OC} to J_{SC}) with a 50 mV/s scan rate. The absorptance measurements were calculated from transmittance and reflectance measurements that were produced using a Perkin Elmer Spectrophotometer Lambda 1050 with an integrating sphere. The top view images were obtained with a Zeiss Ultra-plus FE-SEM system. The cross section images of the complete solar cells were taken using a FEI Helios NanoLab 600 FIB-SEM System.

Results and Analysis

The flame aerosol system discussed earlier (Chapter 3) was used to make flame-made porous SnO_2 (hereafter referred to as porous SnO_2) layers. The as-deposited porous SnO_2 nanostructure is 98% porous and has a low mechanical stability because of its narrow branches and small particles (Fig. 7.1) [153]. The mechanical stability of the as-deposited porous SnO_2 layers can be improved by annealing at a temperature of ≥400°C [153, 213]. The high temperature annealing step fuses and strengthens the inter-particle connections of the SnO_2 nanoparticles thereby increasing the mechanical stability of the as-deposited porous SnO_2 layer. Two different anneal step methods were used: in-situ anneal and furnace anneal method [153, 213]. Both of these annealed porous SnO_2 layers have a similar crystalline structure as shown by the XRD in Fig. 7.1c. The corresponding $MAPbI_3$ solar cells made with these annealed porous SnO_2 layers are discussed next.

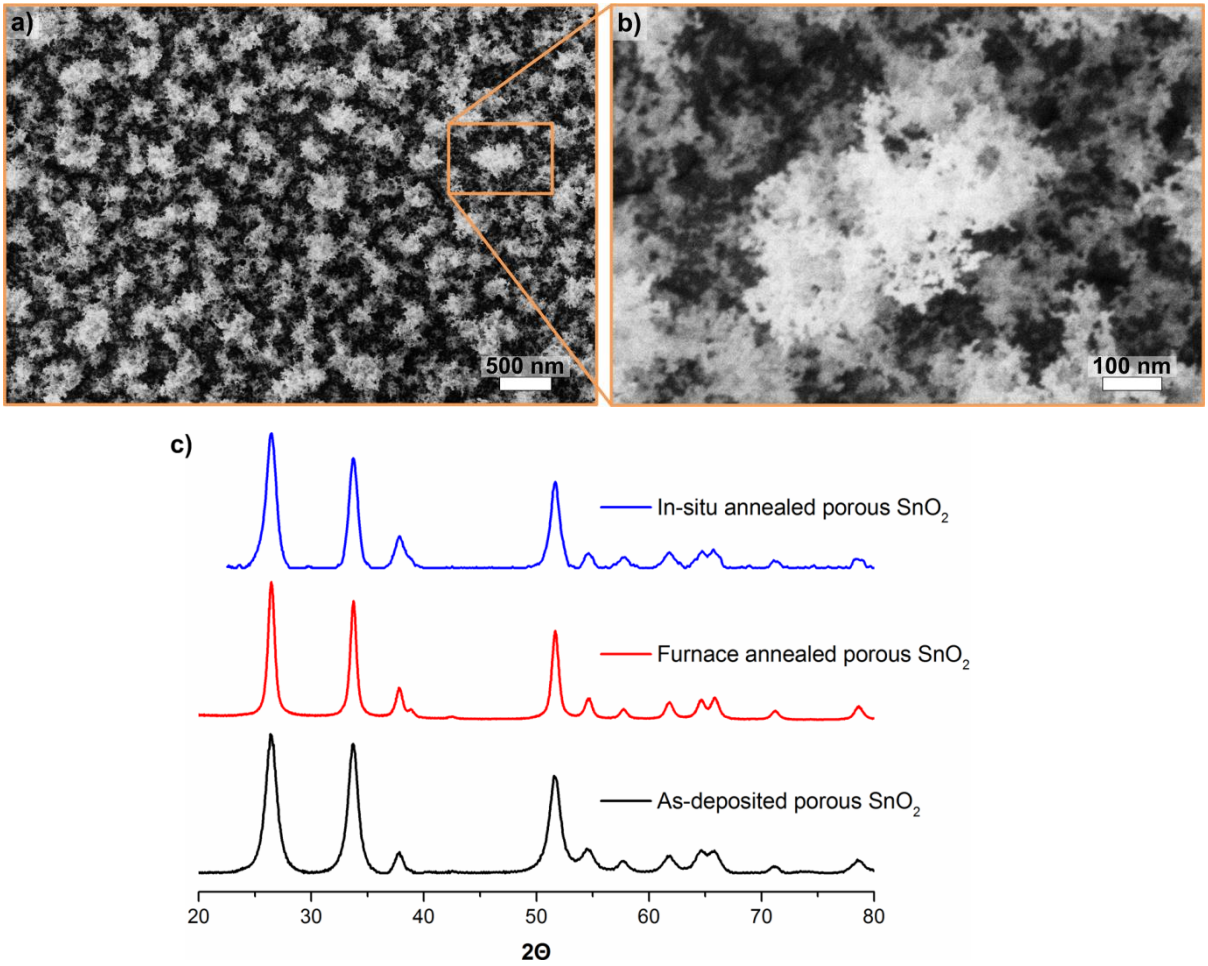

Figure 7.1 Top view image of a 400 nm thick as-deposited porous SnO_2 layer at a) low and b) high magnification by SEM. c) XRD spectra of the as-deposited flame-made porous SnO_2 layer and the in-situ and furnace annealed flame-made porous SnO_2 layer.

In-Situ Anneal

The in-situ anneal step consists of heating the as-deposited porous SnO_2 layer directly with a CH_4/O_2 xylene flame for a short period of time [153]. The in-situ anneal step was performed by placing the porous SnO_2 coated substrate at a distance of 13 cm from the flame aerosol nozzle as shown in Fig. 7.2a [153]. The CH_4/O_2 xylene flame from the nozzle came into direct contact with the porous SnO_2 layer for 10 seconds which decreased the thickness of the as-deposited porous SnO_2 layer by a factor of 5 as shown in Fig. 7.2b. In contrast, the furnace anneal step does not decrease the thickness of the as-deposited porous SnO_2 layer. The in-situ anneal step increased the mechanical stability of the porous SnO_2 layer by compacting and fusing its nanostructure as shown in Fig. 7.2c [153]. The in-situ annealed porous SnO_2 layer has a more compact, robust and thicker nanostructure than the as-deposited porous SnO_2

layer (Fig. 7.2c). As a result, the in-situ anneal step changed the porosity of the porous SnO_2 layer from 98% as-deposited to 60% after the in-situ anneal step [153]. In contrast, the furnace anneal step did not significantly change the nanostructure of the as-deposited porous SnO_2 layer.

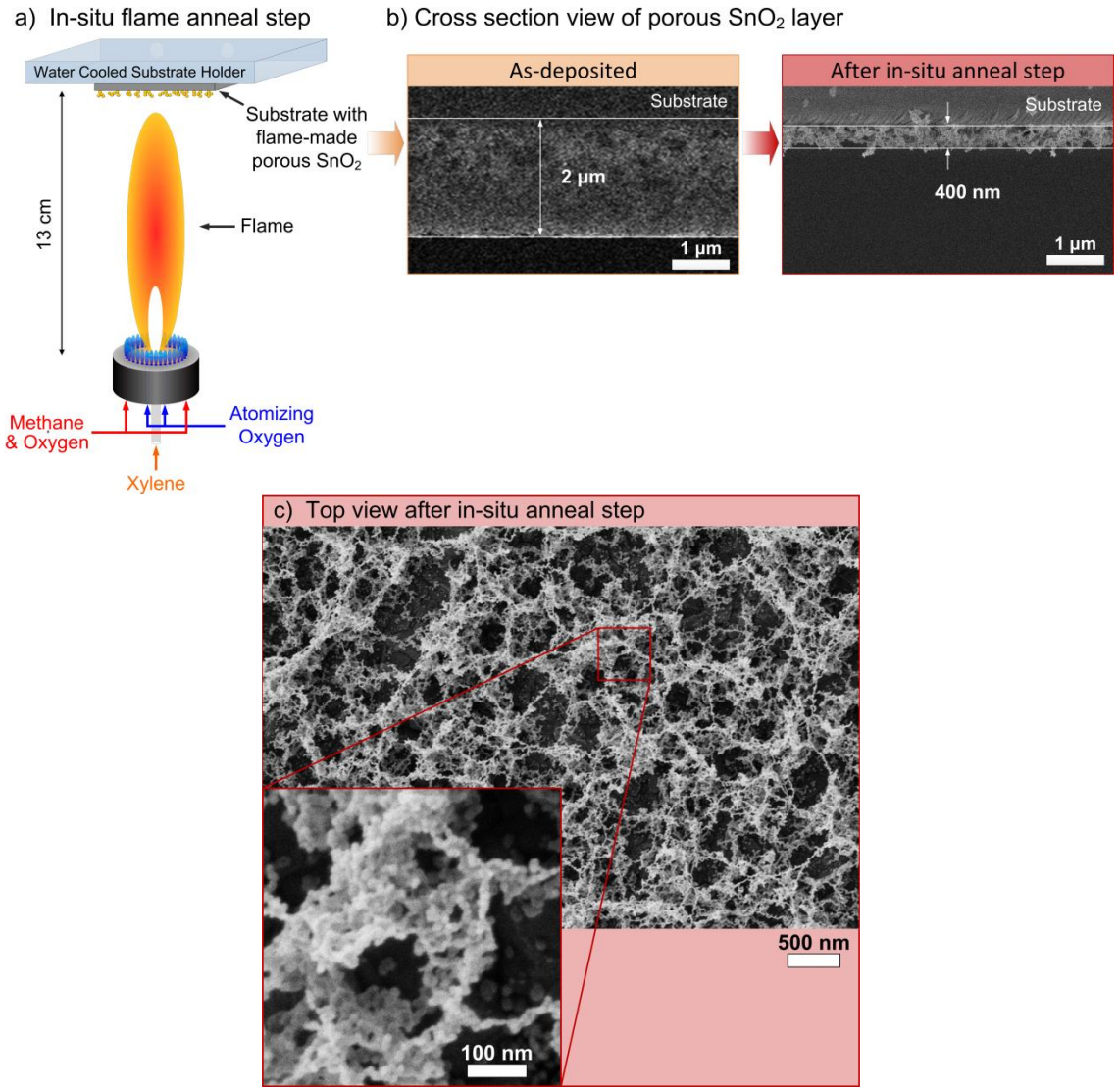

Figure 7.2 a) Schematic of the in-situ anneal step. b) Cross section images of the porous SnO_2 layer before and after the in-situ anneal step. c) Top view image of the in-situ annealed 400 nm thick porous SnO_2 layer.

$MAPbI_3$ solar cells were fabricated using three different thicknesses of the in-situ annealed porous SnO_2 layers: 150 nm, 300 nm and 400 nm. The cross section images of the corresponding $MAPbI_3$ solar cells are shown in Fig. 7.3a-c. A compact TiO_2 layer was used as part of the ETM matrix and spiro-OMeTAD as the HTM. For reasons mentioned previously in this Chapter, it was not possible to substitute the compact

TiO_2 layer with a compact SnO_2 layer. Nevertheless, the solar cells with the combined compact ALD TiO_2 layer and porous SnO_2 layer show promising results as discussed below.

The in-situ annealed porous SnO_2 layer can be seen as a coral-like structure as shown in Fig. 7.3a-c. The 150 nm thick in-situ annealed porous SnO_2 layer is fully covered by the $MAPbI_3$ layer as shown in Fig. 7.3a. However, the top branches of the 300 nm thick in-situ annealed porous SnO_2 layers seem to be extremely close to the top surface of the $MAPbI_3$ layer as shown in Fig. 7.3b. Meanwhile, the top branches of the 400 nm thick in-situ annealed porous SnO_2 layers seem to be at the same level as the top surface of the $MAPbI_3$ layer as shown in Fig. 7.3c.

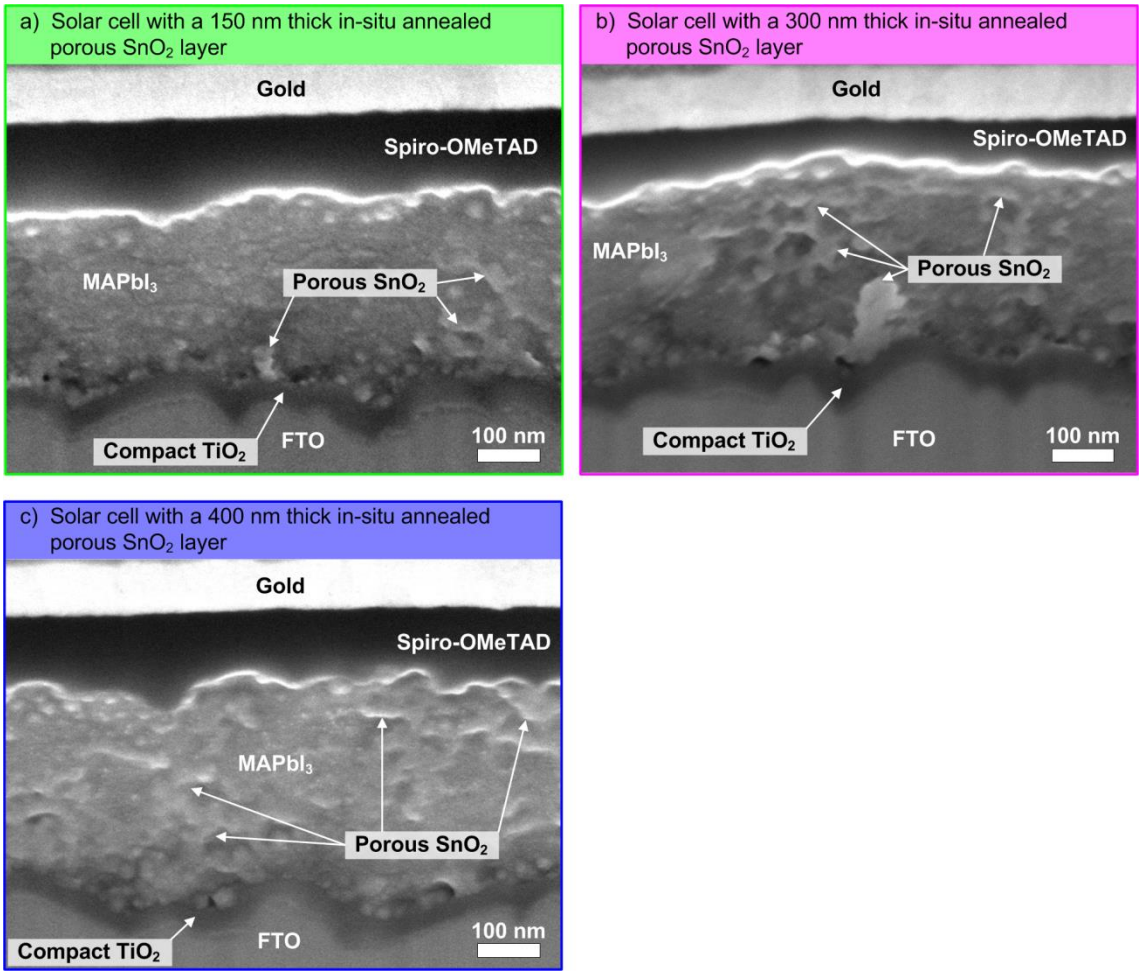

Figure 7.3 Cross section images of the $MAPbI_3$ solar cells with (a) 150 nm (b) 300 nm and (c) 400 nm thick in-situ annealed porous SnO_2 layer.

The measured J-V curves of the best solar cells and their absorptance are shown in Fig. 7.4a-b. The V_{OC}, FF, J_{SC} and efficiency of a batch of 12 $MAPbI_3$ solar cells as a

function of the in-situ annealed porous SnO_2 layer thickness are shown in Fig. 7.4c and Fig. 7.4d. In Figures 7.4c-d the symbols represent the average value and the horizontal bars the variation of the corresponding photovoltaic parameter of the corresponding batch of solar cells. The corresponding photovoltaic parameters of the best $MAPbI_3$ solar cells with an in-situ annealed porous SnO_2 layer are given in Table 7.1.

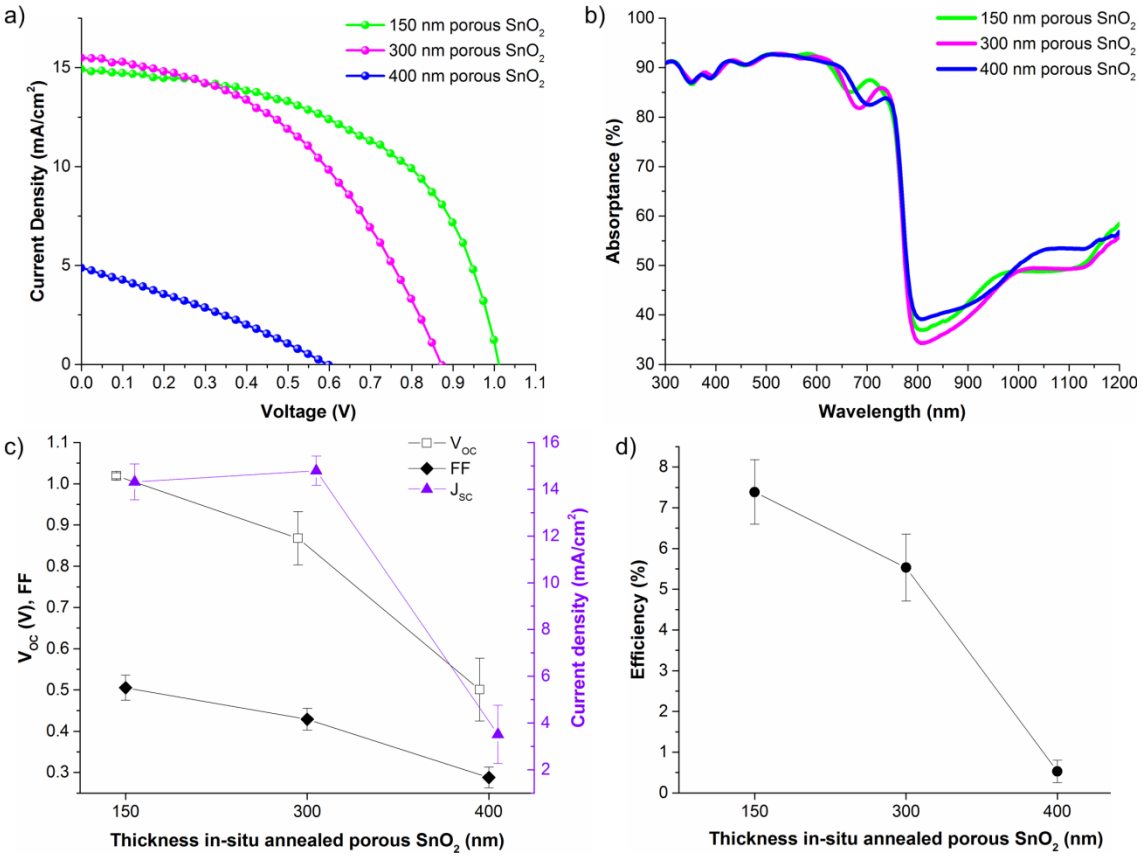

Figure 7.4 a) J-V curves of the best $MAPbI_3$ solar cells with an in-situ annealed porous SnO_2 layer. b) Absorptance as a function of wavelength of the best $MAPbI_3$ solar cells with an in-situ annealed porous SnO_2 layer. c) The V_{OC}, FF, J_{SC} and d) efficiency of the $MAPbI_3$ solar cells with the in-situ annealed porous SnO_2 nanostructured solar cells as a function of the porous SnO_2 layer thickness.

Table 7.1 Photovoltaic parameters of the $MAPbI_3$ perovskite solar cells with a 150 nm, 300 nm or 400 nm thick in-situ annealed porous SnO_2 layer.

Thickness in-situ annealed porous SnO_2 layer (nm)	V_{OC} (V)	J_{SC} (mA/cm^2)	FF	Efficiency (%)
150	1.012	14.7	0.54	8.0
300	0.872	15.5	0.45	6.1
400	0.596	4.9	0.30	0.9

The absorptance of the $MAPbI_3$ solar cells with the 150 nm, 300 nm and 400 nm thick in-situ annealed porous SnO_2 layers is fairly similar, as shown in Fig. 7.4b. Therefore, the differences in the photovoltaic parameters in Table 7.1 and Figs. 7.4a and 7.4c-d are due to recombination losses as discussed below.

As the thickness of the in-situ annealed porous SnO_2 layer is increased the V_{OC} of the relevant $MAPbI_3$ solar cells is decreased as shown in Table 7.1 and Figs. 7.4a and 7.4c. The decrease in V_{OC} is likely to originate from the increase of the contact area between the in-situ annealed porous SnO_2 layer and the spiro-OMeTAD layer as the thickness of the former increases as seen in Fig. 7.3a-c. The contact between the electrically active SnO_2 and the spiro-OMeTAD layer is a point of recombination for the photo-generated carriers. The $MAPbI_3$ solar cell with the thinnest (150 nm) in-situ annealed porous SnO_2 layer has a V_{OC} of 1.012 V that is comparable to the V_{OC} of a control $MAPbI_3$ solar cell with a spin-coated porous TiO_2 layer (1.026 ± 0.016 V), suggesting low recombination losses at open circuit.

The FF of the $MAPbI_3$ solar cells with the in-situ annealed porous SnO_2 layers is lower than with a porous TiO_2 layer because of the resistive losses at the interface between the compact TiO_2 layer and the porous SnO_2 layer. The resistance losses arise from the higher activation energy and resistivity of a SnO_2-TiO_2 composite compared with single SnO_2 or TiO_2 layers [228, 229]. The difference in the energy level of the conduction bands between TiO_2 and SnO_2 creates a relatively high energy barrier to the flow of photo-generated carriers from SnO_2 to TiO_2 [97, 164, 165, 228, 229]. Also the electron mobility of TiO_2 is 100 times smaller than that of SnO_2 which adds resistance to the flow of photo-generated carriers from the porous SnO_2 to compact TiO_2 layers [99-103, 229, 230]. Added to this, the FF is significantly decreased as the thickness of the porous SnO2 increases because of the aforementioned contact area between the porous SnO2 and spiro-OMeTAD layers. This detrimental contact area increases with the thickness of the porous SnO2 layer and has the effect of decreasing the shunt resistance and thus the FF of the solar cell.

The J_{SC} of the $MAPbI_3$ solar cells with the in-situ annealed porous SnO_2 layers is diminished by a low collection efficiency that is caused by the hampered transfer of photo-generated carriers from the porous SnO_2 layer to the compact TiO_2 layer. The

photo-generated carriers that have been transferred from the $MAPbI_3$ to the SnO_2 layer cannot transfer efficiently to the compact TiO_2 layer because of the difference in the energy levels of the conduction bands. The calculated energy band diagrams of TiO_2, SnO_2 and $MAPbI_3$ by Correa et al. (2015) are shown in Fig. 7.5. Correa et al. (2015) also observed a large reduction in J_{SC} caused by a relatively high energy barrier that inhibits the flow of the photo-generated carriers. This recombination loss mechanism could be eliminated by substituting the compact TiO_2 layer with a compact SnO_2 layer.

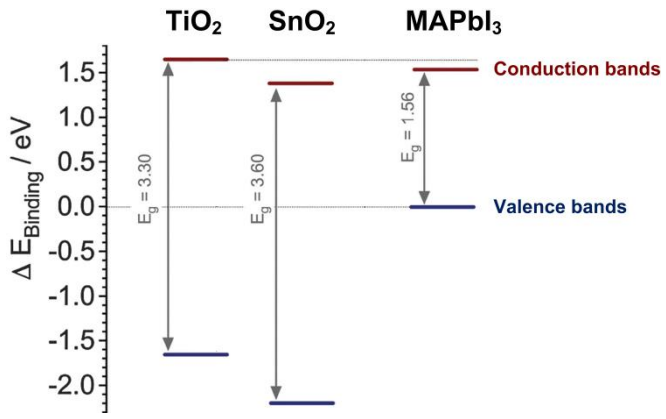

Figure 7.5 Calculated energy band diagram of TiO_2, SnO_2 and $MAPbI_3$ measured by UPS (adapted from Correa et al. 2015).

Additionally, J_{SC} could also be decreased in the $MAPbI_3$ solar cells with the thicker in-situ annealed porous SnO_2 layers because of recombination losses from the likely contact between the porous SnO_2 and spiro-OMeTAD. This recombination loss could be avoided by having a thicker perovskite capping layer on top of the porous SnO_2 layer. The proposed modifications to reduce both of the aforementioned recombination losses could significantly increase the J_{SC} and the FF and thus the efficiency of the $MAPbI_3$ solar cells with an in-situ annealed porous SnO_2 layer.

The following section discusses the photovoltaic performance of the $MAPbI_3$ solar cells with furnace annealed porous SnO_2 layers. The difference in porosity and nanostructure between the furnace annealed and in-situ annealed porous SnO_2 layers impacts the efficiency of the corresponding solar cells, as discussed next.

Furnace Anneal

As an alternative to the in-situ anneal step, a furnace anneal step can also improve the mechanical stability of the as-deposited porous SnO_2 layers by inter-particle sintering and grain boundary necking [151]. The morphology of the as-deposited porous SnO_2 layers is maintained after the furnace anneal step as shown in the test structures of Fig. 7.6a and Fig. 7.6c. The furnace anneal step does not compact the as-deposited porous SnO_2 layer, unlike the in-situ anneal step that reduced the thickness of the porous SnO_2 layer by a factor of 5. Therefore, the furnace anneal step did not reduce the 98% porosity of the as-deposited porous SnO_2 layer. The furnace anneal step provided enough mechanical stability to the porous SnO_2 layer to withstand the subsequent $MAPbI_3$ deposition as demonstrated by the test structures in Fig. 7.6b and Fig. 7.6d. The uppermost nanoparticles of a 500 nm thick furnace annealed porous SnO_2 layer can be seen protruding out of the $MAPbI_3$ layer in Fig. 7.6b. In contrast, a 150 nm thick furnace annealed porous SnO_2 layer was entirely covered by the $MAPbI_3$ layer as shown in Fig. 7.6d.

After testing the mechanical stability of the furnace annealed porous SnO_2 layers, 10 $MAPbI_3$ solar cells were fabricated with a 150 nm thick furnace annealed porous SnO_2 layer. The optimum thickness value of 150 nm for the furnace annealed porous SnO_2 layer was taken from the previously discussed $MAPbI_3$ solar cells with a 150 nm thick in-situ annealed porous SnO_2 layer.

The J-V curve of the best $MAPbI_3$ solar cell with a 150 nm thick furnace annealed porous SnO_2 layer with its corresponding photovoltaic parameters is shown in Fig. 7.7a. The average absorptance as a function of wavelength of the entire batch of 10 $MAPbI_3$ solar cells with a 150 nm thick furnace annealed porous SnO_2 layer is shown in Fig. 7.7b. The V_{OC}, FF, J_{SC} and efficiency of a batch of 10 $MAPbI_3$ solar cells with a 150 nm thick furnace annealed porous SnO_2 layer are shown in Fig. 7.7c. In Figure 7.7c the symbols represent the average value and the horizontal bars the variation of the corresponding photovoltaic parameter of the batch of 10 solar cells.

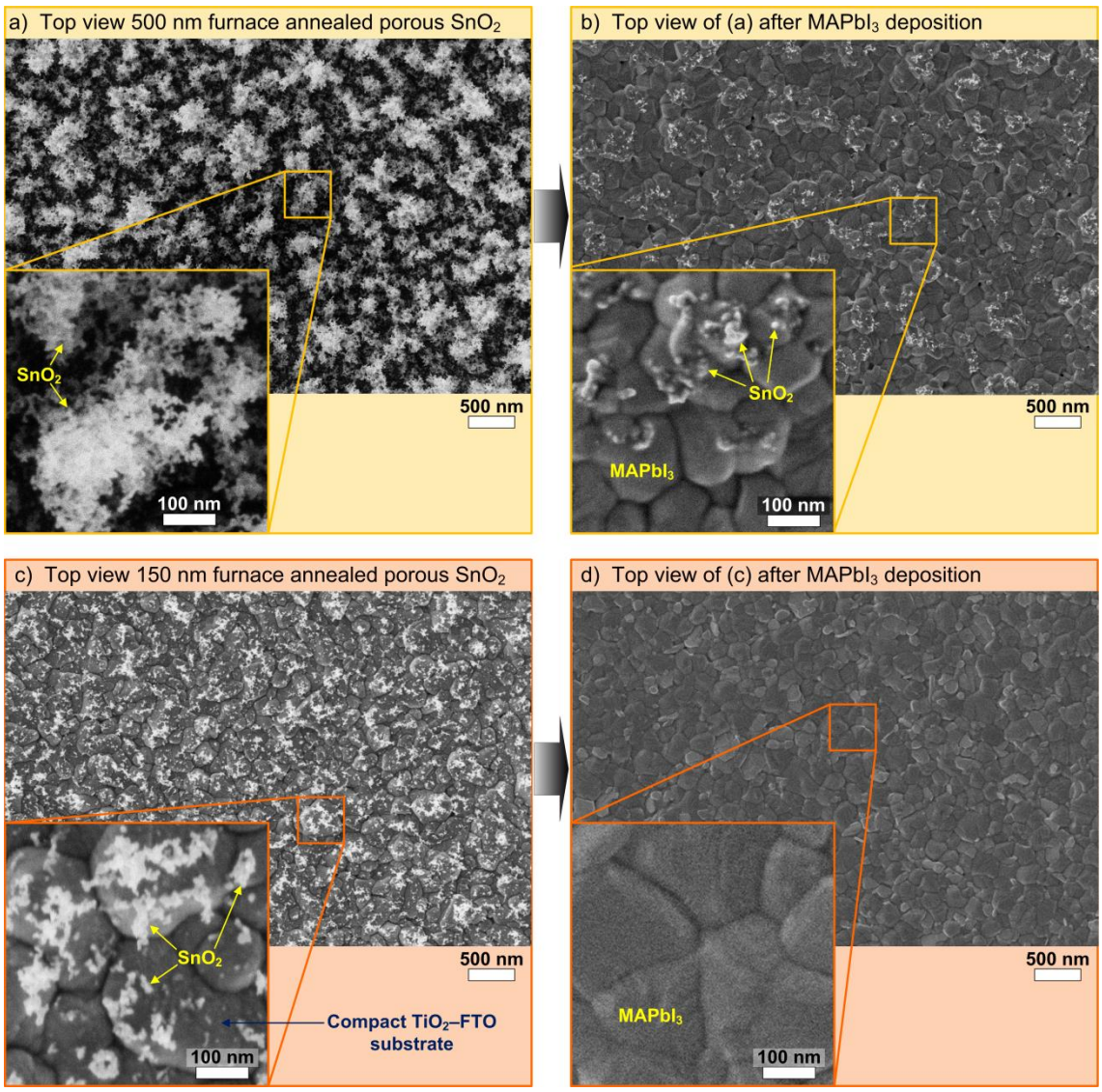

Figure 7.6 a) Top view image of a 500 nm thick furnace annealed porous SnO_2 layer. b) Top view image of the same film as in (a) but after the deposition of the $MAPbI_3$ layer. c) Top view of 150 nm after furnace anneal step and d) top view of the same film as in (c) but after the deposition of the $MAPbI_3$ layer.

The mean J_{SC} value of the $MAPbI_3$ solar cells with a 150 nm thick furnace annealed porous SnO_2 layer is higher than that of the $MAPbI_3$ solar cells with a 150 nm thick in-situ annealed porous SnO_2. This is attributed to the higher porosity of the furnace annealed porous SnO_2 layer. A higher porosity means a smaller overall contact area between the compact TiO_2 and the porous SnO_2 layer which minimises the detrimental effect on J_{SC} from the hindered transfer of carriers from the SnO_2 to the TiO_2 layer. However, planar $MAPbI_3$ solar cells with only a compact TiO_2 layer (without the porous SnO_2 layer) were fabricated and found to have a lower J_{SC}, FF and efficiency. The best

efficiency obtained for a planar $MAPbI_3$ solar cell with only a compact TiO_2 layer was 3.5% with a V_{OC} of 1.024 V, J_{SC} of 8 mA/cm^2 and FF of 0.43. It has been reported elsewhere that generally only pre-conditioned planar $MAPbI_3$ solar cells with a compact TiO_2 layer show a J_{SC} comparable to those using a porous TiO_2 layer [97, 231, 232]. The 150 nm thick porous SnO_2 layer improved the J_{SC} without the need of device pre-conditioning. The porous SnO_2 could have increased J_{SC} by increasing the collection of the photo-generated carriers within the $MAPbI_3$ layer; although further investigation is required to support this possibility.

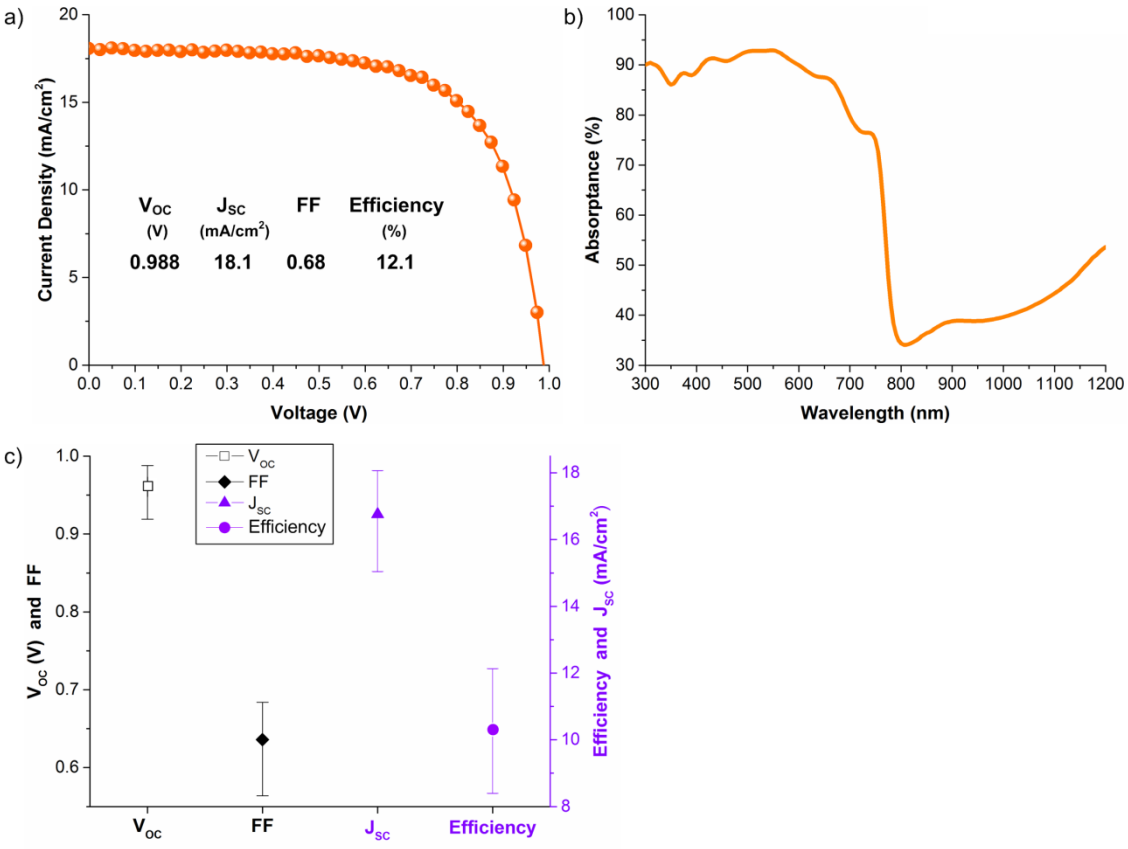

Figure 7.7 a) J-V curve of the best $MAPbI_3$ solar cell with a 150 nm thick furnace annealed porous SnO_2 layer. b) Average absorptance as a function of wavelength of the $MAPbI_3$ solar cells with a 150 nm thick furnace annealed porous SnO_2 layer. c) V_{OC}, FF, J_{SC} and efficiency of a batch of 10 $MAPbI_3$ solar cells with a 150 nm thick furnace annealed porous SnO_2 layer.

The mean V_{OC} of the $MAPbI_3$ solar cells with a 150 nm thick furnace annealed porous SnO_2 is lower than that of the $MAPbI_3$ solar cells with a 150 nm thick in-situ annealed porous SnO_2 layer. Moreover, the variation in V_{OC} is much larger for the solar cells with

the furnace annealed porous SnO_2 than with the in-situ annealed porous SnO_2 layer. The larger variation and lower V_{OC} could be attributed to the mechanical stability of the furnace annealed porous SnO_2 layer which may not be enough to entirely withstand the deposition of the $MAPbI_3$ layer. A few nanoparticles or branches of the furnace annealed porous SnO_2 layer might partially or entirely detach from the main porous SnO_2 nanostructure. These unattached nanoparticles would be a source of recombination that decreases the V_{OC}. However, the mechanical stability has not been quantified.

The mean FF of the $MAPbI_3$ solar cells with the 150 nm thick furnace annealed porous SnO_2 layers is higher than that of the $MAPbI_3$ solar cells with a 150 nm thick in-situ annealed porous SnO_2 layer. This could be attributed to a lower resistance to the flow of photo-generate carriers from the SnO_2 to the TiO_2 layer. The lower resistance may come from the higher porosity of the furnace annealed porous SnO_2 layer which means a smaller overall contact area between the TiO_2 and the SnO_2 layer.

There is a large variation in the FF, J_{SC}, V_{OC} and thus in the efficiency as can be seen in Fig. 7.7c. The large variation in the photovoltaic parameters could be attributed to the sub-optimal mechanical stability of the furnace annealed porous SnO_2 layer to withstand the $MAPbI_3$ deposition. As previously mentioned, the sub-optimal mechanical stability could lead to a partial or entire detachment of nanoparticles or branches of the furnace annealed porous SnO_2 layer. Further increase of the mechanical stability could be attained by coating the as-deposited porous SnO_2 layer with a compact ALD SnO_2 layer prior to the furnace anneal step. These results with the porous SnO_2 layer for $MAPbI_3$ solar cells are promising as there is scope for improvement.

Conclusion

The mechanical stability of the as-deposited porous SnO_2 layer can be increased with either a furnace or an in-situ anneal step. Both anneal steps produce stabilised porous SnO_2 layers with different nanostructures. The in-situ anneal step compresses the as-deposited porous SnO_2 layer and decreases its thickness by a factor of 5. In contrast,

the furnace anneal step does not compress the as-deposited porous SnO_2 layer. The $MAPbI_3$ solar cells made with the in-situ annealed porous SnO_2 layer had a highest efficiency of 8% that was mainly limited by a low FF and J_{SC} caused by resistance and collection losses from the transfer of carriers from the SnO_2 to the TiO_2 layer. The V_{OC} of the best $MAPbI_3$ solar cell with an in-situ annealed porous SnO_2 was as high as the V_{OC} from the control $MAPbI_3$ solar cells with a spin-coated porous TiO_2 layer. This similarity in V_{OC} suggests low recombination losses in the former solar cell. In contrast, the $MAPbI_3$ solar cells with a furnace annealed porous SnO_2 layer had a highest efficiency of 12%. This higher efficiency was a result of an improvement in the J_{SC} and FF of the $MAPbI_3$ solar cells with a furnace annealed porous SnO_2 layer. The improvement in J_{SC} and FF was attributed to the high 98% porosity of the furnace annealed porous SnO_2 layer. There is scope for further improvement of the efficiencies of the solar cells discussed above. A compact ALD SnO_2 layer to substitute the compact TiO_2 layer and a thicker $MAPbI_3$ capping layer could significantly improve the J_{SC} and FF of the solar cells reported here. The inclusion of a compact ALD SnO_2 layer instead of the compact TiO_2 layer could also permit a useful comparison between a full SnO_2 and a full TiO_2 solar cell. Regardless, the flame-made porous SnO_2 layer has the advantage of rapid manufacture that could be integrated into an on-line continuous production system. Plus, the deposition and annealing of the porous SnO_2 could also be performed continuously in the same production line as the FTO and the compact ETM layer.

8. Conclusion

The research discussed in this body of work aims to improve the performance and lower the cost of Sb_2S_3 and $MAPbI_3$ solar cells. Furthermore, the practical results achieved in this work can be applied to advance other sulphur-based and mixed perovskite solar cells.

The goal of the Sb_2S_3 research work was to contribute towards making a low-cost fully inorganic high-efficiency solar cell. Inorganic materials tend to be more stable, cost less and last longer than organic materials. The inorganic material Sb_2S_3 is a chalcogenide absorber with a bandgap of 1.7 eV that could theoretically make low-cost high-efficiency (≈ 25%) solar cells [32, 33, 233]. However, at present the highest reported Sb_2S_3 solar cell efficiency remains low (≤ 7.5%) [54]. The large amount of recombination within Sb_2S_3 itself is the current major limitation for higher efficiencies [59, 60, 62, 115]. The recombination within Sb_2S_3 has previously been attributed [62, 115] to states within its bandgap that could be a result of bulk and surface defects such as dangling bonds, vacancies or substitutional defects [60, 62, 115].

In order to gain a deeper insight into the origin of the Sb_2S_3 recombination losses, the research reported here compared fully inorganic planar Sb_2S_3 solar cells using two different deposition methods for the active layer, while keeping all other cell parameters identical. The thermally evaporated Sb_2S_3 solar cells had a 2-fold increase in efficiency compared to solution deposited Sb_2S_3 solar cells. The IQE was higher for the evaporated Sb_2S_3 solar cells, suggesting longer diffusion lengths in the Sb_2S_3 layer. The preferred crystal plane orientation was different for the evaporated and solution deposited Sb_2S_3 layers, and the grain sizes were about 30% larger in the evaporated Sb_2S_3 layers. Both of these factors result in an increased effective carrier diffusion length in the evaporated Sb_2S_3 layers. The reduction of the recombination losses was attributed to Sb_2S_3 with particular crystal planes. The previously reported lower resistivity and higher mobility along the c-axis of Sb_2S_3 is consistent with the better transport properties of the preferential crystal planes of the evaporated Sb_2S_3 reported here [105]. Additionally, a perfectly planar top Sb_2S_3 surface with an underlying textured (non-planar) substrate was obtained from a sulphur-rich Sb_2S_3 film. The evaporated Sb_2S_3 layer was sulphur rich, which results in the film flattening during the

300°C annealing step. A top flat Sb_2S_3 surface allows the deposition of a thin and uniform HTM layer thus improving the photovoltaic performance by minimising the resistance of the HTM layer and reducing the likelihood of shunts. In contrast, the solution deposited Sb_2S_3 layer is sulphur deficient and does not become planar during the annealing step. These findings provide practical strategies to reduce the recombination losses and improve the efficiency of Sb_2S_3 and other sulphur-based solar cells.

At present, the thickness of a Sb_2S_3 layer for a planar solar cell has to be ≤ 100 nm because of its short diffusion length (≤ 80 nm) [62, 70, 181]. For this reason, a micrometre thick porous TiO_2 layer coated with a 1 nm to 10 nm thick Sb_2S_3 layer is used to make Sb_2S_3 solar cells with a higher J_{SC} and thus higher efficiency [55, 64, 70]. The porous TiO_2 layer increases the effective area of the solar cell, the light absorption and the collection of photo-generated carriers [37]. The micrometre thick porous TiO_2 layer for Sb_2S_3 solar cells is typically screen-printed and has 50% to 60% porosity [55, 57, 58, 61]. However, solar cells with a porous TiO_2 layer can have resistance and recombination losses from the incomplete pore filling by the HTM [47]. Incomplete infiltration of the HTM in the porous TiO_2 layer can hamper the efficiency of the solar cell as the maximum attainable effective contact area is reduced.

In order to enhance the HTM infiltration, porous TiO_2 layers with 97% porosity were fabricated using a house-made flame aerosol system. The mechanical stability of the flame-made porous TiO_2 layers was increased with 10 nm of a compact ALD TiO_2 layer to prevent its disintegration upon the subsequent solar cell fabrication processes. Fully inorganic Sb_2S_3 solar cells were made with flame-made porous TiO_2 layers. The higher porosity of the flame-made porous TiO_2 layer facilitated the infiltration of the Sb_2S_3 and CuSCN thereby increasing the effective active area of the solar cell. Improved infiltration of the Sb_2S_3 and CuSCN into the porous TiO_2 layer results in a higher collection efficiency and a larger J_{SC}. However, the higher attainable J_{SC} and efficiency of the Sb_2S_3 solar cells with a flame-made porous TiO_2 layer was significantly diminished by the effects of a low shunt resistance. The low shunt resistance originated from having a thin CuSCN capping layer (≤ 500 nm) and the non-uniform top surface of the flame-made porous TiO_2 layer. This combination of factors enabled shunts to be formed by the direct contact of the gold layer with the flame-made

porous TiO_2 layer. As well as decreasing the J_{SC}, the low shunt resistance also decreased the V_{OC} and FF of such solar cells. A few micrometres thick CuSCN capping layer is required to avoid the likelihood of shunts because of the extremely thin Sb_2S_3 layer (1 nm to 10 nm) that coats a micrometres thick non-uniform flame-made porous TiO_2 layer.

High efficiency (≥ 20%) perovskite solar cells also have a porous TiO_2 layer which has a thickness of 150 nm to 250 nm and is deposited by spin-coating [89, 93, 96]. However, this 150 nm to 250 nm spin-coated porous TiO_2 layer can be a bottleneck for the low-cost production of such solar cells because spin-coating is not a high-throughput large-area production method. The deposition of a thin flame-made TiO_2 layer can be done in a few seconds over large areas as part of a continuous production process which could contribute to lowering the production cost of perovskite solar cells. The deposition of a flame-made porous TiO_2 layer can be incorporated into the high-throughput fabrication line of the spray-coated FTO and compact TiO_2 layer. With this in mind, $MAPbI_3$ solar cells with a thick flame-made porous TiO_2 layer were fabricated and optimised.

The porosity of the as-deposited flame-made TiO_2 layers was 97% which was then decreased to 87%, 56% and 35% by coating it with a compact ALD TiO_2 layer with thicknesses of 2 nm, 5 nm and 10 nm respectively. The compact ALD TiO_2 layer also provided enough mechanical stability for the flame-made porous TiO_2 layer to remain intact during the $MAPbI_3$ deposition step. The highest efficiency of 13.7% was obtained for a $MAPbI_3$ solar cell with a 300 nm thick flame-made porous TiO_2 layer with 87% porosity. This efficiency is already comparable to that of the control $MAPbI_3$ solar cell with a standard spin-coated porous TiO_2 layer. The high porosity of the flame-made TiO_2 porous layer facilitated the deeper infiltration of the $MAPbI_3$ layer compared to spin-coated TiO_2 porous layers. The deeper infiltration of $MAPbI_3$ into the porous TiO_2 layer could improve the photo-generated current by increasing the collection efficiency. However, the main efficiency limitation of the $MAPbI_3$ solar cells with a flame-made porous TiO_2 layer was the detrimental contact between the HTM and the flame-made porous TiO_2 layer [81, 82]. The high porosity and the hierarchical morphology of the flame-made porous TiO_2 layer hindered the formation of a $MAPbI_3$ capping layer. However, thicker $MAPbI_3$ layers may not improve the efficiency because

$MAPbI_3$ has a short diffusion length [234]. Consequently, a thicker mixed perovskite layer could be used to further improve this efficiency.

At present, perovskite solar cells suffer from hysteresis and long term stability issues [87, 92, 189, 232, 235]. This issue has been partly linked to the oxygen desorption within the TiO_2 upon UV illumination [92]. Stability is a requirement for any commercial solar cell. The issues associated with TiO_2 can be eliminated by replacing it with SnO_2, which is less reactive to UV light and has a higher mobility and conductivity than TiO_2 [99-103, 165, 214]. With this in mind, $MAPbI_3$ solar cells with a flame-made SnO_2 porous layer were also made and investigated. The optimised $MAPbI_3$ solar cells with a 150 nm thick flame-made porous SnO_2 layer with a 98% and 60% porosity had efficiencies of 8% and 12% respectively. The main limitation for a higher efficiency was the hampered flow of photo-generated carriers from the porous SnO_2 layer to the compact TiO_2 layer which decreased the FF and J_{SC} of these solar cells. These are promising results as there is scope for improvement by substituting all the TiO_2 with SnO_2. It should be noted that at the time of this work, it was not possible to substitute the compact ALD TiO_2 layer with a compact ALD SnO_2 layer because the ALD system had a malfunction that rendered the SnO_2 reactant un-usable.

Future Work

The practical results from this work are promising because there is scope for further advances and research opportunities. Maximising the Sb_2S_3 crystal planes perpendicular to the substrate or the proportion of $(Sb_2S_3)_n$ ribbons perpendicular to the substrate could further enhance the efficiency of a planar Sb_2S_3 solar cell. This could be achieved by optimising the pressure, temperature and deposition rate during the deposition of the Sb_2S_3 layer [236, 237]. The efficiency of planar solar cells with a Sb_2S_3 layer with preferential crystal planes could be further improved by sulphurisation and the use an organic HTM. The low shunt resistance of the fully inorganic Sb_2S_3 solar cells with a flame-made porous TiO_2 layer could be improved by depositing a few micrometres thick CuSCN capping layer (though at the cost of increasing the series resistance) [59]. The efficiency of this solar cell could also be improved by using another HTM, such as P3HT, that has a better conductivity than CuSCN [45, 83]. In combination with the aforementioned improvement strategies, the thickness of the

flame-made porous TiO_2 layer could be reduced to minimise the volume of the HTM, albeit at the cost of decreasing the effective active area coated with Sb_2S_3 and thus J_{SC}. Further improvements could be achieved with sulphurisation, another ETM such as SnO_2 and interface engineering [54, 64, 165, 238]. Overall however, the theoretical high efficiencies of the Sb_2S_3 solar cells are still mainly limited by the Sb_2S_3 itself because at this point in time the deposited Sb_2S_3 material has a short diffusion length and intrinsic high recombination losses [62, 115].

The efficiency of perovskite solar cells with a flame-made porous TiO_2 or SnO_2 layer could be improved by using mixed perovskites. The efficiency of $MAPbI_3$ solar cells with a flame-made porous SnO_2 layer reported here could be increased by substituting the compact TiO_2 layer with a compact SnO_2 layer. Also, perovskite solar cell with flame-made porous layers of WO_x, ZnO, MoO_x could be investigated. Large area perovskite solar cells with a flame-made porous ETM layer could be developed incrementally. The mechanical stability of the flame-made porous ETM layers could also be increased via CVD systems. A pilot continuous production line for the TCO, compact and porous ETM layers could be tested. Other spray coating systems for high-throughput deposition of porous ETM layers could also be investigated.

Furthermore, the practical results from this work can also be applied to other devices and materials; particularly for sulphur-based materials where it is possible to deposit a sulphur-rich film and for devices that require a porous oxide layer.

Bibliography

1. *2014: Summary for Policymakers*, in *Climate Change 2014 Synthesis Report* 2014, Cambridge University Press: Cambridge, United Kingdom.
2. Stocker, T.F., D. Qin, G.-K. Plattner, M. Tignor, S.K. Allen, J. Boschung, A. Nauels, Y. Xia, V. Bex and P.M. Midgley (eds.), *2013: Summary for Policymakers*, in *Climate Change 2013: The Physical Science Basis. Contribution of Working Group I to the Fifth Assessment Report of the Intergovernmental Panel on Climate Change*. 2013, Cambridge University Press: Cambridge.
3. Field, C.B., V.R. Barros, D.J. Dokken, K.J. Mach, M.D. Mastrandrea, T.E. Bilir, M. Chatterjee, K.L. Ebi, Y.O. Estrada, R.C. Genova, B. Girma, E.S. Kissel, A.N. Levy, S. MacCracken, P.R. Mastrandrea, and L.L. White (eds.), *2014: Summary for policymakers.*, in *Climate Change 2014: Impacts, Adaptation, and Vulnerability. Part A: Global and Sectoral Aspects. Contribution of Working Group II to the Fifth Assessment Report of the Intergovernmental Panel on Climate Change*. 2014, Cambridge University Press: Cambridge, United Kingdom. p. 34.
4. Edenhofer, O., R. Pichs-Madruga, Y. Sokona, E. Farahani, S. Kadner, K. Seyboth, A. Adler, I. Baum, S. Brunner, P. Eickemeier, B. Kriemann, J. Savolainen, S. Schlömer, C. von Stechow, T. Zwickel and J.C. Minx (eds.), *2014: Summary for Policymakers*, in *Climate Change 2014: Mitigation of Climate Change. Contribution of Working Group III to the Fifth Assessment Report of the Intergovernmental Panel on Climate Change*. 2014, Cambridge University Press: Cambridge, United Kingdom. p. 32.
5. Sturrock, P., ed. *Physics of the Sun* 1986, Kluwer Academic Publishers: Boston.
6. National Renewable Energy Laboratories, *Solar Spectra*. [cited 2016 10 May]; Available from: http://rredc.nrel.gov/solar/spectra/.
7. Green Rhino Energy, *Defining standard spectra for solar panels*. 2013 [cited 2016 10 May]; Available from: http://www.greenrhinoenergy.com/solar/radiation/spectra.php.
8. Newport Corporation, *Introduction to Solar Radiation*. 2016 [cited 2016 12 May]; Available from: http://www.newport.com/Introduction-to-Solar-Radiation/411919/1033/content.aspx.
9. International Energy Agency, *Key World Energy Statistics*. 2015, OECD/IEA. p. 81.
10. Blakers, A., *Sustainable Energy Options.* Asian Perspective, 2015. **39**(4): p. 559-589.
11. Tesla Motors, *PowerWall Tesla Home Battery* 2016 [cited 2016 12 May]; Available from: https://www.teslamotors.com/en_AU/powerwall.
12. The Global Energiewende, *Energy Transition* [cited 2016 11 May]; Available from: http://energytransition.de/.
13. Statista, *Global solar PV manufacturing market size from 2000 to 2013 (in billion U.S. dollars)* The Statistics Portal 2016 [cited 2016 12 May]; Available from: http://www.statista.com/statistics/232859/global-solar-pv-market-size/.
14. International Energy Agency, *Technology Roadmap Solar Photovoltaic Energy*. 2014, p. 60.
15. Fraunhofer Institute for Solar Energy Systems, *Global Cumulative Photovoltaic Installation until 2014* in *Photovoltaic Report*. 2016, ISE with support of PSE AG. p. 43.

16. Martinot, E. *Renewable Energy Market Indicators and References*. Renewable Energy Information on Markets, Policy, Investment, and Future Pathways 2005 [cited 2016 19 March]; Available from: http://www.martinot.info/markets.htm.
17. Statista. *Global cumulative installed solar PV capacity 2015 | Statistic*. 2015 [cited 2016 19 March]; Available from: http://www.statista.com/statistics/280220/global-cumulative-installed-solar-pv-capacity/.
18. International Energy Agency Photovoltaic Power Systems Programme, *2014 Snapshot of Global PV Markets 2014 Photovoltaic Power Systems Programme*. 2015: International Energy Agency. 16.
19. Battaglia, C., A. Cuevas, and S. De Wolf, *High-efficiency crystalline silicon solar cells: status and perspectives.* Energy Environ. Sci., 2016. **9**(5): p. 1552-1576.
20. Green, M.A., et al., *Solar cell efficiency tables (version 47).* Progress in Photovoltaics: Research and Applications, 2016. **24**(1): p. 3-11.
21. Shah, A.V., et al., *Basic efficiency limits, recent experimental results and novel light-trapping schemes in a-Si:H, µc-Si:H and `micromorph tandem' solar cells.* Journal of Non-Crystalline Solids, 2004. **338-340**: p. 639-645.
22. Cester, A., et al., *Degradation mechanisms of Dye-Sensitized Solar Cells: Light, Bias and Temperature Effects.* 2015 Ieee International Reliability Physics Symposium (Irps), 2015.
23. Guerrero, A., et al., *Nanoscale mapping by electron energy-loss spectroscopy reveals evolution of organic solar cell contact selectivity.* Organic Electronics, 2015. **16**: p. 227-233.
24. Lal, N.N., T.P. White, and K.R. Catchpole, *Optics and Light Trapping for Tandem Solar Cells on Silicon.* IEEE Journal of Photovoltaics, 2014. **4**(6): p. 1380-1386.
25. Albrecht, S., et al., *Monolithic perovskite/silicon-heterojunction tandem solar cells processed at low temperature.* Energy Environ. Sci., 2016. **9**(1): p. 81-88.
26. Martí, A. and G.L. Araújo, *Limiting efficiencies for photovoltaic energy conversion in multigap systems.* Solar Energy Materials and Solar Cells, 1996. **43**(2): p. 203-222.
27. Werner, J., et al., *Efficient Monolithic Perovskite/Silicon Tandem Solar Cell with Cell Area >1 cm(2).* J Phys Chem Lett, 2016. **7**(1): p. 161-6.
28. Gifford, J. *Solar Frontier hits 22.3% on CIGS cell*. PV Magazine 2015 2016 [cited 2016 10 May 2016]; Available from: http://www.pv-magazine.com/news/details/beitrag/solar-frontier-hits-223-on-cigs-cell_100022342/#axzz48cC1nYhr.
29. Aspnes, D.E. and A.A. Studna, *Dielectric functions and optical parameters of Si, Ge, GaP, GaAs, GaSb, InP, InAs, and InSb from 1.5 to 6.0 eV.* Physical Review B, 1983. **27**(2): p. 985-1009.
30. ElAnzeery, H., et al., *Refractive index extraction and thickness optimization of Cu2ZnSnSe4thin film solar cells.* physica status solidi (a), 2015. **212**(9): p. 1984-1990.
31. Green, M.A., *Self-consistent optical parameters of intrinsic silicon at 300K including temperature coefficients.* Solar Energy Materials and Solar Cells, 2008. **92**(11): p. 1305-1310.
32. Shockley, W. and H.J. Queisser, *Detailed Balance Limit of Efficiency of p-n Junction Solar Cells.* Journal of Applied Physics, 1961. **32**(3): p. 510.
33. Bowden, C.H.a.S. *PVEducation PVCDROM*. 2014 [cited 2016 19 March 2016]; Available from: http://www.pveducation.org/pvcdrom.

34. Chapin, D.M., C.S. Fuller, and G.L. Pearson, *A New Silicon p-n Junction Photocell for Converting Solar Radiation into Electrical Power.* Journal of Applied Physics, 1954. **25**(5): p. 676.
35. Rappaport, P., *The photovoltaic effect and its utilization.* Solar Energy, 1959. **3**(4): p. 8-18.
36. Reynolds, D., et al., *Photovoltaic effect in cadmium sulfide.* Physical Review, 1954. **96**(2): p. 533.
37. O'regan, B. and M. Grätzel, *Low cost and highly efficient solar cells based on dye-sensitized colloidal TiO2 films.* Nature, 1991. **335**(24): p. 737-740.
38. Chandiran, A.K., M.K. Nazeeruddin, and M. Grätzel, *The Role of Insulating Oxides in Blocking the Charge Carrier Recombination in Dye-Sensitized Solar Cells.* Advanced Functional Materials, 2014. **24**(11): p. 1615-1623.
39. Chandiran, A.K., et al., *Subnanometer Ga2O3 tunnelling layer by atomic layer deposition to achieve 1.1 V open-circuit potential in dye-sensitized solar cells.* Nano Lett, 2012. **12**(8): p. 3941-7.
40. Mathew, S., et al., *Dye-sensitized solar cells with 13% efficiency achieved through the molecular engineering of porphyrin sensitizers.* Nat Chem, 2014. **6**(3): p. 242-7.
41. Vogel, R., P. Hoyer, and H. Weller, *Quantum-sized PbS, CdS, Ag2S, Sb2S3, and Bi2S3 particles as sensitizers for various nanoporous wide-bandgap semiconductors.* The Journal of Physical Chemistry, 1994. **98**(12): p. 3183-3188.
42. Ren, Z., et al., *Amorphous TiO2Buffer Layer Boosts Efficiency of Quantum Dot Sensitized Solar Cells to over 9%.* Chemistry of Materials, 2015. **27**(24): p. 8398-8405.
43. Tennakone, K., et al., *A dye-sensitized nano-porous solid-state photovoltaic cell.* Semiconductor Science and Technology, 1995. **10**(12): p. 1689.
44. O'Regan, B. and D.T. Schwartz, *Efficient dye-sensitized charge separation in a wide-band-gap p-n heterojunction.* Journal of Applied Physics, 1996. **80**(8): p. 4749.
45. Kumara, G.R.R.A.K., A.; Senadeera, G. K. R.; Jayaweera, P. V. V.; De Silva, D. B. R. A.; Tennakone, K., *Dye-sensitized solar cell with the hole collector p-CuSCN deposited from a solution in n-propyl sulphide.* Solar Energy Materials & Solar Cells, 2001. **69**: p. 195–199.
46. Bach, U., et al., *Solid-state dye-sensitized mesoporous TiO2 solar cells with high photon-to-electron conversion efficiencies.* Nature, 1998. **395**(6702): p. 583-585.
47. Ding, I.K., et al., *Pore-Filling of Spiro-OMeTAD in Solid-State Dye Sensitized Solar Cells: Quantification, Mechanism, and Consequences for Device Performance.* Advanced Functional Materials, 2009. **19**(15): p. 2431-2436.
48. Kron, G., et al., *Electrical characterisation of dye sensitised nanocrystalline TiO2 solar cells with liquid electrolyte and solid-state organic hole conductor.* Thin Solid Films, 2002. **403**: p. 242-246.
49. Carey, G.H., et al., *Record Charge Carrier Diffusion Length in Colloidal Quantum Dot Solids via Mutual Dot-To-Dot Surface Passivation.* Adv Mater, 2015. **27**(21): p. 3325-30.
50. Tennakone, K., et al., *Nanoporous n-TiO2/selenium/p-CuCNS photovoltaic cell.* Journal of Physics D: Applied Physics, 1998. **31**(18): p. 2326-2330.

51. Jackson, P., et al., *Effects of heavy alkali elements in Cu(In,Ga)Se2 solar cells with efficiencies up to 22.6%.* physica status solidi (RRL) - Rapid Research Letters, 2016. **10**(8): p. 583-586.
52. K.K., S.F. *Solar Frontier CIS Modules Made In Japan*. 2017; Available from: http://www.solar-frontier.com/eng/index.html.
53. Haaren, R., M. Morjaria, and V. Fthenakis, *Empirical assessment of short-term variability from utility-scale solar PV plants.* Progress in Photovoltaics: Research and Applications, 2014. **22**(5): p. 548-559.
54. Choi, Y.C., et al., *Highly Improved Sb2S3 Sensitized-Inorganic-Organic Heterojunction Solar Cells and Quantification of Traps by Deep-Level Transient Spectroscopy.* Advanced Functional Materials, 2014. **24**(23): p. 3587-3592.
55. Itzhaik, Y.N., O.; Page, M.; Hodes G., *Sb2S3-Sensitized Nanoporous TiO2 Solar Cells.* J. Phys. Chem. C, 2009. **113**(11): p. 4254–4256.
56. Nair, P.K.N., M. T. S.; Garcıa, V. M.; Arenas, O. L.; Pena, Y.; Castillo, A.; Ayala, I. T.; Gomezdaza, O.; Sanchez, A.; Campos, J.; Hu, H.; Suarez, R.; Rincon M. E., *Semiconductor thin films by chemical bath deposition for solar energy related applications.* Solar Energy Materials and Solar Cells, 1998. **52**: p. 313—344.
57. Nezu, S.L., G.; Chone, C.; Jacob, A.; Delatouche, B.; Pere, D.; Moisan C., *Light Soaking and Gas Effect on Nanocrystalline TiO2/Sb2S3/CuSCN Photovoltaic Cells following Extremely Thin Absorber Concept.* J. Phys. Chem. C, 2010. **114**: p. 6854–6859.
58. Larramona, G., et al., *Nanostructured photovoltaic cell of the type titanium dioxide, cadmium sulfide thin coating, and copper thiocyanate showing high quantum efficiency.* Chemistry of materials, 2006. **18**(6): p. 1688-1696.
59. Boix, P.P.L., G.; Jacob, A.; Delatouche, B.; Mora-Sero, I.; Bisquert, J., *Hole Transport and Recombination in All-Solid Sb2S3-Sensitized TiO2 Solar Cells Using CuSCN As Hole Transporter.* J. Phys. Chem. C, 2012. **116**: p. 1579–1587.
60. Christians, J.A.K., P. V., *Trap and Transfer. Two-Step Hole Injection Across the Sb2S3/CuSCN Interface in Solid-State Solar Cells.* American Chemical Society Nano, 2013. **7**(9): p. 7967–7974.
61. Ito, S., et al., *Fabrication of thin film dye sensitized solar cells with solar to electric power conversion efficiency over 10%.* Thin Solid Films, 2008. **516**(14): p. 4613-4619.
62. Darga, A.M., D.; Longeaud, C.; Savenije, T. J.; O'Regan, B.; Bourdais, S.; Muto, T.; Delatouche, B.; Dennler G., *On Charge Carrier Recombination in Sb2S3 and Its Implication for the Performance of Solar Cells.* J. Phys. Chem. C, 2013. **117**: p. 20525−20530.
63. Wedemeyer, H.M., J.; Chmielowski, R.; Bourdais, S.; Muto, T.; Sugiura, M.; Dennler G.; Bachmann, J., *Nanocrystalline solar cells with an antimony sulfide solid absorber by atomic layer deposition.* Energy Environ. Sci., 2013. **6**: p. 67-71.
64. Tsujimoto, K.N., D.; Ito, S.; Nishino, H.; Matsuyoshi, H.; Konno, A.; Kumara, G. R. A.; Tennakone, K., *TiO2 Surface Treatment Effects by Mg2+,Ba2+, and Al3+ on Sb2S3 Extremely Thin Absorber Solar Cells.* J. Phys. Chem. C, 2012. **116**: p. 13465−13471.
65. Ito, S.T., K.; Nguyen, D.; Manabe, K.; Nishino, H., *Doping effects in Sb2S3 absorber for full-inorganic printed solar cells with 5.7% conversion efficiency.* International journal of hydrogen energy, 2013: p. 1-6.

66. Boix, P.P.L., Y. H.; Fabregat-Santiago, F.; Im, S. H.; Mora-Sero, I.; Bisquert, J.; Seok, S. I., *From Flat to Nanostructured Photovoltaics: Balance betweenThickness of the Absorber and Charge Screening in Sensitized Solar Cells.* Am. Chem. Soc. Nano, 2012. **6**(1): p. 873–880.
67. Chang, J.A.R., J. H.; Im, S. H.; Lee, Y. H.; Kim, H.; Seok, S. I.; Nazeeruddin, Md. K.; Gratzel M., *High-Performance Nanostructured Inorganic-Organic Heterojunction Solar Cells.* Nano Lett., 2010. **10**: p. 2609–2612.
68. Im, S.H., et al., *Toward interaction of sensitizer and functional moieties in hole-transporting materials for efficient semiconductor-sensitized solar cells.* Nano Lett, 2011. **11**(11): p. 4789-93.
69. Moon, S.I., Y.; Yum, J.; Zakeeruddin, S. M.; Hodes, G.; Gratzel M., *Sb2S3-Based Mesoscopic Solar Cell using an Organic Hole Conductor.* J. Phys. Chem. Lett., 2010. **1**: p. 1524–1527.
70. Muto, T.L., G.; Dennler, G., *Unexpected Performances of Flat Sb2S3-Based Hybrid Extremely Thin Absorber Solar Cells.* Applied Physics Express, 2013. **6**(072301): p. 4.
71. Kim, D.H., et al., *Highly reproducible planar Sb2S3-sensitized solar cells based on atomic layer deposition.* Nanoscale, 2014. **6**(23): p. 14549-54.
72. Liu, C.P.W., H.E.; Ng, T.W.; Chen, Z. H.; Zhang, W. F.; Yan, C.; Tang, Y. B.; Bello, I.; Martinu, L.; Zhang, W. J.; Jha, S. K., *Hybrid photovoltaic cells based on ZnO/Sb2S3/P3HT heterojunctions.* Phys. Status Solidi, 2012. **B 249**(3): p. 627–633.
73. Kojima, A., et al., *Novel Photoelectrochemical Cell with Mesoscopic Electrodes Sensitized by Lead-Halide Compounds (2)*, in *210th ECS Meeting*. 2006, The Electrochemical Society: Cancun, Mexico. p. 1.
74. Kojima, A., et al., *Organometal halide perovskites as visible-light sensitizers for photovoltaic cells.* Journal of the American Chemical Society, 2009. **131**(17): p. 6050-6051.
75. Im, J.H., et al., *6.5% efficient perovskite quantum-dot-sensitized solar cell.* Nanoscale, 2011. **3**(10): p. 4088-93.
76. Kim, H.S., et al., *Lead iodide perovskite sensitized all-solid-state submicron thin film mesoscopic solar cell with efficiency exceeding 9%.* Sci Rep, 2012. **2**: p. 591.
77. Lee, M.M., et al., *Efficient hybrid solar cells based on meso-superstructured organometal halide perovskites.* Science, 2012. **338**(6107): p. 643-7.
78. Etgar, L., et al., *Mesoscopic CH3NH3PbI3/TiO2 heterojunction solar cells.* J Am Chem Soc, 2012. **134**(42): p. 17396-9.
79. R. Komiya, A.F., N. Murofushi, N. Koide, R. Yamanaka, H. Katayama. *Improvement of the conversion efficiency of a monolithic type dye-sensitized solar cell module.* in *21st International Photovoltaic Science and Engineering Conference*. 2011. Fukuoka, Japan.
80. Liu, M., M.B. Johnston, and H.J. Snaith, *Efficient planar heterojunction perovskite solar cells by vapour deposition.* Nature, 2013. **501**(7467): p. 395-8.
81. Ball, J.M., et al., *Low-temperature processed meso-superstructured to thin-film perovskite solar cells.* Energy & Environmental Science, 2013. **6**(6): p. 1739.
82. Leijtens, T., et al., *The Importance of Perovskite Pore Filling in Organometal Mixed Halide Sensitized TiO2-Based Solar Cells.* J Phys Chem Lett, 2014. **5**(7): p. 1096-102.

83. Heo, J.H., et al., *Efficient inorganic–organic hybrid heterojunction solar cells containing perovskite compound and polymeric hole conductors.* Nature Photonics, 2013. **7**(6): p. 486-491.
84. Ryu, S., et al., *Voltage output of efficient perovskite solar cells with high open-circuit voltage and fill factor.* Energy & Environmental Science, 2014. **7**(8): p. 2614.
85. Zhang, W., et al., *Systematic improvement in charge carrier mobility of air stable triarylamine copolymers.* J Am Chem Soc, 2009. **131**(31): p. 10814-5.
86. *Toronto Research Chemicals*. 19 March 2016]; Products for innovative research]. Available from: http://www.trc-canada.com/.
87. Jeon, N.J., et al., *Solvent engineering for high-performance inorganic-organic hybrid perovskite solar cells.* Nat Mater, 2014. **13**(9): p. 897-903.
88. Xiao, M., et al., *A Fast Deposition-Crystallization Procedure for Highly Efficient Lead Iodide Perovskite Thin-Film Solar Cells.* Angewandte Chemie, 2014. **126**(37): p. 10056-10061.
89. Yang, W.S., et al., *High-performance photovoltaic perovskite layers fabricated through intramolecular exchange.* Science, 2015. **348**(6240): p. 1234-7.
90. Burschka, J., et al., *Sequential deposition as a route to high-performance perovskite-sensitized solar cells.* Nature, 2013. **499**(7458): p. 316-9.
91. Pellet, N., et al., *Mixed-organic-cation perovskite photovoltaics for enhanced solar-light harvesting.* Angew Chem Int Ed Engl, 2014. **53**(12): p. 3151-7.
92. Leijtens, T., et al., *Overcoming ultraviolet light instability of sensitized TiO2 with meso-superstructured organometal tri-halide perovskite solar cells.* Nat Commun, 2013. **4**: p. 2885.
93. Yi, C., et al., *Perovskite Photovoltaics with Outstanding Performance Produced by Chemical Conversion of Bilayer Mesostructured Lead Halide/TiO2 Films.* Adv Mater, 2016. **28**(15): p. 2964-70.
94. Noh, J.H., et al., *Chemical management for colorful, efficient, and stable inorganic-organic hybrid nanostructured solar cells.* Nano Lett, 2013. **13**(4): p. 1764-9.
95. Jeon, N.J., et al., *Compositional engineering of perovskite materials for high-performance solar cells.* Nature, 2015. **517**(7535): p. 476-80.
96. Saliba, M., et al., *Cesium-containing triple cation perovskite solar cells: improved stability, reproducibility and high efficiency.* Energy Environ. Sci., 2016. **9**(6): p. 1989-1997.
97. Correa Baena, J.P., et al., *Highly efficient planar perovskite solar cells through band alignment engineering.* Energy Environ. Sci., 2015. **8**(10): p. 2928-2934.
98. Tricoli, A., A.S. Wallerand, and M. Righettoni, *Highly porous TiO2 films for dye sensitized solar cells.* Journal of Materials Chemistry, 2012. **22**(28): p. 14254.
99. Cavicchi, R.E., et al., *Layer-by-layer growth of epitaxial SnO2 on sapphire by reactive sputter deposition.* Applied Physics Letters, 1992. **61**(16): p. 1921.
100. Choi, D.-w. and J.-S. Park, *Highly conductive SnO2 thin films deposited by atomic layer deposition using tetrakis-dimethyl-amine-tin precursor and ozone reactant.* Surface and Coatings Technology, 2014. **259**: p. 238-243.
101. Elam, J.W., et al., *Atomic layer deposition of tin oxide films using tetrakis(dimethylamino) tin.* Journal of Vacuum Science & Technology A: Vacuum, Surfaces, and Films, 2008. **26**(2): p. 244.

102. Khan, A.F., et al., *Effect of annealing on electrical resistivity of rf-magnetron sputtered nanostructured SnO2 thin films.* Applied Surface Science, 2009. **255**(20): p. 8562-8565.
103. Stjerna, B., E. Olsson, and C.G. Granqvist, *Optical and electrical properties of radio frequency sputtered tin oxide films doped with oxygen vacancies, F, Sb, or Mo.* Journal of Applied Physics, 1994. **76**(6): p. 3797.
104. Wang, C.Y., *Antimony: Its history, chemistry, mineralogy, geology, matallurgy, uses, preparations, analysis, production, and valuation; with complete bibliographies.* 2nd ed. 1919, London: Charles Griffin & Company, Limited.
105. Bohac, P. and P. Kaufmann, *Zone refining of antimony trisulfide.* Materials Research Bulletin, 1975. **10**(7): p. 613-622.
106. Mills, K.C., *Thermodynamic Data for Inorganic Sulphides, Selenides and Tellurides*. 1974, London: Butterworths.
107. Kuze, S., et al., *X-ray diffraction evidence for a monoclinic form of stibnite, Sb2S3, below 290 K.* American Mineralogist, 2004. **89**(7): p. 1022-1025.
108. Zakaznova-Herzog, V.P., et al., *High resolution XPS study of the large-band-gap semiconductor stibnite (Sb2S3): Structural contributions and surface reconstruction.* Surface Science, 2006. **600**(2): p. 348-356.
109. Scherrer, P., *Bestimmung der Größe und der inneren Struktur von Kolloidteilchen mittels Röntgenstrahlen.* Nachrichten von der Gesellschaft der Wissenschaften zu Göttingen, Mathematisch-Physikalische Klasse, 1918. **1918**: p. 98-100.
110. Zhang, L., et al., *Preparation of shuttle-like Sb2S3 nanorod-bundles via a solvothermal approach under alkaline condition.* Crystal Research and Technology, 2010. **45**(2): p. 178-182.
111. Instruments, O. *EDS for SEM and FIB - Oxford Instruments*. 2016 [cited 2014 14 September]; Available from: http://www.oxford-instruments.com/products/microanalysis/energy-dispersive-x-ray-systems-eds-edx.
112. Choi, Y.C. and S.I. Seok, *Efficient Sb2S3-Sensitized Solar Cells Via Single-Step Deposition of Sb2S3 Using S/Sb-Ratio-Controlled SbCl3-Thiourea Complex Solution.* Advanced Functional Materials, 2015. **25**(19): p. 2892-2898.
113. Gui, E.L.K., A. M.; Pramana, S. S.; Yantara, N.; Mathews, N.; Mhaisalkar, S., *Effect of TiO2 Mesoporous Layer and Surface Treatments in Determining Efficiencies in Antimony Sulfide-(Sb2S3) Sensitized Solar Cells.* Journal of The Electrochemical Society, 2012. **159**: p. B247-B250.
114. Maiti, N.I., S. H.; Lim C.; Seok, S. I., *A chemical precursor for depositing Sb2S3 onto mesoporous TiO2 layers in nonaqueous media and its application to solar cells.* Dalton Trans., 2012. **41**: p. 11569-11572.
115. Lee, D.U., et al., *Defect states in hybrid solar cells consisting of Sb2S3 quantum dots and TiO2 nanoparticles.* Applied Physics Letters, 2013. **103**(2): p. 023901.
116. Calixto-Rodriguez, M., et al., *A comparative study of the physical properties of Sb2S3 thin films treated with N2 AC plasma and thermal annealing in N2.* Applied Surface Science, 2010. **256**(8): p. 2428-2433.
117. Ghraïri, N., et al., *Comparative studies of the properties of thermal annealed Sb2S3 thin films.* Chalcogenide Letters, 2010. **7**(3): p. 217-225.
118. Ito, S., et al., *Effects of Surface Blocking Layer of Sb2S3 on Nanocrystalline TiO2 for CH3NH3PbI3 Perovskite Solar Cells.* The Journal of Physical Chemistry C, 2014. **118**(30): p. 16995-17000.

119. Savadogo, O. and K.C. Mandal, *Studies on new chemically deposited photoconducting antimony trisulphide thin films.* Solar energy materials and solar cells, 1992. **26**(1-2): p. 117-136.
120. Tigau, N., *Influence of thermoannealing on crystallinity and optical properties of Sb2S3 thin films.* Crystal Research and Technology, 2007. **42**(3): p. 281-285.
121. Versavel , M.Y.H., J. A., *Structural and optical properties of amorphous and crystalline antimony sulfide thin-films.* Thin Solid Films, 2007. **515**: p. 7171-7176.
122. Messina, S., M.T.S. Nair, and P.K. Nair, *Antimony sulfide thin films in chemically deposited thin film photovoltaic cells.* Thin Solid Films, 2007. **515**(15): p. 5777-5782.
123. Nair, M., et al., *Chemically Deposited Sb2S3 and Sb2S3-CuS Thin Films.* Journal of The Electrochemical Society, 1998. **145**(6): p. 2113-2120.
124. Ted Paella, I. *Vacuum Deposition Techniques and Tables*. 2016 [cited 2014 14 September]; Available from: http://www.tedpella.com/company_html/Vacuum-Deposition-Techniques-and-Tables.htm.
125. Filip, M.R., et al., *Steric engineering of metal-halide perovskites with tunable optical band gaps.* Nat Commun, 2014. **5**: p. 5757.
126. Volonakis, G., et al., *Lead-Free Halide Double Perovskites via Heterovalent Substitution of Noble Metals.* J Phys Chem Lett, 2016. **7**(7): p. 1254-9.
127. Christians, J.A., P.A. Miranda Herrera, and P.V. Kamat, *Transformation of the excited state and photovoltaic efficiency of CH3NH3PbI3 perovskite upon controlled exposure to humidified air.* J Am Chem Soc, 2015. **137**(4): p. 1530-8.
128. Conings, B., et al., *Intrinsic Thermal Instability of Methylammonium Lead Trihalide Perovskite.* Advanced Energy Materials, 2015. **5**(15): p. 1500477.
129. Jacobsson, T.J., et al., *Room Temperature as a Goldilocks Environment for CH3NH3PbI3 Perovskite Solar Cells: The Importance of Temperature on Device Performance.* The Journal of Physical Chemistry C, 2016. **120**(21): p. 11382-11393.
130. Misra, R.K., et al., *Temperature- and Component-Dependent Degradation of Perovskite Photovoltaic Materials under Concentrated Sunlight.* J Phys Chem Lett, 2015. **6**(3): p. 326-30.
131. Stoumpos, C.C., C.D. Malliakas, and M.G. Kanatzidis, *Semiconducting tin and lead iodide perovskites with organic cations: phase transitions, high mobilities, and near-infrared photoluminescent properties.* Inorg Chem, 2013. **52**(15): p. 9019-38.
132. Laban, W.A. and L. Etgar, *Depleted hole conductor-free lead halide iodide heterojunction solar cells.* Energy & Environmental Science, 2013. **6**(11): p. 3249.
133. Shi, D., et al., *Solar cells. Low trap-state density and long carrier diffusion in organolead trihalide perovskite single crystals.* Science, 2015. **347**(6221): p. 519-22.
134. Schulz, P., et al., *Interface energetics in organo-metal halide perovskite-based photovoltaic cells.* Energy & Environmental Science, 2014. **7**(4): p. 1377.
135. Supasai, T., et al., *Formation of a passivating CH3NH3PbI3/PbI2 interface during moderate heating of CH3NH3PbI3 layers.* Applied Physics Letters, 2013. **103**(18): p. 183906.

136. Shi, T., W.-J. Yin, and Y. Yan, *Predictions for p-Type CH3NH3PbI3Perovskites.* The Journal of Physical Chemistry C, 2014. **118**(44): p. 25350-25354.
137. Yin, W.-J., T. Shi, and Y. Yan, *Unusual defect physics in CH3NH3PbI3 perovskite solar cell absorber.* Applied Physics Letters, 2014. **104**(6): p. 063903.
138. Scanlon, D.O., et al., *Band alignment of rutile and anatase TiO2.* Nat Mater, 2013. **12**(9): p. 798-801.
139. Yang, S., et al., *Crystal shape engineering of anatase TiO2and its biomedical applications.* CrystEngComm, 2015. **17**(35): p. 6617-6631.
140. Li, G., et al., *Synergistic effect between anatase and rutile TiO2 nanoparticles in dye-sensitized solar cells.* Dalton Trans, 2009(45): p. 10078-85.
141. Tang, H., et al., *Electrical and optical properties of TiO2 anatase thin films.* Journal of Applied Physics, 1994. **75**(4): p. 2042.
142. Grätzel, M., *Photoelectrochemical cells.* Nature, 2001. **414**(6861): p. 338-344.
143. Xiong, G., et al., *Photoemission Electron Microscopy of TiO2 Anatase Films Embedded with Rutile Nanocrystals.* Advanced Functional Materials, 2007. **17**(13): p. 2133-2138.
144. Leskelä, M. and M. Ritala, *Atomic layer deposition (ALD): from precursors to thin film structures.* Thin solid films, 2002. **409**(1): p. 138-146.
145. Triani, G., et al. *Atomic layer deposition of TiO2/Al2O3 films for optical applications*. in *Advances in Thin-Film Coatings for Optical Applications II*. 2005. San Diego, California, USA: SPIE.
146. Beneq ©. *Beneq | Thin Film Equipment*. 2016 [cited 2013 September]; Available from: http://beneq.com/.
147. Hagleitner, C., et al., *Smart single-chip gas sensor microsystem.* Nature, 2001. **414**(6861): p. 293-6.
148. Kühne, S., et al., *Wafer-level flame-spray-pyrolysis deposition of gas-sensitive layers on microsensors.* Journal of Micromechanics and Microengineering, 2008. **18**(3): p. 035040.
149. Mädler, L., et al., *Direct formation of highly porous gas-sensing films by in situ thermophoretic deposition of flame-made Pt/SnO2 nanoparticles.* Sensors and Actuators B: Chemical, 2006. **114**(1): p. 283-295.
150. Mueller, R., L. Madler, and S.E. Pratsinis, *Nanoparticle synthesis at high production rates by flame spray pyrolysis.* Chemical Engineering Science, 2003. **58**(10): p. 1969-1976.
151. Nasiri, N., et al., *Ultraporous Electron-Depleted ZnO Nanoparticle Networks for Highly Sensitive Portable Visible-Blind UV Photodetectors.* Adv Mater, 2015. **27**(29): p. 4336-43.
152. Teleki, A., et al., *Sensing of organic vapors by flame-made TiO2 nanoparticles.* Sensors and Actuators B: Chemical, 2006. **119**(2): p. 683-690.
153. Tricoli, A., et al., *Micropatterning Layers by Flame Aerosol Deposition-Annealing.* Advanced Materials, 2008. **20**(16): p. 3005-3010.
154. Barsan, N. and U. Weimar, *Conduction model of metal oxide gas sensors.* Journal of Electroceramics, 2001. **7**(3): p. 143-167.
155. Cox, D.F., T.B. Fryberger, and S. Semancik, *Oxygen vacancies and defect electronic states on theSnO2(110)-1×1surface.* Physical Review B, 1988. **38**(3): p. 2072-2083.
156. Mullings, M.N., C. Hägglund, and S.F. Bent, *Tin oxide atomic layer deposition from tetrakis(dimethylamino)tin and water.* Journal of Vacuum Science & Technology A: Vacuum, Surfaces, and Films, 2013. **31**(6): p. 061503.

157. Choi, D.-w., W.J. Maeng, and J.-S. Park, *The conducting tin oxide thin films deposited via atomic layer deposition using Tetrakis-dimethylamino tin and peroxide for transparent flexible electronics.* Applied Surface Science, 2014. **313**: p. 585-590.
158. Fonstad, C.G. and R.H. Rediker, *Electrical Properties of High-Quality Stannic Oxide Crystals.* Journal of Applied Physics, 1971. **42**(7): p. 2911.
159. Goodchild, R.G., J.B. Webb, and D.F. Williams, *Electrical properties of highly conducting and transparent thin films of magnetron sputtered SnO2.* Journal of Applied Physics, 1985. **57**(6): p. 2308.
160. Batzill, M., et al., *Tuning surface properties of SnO2(101) by reduction.* Journal of Physics and Chemistry of Solids, 2006. **67**(9-10): p. 1923-1929.
161. Chang, S.-S., S.O. Yoon, and H.J. Park, *Characteristics of SnO2 annealed in reducing atmosphere.* Ceramics International, 2005. **31**(3): p. 405-410.
162. Minami, T., T. Miyata, and T. Yamamoto, *Work function of transparent conducting multicomponent oxide thin films prepared by magnetron sputtering.* Surface and Coatings Technology, 1998. **108**: p. 583-587.
163. Feucht, D.L., *Heterojunctions in photovoltaic devices.* Journal of Vacuum Science and Technology, 1977. **14**(1): p. 57.
164. Liu, T., et al., *Interface Study of ITO/ZnO and ITO/SnO2 Complex Transparent Conductive Layers and Their Effect on CdTe Solar Cells.* International Journal of Photoenergy, 2013. **2013**: p. 1-8.
165. Trost, S., et al., *Tin Oxide (SnOx) as Universal "Light-Soaking" Free Electron Extraction Material for Organic Solar Cells.* Advanced Energy Materials, 2015. **5**(17): p. 1500277.
166. Tennakone, K., et al., *Semiconducting and Photoelectrochemical Properties of n- and p-Type β-CuCNS.* Physica Status Solidi (a), 1987. **103**(2): p. 491-497.
167. Edri, E., H. Cohen, and G. Hodes, *Band alignment in partial and complete ZnO/ZnS/CdS/CuSCN extremely thin absorber cells: an X-ray photoelectron spectroscopy study.* ACS Appl Mater Interfaces, 2013. **5**(11): p. 5156-64.
168. Perera, V.P.S., et al., *Doping CuSCN films for enhancement of conductivity: Application in dye-sensitized solid-state solar cells.* Solar Energy Materials and Solar Cells, 2005. **86**(3): p. 443-450.
169. Premalal, E.V., et al., *Tuning chemistry of CuSCN to enhance the performance of TiO2/N719/CuSCN all-solid-state dye-sensitized solar cell.* Chem Commun (Camb), 2010. **46**(19): p. 3360-2.
170. *Nanostructured and Photoelectrochemical Systems for Solar Photon Conversion*. Series on Photoconversion of Solar Energy, ed. M.D. Archer. London: Imperial College Press. 781.
171. Liu, D., J. Yang, and T.L. Kelly, *Compact layer free perovskite solar cells with 13.5% efficiency.* J Am Chem Soc, 2014. **136**(49): p. 17116-22.
172. Snaith, H.J. and M. Grätzel, *Enhanced charge mobility in a molecular hole transporter via addition of redox inactive ionic dopant: Implication to dye-sensitized solar cells.* Applied Physics Letters, 2006. **89**(26): p. 262114.
173. Canestraro, C.D., et al., *Strong inter-conduction-band absorption in heavily fluorine doped tin oxide.* Applied Surface Science, 2008. **255**(5): p. 1874-1879.
174. Helander, M.G., et al., *Work function of fluorine doped tin oxide.* Journal of Vacuum Science & Technology A: Vacuum, Surfaces, and Films, 2011. **29**(1): p. 011019.

175. Bröker, B., et al., *Gold work function reduction by 2.2eV with an air-stable molecular donor layer.* Applied Physics Letters, 2008. **93**(24): p. 243303.
176. Mane, R.S.L., C. D., *Thickness-dependent properties of chemically deposited Sb2S3 thin films.* Materials Chemistry and Physics, 2003. **82**: p. 347-354.
177. El Zawawi, I.K.A.-M., A.; Terra, F. S.; Mounir M., *Substrate temperature effect on the optical and electrical properties of antimony trisulfide thin films.* Thin Solid Films, 1998. **324**: p. 300–304.
178. El-Shazly, A.A.S., M. A. M.; El-Samanoudy, M. M.; Ammar, A. H.; Assim, E. M., *The effect of deposition rate and heat treatment on conduction and charge carrier transport mechanisms in Sb2S3 films.* Applied Surface Science, 2002. **189**: p. 129-137.
179. Heo, J.H.I., S. H.; Kim, H.; Boix, P. P.; Lee, S. J.; Seok, S. I.; Mora-Seró, I.; Bisquert, J., *Sb2S3‑Sensitized Photoelectrochemical Cells: Open Circuit VoltageEnhancement through the Introduction of Poly-3-hexylthiophene Interlayer.* J. Phys. Chem. C, 2012. **116**: p. 20717−20721.
180. Liu, C.P.C., Z. H.; Wang, H. E.; Jha, S. K.; Zhang, W. J.; Bello I.; Zapien, J. A., *Enhanced performance by incorporation of zinc oxide nanowire array for organic-inorganic hybrid solar cells.* Appl. Phys. Lett., 2012. **100**: p. 243102.
181. Rajpure, K.Y.B., C. H., *(Photo)electrochemical investigations on spray deposited n-Sb2S3 thin film/polyiodide/C photoelectrochemical solar cells.* Materials Chemistry and Physics, 2000. **63**: p. 263-269.
182. Georgiev, D.G.B.P.M., M., *Rigidity transitions and molecular structure of AsxSe1-x glasses.* PHYSICAL REVIEW B, 2000. **62**(14): p. 4.
183. Zhou, Y., et al., *Thin-film Sb2Se3 photovoltaics with oriented one-dimensional ribbons and benign grain boundaries.* Nature Photonics, 2015. **9**(6): p. 409-415.
184. Choi, Y.C., et al., *Efficient Inorganic-Organic Heterojunction Solar Cells Employing Sb2(Sx/Se1-x)3 Graded-Composition Sensitizers.* Advanced Energy Materials, 2014. **4**(7): p. 1301680.
185. Bach, U. and T. Daeneke, *A solid advancement for dye-sensitized solar cells.* Angew Chem Int Ed Engl, 2012. **51**(42): p. 10451-2.
186. Asahi, R., et al., *Nitrogen-doped titanium dioxide as visible-light-sensitive photocatalyst: designs, developments, and prospects.* Chem Rev, 2014. **114**(19): p. 9824-52.
187. Wolf, M. and H. Rauschenbach, *Series resistance effects on solar cell measurements.* Advanced Energy Conversion, 1963. **3**(2): p. 455-479.
188. Heo, J.H. and S.H. Im, *CH3NH3PbI3/poly-3-hexylthiophen perovskite mesoscopic solar cells: Performance enhancement by Li-assisted hole conduction.* physica status solidi (RRL) - Rapid Research Letters, 2014. **8**(10): p. 816-821.
189. Gratzel, M., *The light and shade of perovskite solar cells.* Nat Mater, 2014. **13**(9): p. 838-42.
190. Park, N.G., *Organometal Perovskite Light Absorbers Toward a 20% Efficiency Low-Cost Solid-State Mesoscopic Solar Cell.* Journal of Physical Chemistry Letters, 2013. **4**(15): p. 2423-2429.
191. Snaith, H.J., *Perovskites: The Emergence of a New Era for Low-Cost, High-Efficiency Solar Cells.* Journal of Physical Chemistry Letters, 2013. **4**(21): p. 3623-3630.
192. Green, M.A., A. Ho-Baillie, and H.J. Snaith, *The emergence of perovskite solar cells.* Nature Photonics, 2014. **8**(7): p. 506-514.

193. Blakers, A.W., et al., *22.8% efficient silicon solar cell.* Applied Physics Letters, 1989. **55**(13): p. 1363.
194. Snaith, H.J., et al., *Charge collection and pore filling in solid-state dye-sensitized solar cells.* Nanotechnology, 2008. **19**(42): p. 424003.
195. Tsekouras, G., et al., *Charge Transport in Dye-Sensitized Solar Cells Based on Flame-made TiO2 Nanoparticles.* IEEE Journal of Selected Topics in Quantum Electronics, 2010. **16**(6): p. 1641-1648.
196. Adli, H.K., et al., *Effects of Porosity and Amount of Surface Hydroxyl Groups of a Porous TiO2 Layer on the Performance of a CH3NH3PbI3 Perovskite Photovoltaic Cell.* The Journal of Physical Chemistry C, 2015. **119**(39): p. 22304-22309.
197. Gardon, M. and J.M. Guilemany, *Milestones in Functional Titanium Dioxide Thermal Spray Coatings: A Review.* Journal of Thermal Spray Technology, 2014. **23**(4): p. 577-595.
198. Di Fonzo, F., et al., *Hierarchically organized nanostructured TiO2 for photocatalysis applications.* Nanotechnology, 2009. **20**(1): p. 015604.
199. Sauvage, F., et al., *Hierarchical TiO2 photoanode for dye-sensitized solar cells.* Nano Lett, 2010. **10**(7): p. 2562-7.
200. Thimsen, E. and P. Biswas, *Nanostructured photoactive films synthesized by a flame aerosol reactor.* AIChE Journal, 2007. **53**(7): p. 1727-1735.
201. Thimsen, E., N. Rastgar, and P. Biswas, *Nanostructured TiO2 Films with Controlled Morphology Synthesized in a Single Step Process: Performance of Dye-Sensitized Solar Cells and Photo Watersplitting.* The Journal of Physical Chemistry C, 2008. **112**(11): p. 4134-4140.
202. Chuangchote, S., T. Sagawa, and S. Yoshikawa, *Efficient dye-sensitized solar cells using electrospun TiO2 nanofibers as a light harvesting layer.* Applied Physics Letters, 2008. **93**(3): p. 033310.
203. Fujihara, K., et al., *Spray deposition of electrospun TiO2 nanorods for dye-sensitized solar cell.* Nanotechnology, 2007. **18**(36): p. 365709.
204. Song, M.Y., et al., *Electrospun TiO2 electrodes for dye-sensitized solar cells.* Nanotechnology, 2004. **15**(12): p. 1861-1865.
205. Di Fonzo, F., et al., *Growth regimes in pulsed laser deposition of aluminum oxide films.* Applied Physics A, 2008. **93**(3): p. 765-769.
206. Pawlowski, L., *The science and eng. of thermal spray coating*. 2nd ed. 2008, Great Britain: John Wiley & Sons Ltd. 656.
207. Perednis, D. and L.J. Gauckler, *Thin film deposition using spray pyrolysis.* Journal of Electroceramics, 2005. **14**(2): p. 103-111.
208. Corporation, S.-T. *Sono-Tek Ultrasonic Spray Systems - Precision High Performance Coating Solutions*. 2016 [cited 2016 7 July]; Sono-Tek Corporation is the world leader in ultrasonic spray systems for applying precise, thin film coatings.]. Available from: http://www.sono-tek.com/.
209. Inc., S. *Automated Ultrasonic Automatic Nozzle Spraying Equipment*. 2000 [cited 2016 7 July]; Available from: http://www.sonozap.com/.
210. Mochel, J.M., *Electrically conducting coatings on glass and other ceramic bodies*, U.S.p. office, Editor. 1951: USA.
211. Nippon Sheet Glass Co., L. *TCO Glass, Transparent Conductive Oxide*. NSG TEC 2016 [cited 2016 7 July]; NSG TEC™ is a group of products, including a comprehensive range of TCO glass (Transparent Conductive Oxide coated glass), optimised to suit a variety of thin film photovoltaics, with different haze

and conductivity levels.]. Available from: http://www.pilkington.com/products/bp/bybenefit/solarenergy/tec/home.htm
212. Grätzel, M., *Dye-sensitized solar cells.* Journal of Photochemistry and Photobiology C: Photochemistry Reviews, 2003. **4**(2): p. 145-153.
213. Nasiri, N., et al., *Self-assembly dynamics and accumulation mechanisms of ultra-fine nanoparticles.* Nanoscale, 2015. **7**(21): p. 9859-67.
214. Tiwana, P., et al., *Electron mobility and injection dynamics in mesoporous ZnO, SnO2, and TiO2 films used in dye-sensitized solar cells.* ACS Nano, 2011. **5**(6): p. 5158-66.
215. Edri, E., et al., *Why lead methylammonium tri-iodide perovskite-based solar cells require a mesoporous electron transporting scaffold (but not necessarily a hole conductor).* Nano Lett, 2014. **14**(2): p. 1000-4.
216. Dong, Q., et al., *Insight into Perovskite Solar Cells Based on SnO2 Compact Electron-Selective Layer.* The Journal of Physical Chemistry C, 2015. **119**(19): p. 10212-10217.
217. Duan, J., et al., *Low-temperature processed SnO2 compact layer for efficient mesostructure perovskite solar cells.* Applied Surface Science, 2016.
218. Ke, W., et al., *Low-temperature solution-processed tin oxide as an alternative electron transporting layer for efficient perovskite solar cells.* J Am Chem Soc, 2015. **137**(21): p. 6730-3.
219. Liu, P., et al., *Interfacial electronic structure at the CH3NH3PbI3/MoOx interface.* Applied Physics Letters, 2015. **106**(19): p. 193903.
220. Liu, Q., et al., *Enhanced Stability of Perovskite Solar Cells with Low-Temperature Hydrothermally Grown SnO2 Electron Transport Layers.* Advanced Functional Materials, 2016.
221. Murugadoss, G., et al., *An efficient electron transport material of tin oxide for planar structure perovskite solar cells.* Journal of Power Sources, 2016. **307**: p. 891-897.
222. Son, D.-Y., et al., *11% Efficient Perovskite Solar Cell Based on ZnO Nanorods: An Effective Charge Collection System.* The Journal of Physical Chemistry C, 2014. **118**(30): p. 16567-16573.
223. Song, J., et al., *Low-temperature SnO2-based electron selective contact for efficient and stable perovskite solar cells.* J. Mater. Chem. A, 2015. **3**(20): p. 10837-10844.
224. Song, J., et al., *Low-temperature-processed ZnO–SnO2 nanocomposite for efficient planar perovskite solar cells.* Solar Energy Materials and Solar Cells, 2016. **144**: p. 623-630.
225. Wang, K., et al., *Low-Temperature and Solution-Processed Amorphous WO(x) as Electron-Selective Layer for Perovskite Solar Cells.* J Phys Chem Lett, 2015. **6**(5): p. 755-9.
226. Xiong, L., et al., *Performance enhancement of high temperature SnO2-based planar perovskite solar cells: electrical characterization and understanding of the mechanism.* J. Mater. Chem. A, 2016. **4**(21): p. 8374-8383.
227. Manifacier, J.C., et al., *Optical and electrical properties of SnO2 thin films in relation to their stoichiometric deviation and their crystalline structure.* Thin Solid Films, 1977. **41**(2): p. 127-135.
228. Komornicki, S., M. Radecka, and M. Rekas, *Frequency-dependent electrical properties in the system SnO2-TiO2.* Journal of Materials Science: Materials in Electronics, 2001. **12**(1): p. 11-16.

229. Radecka, M., et al., *Transport properties of (Sn,Ti)O2 polycrystalline ceramics and thin films.* Solid State Ionics, 1999. **119**(1): p. 43-48.
230. Dyalsingh, H.M. and J. Kakalios, *Thermopower and conductivity activation energies in hydrogenated amorphous silicon.* Phys Rev B Condens Matter, 1996. **54**(11): p. 7630-7633.
231. Tao, C., et al., *17.6% stabilized efficiency in low-temperature processed planar perovskite solar cells.* Energy Environ. Sci., 2015. **8**(8): p. 2365-2370.
232. Wojciechowski, K., et al., *C60 as an Efficient n-Type Compact Layer in Perovskite Solar Cells.* J Phys Chem Lett, 2015. **6**(12): p. 2399-405.
233. Polman, A., et al., *Photovoltaic materials: Present efficiencies and future challenges.* Science, 2016. **352**(6283): p. aad4424.
234. Stranks, S.D., et al., *Electron-hole diffusion lengths exceeding 1 micrometer in an organometal trihalide perovskite absorber.* Science, 2013. **342**(6156): p. 341-4.
235. Niu, G.D., et al., *Study on the stability of CH3NH3PbI3 films and the effect of post-modification by aluminum oxide in all-solid-state hybrid solar cells.* Journal of Materials Chemistry A, 2014. **2**(3): p. 705-710.
236. Bao, D., H. Gu, and A. Kuang, *Sol-gel-derived c-axis oriented ZnO thin films.* Thin solid films, 1998. **312**(1): p. 37-39.
237. Iijima, K., et al., *Preparation of c-axis oriented PbTiO3 thin films and their crystallographic, dielectric, and pyroelectric properties.* Journal of applied physics, 1986. **60**(1): p. 361-367.
238. Kang, H.W., J.W. Lee, and N.G. Park, *Effect of double blocking layers at TiO2/Sb2S3 and Sb2S3/spiro-MeOTAD interfaces on photovoltaic performance.* Faraday Discuss, 2014. **176**: p. 287-99.